Fiber-Reinforced Cement Composites: Mechanical Properties and Structural Implications 2019

Lead Guest Editor: Doo-Yeol Yoo
Guest Editors: Nemkumar Banthia, Kazunori Fujikake, Young H. Kim, and Rishi Gupta

Fiber-Reinforced Cement Composites: Mechanical Properties and Structural Implications 2019

Fiber-Reinforced Cement Composites: Mechanical Properties and Structural Implications 2019

Lead Guest Editor: Doo-Yeol Yoo
Guest Editors: Nemkumar Banthia, Kazunori Fujikake, Young H. Kim, and Rishi Gupta

Editorial Board

Contents

Editorial

Fiber-Reinforced Cement Composites: Mechanical Properties and Structural Implications 2019

Doo-Yeol Yoo [ID],[1] **Nemkumar Banthia** [ID],[2] **Kazunori Fujikake,**[3] **Young Hoon Kim** [ID],[4] **and Rishi Gupta** [ID][5]

[1]*Department of Architectural Engineering, Hanyang University, 222 Wangsimni-ro, Seongdong-gu, Seoul 04763, Republic of Korea*
[2]*Department of Civil Engineering, The University of British Columbia, 6250 Applied Science Lane, Vancouver, BC V6T 1Z4, Canada*
[3]*Department of Civil and Environmental Engineering, National Defense Academy, Yokosuka 239 8686, Japan*
[4]*Department of Civil and Environmental Engineering, University of Louisville, Louisville, KY 40292, USA*
[5]*Department of Civil Engineering, University of Victoria, 3800 Finnerty Road, Victoria, BC V8W 2Y2, Canada*

Correspondence should be addressed to Doo-Yeol Yoo; dyyoo@hanyang.ac.kr

Received 18 July 2019; Accepted 18 July 2019; Published 4 August 2019

In order to overcome inherent brittleness of concrete, numerous studies on the development of high ductility fiber-reinforced cement composites have been performed thus far. Several different types of fiber-reinforced cement composites with metallic, polymer, carbon, glass, nylon, and waste tire fibers have been successfully developed and effectively applied for building structures due to their benefits of limiting crack propagation and widening from fiber bridging. High-performance fiber-reinforced cement composites showing strain- or deflection-hardening behavior with multiple microcracks were recently developed, and various relevant studies are actively underway.

This special issue gives a comprehensive overview on fiber-reinforced cement composites, including aspects related to material behavior, strengthening performance, numerical simulation and modeling, and structural implication under various loading conditions (i.e., static, impact, blast, fire, fatigue, etc.). The selection of papers in this special issue was very rigorous.

A number of studies developed a new type of fiber-reinforced cement composites and evaluated their mechanical properties. K. Patel et al. studied to practically use recycled glass fibers as a reinforcement for concrete recovered from industrial GFRP-acrylic waste. The maximum enhancement of 22% was achieved for 0.3% (by volume) of recycled glass fibers compared to the control concrete sample under the compressive loads, regardless of curing regime, and also the tensile samples having 0.3 vol.% recycled glass fibers exhibited the maximum tensile strength of 3.46 MPa, which is higher than that (2.48 MPa) of control sample. Z. Yao et al. evaluated several mechanical properties of the macro polypropylene (PP) fiber-reinforced concrete, including the flexural and tensile strengths, fracture toughness, and fracture energy. They reported that the inclusion of macro PP fibers is effective in enhancing the strength and energy absorption capacity of plain concrete. At the fiber content of 1% or 1.5%, 29.3% and 21.4% higher flexural and tensile strengths were obtained as compared to those of plain concrete, and the fracture energy was also improved with increasing the fiber content. S. Karthiyaini et al. successfully predicted the mechanical strength of fiber-reinforced cement composites using multiple regression analysis (MRA) and artificial neural network (ANN). They effectively predicted the compressive strength through ANN model with a coefficient of determination (R^2) of 0.93, while the split tensile and flexural strengths were well simulated by using the MRA model. L. Wang et al. studied the effectiveness of calcium carbonate ($CaCO_3$) whisker and fly ash on the mechanical properties of cement mortar under high temperatures and reported that the hybrid use of $CaCO_3$

whisker and fly ash possess preferable high-temperature resistance capacity due to the filler and crack bridging effect of the whisker and accelerated pozzolanic reaction of fly ash. X.-Y. Wang suggested an integrated hydration-strength model for cement-limestone-metakaolin ternary blends. Based on parameter analysis, the synergetic effect on strength development was examined and he suggested optimal combinations of cement-limestone-metakaolin ternary blends. From the early age to later age, the optimum combination of ternary blends shift from high limestone-low metakaolin to low limestone-high metakaolin.

The studies related to the electrical properties on the fiber-reinforced cement composites have been conducted by C. Liu et al. and J. Zheng et al. C. Liu et al. evaluated the self-sensing capability of engineered cementitious composites (ECCs) including multiwalled carbon nanotubes (CNTs) and reported that the percolation threshold value is around 0.3% by weight and ECCs containing CNTs show good self-sensing ability under flexural loading conditions. The amounts of CNTs significantly affected the self-sensing capacity, and with the increased CNT contents, the amplitude of fractional change in resistivity was reduced. J. Zheng et al. presented a novel coupling electromechanical cell-based smoothed finite element method to accurately simulate the dynamic response of piezoelectric composite material (PCM) structures and noted that it is a robust tool for analyzing the mechanical properties of PCM structures due to its higher accuracy and reliability than the conventional finite element method.

Several researchers have investigated the implications of fiber-reinforced cement composites on the structural elements. I.-H. Yang et al. studied the flexural behavior of high-performance fiber-reinforced concrete beams and predicted their tensile strengths by fitting the moment-curvature curves based on sectional analysis. They reported that flexural strength increased with the steel fiber content and the tensile strength obtained from the material test was greatly different from that calculated from the structural beam test results. The calculated tensile strengths were 23.7–60.7% lower than those obtained from the material test. In addition, the tensile strength increased with the compressive strength. S.-H. Kim et al. experimentally evaluated the long-term ring deflection of the GFRP mortar pipe and noted that reduced stiffness leads to excessive deflections under long-term pressure. Based on the field test results of the buried GFRP pipes for 664 days, it was verified that the long-term deflection was less than 5% pipe deflection, suggested by the existing specifications, i.e., ASTM D5365 and AWWA M45. So, the safety of the buried GFRP pipe was verified by the field tests. I. Iskhakov and Y. Ribakov studied the effect of steel fibers to solve the brittle behavior of high-strength concrete and to enhance its elastic-plastic deformation. The applied steel fibers proved to be high efficiency and led to ductile behavior of compressed high-strength concrete elements along with the desired effect at long-term loading. In addition, there was an obvious dependence of transverse deformation on the longitudinal behavior at the ultimate limit state. Lastly, H. Ju et al. estimated the minimum torsional reinforcement of reinforced concrete (RC) and steel fiber-reinforced concrete (SFRC) beams. They reported that the addition of steel fibers improves the crack control of RC beams at the same reinforcement ratio and the higher amount of torsional reinforcement is required to ensure the reserved strength when the compressive strength of concrete becomes higher. Their proposed prediction model also well evaluated the torsional failure mode of the RC and SFRC beams according to the reserved strength ratio.

Guest editors hope that readers can obtain useful information and discover some recent research trends regarding the fiber-reinforced cement composites. They also wish that their academic curiosities are able to be satisfied from the valuable research results in this special issue. This publication considers a wide range of disciplines, including civil, architectural, and construction engineering, and may appeal to the engineers and scientists in the field.

Conflicts of Interest

The editors declare that they have no conflicts of interest regarding the publication of this special issue.

Doo-Yeol Yoo
Nemkumar Banthia
Kazunori Fujikake
Young Hoon Kim
Rishi Gupta

Research Article

Development of FRC Materials with Recycled Glass Fibers Recovered from Industrial GFRP-Acrylic Waste

Kishan Patel,[1] Rishi Gupta [ID],[2] Mohit Garg,[2] Boyu Wang,[2] and Urmil Dave[1]

[1]*Department of Civil Engineering, Nirma University, Ahmedabad 382 481, India*
[2]*Department of Civil Engineering, University of Victoria, Victoria V8W 2Y2, Canada*

Correspondence should be addressed to Rishi Gupta; guptar@uvic.ca

Fiber-reinforced concrete (FRC) and engineered cementitious composite materials have demonstrated promising requisite in construction industry owing to its superior mechanical and durability properties. In this study, a sustainable approach was taken, i.e., to use industry waste as a reinforcement with improved interfacial bonding leading to enhanced mechanical performance of FRC. An efficient *in situ* recycling process allowed the authors to extract glass fibers from glass fiber-reinforced polymer acrylic waste. Concrete mixes with low fiber dosages including 0.1%, 0.2%, and 0.3% (by volume) of recycled as well as virgin glass fibers were prepared. The slump of concrete was maintained ~150 mm by using high water-reducing admixture (HWRA). Notably, lower amount of HWRA was required for raw glass fibers vis-à-vis recycled ones due to its hydrophobic nature. Overall, FRC enclosing 0.3% recycled glass fiber demonstrated >20% enhancement in compressive, split tensile, and flexural strength as compared to control (after 28 days of curing), also supported by morphological analysis.

1. Introduction

Cement-based composite materials demonstrate better performance under compression rather than in the tensile mode. Usually, ancient structures such as arches and masonry are not reinforced with steel bars. The sole purpose of steel bars in concrete is to act as the primary material that can sustain enormous tensile stresses, thus increasing the overall ductility of the structural member. With the advancement in technology, researchers started looking for other alternatives to provide structural reinforcement. Since corrosion of steel bars significantly affected the material properties, which ultimately led to structural failure, one of the possible solutions identified was to use either natural or synthetic fibers. Randomly distributed fiber reinforcement in matrices such as polymer/concrete has gained enormous appreciation and acceptability in commercial applications for more than two decades now, mostly in construction, automobile, marine, and aeronautical sectors [1–8].

Glass fiber-reinforced polymer (GFRP) material has properties such as high strength-to-weight ratio, high corrosion resistance and low maintenance, and ease of fabrication. As a result, GFRP-based materials can handle high structural load, increase the durability, serve as an excellent cost-effective repair material, and thus is a great alternative to conventional materials [3–5, 8–12]. The commercially viable products manufactured using GFRP include mostly automotive parts, bathtubs, printed circuit boards, boats, and aerospace components. Researchers have also attempted to integrate fiber reinforcement in the concrete material, referred to as fiber-reinforced concrete (FRC) [1, 13–20]. FRC or GFRP fabricated sheets are retrofitted on beams, columns, and slabs to prevent the structure against corrosion as well as enhancing its longevity [21]. Fibers that have been successfully used in improving the strength and longevity of concrete infrastructures are glass [1, 7, 10, 11, 18, 22, 23], steel [1, 10, 11, 14, 15, 17, 24], carbon fibers [24–28], and polypropylene fibers [13, 15, 17, 29]. In particular, flexural and shrinkage properties have shown significant improvements with the addition of fibers in cement [16, 18, 22, 30]. Specifically, the work carried out by Banthia's group [16, 22, 30] has

demonstrated that the improved properties of FRC depend on parameters such as fiber orientation, water/cement ratio, fiber volume fraction, and intrinsic characteristics of the fiber itself. It is due to these factors and anisotropic behavior of monofilament fibers (in particular glass fibers) that researchers have reported diverse results. As a result, there has been a significant increase in synthesis of glass fiber and then using it as reinforcement for diverse applications around the globe.

For example, in the early 1900's, sanitary industry manufactured bathtubs with ceramic material, but with the advancements of technology, it got replaced with GFRP composites. GFRP composites are fabricated either using a thermosetting polymer (such as epoxy) or thermoplastic polymer (such as acrylic) along with glass fibers, and after curing, it results in a lightweight, high strength, and durable composite material. The 3D cross-linked structure of the material improves its performance and durability vis-à-vis ceramic one. Presently, most of the thermoset-based FRP waste is either being incinerated or landfilled, leading to negative environmental impacts and additional costs to FRP producers and suppliers [9, 31–36]. Furthermore, it has been observed by researchers that recycling of thermoset-based GFRP waste is a challenging task [9, 23, 31, 37–39] and also adds as a nonvalue cost to the owner for using it in the manufacturing process. Hence, an increased use of GFRP for commercial applications also results in an increase in the production of GFRP waste.

The sanitation industry took the benefit of this concept of constructing composites like GFRP. The waste produced from the sanitation industry (coming from discarded products and trims that are cut out) is posing a major challenge [40, 41]. In addition, this waste as compared to traditional GFRP is even more challenging to recycle as it not only constitutes resin reinforced with glass fibers but also a thin coating of acrylic, poly(methyl methacrylate) (PMMA) a thermoplastic resin as the finishing surface, from an environmental and economic perspective [41–43]. The authors define this waste as glass fiber-reinforced polymer acrylic (GFRPA) waste in this paper. The advanced thermochemical methods such as pyrolysis and fluidized bed techniques have shown positive results in terms of recycling of GFRPA waste and to reclaim glass fibers as well as resin [31, 41]. In particular, Esmizadeh et al. [41] described the benefits as well as disadvantages of different mechanisms to recycle PMMA such as thermal cracking, catalytic cracking, high heat application, and pyrolysis. An effort was made by the author to develop nanocomposites by reusing recycled PMMA waste. But on the contrary, the recycling process has resulted in a detrimental effect in terms of tensile strength of recycled glass fibers where the fiber strength was reduced to 50%–90% as compared to virgin fibers [23]. In addition to this, harmful gases such as CO and CO_2 are also released during this process, which leads to environmental contamination [35, 44]. Thus, recyclability of both the production waste and end-of-life (EOL) products has become an important and vital issue globally. The studies on GFRPA waste recycling and the reuse of sequent recyclates are limited [40, 45]. Cousins et al. [45] utilized the dissolution process to recover

the constituent materials from a thermoplastic composite waste part and further used the reclaimed glass fibers to fabricate the new material. It is interesting to note that the new material with recycled glass fibers reported higher stiffness and mechanical strength as compared to the virgin fibers, thus suggesting reusability of recycled glass fibers and possibility of selling the fibers and resin at a cheaper price to different industries. However, Correia et al. [23] reported worsened concrete performance (mechanical and durability related) by using thermoset-based GFRP waste in concrete mix and suggested to utilize low dosage of GFRP waste in nonstructural applications as a means to support waste management of FRP materials. However, with increased awareness of environmental matters, researchers identified and implemented few methods in the past to extract the glass fibers from the acrylic waste [41, 45], but still the results were not that promising. Also, the work reported so far in using GFRPA waste is very limited in terms of environmentally friendly extraction techniques and use as reinforcement in concrete.

Therefore, in this paper, the authors present an economical and ecofriendly technique to extract glass fibers as well as acrylic powder from an industrial waste. Till date, various chemical and mechanical processes have been reported in literature; however, they all seem to have an environmental impact as well as higher cost associated with the process [40, 41, 45].

Furthermore, the present study investigates the effect of using that recycled glass fibers from acrylic waste for various mechanical properties such as compressive and flexural strength and split tensile strength, when used as a reinforcement in concrete. Lastly, cost-effectiveness is more accurately assessed by comparing the mechanical test results obtained for analogous concrete mixes reinforced with virgin glass fibers and by observing the morphology of virgin and recycled glass fibers under an electron microscope.

2. Materials and Methods

One of the interesting methodologies reported in this study is the lab-scale separation of glass fibers and polymer resin from the GFRPA waste. The authors developed an *in situ* mechanical recycling process that is able to collect quantitative recycled glass fibers from GFRPA waste, thus providing an ecofriendly solution for the industry. Additionally, these recycled glass fibers also hold a strong potential in developing the ecofriendly concrete repair material. As a result, the recycled glass fibers were analysed for their morphological structure, using a scanning electron microscope (SEM), and for chemical composition, using EDX, and then is compared with virgin (raw) fibers.

Concrete cylinders of diameter 100 mm (4″) and height 200 mm (8″) were cast for investigating both the compressive and split tensile strength of concrete. On the contrary, prism specimens of dimension 100 mm × 100 mm × 350 mm were cast to assess the flexural strength of the concrete mix. For each of the tests mentioned above, three samples with and/or without fiber reinforcement were cast. The parameters of the study include control (no fiber) and 2 fiber types (recycled and

raw glass fiber), each with a dosage of fibers of 0.1%, 0.2%, and 0.3%. These results in a total of 105 test specimens (84 cylinder shaped and 21 prismatic shaped). The details on how to prepare these specimens has been discussed in Section 2.2.

2.1. Materials. General use, Type 10, Ordinary Portland cement (OPC) was used in the present study as it fulfils the requirement of Type I and Type II cement as per ASTM C150 standards [46]. Naturally, available aggregates found in the Sechelt pit in British Columbia (Canada) were used in the study as coarse aggregates. These aggregates had a maximum size of 25 mm and 0.69% absorption characteristics.

Furthermore, natural sand available in the same pit was used as fine aggregates in this experimental work. The sand collected from the pit was subjected to sieve shaker to identify the different particle size. The results have been summarized in Table 1. Notably, the fine aggregates had a fineness modulus of 2.61 and an absorption of 0.79%.

In addition, the authors used high-range water-reducing agent (HWRA) or superplasticizer, MasterGlenium® 3030. This superplasticizer has a polycarboxylate ether chemical, which acts as a catalyst to enhance the workability or slump value of concrete mix. A study by Asokan et al. [47] stated that the addition of 2 vol% of superplasticizer increases the compressive strength of concrete prepared with GFRP waste by 11%. Furthermore, the author reported a positive effect by including the waste from GFRP on drying shrinkage as well as compactness of concrete for potential use in structural and nonstructural applications.

As stated earlier, in the present study, two types of glass fibers were chosen, i.e., raw glass fibers (pristine) and recycled glass fibers. The properties of raw and recycled fibers are mentioned in Table 2. It can be seen that recycled glass fibers are about the same in diameter as virgin ones but have shorter length. This would be expected as process of manufacturing bathtubs does not change fiber diameter. Furthermore, the diameters of virgin and recycled glass fibers were supported by SEM analysis as well (for more details, refer Section 3.1). In general, the virgin E-glass fibers possess a tensile strength ranging from 3.1 to 3.8 GPa. In this paper, the innovative and cost-effective extraction and preparation of recycled fibers as a reinforcement in concrete has been discussed in detail in Section 2.4.

2.2. Mix Design. In the present study, ACI 211.1-91 [48] guidelines were followed for determining the mix design of normal concrete. The mix proportions for manufacturing of concrete specimens are discussed below.

In order to maintain a 150 mm slump, 25 mm of maximum aggregate size and non-air-entrained cement was used. Furthermore, water: cement ratio of 0.45 was chosen from Table A 1.5.3.4(a) of ACI 211.1 in order to prepare concrete samples with reasonable compressive strength. Additionally, according to the ACI standard, 0.67 m^3 of dry rodded coarse aggregate was required for 1 m^3 of concrete. Taking this into consideration the quantity of fine aggregates required was calculated. Table 3 summarizes the mix design

Table 1: Sieve analysis of fine aggregates.

Sieve size (mm)	% retained	% passing
10	0	100
5	0	100
2.5	10.3	89.7
1.25	17.7	72
0.63	21.9	50.2
0.315	28.6	21.5
0.16	16.2	5.3
0.08	4.1	1.2
PAN	1.2	0
Total	100	

used in the present study to develop FRC concrete with GFRPA waste.

Moreover, according to ACI 211.1-91, it is advisable to add 10% extra water for the lab trials to achieve the required slump. However, in this study, the authors considered adding 0.3% HWRA instead of adding extra water to maintain slump value close to 150 mm, compressive strength around 50 MPa for control concrete, and to aid in the dispersion of fibers in the concrete mix.

In the present study, the several parameters considered resulted in 7 different concrete mixes, where 6 of them were based on reclaimed and raw glass fibers (Table 3). The glass fibers were used as a partial substitute for fine aggregates at varying volume concentrations of the cement to cast FRC samples. As stated in Table 3, CV1, CV2, and CV3 acronyms refer to concrete mixes that contain 0.1, 0.2, and 0.3 vol% of virgin (raw or pristine) glass fibers, respectively. Similarly, CR1, CR2, and CR3 concrete were prepared using 0.1, 0.2, and 0.3 vol% of recycled glass fibers, respectively. The mix, CCON as stated in Table 3, was prepared to carry out a comparative analysis of the control mix with respect to FRC samples. The mix proportions along with per cubic meter weight (in kg/m^3) of cement, sand, aggregates, water, superplasticizer, and fibers has also been reported in Table 3.

2.3. Mixing and Curing Procedure. All the ingredients of concrete such as cement, coarse and fine aggregates, water, glass fibers, and HWRA were weighed using a digital scale. During batching, first all coarse and fine aggregates along with glass fibers were mixed at moderate speed via a drum mixer for 1 minute to obtain a uniform dry mix. Following that cement was added into the dry mix through a continuous blending process while gradually pouring 70% of required water to transform into a paste. The remaining quantity of water was added into the cement paste to obtain a concrete with a reasonable workability, cross-verified by recording the slump value and then finally placing the paste into the moulds. Notably, a synthetic chemical was sprayed onto the sides of inner surface of moulds to prevent the adhesion of concrete onto the mould for easier fabrication. After the moulds were filled with concrete, they were subjected to compaction on the vibrating table for 1 minute to avoid honey combing.

Lastly, the fresh mix was left to cure at room temperature (15 ± 3°C) for 24 hrs to harden. After 24 hrs, specimens were

TABLE 2: Raw and recycled glass fiber information.

	Length (mm)	Tensile strength (GPa)	Diameter of a single fiber, monofilament (μm)
Raw glass fiber	15	3.1–3.8	14
Recycled glass fiber	≤15	N/A	13.6

TABLE 3: Mix proportion of aggregates and water-cement ratio in developing FRC concrete with GFRPA waste.

Specimen type	Units (kg/m^3)						
	Cement	Water	Dry coarse aggregates	Dry fine aggregates	Virgin fibers	Recycled glass fibers	Plasticizer
Control (CCON)	448.89	202	1072	643.45	0	0	1.18
Virgin glass fiber-reinforced concrete (CV1), 0.1%	448.89	202	1072	643.45	2.5	0	2.37
CV2, 0.2%	448.89	202	1072	643.45	5	0	3.15
CV3, 0.3%	448.89	202	1072	643.45	7.5	0	3.95
Reclaimed glass fiber-reinforced concrete (CR1), 0.1%	448.89	202	1072	643.45	0	2.5	1.58
CR2, 0.2%	448.89	202	1072	643.45	0	5	2.37
CR3, 0.3%	448.89	202	1072	643.45	0	7.5	3.15

removed from the mould and placed into a water bath at $23 \pm 2°C$ for 7 and 28 days of curing.

The next section details about the creative approach attempted by the authors in order to extract glass fibers from the industrial waste.

2.4. Extraction of Glass Fibers from Acrylic Waste.

The manufacturing process includes preparing the bathtub using a blend of Aropol resin with a hardener as it wets the random glass fiber strands within a mould until it solidifies.

This process involved chopping a glass fiber tow using a chopper and inclusion of heated liquid resin. It should also be noted that this is done manually using a spray gun and the material received on the receiving mould is subject to human judgement. Upon solidification, a thin sheet of acrylic, PMMA, is thermomoulded onto the top surface of bathtubs to promote high scratch and impact resistance of the finished product. PMMA is considered an economical alternative to polycarbonate (PC) owing to its moderate properties, easier handling and processing, low cost, and transparency characteristics. The waste received from the industry reports a target fiber volume of about 10–15% in the polymer matrix, which results in a fiber volume of 6–9% when the total acrylic and resin is considered as the matrix. From here onwards, the authors would use the word "matrix" as a term to refer to combination of resin and PMMA in order to elucidate the readers. Overall, during the manufacturing process, leftovers (edges and small pieces) of acrylic are collected primarily during cutting and assembly processes of vacuum forming, referred to as GFRPA waste.

The authors were able to collect a quantitative GFRPA waste primarily from two areas in the industrial site: production line and quality inspection. The workers cut the extra edges hanging after bathtub manufacturing by using a cutter, which resulted in a sample, as shown in Figure 1. The authors identified that, at present, these acrylic wastes (from the industry) are being landfilled by the industry. However,

FIGURE 1: Sample of GFRPA waste.

they strongly believed from an engineering perspective that recycling of this waste could have dual benefits, i.e., environmental and economic.

2.4.1. Composition and Properties of GFRPA Waste.

Firstly, the authors identified the physical and chemical properties of the waste, which are as follows:

(i) Size: varies between 150 mm and 200 mm

(ii) Thickness of waste: 4.70 mm to 5.00 mm

(iii) Resin for glass fibers reinforcement: Aropol TM K 1866–18 C resin (45% styrene)

(iv) Proportion of GFRPA waste (by volume): glass fibers 6–9%, resin 65–70%, and PMMA~25%

Aropol is categorized as an unsaturated polyester resin, which has the property that once its cured, i.e., cross-linked with styrene, liquid turns into a solid and maintains the shape of the mould. This resin illustrates exceptionally high strength and durability characteristics. Combination of the

resin with PMMA polymer and hardener results in a material that is lightweight, has high strength, shows resistance to chemicals, and provides excellent surface finish and water repellency and hence an excellent source for bathtub manufacturing.

As discussed earlier in Section 1, the recycling of GFRPA waste is a challenging task and poses a concern for a healthier community. The current practices tend to produce harmful gases such as CO and CO_2 during the process, which eventually leads to environmental contamination. Considering the above-stated facts and for developing a low-cost recycling process (in situ), the authors preferred mechanical (ecofriendly) methodology to extract glass fibers from the acrylic waste. In brief, mechanical recycling and shredding process have benefits such as (i) no atmospheric pollution by gas emission, (ii) much simpler equipment is required as compared to ovens necessary for the thermal process, and (iii) no need of chemical solvents with subsequent environmental impacts [9, 23, 49, 50]. Hedlund-åström [50] considered life cycle assessment (LCA) and end-of-life (EOL) of polymer composite materials and proposed a recycling model that could be utilized for existing high volume of GFRP waste that is cost-effective and environmentally friendly. Similarly, Ribeiro et al. [49] and Meira Castro et al. [9] manufactured polyester polymer mortars that contained GFRP waste obtained by means of the shredding and milling process and reported improved mechanical properties with recycled reinforcement as a filler.

Taking into account the findings from the literature, the authors present in this paper the 3-stage ecofriendly mechanical recycling process carried out on a commercial "Crushing and Milling System," as illustrated in Figure 2, with a power of 45 kW, procured from Zhangjiagang City Yili Machinery Co. Ltd., China, to obtain recycled GFRPA waste. The process is summarized below:

2.4.2. Mechanical Shredding.
The equipment was operated by a trained technician, who would feed large rectangular pieces of leftover acrylic composite waste (either 150×150 mm or 200×200 mm in dimension) for shredding. The shredder broke down those large GFRPA sheets into small granular (10–50 mm) size, as illustrated in Figure 3, in approximately 3–5 minutes (depending upon the volume). The simultaneous water-cooling system in the grinding machine would allow it to run continuously and effectively until all the required volume was shredded. At the end of this process, small GFRPA waste was collected in a pan at the bottom of the shredder, which was a mixture of glass fibers with PMMA coating on the top. The next step was to separate the GFRP reinforcement from the PMMA layer.

2.4.3. Reclamation of Glass Fibers.
At Step 2, the shredded GFRPA waste from Step 1 served as an input, which helped in the separation of the PMMA sheet and some resin from GFRP reinforcement with the help of a high speed, commercially available fan. As the shredded waste freely fell in front of the fan, due to the winnowing effect of a fan, the lower density fibers landed farther away resulting in

Figure 2: Crushing and milling system.

separation of the main layer of PMMA (and some resin) from GFRP samples. As shown in Figure 4, the reclaimed glass fibers may contain some bonded resin. Likewise, the separate acrylic chunks include resin and some fraction of fibers that are embedded in the PMMA chunks.

The authors observed this process to be repeatable, having an efficiency of 80–90% to reclaim glass fibers. Following that, a 600 μm sieve was used to separate the fine dust from the glass fibers obtained.

2.4.4. Grinding of Polymer Waste.
Lastly, in Step 3, the objective was to prepare a fine powder of the polymer waste by using a grinding machine. As a result, the authors passed big chunks of acrylic waste and small granulates of acrylic collected in the previous two steps through an industrial crusher. At the end, the authors obtained a very fine powder, as shown in Figure 5. This fine powder holds the potential to be used as a reinforcing filler material in developing polymer composite and cement composite materials. The integration of the powder as a partial replacement for cement in concrete has been kept as a future scope of this study. On the contrary, the recycled fibers collected illustrated strong bonding with each other, probably due to the resin attached to its surface. Hence, from these observations, the authors hypothesize that this bonding may affect fiber dispersion in cement.

2.5. Characterization

2.5.1. Workability.
Workability of GFRC and normal concrete samples was measured using ASTM C143.

2.5.2. Compressive Strength of Concrete.
Compressive strength of GFRC and normal concrete samples was obtained using ASTM C39 [51]. All the compression tests were
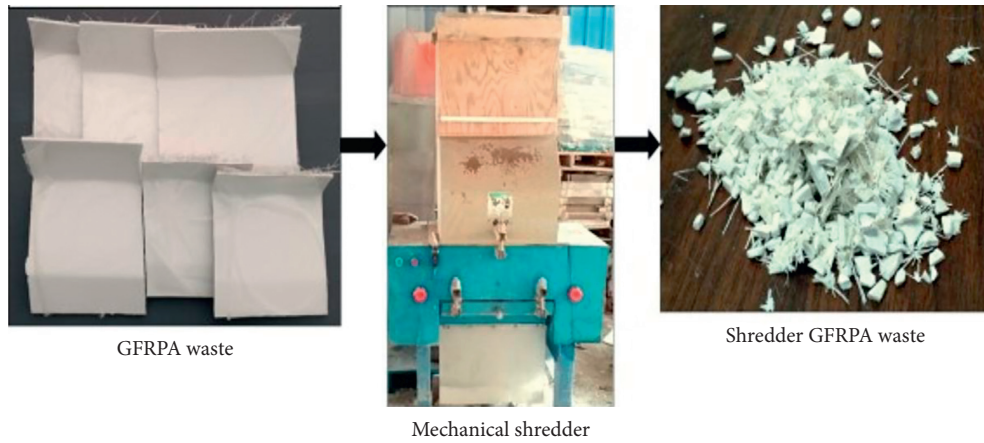
Figure 3: Step 1 for GFRPA waste—mechanical shredding.
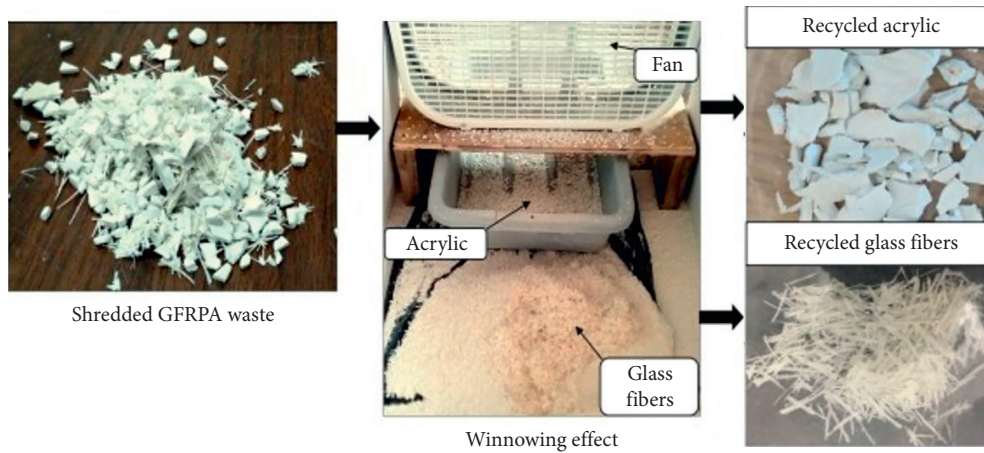
Figure 4: Step 2 for GFRPA waste—reclamation of glass fibers from acrylic waste.
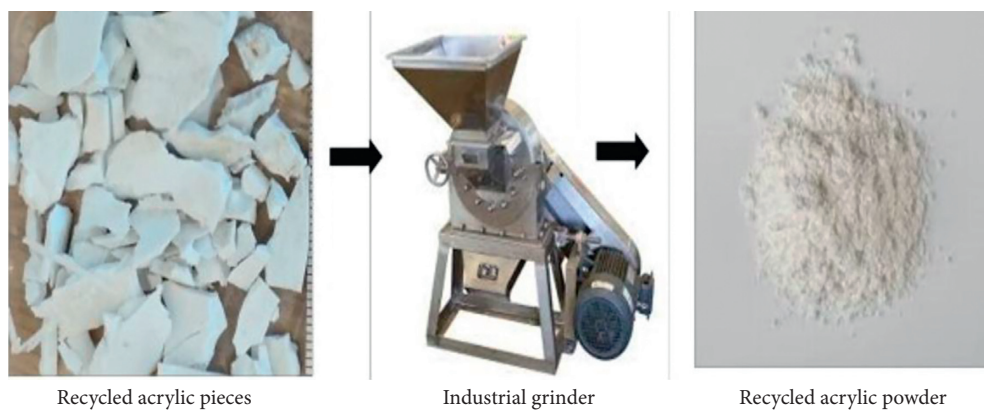
Figure 5: Step 3 for GFRPA waste—grinding of polymer waste using a crusher.

performed using a 650 kip capacity Forney test pilot. The cylinder-shaped samples, 100 mm (4″) diameter and 200 mm (8″) in length, with control concrete and FRC were tested after 7 and 28 days of curing to determine the compressive strength. The sample preparation involved concrete cylinders being ground to remove the rough surface. Later, compressive axial load was applied gradually to the cylinders until the failure occurred, and then the peak load was noted. Subsequently, this information was used to calculate the compressive strength of the material. For each mix, 3 samples were tested, and an average value has been reported in this paper.

2.5.3. Split Tensile Strength. ASTM C496 was used to measure the split tensile strength of concrete [52]. The split tensile tests were carried out on all concrete mixes and three samples of each mix, and the average value has been reported in this paper. Cylindrical concrete specimens of diameter 100 mm (2″) and length of 200 mm (4″) were tested using 65000 lb capacity Forney test pilot. Diametric compressive force along the length of a cylinder was applied until the failure occurred, and the peak load was recorded. As a result, splitting tensile strength was calculated by using the following formula:

$$\text{split tensile strength} = \frac{2 \times P}{\pi \times l \times d}, \quad (1)$$

where $P =$ peak load in Newton's, $l =$ length of cylinder in mm, and $d =$ diameter of the cylinder in mm.

2.5.4. Flexural Properties of Concrete Samples Using a Closed-Loop System. To evaluate the flexural performance of GFRC, ASTM C1609 [53] was used in the present study. Four-point bending using the closed-loop and servo-controlled testing system, MTS 250 K, having a capacity of 250 kN was used in order to obtain the load-deflection curve. The flexural performance of the prism/beam samples (having dimensions: 100 mm (4″) × 100 mm (4″) × 350 mm (14″)) was then calculated using the parameters derived from the load-deflection curves.

The closed-loop system was used for loading; the deflection at centre of the prism was measured and used to control the rate of the deflection. The span of the prism was kept constant at 300 mm (12″), and distance between the loading roller was held at 100 mm (4″). In order to achieve the closed-loop mode, the authors ensured that the jig assembly remained attached to the beam to hold the LVDT (linear variable differential transformer) properly. Two LVDTs, as shown in Figure 6, effectively maintained deflection at a rate of 0.025 mm/min up to L/900 deflection and 0.05 mm/min beyond L/900. The flexural performance of GFRC up to the cracking stage was determined from the first peak strength. However, for a particular deflection, the residual strength characterized the residual capacity after the cracking. The first peak strength was calculated using the following formula. The same formula can be used to calculate the modulus of rupture at a particular deflection:

$$\text{strength, } f = \frac{P \times L}{b \times d^2}, \quad (2)$$

where $P =$ load in Newton's, $L =$ span length in mm, $b =$ width of specimen in mm, and $d =$ depth of specimen in mm.

2.5.5. Morphological and Chemical Analysis. HITACHI S-4800 scanning electron microscope was used for analysing the surface morphology of concrete samples, while EDX provided the chemical composition of recycled glass fibers and raw glass fibers. Also, the specimens were coated with a 10 nm carbon layer in order to make the sample surface conductive and for higher production rate of secondary electrons.

3. Results and Discussion

3.1. Properties of Glass Fibers

3.1.1. Raw Glass Fibers. Chopped virgin glass fibers from the bathtub manufacturing industry were collected for this study, as shown in Figure 7(a). A chopping gun was used to shorten their length to 15 mm from the roving. Furthermore, SEM and EDX characterization of these raw glass fibers were carried out to record the physical and chemical properties. From the morphological analysis, it was observed that fibers had a diameter of $14 \mu m$ (Figure 7(b)), while the EDX analysis in Figure 7(c) reveals the absence of zirconium (Zr). It is observed that glass fibers are sensitive to alkalis in Portland cement paste, but fibers with Zr demonstrated resistance to alkali degradation [54, 55].

3.1.2. Recycled Glass Fibers. Furthermore, to compare the reclaimed glass fibers with raw ones, the authors conducted the morphological and chemical analysis of the samples collected after the extraction process was complete (Section 2.4). During the SEM analysis, the authors observed that the diameter of an individual recycled glass fiber was similar to the virgin glass fibers, i.e., $\sim 14 \mu m$ (Figure 8(a)). Additionally, thicker bundles of recycled fibers were observed under the microscope owing to the polymer resin holding several fiber strands together (Figure 8(b)). Lastly, the chemical composition (Figure 8(c)) of resin-doped recycled glass fiber demonstrates a maximum concentration of ions such as Ca, S, and O, which highlights the abundant calcium sulphate presence. The extra calcium sulphate would undergo the hydration reaction and act as a catalyst in improving the compressive strength of concrete.

3.2. Workability of Concrete.

In preparing fiber-reinforced concrete samples, it is important to maintain the workability which is generally done by recording the slump value. It has been observed that, with the addition of fibers in concrete, it tends to affect its workability. As a result, researchers overcame this challenge by mixing the high-water reducing agent (HWRA), also known as superplasticizer, into the cement. Researchers have recommended a maximum of 2% concentration (of cement content) for FRC samples to maintain the concrete slump value above 150 mm. Taking into consideration this phenomenon, the authors conducted a series of experiments, and each time, the slump of concrete was measured using the cone, as described earlier. The slump values obtained for various concrete mixes are mentioned in Table 4.

The values in Table 4 reveal that the concentration of HWRA varied with the type of fiber as well as with the fiber dosage in cement. Virgin glass fiber (CV) samples required higher concentration vis-à-vis recycled glass fiber (CR) samples. Interestingly, CV3 mix, having 0.3% raw glass fibers, had the minimum slump, i.e., 130 mm, but highest HWRA
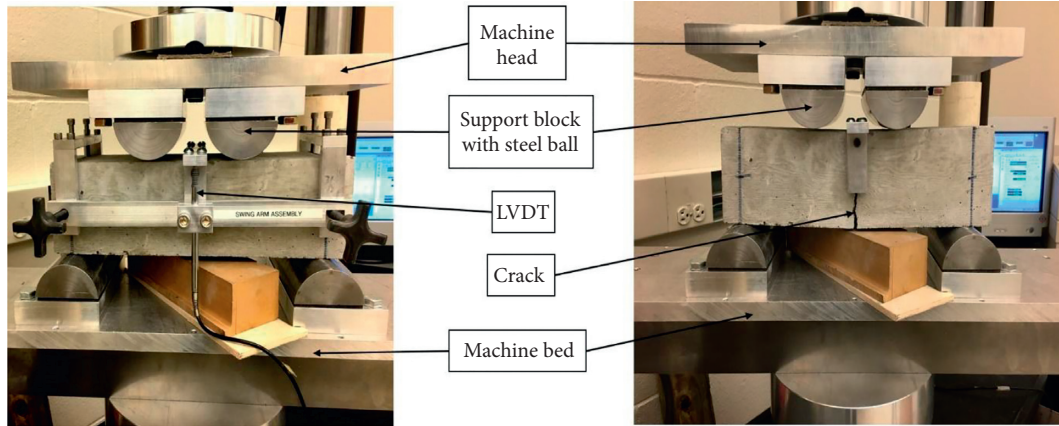
FIGURE 6: Flexural setup.

(a)

(b)
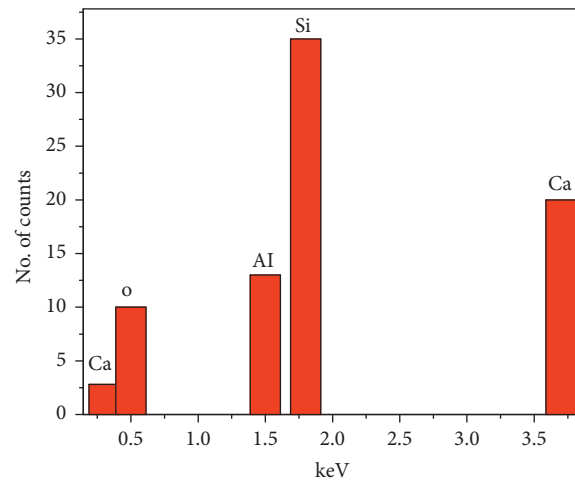
(c)

FIGURE 7: Virgin glass fibers: (a) sample; (b) SEM image; (c) EDX analysis.

(a)

(b)

(c)
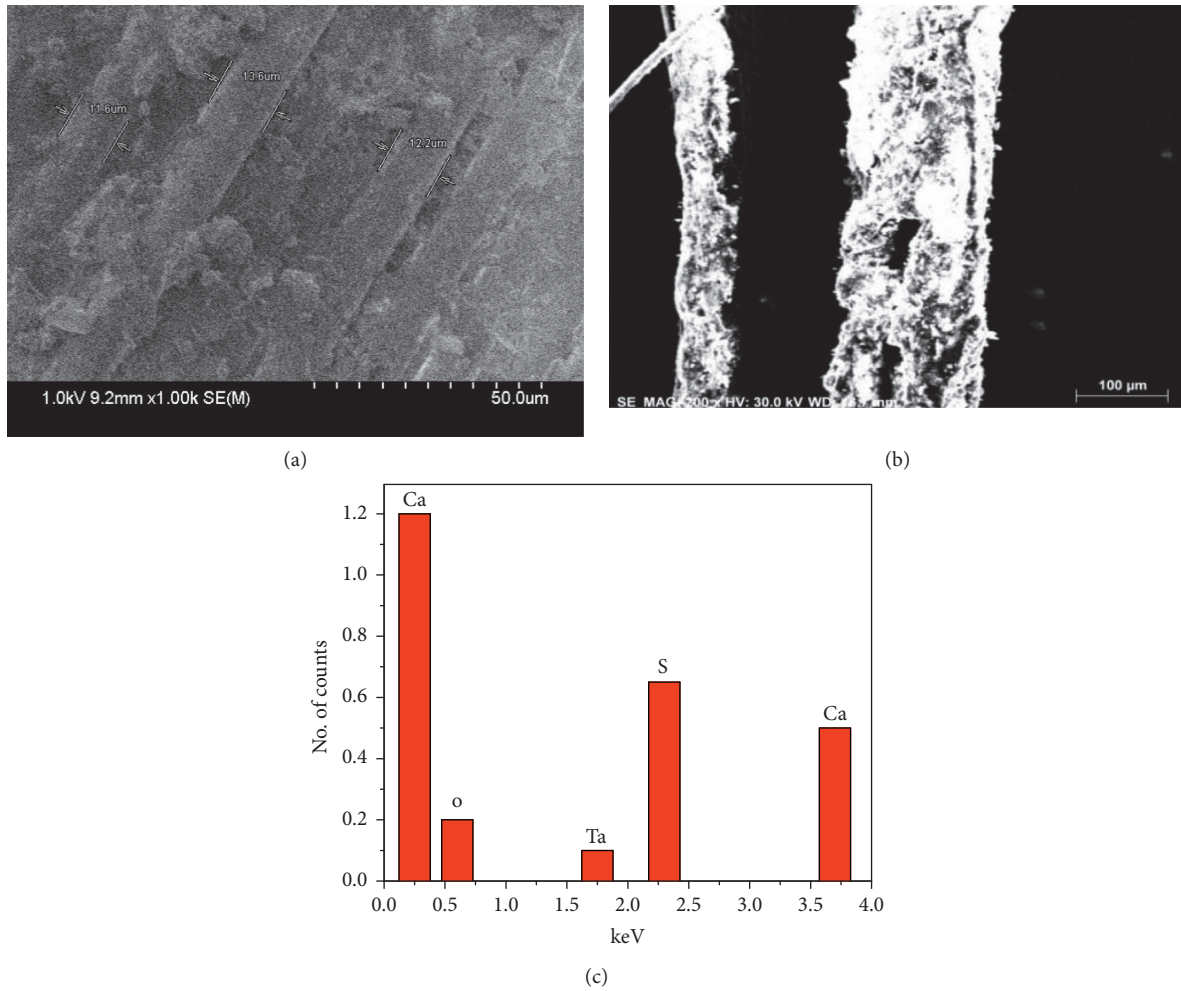
FIGURE 8: Recycled glass fibers: (a) SEM image; (b) fibers doped with resin; (c) EDX analysis.

TABLE 4: Workability of different concrete mixes.

Type of concrete mix	Slump value (mm)	Dosage of glass fiber (%)	HWRA content (%)
CCON	165	0.0	0.3
CV1	152	0.1	0.6
CV2	143	0.2	0.8
CV3	130	0.3	1
CR1	162	0.1	0.4
CR2	160	0.2	0.6
CR3	155	0.3	0.8

content of 1%. The use of 1% superplasticizer in FRC's is considered to be a higher dosage according to Aruntas et al. [56]. Also, the experimental results demonstrate that as the percentage of glass fiber increases, a higher dosage of HWRA is required to maintain the slump close to 150 mm and combat the stiffening effect of reinforcing fibers. Also, higher quantity of HWRA in concrete acted as a catalyst to overcome the hydrophilic behavior of glass fibers. Notably, less amount of HWRA was required for concrete prepared with recycled glass fibers as compared to raw glass fibers. It is possibly due to the fact that recycled glass fibers existed in bundle form and there was also a coating of resin on its surface. The coating possibly reduced the water adsorption by the fibers, and thus, less amount of HWRA was required for that concrete mix. Thus, it can be stated that the addition of fibers affects the workability of concrete, and it is further dependent on the type and quantity of fibers. In particular, the recycled glass fibers have shown better performance than raw ones in concrete. It is interesting to observe the consequences of workability on different mechanical properties, which has been discussed in the following sections of the paper.

3.3. Compressive Strength. Figure 9 illustrates the absolute values of average compressive strength after 7 and 28 days of
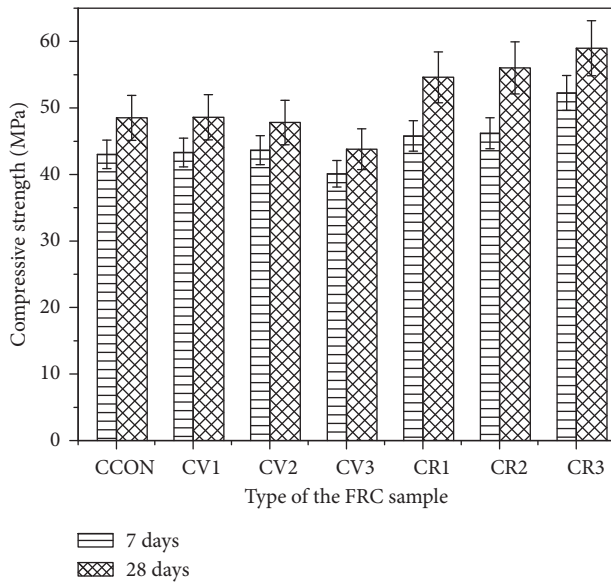
FIGURE 9: Effect of fiber reinforcement in concrete on compressive strength after 7 and 28 days of curing.

curing regime for both recycled and raw glass fibers with varying fiber concentrations as compared to the control one.

The FRC prepared using 0.3% recycled glass fibers revealed the maximum increase, 21.46% (from 43.02 to 52.25 MPa), as compared to the control samples. Notably, an increasing trend in strength was witnessed for an increasing dosage of recycled glass fibers. A possible reason to explain this explicit behavior can be credited to an increase in calcium sulphate content in the matrix, contributed by recycled glass fibers present in the sample. On the contrary, no significant change was observed when concrete samples were reinforced with virgin glass fibers. Even by increasing the fiber dosage to 0.2%, the strength increased only by 1.47%. The strength dropped significantly (to 40.11 MPa), when the fiber dosage was increased to 0.3%, as shown in Figure 9. A possible explanation for the low strength of CV3 mix vis-à-vis control mix owes to its low workability, which led to a less dense microstructure as compared to other mixes.

Furthermore, 28 days curing of the samples and testing thereafter demonstrated a similar behavior as can be seen in Figure 9. The authors made an important observation that the compressive strength of FRC samples, prepared with recycled glass fibers increased by approximately 20%, specifically for 0.1 and 0.2% fiber dosage as compared to similar samples when cured for 7 days. This illustrates that concrete had gained 90% of its strength within the first 7 days, thus demonstrating reliability of the experimental study. Furthermore, the average compressive strength recorded for the 0.3% recycled glass fiber sample was still maximum, 59 MPa, as compared to 48 MPa for the control. On the contrary, concrete samples prepared using virgin glass fibers continued to demonstrate deterioration with curing time as well as with increments of fiber dosage when tested at 28 days.

Hence, from this test, it can be inferred that the recycled glass fibers have outperformed in terms of compressive strength as compared to both control and virgin glass fiber concrete samples.

3.4. Split Tensile Strength. The tensile strength is considered as one of the basic and important properties of concrete. In general, concrete is very weak in tension due to its brittle behavior and is thus not expected to resist the tension forces acting on it, resulting in crack formation. It is due to these reasons that the authors were interested in identifying the peak load at which the fiber-reinforced concrete members may crack and also if there was any change in the failure mechanism such as brittle to ductile.

Figure 10 illustrates the split tensile strength obtained for two types of fiber along with 3 different dosages vis-à-vis control sample after the 7 day curing regime. From Figure 10, it can be observed that the control sample had a split tensile strength of 2.45 MPa, and with the incorporation of fibers, as a reinforcing material, there is an increase in strength for different fiber dosages.

Interestingly, FRC prepared with 0.3% recycled glass fiber dosage revealed a maximum increase of 22%, 2.45 to 2.99 MPa, vis-à-vis control sample. The stronger bonding between the fiber surface and cementitious matrix is possibly resisting the external forces being applied during the testing and thus resulting in enhanced compressive and tensile strength. On the contrary, the tensile strength of FRC prepared with raw glass fibers (CV1, CV2, and CV3) has also shown improvement as compared to the control mix. However, in this case, the strength of 2.86 MPa was recorded for 0.2% raw fiber dosage, while it slightly dropped to 2.83 MPa for 0.3% dosage. This illustrates once again that increasing the fiber dosage possibly resulted in poor workability and agglomeration of fibers in the matrix which tends to affect the properties of the concrete mix.

Further curing of the samples up to 28 days showed an improvement in split tensile strength, as shown in Figure 11, and as observed earlier for compressive strength results (Figure 9). When compared to 7-day curing regime samples, a similar pattern in tensile strength is visualized for the FRC samples, i.e., a maximum of 3.46 MPa is recorded for 0.3% recycled glass fiber concrete sample. The split tensile strength of the CR3 sample increased by 24% and 11% as compared to control and CV3, respectively. Also, as the percentage of recycled glass fiber increases, the split tensile strength increases. A glimpse of Figure 11 shows that the increase in split tensile strength at 28 days for CV1 and CV2 mix is higher as compared to CR1 and CR2 mix. Hence, from this test, it can be stated that the reinforcement of raw glass fibers with 0.1% content also has a significant positive effect on the split tensile strength of concrete. Similar improvement in tensile strength was also reported by Gupta and Banthia [16] upon reinforcing concrete with various virgin fiber types.

Thus, it can be stated that the recycled glass fibers have shown better performance than raw glass fibers and control concrete in terms of both compressive and split tensile strength, in particular at 0.3% fiber dosage. The authors believe that better performance with higher dosage of
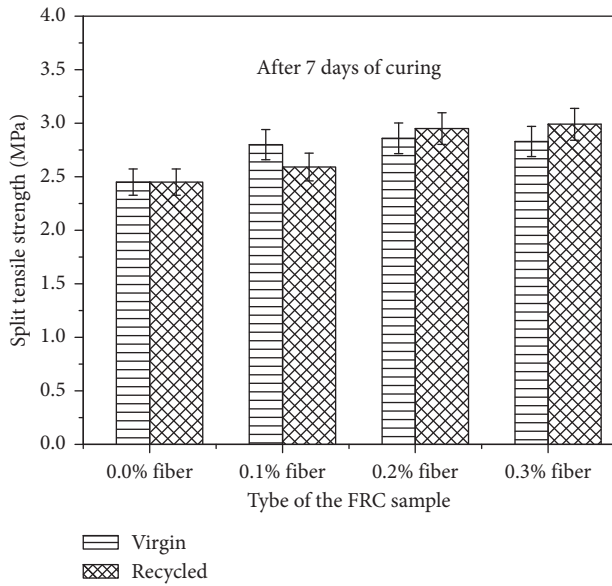
FIGURE 10: Effect of fiber reinforcement in concrete on spilt tensile strength after 7 days of curing.
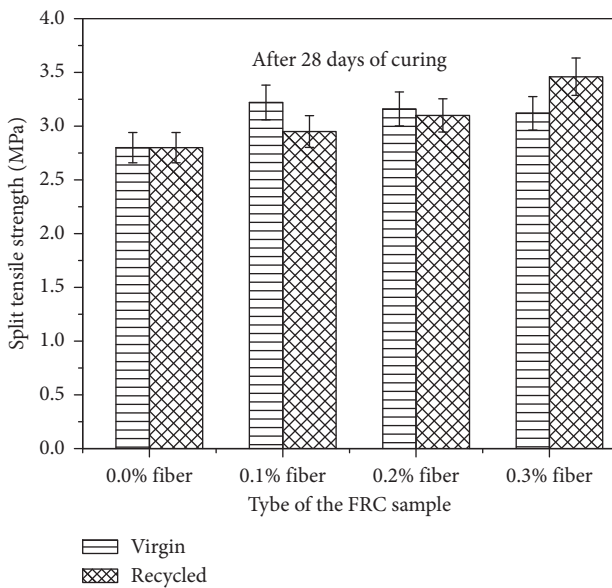
FIGURE 11: Effect of fiber reinforcement in concrete on spilt tensile strength after 28 days of curing.

recycled glass fibers in FRC supports the waste management of FRP materials.

3.5. *Flexural Strength.* After investigating the behavior of FRC in both compressive and tensile loading conditions, it became interesting to observe the effect of fibers under flexural loading conditions too. For that purpose, the authors carried out four-point bending test using a closed-loop system as described earlier in the paper for all mixes. The absolute values of average flexural strength obtained from the experimental study after 28 days of curing have been presented in Figure 12.
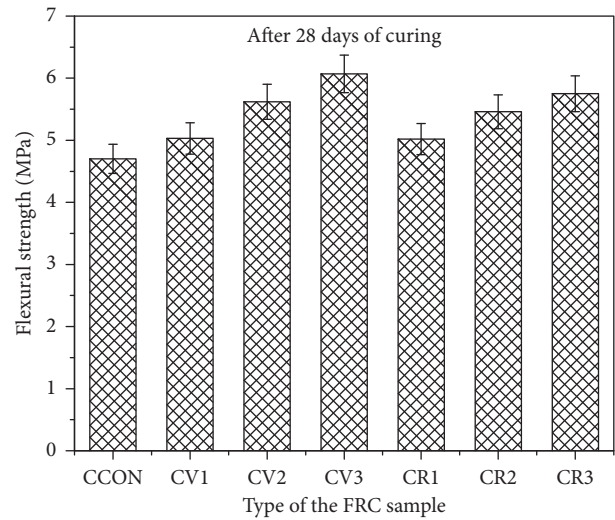
FIGURE 12: Effect of fiber reinforcement in concrete on flexural strength after 28 days of curing.

The control concrete sample had an average flexural strength of 4.70 MPa. By analysing Figure 12, it is evident that an increase in fiber dosage results in improving the strength of the material. Interestingly, at 0.1% dosage, both raw and recycled glass fiber concrete samples illustrate a similar increase in strength, at about 7%. On the contrary, the flexural strength of CV2 and CV3 mixes was comparatively higher than CR2 and CR3 mix, respectively. Furthermore, net deflection at cracking was also found to be higher for CV3 mix as compared to CV1 mix. A possible reason for this behavior is credited to the higher compressive strength obtained for CV1 mix vis-à-vis CV3 mix. Similar behavior was also observed by the authors for CR1 than CR3 mix. The analysis of this test reveals that the addition of 0.3% of raw glass fibers increases flexural strength by 28.93%, while the addition of recycled glass fibers with the same concentration increased the strength by 22.16%. Similar improvement in flexural strength with the incorporation of GFRP waste [33] and proper orientation of fibers in the cementitious matrix [22] have been reported previously.

Hence, it can be stated that raw glass fibers performed better specifically for flexural strength, but overall, recycled glass fibers have shown better improvement in other mechanical properties. Therefore, the positive experimental results obtained with utilizing recycled glass fibers still support the authors belief about recycled glass fibers as it holds the potential to provide a better sustainable, eco-friendly, and cost-effective solution for the future structural developments by the construction industry at large.

So far, the authors have reported the mechanical effect, but it is also important to analyse the effect of the fibers and different fiber concentrations on the fiber-matrix interface, which has been carried out by analysing the morphology of the fractured samples.

3.6. *Morphological Analysis.* The fractured surfaces of two samples, i.e., concrete reinforced with raw and recycled glass

(a)

(b)

Mass percent (%)

Spectrum	O	Na	Mg	Al	Si	S	K	Ca	Ti	Mn	Fe
PA 58	30.35	0.40	0.29	5.39	19.73	0.09	0.80	42.31	0.02	0.00	0.62
PA 59	44.77	0.47	0.09	1.56	6.57	0.00	0.44	45.66	0.06	0.00	0.35
PA 60	34.28	0.00	0.00	5.85	27.41	0.06	0.72	30.09	0.17	0.08	1.05
Mean value	36.57	0.29	0.12	4.27	17.91	0.05	0.65	39.35	0.09	0.03	0.67
Sigma	7.41	0.25	0.15	2.36	10.54	0.04	0.19	8.20	0.07	0.04	0.35
Sigma mean	4.28	0.15	0.08	1.36	6.08	0.03	0.11	4.73	0.04	0.03	0.20

(c)
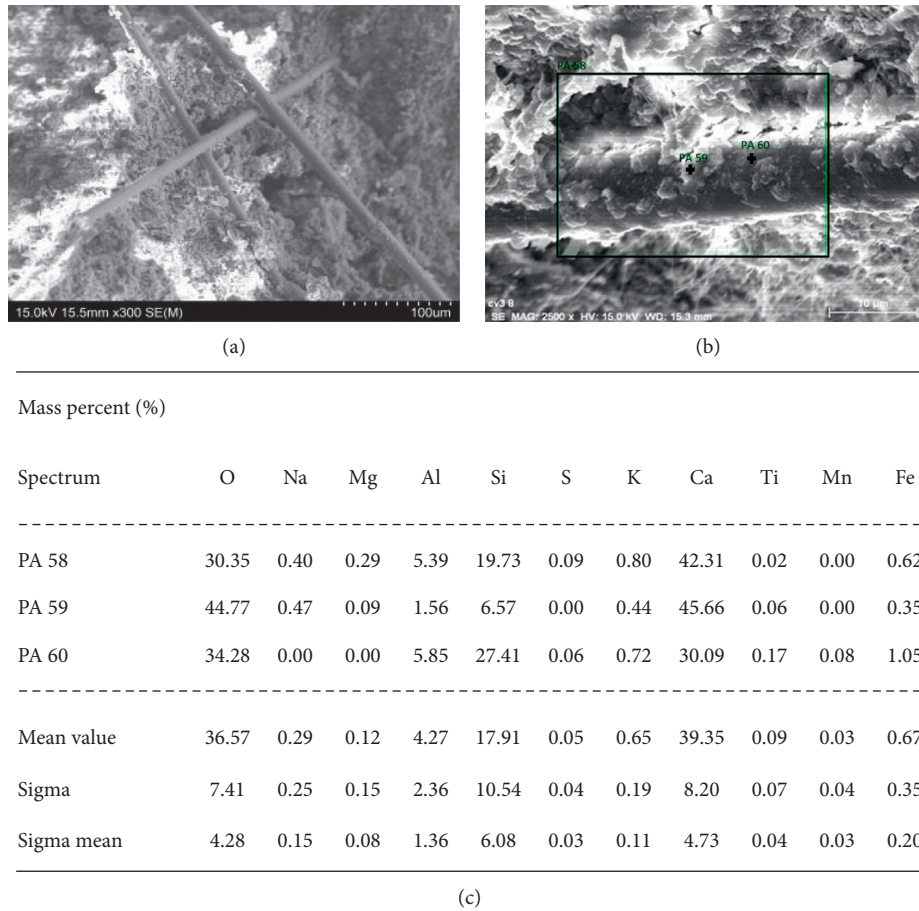
FIGURE 13: CV3 (virgin glass fiber) sample: (a) SEM image; (b) location for EDX analysis; (c) EDX analysis.

fibers with 0.3% dosage, were analysed to study the fiber-matrix interface and chemical composition. In view of this, the samples were made moisture-free by placing in a vacuum chamber for couple of hours prior to SEM analysis. Following that, the samples were coated with the 15 nm thick carbon layer. The morphology of CV3 (raw fibers) and CR3 (recycled fibers) samples differed as illustrated in Figures 13(a)–13(c) and 14(a)–14(c), respectively.

Figure 13(a) depicts the SEM image captured at magnification of 300x, clearly illustrating that raw glass fibers were randomly oriented in concrete in the form of agglomerates while fiber pull-outs were also visible. The presence of fiber pull-out highlights the poor interfacial bonding of fibers with the concrete mixture, which in turn justifies the lower compressive strength and split tensile strength reported earlier in this paper. Additionally, at a higher magnification (Figure 13(b)), chemical composition of a particular section on the sample surface was investigated, and the results have been tabulated, as shown in Figure 13(c). From the table (represented in Figure 13(c)), it can be interpreted that, at 3 different locations, in particular PA 60 which refers to raw glass fiber, the main concentration is silicon, which is the basic constituent in a glass fiber. However, PA 58 and 59 report the presence of silica, aluminium, and calcium ions, which is possibly due to some

covalent bonding between glass fibers and C-S-H as well as C-A-H gel inside the interface.

On the contrary, the microscopic analysis of recycled glass fiber-reinforced concrete (as shown in Figure 14) is quite different than those prepared with raw glass fibers. In Figure 14(a), the glass fibers seem to be oriented in the longitudinal direction, surrounded by the thick matrix layer and present in small bundles. It highlights the fact that there was better interfacial bonding between the cementitious materials and the glass fibers, due to which the samples demonstrated significantly better performance during various mechanical tests. Carefully analysing Figures 14(c) and 13(c), it can be noted that there is higher combined concentration of calcium, silicon, sulfur, and aluminium in recycled glass fiber concrete vis-à-vis raw glass fiber. The slightly higher concentration of calcium silicate hydrate in the interface explains the positive affect observed earlier on the compressive strength of concrete. Hence, the mechanical performance of FRC seems to be justified after analysing the fractured surfaces.

The authors believe that this research can be extended by increasing the dosage of recycled glass fiber in cement to investigate the effect on shrinkage properties. Also, the residual fine powder collected by sieving of glass fibers can act as one of the fillers in preparing the concrete material,

(a)

(b)

Mass percent (%)

Spectrum	O	Na	Mg	Al	Si	S	K	Ca	Ti	Mn	Fe
PA 73	53.41	0.97	0.82	2.33	8.13	2.07	0.22	30.35	0.05	0.09	1.57
PA 74	48.02	1.02	1.11	7.87	25.60	0.12	0.31	15.57	0.10	0.08	0.19
Mean value	50.72	1.00	0.97	5.10	16.86	1.10	0.27	22.96	0.07	0.08	0.88
Sigma	3.81	0.04	0.21	3.91	12.35	1.37	0.06	10.45	0.04	0.01	0.97
Sigma mean	2.69	0.03	0.15	2.77	8.74	0.97	0.04	7.39	0.03	0.00	0.69

(c)
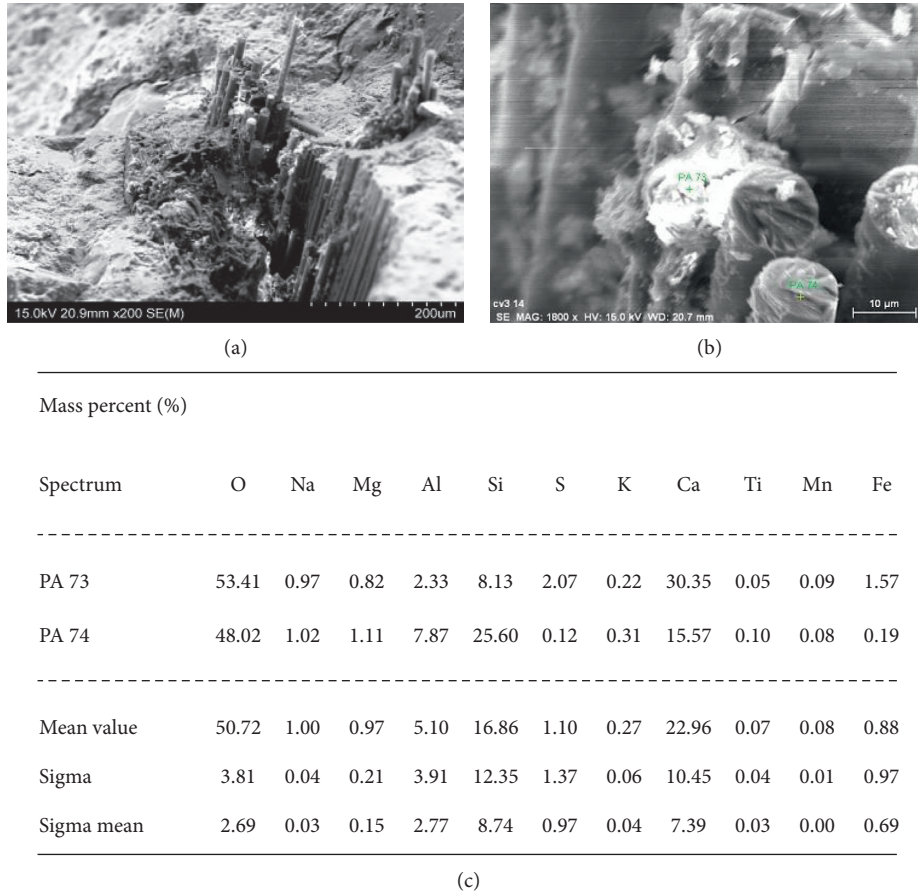
FIGURE 14: CR3 (recycled glass fiber) sample: (a) SEM image; (b) location for EDX analysis; (c) EDX.

which can lead to an ecofriendly and cost-effective alternative to use of Portland cement. Following that, the mechanical properties of the concrete can be investigated.

4. Conclusions

Based on the results of this experimental investigation, the following conclusions are drawn:

(1) *In situ* mechanical method of recycling demonstrated quantitative reclamation of glass fibers and PMMA powder from GFRPA waste. The winnowing technique was efficient in separating the GFRPs from the shredded waste. Following that, a fine sieve assisted in removing the fine polymer powder from the recycled glass fibers.

(2) The recycled glass fibers appeared to have a resin coating which promoted their existence in bundles, as visualized under SEM. Calcium silicate (gypsum) ions were identified in the fiber-matrix interface using EDX analysis, which assisted in improving the mechanical performance in concrete. The sharp fractured edges of glass fibers confirmed the brittle failure of the concrete material during mechanical tests.

(3) The compressive strength of concrete mix increased as the percentage of recycled glass fibers increased for both 7 and 28 days of curing schedule. In the case of FRC mixes reinforced with virgin fibers, compressive strength decreased for 0.2% (28 days of curing) and 0.3% (7 and 28 days of curing) fiber dosages, vis-à-vis the control mix. On the contrary, maximum enhancement of 22% was achieved for 0.3% volume fraction of recycled glass fibers as compared to control the concrete sample for both 7 and 28 days of curing regime.

(4) Incorporation of both types of glass fibers demonstrated a positive impact on the split tensile strength of concrete. Furthermore, an increase in dosage of fibers in the mix showed an increase in strength for both 7 and 28 days of curing cycle. Interestingly, once again 0.3% recycled glass fibers had a maximum tensile strength of 3.46 MPa vs 2.48 MPa (control). Also, lower concentration of raw glass fiber concrete samples showed slightly better strength than the other fibers. The authors believe that the results of split tensile strength were partially influenced by the compressive strength of the concrete for that mix.

(5) Lastly, the reinforcement of virgin and recycled glass fibers (with an increasing concentration) also

enhanced the flexural strength of concrete. As compared to the control sample, average flexural strength was enhanced by 29% and 22% for virgin and recycled glass fiber samples, respectively, after 28 days of curing at 0.3% volume fraction of the mix. However, all concrete mixes had a brittle failure, and no postcrack deflection was observed.

Data Availability

The experimental data used to support the findings of this study will be made available upon request.

Conflicts of Interest

The authors declare that there are no conflicts of interest regarding the publication of this paper.

Acknowledgments

References

[1] C. E. Bakis, L. C. Bank, V. L. Brown et al., "Fiber-reinforced polymer composites for construction—state-of-the-art review," *Journal of Composites for Construction*, vol. 6, no. 2, pp. 73–87, 2002.

[2] G. Sun, R. Liang, J. Zhang, Z. Li, and L.-T. Weng, "Mechanism of cement paste reinforced by ultra-high molecular weight polyethylene powder and thermotropic liquid crystalline copolyester fiber with enhanced mechanical properties," *Cement and Concrete Composites*, vol. 78, pp. 57–62, 2017.

[3] M. Garg, S. Sharma, S. Sharma, and R. Mehta, "Effect of hygrothermal aging on GFRP composites in marine environment," *Steel and Composite Structures*, vol. 25, pp. 93–104, 2017.

[4] M. Mastali, A. Dalvand, and A. R. Sattarifard, "The impact resistance and mechanical properties of reinforced self-compacting concrete with recycled glass fibre reinforced polymers," *Journal of Cleaner Production*, vol. 124, pp. 312–324, 2016.

[5] M. Garg, S. Sharma, and R. Mehta, "Carbon nanotube-reinforced glass fiber epoxy composite laminates exposed to hygrothermal conditioning," *Journal of Materials Science*, vol. 51, no. 18, pp. 8562–8578, 2016.

[6] J. Broekel and G. Scharr, "The specialities of fibre-reinforced plastics in terms of product lifecycle management," *Journal of Materials Processing Technology*, vol. 162-163, pp. 725–729, 2005.

[7] N. Banthia, K. Chokri, Y. Ohama, and S. Mindess, "Fiber-reinforced cement based composites under tensile impact," *Advanced Cement Based Materials*, vol. 1, no. 3, pp. 131–141, 1994.

[8] L. C. Bank, *Composites for Construction: Structural Design with FRP Materials*, John Wiley & Sons, New Jersey, NJ, USA, 2007, https://onlinelibrary.wiley.com/doi/book/10.1002/9780470121429.

[9] A. C. Meira Castro, M. C. S. Ribeiro, J. Santos et al., "Sustainable waste recycling solution for the glass fibre reinforced polymer composite materials industry," *Construction and Building Materials*, vol. 45, pp. 87–94, 2013.

[10] S. Ghazizadeh and C. A. Cruz-Noguez, "Damage-resistant reinforced concrete low-rise walls with hybrid GFRP-steel reinforcement and steel fibers," *Journal of Composites for Construction*, vol. 22, no. 2, article 04018002, 2018.

[11] S. Ghazizadeh, C. A. Cruz-Noguez, and Y. Li, "Numerical study of hybrid GFRP-steel reinforced concrete shear walls and SFRC walls," *Engineering Structures*, vol. 180, pp. 700–712, 2019.

[12] M. A. Aboelseoud and J. J. Myers, "Hybrid composite beam bridge superstructure design considerations for thermal gradient," *Journal of Composites for Construction*, vol. 22, no. 3, article 04018005, 2018.

[13] H. Nguyen, V. Carvelli, E. Adesanya, P. Kinnunen, and M. Illikainen, "High performance cementitious composite from alkali-activated ladle slag reinforced with polypropylene fibers," *Cement and Concrete Composites*, vol. 90, pp. 150–160, 2018.

[14] M. Alberti, A. Enfedaque, and J. Galvez, "Fibre reinforced concrete with a combination of polyolefin and steel-hooked fibres," *Composite Structures*, vol. 171, pp. 317–325, 2017.

[15] M. Saidani, D. Saraireh, and M. Gerges, "Behaviour of different types of fibre reinforced concrete without admixture," *Engineering Structures*, vol. 113, pp. 328–334, 2016.

[16] R. Gupta and N. Banthia, "Correlating plastic shrinkage cracking potential of fiber reinforced cement composites with its early-age constitutive response in tension," *Materials and Structures*, vol. 49, no. 4, pp. 1499–1509, 2016.

[17] V. Afroughsabet and T. Ozbakkaloglu, "Mechanical and durability properties of high-strength concrete containing steel and polypropylene fibers," *Construction and Building Materials*, vol. 94, pp. 73–82, 2015.

[18] A. B. Kizilkanat, N. Kabay, V. Akyüncü, S. Chowdhury, and A. H. Akça, "Mechanical properties and fracture behavior of basalt and glass fiber reinforced concrete: an experimental study," *Construction and Building Materials*, vol. 100, pp. 218–224, 2015.

[19] M. Mastali, I. B. Valente, J. A. O. Barros, and D. M. F. Gonçalves, "Development of innovative hybrid sandwich panel slabs: experimental results," *Composite Structures*, vol. 133, pp. 476–498, 2015.

[20] Z. Lin and V. C. Li, "Crack bridging in fiber reinforced cementitious composites with slip-hardening interfaces," *Journal of the Mechanics and Physics of Solids*, vol. 45, no. 5, pp. 763–787, 1997.

[21] J. Rimen and D. Arghya, "Size effect in FRP-confined concrete under axial compression," *Journal of Composites for Construction*, vol. 21, no. 6, article 4017045, 2017.

[22] D.-Y. Yoo, N. Banthia, S.-T. Kang, and Y.-S. Yoon, "Effect of fiber orientation on the rate-dependent flexural behavior of ultra-high-performance fiber-reinforced concrete," *Composite Structures*, vol. 157, pp. 62–70, 2016.

[23] J. R. Correia, N. M. Almeida, and J. R. Figueira, "Recycling of FRP composites: reusing fine GFRP waste in concrete mixtures," *Journal of Cleaner Production*, vol. 19, no. 15, pp. 1745–1753, 2011.

[24] Y. Ding, G. Liu, A. Hussain, F. Pacheco-Torgal, and Y. Zhang, "Effect of steel fiber and carbon black on the self-sensing ability of concrete cracks under bending," *Construction and Building Materials*, vol. 207, pp. 630–639, 2019.

[25] J. E. Woods, D. T. Lau, and C. A. Cruz-Noguez, "In-plane seismic strengthening of non-ductile reinforced concrete

shear walls using externally bonded CFRP sheets," *Journal of Composites for Construction*, vol. 20, no. 6, article 04016052, 2016.

[26] W.-Q. Li, J.-H. Zhu, P.-Y. Chen, F. Xing, D. Li, and M. Su, "Evaluation of carbon fiber reinforced cementitious matrix as a recyclable strengthening material," *Journal of Cleaner Production*, vol. 217, pp. 234–243, 2019.

[27] J. L. G. Lim, S. N. Raman, M. Safiuddin, M. F. M. Zain, and R. Hamid, "Autogenous shrinkage, microstructure, and strength of ultra-high performance concrete incorporating carbon nanofibers," *Materials*, vol. 12, no. 2, p. 320, 2019.

[28] A. Saccani, S. Manzi, I. Lancellotti, and L. Lipparini, "Composites obtained by recycling carbon fibre/epoxy composite wastes in building materials," *Construction and Building Materials*, vol. 204, pp. 296–302, 2019.

[29] A. El-Newihy, P. Azarsa, R. Gupta, and A. Biparva, "Effect of polypropylene fibers on self-healing and dynamic modulus of elasticity recovery of fibre reinforced concrete," *Fibers*, vol. 6, no. 1, p. 9, 2018.

[30] R. Gupta and N. Banthia, "Plastic shrinkage cracking prediction in cement-based materials using factorial design," *Journal of Materials in Civil Engineering*, vol. 27, no. 9, article 04014244, 2015.

[31] A. C. Meira Castro, J. P. Carvalho, M. C. S. Ribeiro et al., "An integrated recycling approach for GFRP pultrusion wastes: recycling and reuse assessment into new composite materials using fuzzy boolean nets," *Journal of Cleaner Production*, vol. 66, pp. 420–430, 2014.

[32] F. Tittarelli and S. P. Shah, "Effect of low dosages of waste GRP dust on fresh and hardened properties of mortars: part 1," *Construction and Building Materials*, vol. 47, pp. 1532–1538, 2013.

[33] P. Asokan, M. Osmani, and A. D. F. Price, "Assessing the recycling potential of glass fibre reinforced plastic waste in concrete and cement composites," *Journal of Cleaner Production*, vol. 17, no. 9, pp. 821–829, 2009.

[34] D. Van Gemert, L. Czarnecki, M. Maultzsch et al., "Cement concrete and concrete–polymer composites: two merging worlds: a report from 11th ICPIC Congress in Berlin, 2004," *Cement and Concrete Composites*, vol. 27, no. 9-10, pp. 926–933, 2005.

[35] A. M. Cunliffe and P. T. Williams, "Characterisation of products from the recycling of glass fibre reinforced polyester waste by pyrolysis," *Fuel*, vol. 82, no. 18, pp. 2223–2230, 2003.

[36] N. Kale, M. Madurwar, and R. Ralegaonkar, "Analyzing the strength behavior of cement composites with waste glass fibers," in *Advances in Waste Management*, A. Kalamdhad, J. Singh, and K. Dhamodharan, Eds., Springer, Singapore, pp. 203–213, 2018.

[37] J. Beauson, H. Lilholt, and P. Brøndsted, "Recycling solid residues recovered from glass fibre-reinforced composites—a review applied to wind turbine blade materials," *Journal of Reinforced Plastics and Composites*, vol. 33, no. 16, pp. 1542–1556, 2014.

[38] S. J. Pickering, "Recycling technologies for thermoset composite materials—current status," *Composites Part A: Applied Science and Manufacturing*, vol. 37, no. 8, pp. 1206–1215, 2006.

[39] S. Pimenta and S. T. Pinho, "Recycling carbon fibre reinforced polymers for structural applications: technology review and market outlook," *Waste Management*, vol. 31, no. 2, pp. 378–392, 2011.

[40] G. Kočevar and A. Kržan, "Recycling of an acrylate–glass fiber reinforced polyester composite," *Journal of Material Cycles and Waste Management*, vol. 20, no. 2, pp. 1106–1114, 2018.

[41] E. Esmizadeh, S. Khalili, A. Vahidifar, G. Naderi, and C. Dubois, "Waste polymethyl methacrylate (PMMA): recycling and high-yield monomer recovery," in *Handbook of Ecomaterials*, L. Martínez, O. Kharissova, and B Kharisov, Eds., Springer, Cham, Switzerland, pp. 2977–3009, 2019.

[42] K. Jaan, K. Priit, G. Dimitri, and M. Valdek, "Reprocessing technology of composite plastic scrap and properties of materials from recycled plastics," *Proceedings of the Estonian Academy of Sciences*, vol. 13, pp. 105–116, 2007.

[43] H. U. Sokoli and E. G. Søgaard, "Supercritical degradation of unsaturated polyester resin composites using alcohols," *Chemical Engineering Transactions*, vol. 43, pp. 967–972, 2015.

[44] A. Conroy, S. Halliwell, and T. Reynolds, "Composite recycling in the construction industry," *Composites Part A: Applied Science and Manufacturing*, vol. 37, no. 8, pp. 1216–1222, 2006.

[45] D. S. Cousins, Y. Suzuki, R. E. Murray, J. R. Samaniuk, and A. P. Stebner, "Recycling glass fiber thermoplastic composites from wind turbine blades," *Journal of Cleaner Production*, vol. 209, pp. 1252–1263, 2019.

[46] ASTM C150/C150M-18, *Standard Specification for Portland Cement*, ASTM International, West Conshohocken, PA, USA, 2018.

[47] P. Asokan, M. Osmani, and A. Price, "Improvement of the mechanical properties of glass fibre reinforced plastic waste powder filled concrete," *Construction and Building Materials*, vol. 24, no. 4, pp. 448–460, 2010.

[48] ACI 211.1-91, *Standard Practice for Selecting Proportions for Normal, Heavyweight, and Mass Concrete (ACI 211.1-91)*, ACI Committee 211, Farmington Hills, MI, USA, 2002.

[49] M. C. S. Ribeiro, A. Fiúza, A. C. M. Castro et al., "Mix design process of polyester polymer mortars modified with recycled GFRP waste materials," *Composite Structures*, vol. 105, pp. 300–310, 2013.

[50] A. Hedlund-åström, *Model for end of life treatment of polymer composite materials*, KTH, Stockholm, Sweden, Ph.D. dissertation, 2005.

[51] ASTM C39, *Standard Test Method for Compressive Strength of Cylindrical Concrete Specimens*, American Society for Testing and Materials, West Conshohocken, PA, USA, 2016.

[52] ASTM C496/C496M-17, *Standard Test Method for Splitting Tensile Strength of Cylindrical Concrete Specimens ASTM C-496*, ASTM International, West Conshohocken, PA, USA, 2011.

[53] ASTM C1609, *C 1609/C 1609M-05 Standard Test Method for Flexural Performance of Fiber-Reinforced Concrete (Using Beam with Third-Point Loading)*, ASTM International, West Conshohocken, PA, USA, 2005.

[54] A. G. Tallentire, "Glass fiber cement applications," *Precast Concrete*, vol. 8, no. 2, pp. 95–97, 1977.

[55] R. Ironman, "Stronger market seen for glass-fiber concrete," *Concrete Producer*, vol. 79, no. 1, pp. 42–44, 1976.

[56] H. Y. Aruntaş, S. Cemalgil, O. Şimşek, G. Durmuş, and M. Erdal, "Effects of super plasticizer and curing conditions on properties of concrete with and without fiber," *Materials Letters*, vol. 62, no. 19, pp. 3441–3443, 2008.

Research Article

Mechanical and Self-Sensing Properties of Multiwalled Carbon Nanotube-Reinforced ECCs

Chuanbo Liu,[1] Guozhen Liu,[2] Zhi Ge [ID],[3] Yanhua Guan,[3] Zhiyong Cui,[4] and Jian Zhou[3]

[1]*Jinan Highway Administration, Jinan 2500123, China*
[2]*Zhangqiu Highway Administration, Jinan 250200, China*
[3]*School of Qilu Transportation, Shandong University, Jinan 250002, China*
[4]*Taian Department of Transportation, Taian 271000, China*

Correspondence should be addressed to Zhi Ge; zhige@sdu.edu.cn

This paper investigates the effect of type and dosage of multiwalled carbon nanotubes (MWCNTs) on the mechanical and self-sensing properties of engineered cementitious composites (ECCs). Two types of MWCNTs (MWCNTa and MWCNTb) were employed. The tensile and flexural strengths of CNT-reinforced ECCs were improved compared with normal ECCs, while the ultimate tensile strain and midspan deflection were reduced. Compared with the dosage of MWCNTs, the type had less effect on these properties. The percolation threshold was around 0.3 wt.%. ECCs containing MWCNTs had good self-sensing ability under different loading conditions. When the midspan deflection increased from 0.1 to 0.6 mm, the fractional change in resistivity reached 9%. The dosage of MWCNTs had a significant effect on the self-sensing ability. As the MWCNT content increased, the amplitude of fractional change in resistivity decreased.

1. Introduction

Concrete structures deteriorate during their service life because of continuous use, environment, difficulties in proper inspection methods, lack of maintenance, etc. Therefore, structural health monitoring (SHM) is critical because of the huge loss of life and property caused by structural failure. One of the key components of SHM is data acquisition. Currently, sensors are used to collect strain, temperature, stress, etc. However, these sensors have disadvantages of high cost, loss of mechanical properties in structure, and poor durability [1, 2]. Self-sensing materials on the other hand could overcome the drawbacks of traditional sensors and be used for data collection because they are structural materials themselves and able to sense their own strain and damage [3]. Currently, carbon nanofibres (CNFs), carbon nanotubes (CNTs), and graphite nanoplatelets (GNPs) are incorporated into cementitious materials to produce intrinsic self-sensing cementitious materials to develop self-sensing cement composites. Currently, most studies focus on type and dosage of additives, mixing method, and self-sensing ability of materials or structures [1–10]. Studies show that the resistivity and piezoresistivity of the CNT-cement composite depend on the conductivity network in the composite. Different optimal dosages of CNTs for better sensing abilities were reported. For example, Han et al. [5] found that composites with 0.1 wt.% CNTs had better performance. However, Luo et al. [6] concluded that 0.5 wt.% of CNTs showed better stability. Dispersion of CNTs will also affect the properties of the CNT-cement composite. In order to achieve improved mechanical and electrical properties, the CNTs should be dispersed effectively in the cement paste. Al-Dahawi et al. [10] investigated the effect of different dispersion methods on the electrical resistivity and found that mechanical mixing with shear effect was very influential in dispersing CNTs. Currently, most studies used cement. However, traditional cement-based materials are typically quasi-brittle material with low tensile strain capacity. In this case, it is impossible

to monitor large deformation of the structure by these self-sensing cement composites.

Engineered cementitious composites (ECCs) are fiber-reinforced cementitious composites with excellent tensile ductility and good durability under harsh environment [11–19]. The research found that incorporating conductive filler into ECCs could make it self-sensing [18–23]. Lin et al. found that adding a small dosage of carbon black (CB) into the ECC system could enhance matrix tensile strength and achieve self-sensing ability [20]. Al-Dahawi et al. [21] found the percolation threshold of multiwalled carbon nanotubes, graphene nano-platelets, carbon black, and carbon fiber in ECCs was around 0.55%, 2.00%, 2.00%, and 1.00%, respectively. These carbon-based materials improved compressive strength and self-sensing ability under both compressive and flexural tests [22]. Current research shows that it is possible to use modified ECCs for SHM. However, few research was conducted to investigate the influence of types of CNTs on the mechanical and self-sensing properties of CNT-reinforced ECCs at different midspan deflection ranges. In this study, the uniaxial tensile test and four-point flexural test were employed to study the mechanical and self-sensing ability of ECCs containing different dosages and types of CNTs.

2. Experimental Work

2.1. Materials. The P.O. 42.5 ordinary Portland cement and Class F fly ash, produced in Jinan, China, were used. The main chemical compositions are presented in Table 1. The 0.096–0.18 mm sand was local silica sand. The polyvinyl alcohol (PVA) fiber had a length of 12 mm, diameter of 39 mm, nominal tensile strength of 1620 MPa, specific gravity of 1.3, and elastic modulus of 42.8 GPa. Figure 1 shows the microstructure of PVA fiber. Two types of multiwalled carbon nanotubes were adopted. The main properties are summarized in Table 2. The surfactant for the dispersion of MWCNTs was polyvinylpyrrolidone (PVP), a white powder produced in Jinan. The polycarboxylate-based high-range water reducer (HRWR) was employed. The water used was distilled water produced in the laboratory.

2.2. Preparation of ECC Specimen. The uniform dispersion of MWCNTs without agglomerations is critical for specimen's mechanical properties and electrical conductivity by forming continuous conductive network [10, 24]. In this study, PVP (PVP to MWCNT ratio of 0.8) was first added into the distilled water and then stirred using a magnetism stirrer until fully dissolved. Subsequently, MWCNTs were added into the solution and sonicated with a probe sonicator (Ningbo Scientz Biotechnology, Model JY92-IIN, 640 W ultrasonic power and 40% amplitude) for 15 minutes.

To prepare the specimen, the cement, fly ash, and sand were first mixed at low speed (140 rpm) for 2 minutes. The HRWR was added into the well-dispersed MWCNT solution and then poured into the mixer. All materials were mixed at low speed for 1 minute, followed by 2 minutes at high speed (285 rpm). After that, the PVA fibers were slowly added into the mix and continuously mixed at high speed for three

TABLE 1: Main chemical compositions of cement and fly ash.

Composition (%)	CaO	SiO$_2$	Al$_2$O$_3$	MgO	Fe$_2$O$_3$	SO$_3$	Na$_2$O
Cement	64.63	21.96	4.73	2.59	0.03	0.3	0.56
Fly ash	3.88	45.66	31.52	0.89	9.70	0.37	3.02
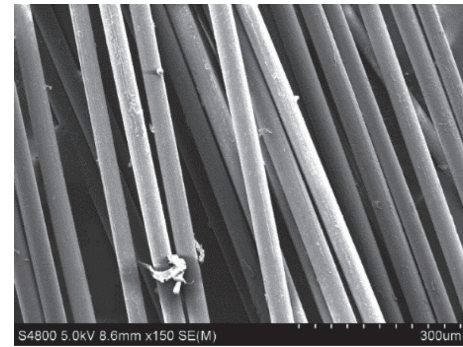
(a)
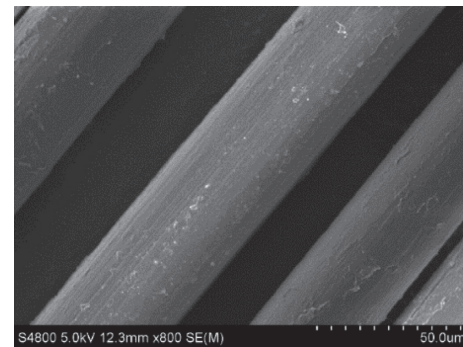
(b)

FIGURE 1: Microstructure of PVA fiber.

more minutes to ensure uniform dispersion of the PVA fibers. After mixing, the mix was poured into the mold. The specimens were demolded after 1 day and cured at a standard curing room with a temperature of $22 \pm 2°C$ and relative humidity of 98% for 28 days.

2.3. Experimental Design. This paper studied the effect of MWCNT type and dosage on the mechanical and self-sensing properties. Two types of MWCNTs (MWCNTa and MWCNTb) and four dosage levels were adopted. Therefore, total 9 mixes were designed. The different mix proportions are listed in Table 3. In all mixes, the PVP to MWCNT ratio was 0.8. Different amount of HRWR was used for different mixes to achieve similar workability of ECC mortar (before adding fiber) because workability of the matrix significantly influences fiber dispersion uniformity, which results in different strain capacities [25].

2.4. Testing Methods. Uniaxial tensile and four-point bending tests were conducted to evaluate the strain-hardening property of ECCs. For each test, three 5 mm × 50 mm × 170 mm specimens were used. The average

TABLE 2: Main physical properties of MWCNTs.

Type	OD (nm)	Length (μm)	Purity (wt.%)	Ash (wt.%)	−COOH (wt.%)	Specific surface area ($m^2 \cdot g^{-1}$)
MWCNTa	8–15	~50	>95	<1.5	2.56	>130
MWCBTb	30–50	<10	>98	<1.5	0.73	>100

TABLE 3: Mix proportions of MWCNT-reinforced ECCs.

No.	Normal ECC mix proportions						MWCNTs (wt.%)	
	Cement (kg/m^3)	Fly ash (kg/m^3)	Sand (kg/m^3)	Water (kg/m^3)	HRWR (kg/m^3)	Fiber (kg/m^3)	MWCNTa	MWCNTb
1	570	684	455	331	5.5	27	0	0
2	570	684	455	331	7	26	0.1	0
3	570	684	455	331	8.5	26	0.3	0
4	570	684	455	331	10	26	0.5	0
5	570	684	455	331	12	26	0.7	0
6	570	684	455	331	6.5	26	0	0.1
7	570	684	455	331	7	26	0	0.3
8	570	684	455	331	7.5	26	0	0.5
9	570	684	455	331	8	26	0	0.7

value was presented. For direct tensile testing, the LVDT displacement sensor was employed to measure displacement. The load was applied at 0.2 mm/min by the WDW-100E universal testing machine (Figure 2(a)).

The bending test could be used as an indirect evaluation method for the strain-hardening properties of ECCs. The 15 mm × 50 mm × 170 mm specimen was loaded at 0.5 mm/min using the WDW-100E universal testing machine (Figure 2(b)). The midspan deflection was monitored by the LVDT displacement sensor.

The two-probe method was adopted to measure the electrical resistivity of the ECC specimen (Figure 3). The voltage between two electrodes (70 mm apart) was automatically measured by using a Keithley 2100 multimeter. The electrical resistance was calculated by Ohm's law. The electrical resistivity (ρ) and the fractional change in resistivity were calculated by using the following equations:

$$\rho = R \frac{A}{l},$$

$$\frac{\Delta\rho}{\rho_0} = \frac{\rho_L - \rho_0}{\rho_0} \times 100\%, \tag{1}$$

where R is the material's electrical resistance (Ω), l is the electrode interval (m), A is the electrode area (m^2), and ρ_0 is the initial electrical resistivity ($\Omega \cdot m$), and ρ_L is the electrical resistivity during flexural loading ($\Omega \cdot m$).

The self-sensing ability of MWCNT-reinforced ECCs was investigated under three loading scenarios: (1) continuous flexural loading: the specimen was continuously loaded at a constant rate of 0.5 mm/min until failure; (2) multiple-stage loading: the specimen was loaded at five stages. For each stage, the flexural load was applied at 0.5 mm/min for 1 minute and then kept the deflection constant for one more minute; (3) cyclic flexural loading: the flexural load was applied and released four times until reaching the specified midspan deflection. The specimen was dried under 60°C in the oven for two days to eliminate the effect of moisture.

3. Results and Discussion

3.1. Mechanical Properties. As shown in Figure 4, the ECC exhibits strain hardening behavior under both loading conditions. The strain first increased almost linearly with stress before the first cracking, which is the defined as the first inflection point. After that, more cracks developed, resulting in the plastic strain at increasing stress. The effect of MWCNTs on the first cracking strength, first cracking strain or deflection, ultimate strength, and ultimate strain or deflection was discussed in the following section.

Figure 5 shows the effect of MWCNT type and dosage on the uniaxial tensile properties. Figure 5(a) shows that the first cracking strength increased with the increase of MWCNT dosage. The specimens with different MWCNTs had similar strength. The first cracking strength increased by 18.2%, 34.8%, 40.3%, and 45.9%, as the MWCNTa dosage increased from 0 to 0.1%, 0.3%, 0.5%, and 0.7%, respectively. When MWCNTb was added, the first cracking strength increased by 8.8%, 26.0%, 33.1%, and 43.1%, respectively. Figure 5(b) indicates that when MWCNT content increased from 0% to 0.7%, the ultimate tensile strength for the ECC with MWCNTa increased by 6.2%, 11.7%, 23.1%, and 31.7%, respectively, and for the ECC with MWCNTb, the ultimate tensile strength increased by 3.8%, 9.0%, 20.7%, and 33.1%, respectively. These two types of MWCNTs had a similar effect on ultimate tensile strength. The increase of strength by adding MWCNTs could be possibly caused by several reasons. First, MWCNTs could act as the filler inside the skeleton of hardened cement paste, resulting in denser structure. Second, MWCNTs could accelerate early-age cement hydration. Third, MWCNTs are able to bridge the microcracks due to its very high length to diameter ratio [20, 26].

Different from strength, the first cracking and ultimate tensile strains decreased as MWCNTs were added. As shown in Figure 5(c), when MWCNT content increased from 0% to 0.7%, the first cracking tensile strain reduced 6.3%, 25.0%, 34.4%, and 25.0% for the MWCNTa-ECC, and by 25.0%, 31.3%, 40.6%, and 12.5% for the MWCNTb-ECC,

(a)

(b)
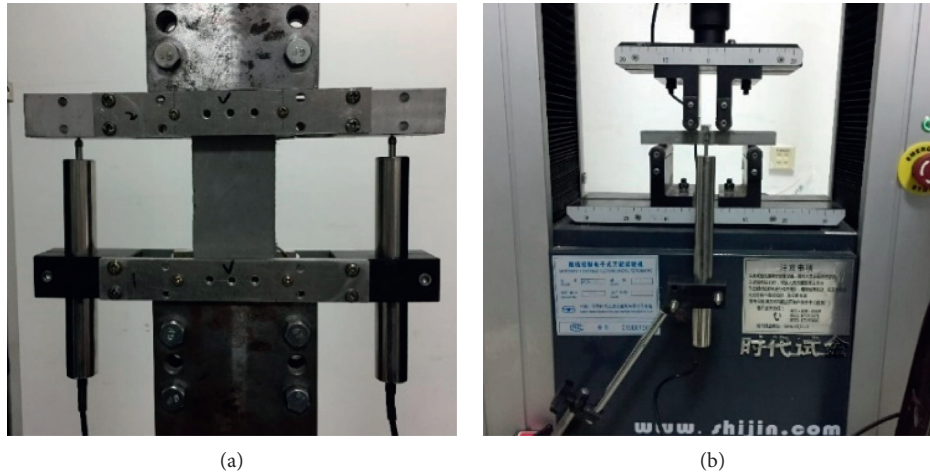
Figure 2: Testing setups for mechanical behavior: (a) uniaxial tensile test and (b) four-point bending test.
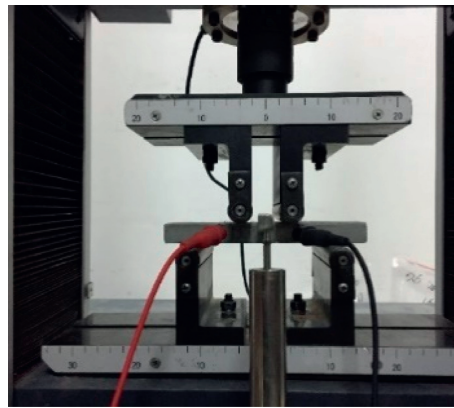
Figure 3: Testing setup for electrical resistivity of the ECC.

(a)

(b)
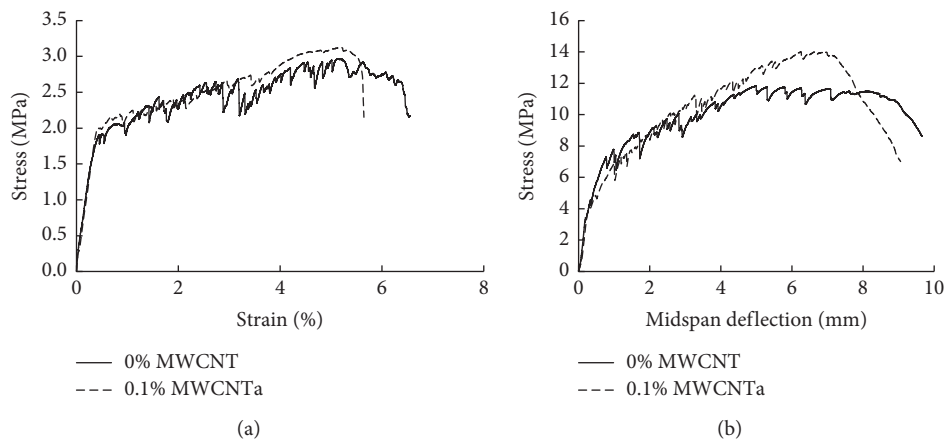
Figure 4: Typical mechanical behavior of different ECC mixes. (a) Uniaxial tensile stress-strain curve. (b) Midspan deflection under flexural loading.

respectively. The reduction could be caused by the increased modulus and also the bridging effect of MWCNTs, which limits the deformation of the ECC matrix when the ECC starts to crack. The reduction of ultimate tensile strain was higher than that of the first cracking strain. The ultimate tensile strain was decreased by 13.7%, 25.1%, 30.0%, and 27.6% for the MWCNTa-ECC and by 4.5%, 15.9%, 21.5%, and 20.1% for the MWCNTb-ECC, respectively. The reduction of the ultimate tensile strain could be caused by the improved fiber-to-matrix bond.

(a)

(b)

(c)

(d)
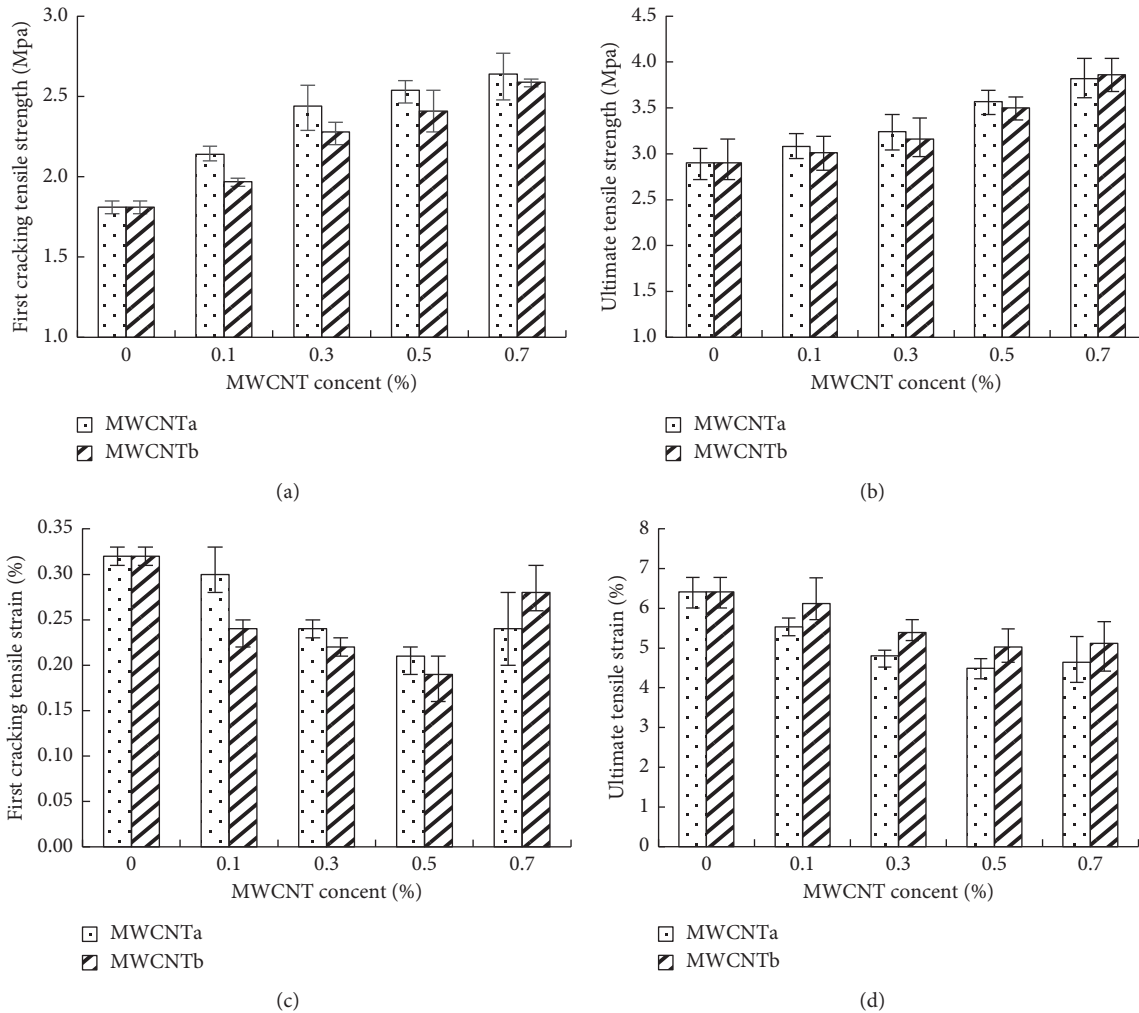
FIGURE 5: Characteristics of stress-strain curves of the uniaxial tensile test for MWCNT-reinforced ECCs. (a) First cracking tensile strength. (b) Ultimate tensile strength. (c) First cracking tensile strain. (d) Ultimate tensile strain.

Figure 6 shows the flexural behavior of ECCs with different dosages and types of MWCNTs. As shown in Figure 6(a), MWCNTs had significant effect on the first cracking flexural strength, which increased as the dosage of MWCNTs increased. When MWCNT content increases from 0% to 0.7%, the strength increased by 78.2%, 94.0%, 130.9%, and 125.6% for the MWCNTa-ECC and by 77.7%, 81.4%, 97.2%, and 105.3% for the MWCNTb-ECC. However, MWCNTs had less effect on ultimate flexural strength (Figure 6(b)). When MWCNT content increases from 0% to 0.7%, the ultimate flexural strength increased 17.2%, 22.1%, 27.3%, and 22.6%, respectively, for the MWCNTa-ECC and 12.8%, 19.0%, 4.1%, and 28.4%, respectively, for the MWCNTb-ECC. This trend is consistent with current research [28]. As observed by Sakulich and Li [28], CNTs consolidated around the PVA fibers and could increase mechanical properties by bridging microcracks. Therefore, the first cracking strength increased. Different from the first cracking strength, the ultimate flexural strength depends more on fiber-to-matrix bonding and the matrix's elastic modulus

[29, 30]. MWCNTs may form a strong matrix-to-CNT bond, but the effect could be reduced by the improved matrix density and stiffness [27].

Similar to the tensile strain, MWCNTs reduced the midspan first cracking and ultimate deflection. As shown in Figure 6(c), the MWCNTa-ECC had higher midspan first cracking deflection than the MWCNTb-ECC, except when 0.7% MWCNTs was added. The MWCNTa-ECC, however, had lower ultimate deflection than the MWCNTb-ECC. The highest reduction of ultimate deflection was 41.1% and 22.0% for the MWCNTa-ECC and MWCNTb-ECC, respectively.

3.2. Self-Sensing Behavior. Figure 7 shows that the addition of MWCNTs, regardless of the type of MWCNTs, reduced the electrical resistivity. As the dosage of MWCNTs increased from 0.1% to 0.3%, the resistivity was reduced around 54% for both types of ECCs. After that, the resistivity started to decrease slowly with the increase of MWCNTs. The resistivity of the ECC was determined by

(a)

(b)

(c)

(d)
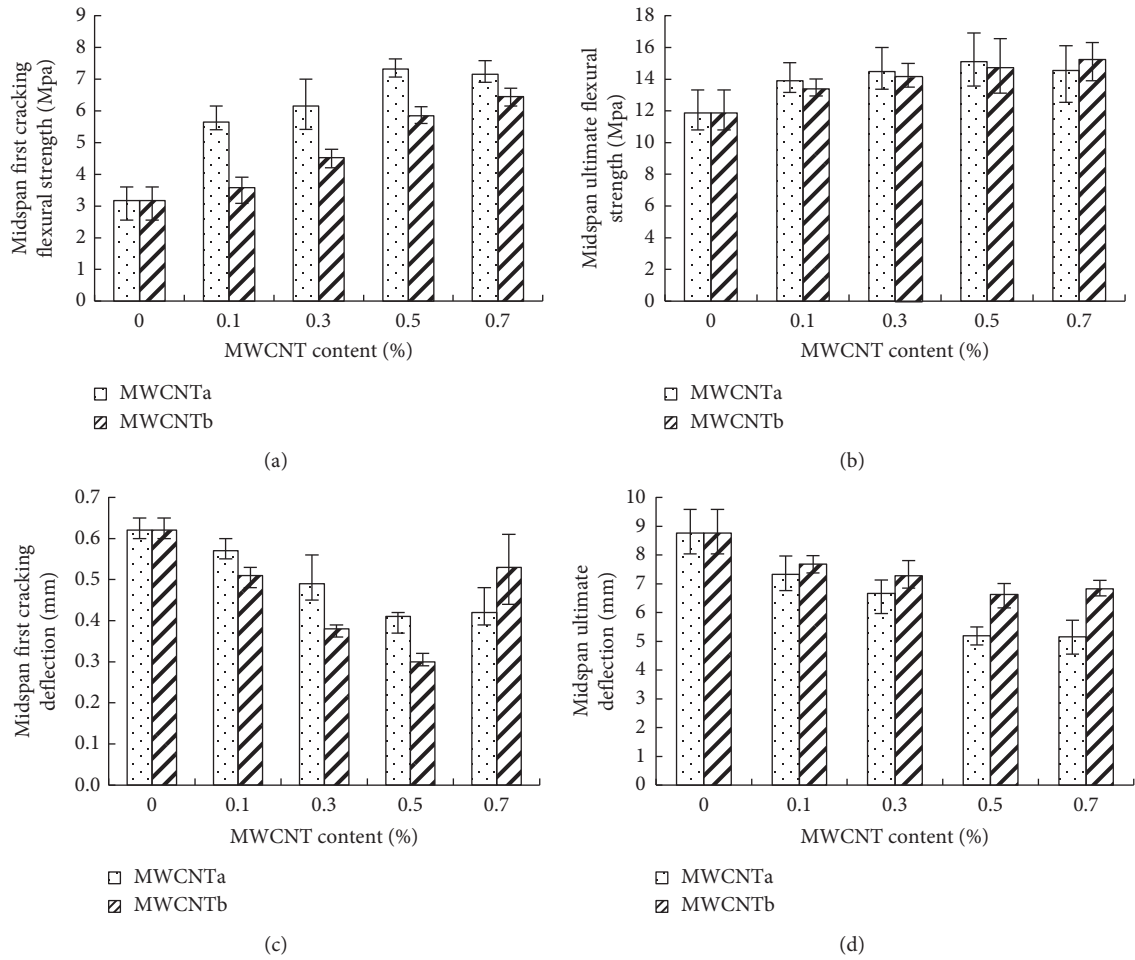
FIGURE 6: Stress-deflection curves of the flexural test for ECCs containing different MWCNTs. (a) First cracking flexural strength of MWCNT-ECCs. (b) Ultimate flexural strength of MWCNT-ECCs. (c) Midspan first cracking deflection of MWCNT-ECCs. (d) Midspan ultimate deflection of MWCNT-ECCs.
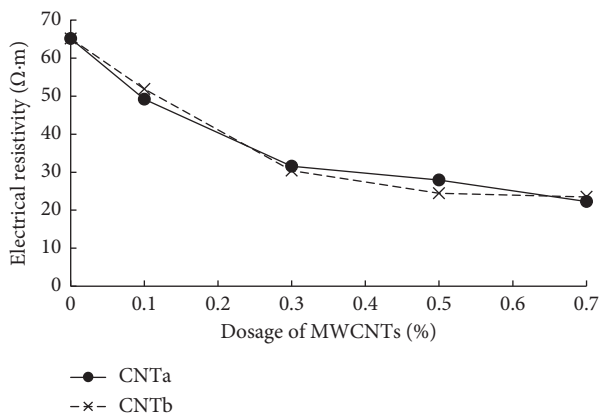
FIGURE 7: Electrical resistivity of ECCs containing different types of MWCNTs.

two aspects: (1) the intrinsic resistance of the cement matrix and MWCNTs and (2) the contact resistivity of MWCNTs, including resistance between the connected MWCNTs and the tunnelling resistance effect, which depends on the thickness and the conductive properties of the matrix filling

the tunnelling gap [27]. As the dosage of MWCNTs increased, more and more MWCNTs are connected, resulting in lower contact resistance and smaller thickness of gaps among unconnected MWCNTs, which in turn reduces tunnelling resistance. Therefore, the resistivity of the ECC reduces with the increase of MWCNT dosage. When the connected MWCNT network is formed, the resistivity is mainly determined by direct contact resistivity of MWCNTs. Therefore, the further increase of MWCNTs will not significantly decrease the resistivity [22]. This phenomenon is called electrical percolation [31]. Figure 7 indicates that MWCNT-reinforced ECCs had typical features of electrical percolation phenomenon. The percolation threshold of ECCs containing MWCNTs was around 0.3% by weight, over which resistivity drops sharply. Since the type of MWCNTs had no significant effect on resistivity, the ECC with MWCNTa was selected to investigate the self-sensing behavior.

Figure 8 illustrates the self-sensing behavior of ECCs with 0.3% MWCNTa subjected to continuous four-point flexural loading. As shown in the figure, the fractional change in resistivity (FCR) increased with time. The FCR
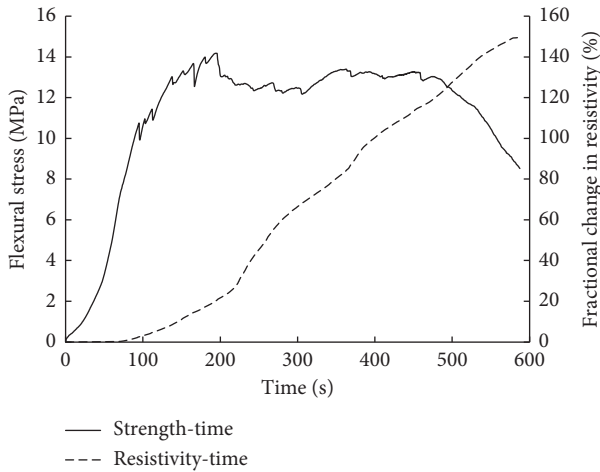
Figure 8: Self-sensing behavior of ECCs subjected to flexural loading.
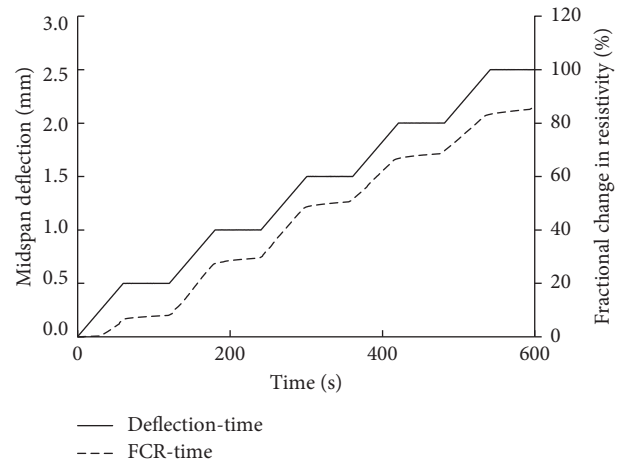
Figure 9: Self-sensing behavior of MWCNT-reinforced ECCs subjected to multiple-stage loading.

curve could be divided into two stages: before and after the first crack. Before the first crack, the FCR increased slowly. At this stage, as the stress increased, the distance among MWCNTs increased and some connected MWCNTs were separated, resulting in higher resistivity [26, 27]. After the first crack, multiple cracks developed and crack width increased. The cracks cut off some electric channels, resulting in much higher resistivity. Therefore, FCR increases quickly. Figure 9 shows the self-sensing behavior of ECCs subjected to multiple-step loading. The FCR changed simultaneously with the deflection. The FCR was constant when the deflection was kept unchanged. The FCR was over 80% when the deflection increased to 3.5 mm. According to Figures 8 and 9, ECCs with MWCNTs had good self-sensing ability.

Figure 10 illustrates the self-sensing behavior of ECCs containing 0.3% MWCNTa under cyclic loading at different midspan deflection ranges. Generally, the resistivity increased upon loading and decreased upon unloading in every cycle. When the midspan deflection was between 0.1 and 0.6 mm, the resistivity was also reversible, indicating better self-sensing ability. When the midspan deflection was less than 0.2 mm, specimen was under elastic stage without no apparent cracks. During this stage, the change of resistivity was mainly caused by the separation of MWCNTs, leading to higher contact resistivity. When the defection reached 0.6 mm, the specimen was in the plastic range and cracks were formed. The change of resistivity was mainly caused by crack opening and closing. As shown in the figure, FCR reached 9% when the deflection was from 0.1 to 0.6 mm.

Figure 11 indicates that the dosage of MWCNTs had significant effect on the self-sensing ability. For MWCNT content up to 0.7%, the FCR had good relationship with the midspan deflection. However, as the MWCNT content increased, the amplitude of FCR decreased. The FCR decreased from 9% to 4.1% and 2.5% when the dosage of MWCNTs increased from 0.3% to 0.5% and 0.7%, respectively. This could be caused by the MWCNT network inside ECCs. As the MWCNT content increased, the tunnelling gap would be
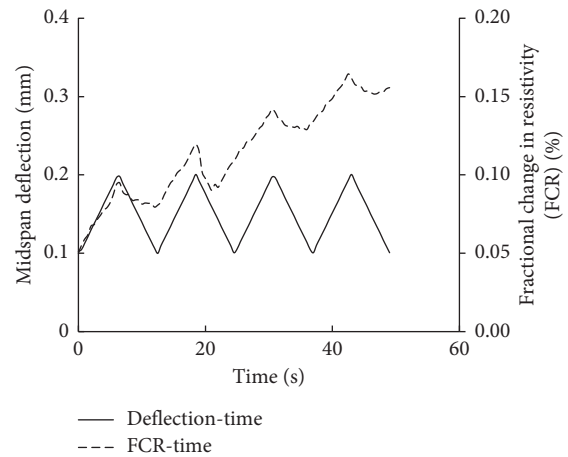
(a)
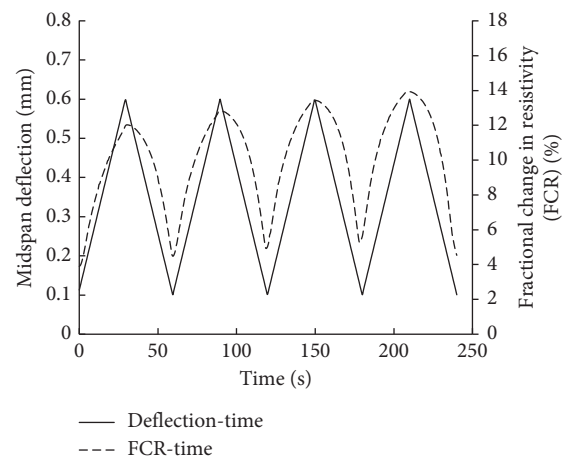
(b)

Figure 10: Self-sensing behavior of MWCNT-reinforced ECCs subjected to cyclic flexural loading. (a) 0.1-0.2 mm. (b) 0.1–0.6 mm.

shortened, and then the MWCNT network was getting stabilized and hard to change under loading, resulting in lower FCR.
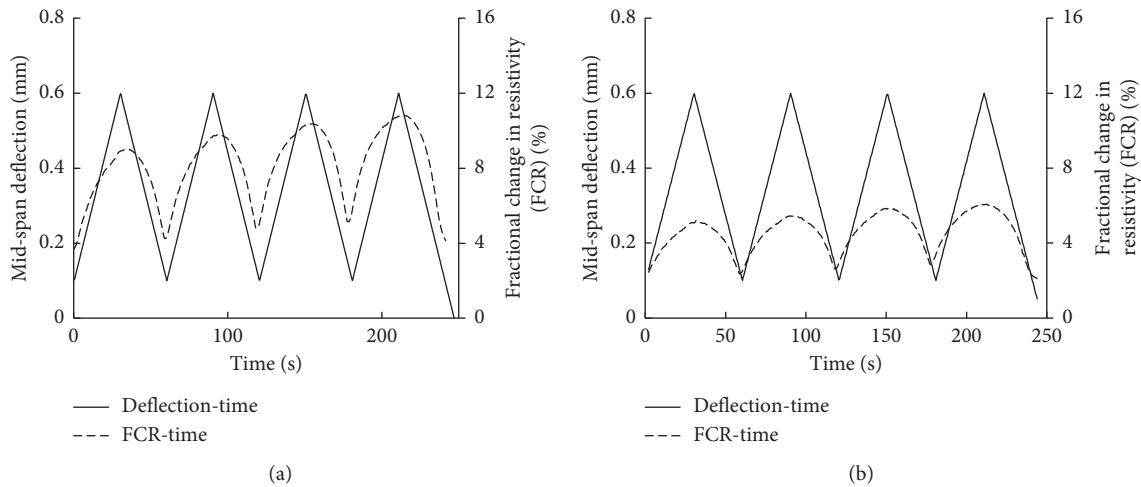
FIGURE 11: Effect of dosage of MWCNTs on the self-sensing ability: (a) 0.5% MWCNT and (b) 0.7% MWCNT.

4. Conclusions

This paper studied the mechanical and self-sensing properties of MWCNT-reinforced ECCs. The conclusions are listed as follows:

(1) MWCNTs improved first cracking tensile strength and ultimate tensile strength under the uniaxial tensile test while reducing first cracking tensile strain and ultimate tensile strain. For the four-point flexural testing, MWCNTs improved first cracking flexural strength and ultimate flexural strength, while reducing midspan first cracking deflection and midspan ultimate deflection.

(2) The percolation threshold of ECCs containing MWCNTs was around 0.3% by weight.

(3) ECCs containing MWCNTs had good self-sensing ability under both continuous flexural loading, multiple-step loading, and cyclic loading conditions. When the midspan deflection was between 0.1 and 0.6 mm, the FCR reached 9%.

(4) The dosage of MWCNTs had significant effect on the self-sensing ability. As the MWCNT content increased, the amplitude of FCR decreased.

Data Availability

The data used to support the findings of this study are included within the article.

Conflicts of Interest

The authors declare that there are no conflicts of interest regarding the publication of this paper.

Acknowledgments

References

[1] W. A. Li, "Method for structural safety monitoring of composite carbon fiber reinforced concrete," *China Safety Science Journal*, vol. 15, pp. 109–112, 2015.

[2] Z. Ge, D. Wang, R. Sun, and M. Oeser, "Einsatz von kohlenstoffnanoröhren im straßenbeton zur selbstüberwachung," *Bautechnik*, vol. 92, no. 3, pp. 189–195, 2015.

[3] B. Han, S. Sun, S. Ding, L. Zhang, X. Yu, and J. Ou, "Review of nanocarbon-engineered multifunctional cementitious composites," *Composites Part A: Applied Science and Manufacturing*, vol. 70, pp. 69–81, 2015.

[4] G. Y. Li, P. M. Wang, and X. Zhao, "Mechanical behavior and microstructure of cement composites incorporating surface-treated multi-walled carbon nanotubes," *Carbon*, vol. 43, no. 6, pp. 1239–1245, 2005.

[5] B. Han, X. Yu, E. Kwon, and J. Ou, "Effects of CNT concentration level and water/cement ratio on the piezoresistivity of CNT/cement composites," *Journal of Composite Materials*, vol. 46, no. 1, pp. 19–25, 2012.

[6] J. L. Luo, Z. D. Duan, T. J. Zhao, and Q. Y. Li, "Effect of compressive strain on electrical resistivity of carbon nanotube cement-based composites," *Key Engineering Materials*, vol. 483, pp. 579–583, 2011.

[7] A. Yazdanbakhsh, Z. Grasley, B. Tyson, and R. Abu Al-Rub, "Challenges and benefits of utilizing carbon nanofilaments in cementitious materials," *Journal of Nanomaterials*, vol. 2012, Article ID 371927, 8 pages, 2012.

[8] D. D. L. Chung, "Piezoresistive cement-based materials for strain sensing," *Journal of Intelligent Material Systems and Structures*, vol. 13, no. 9, pp. 599–609, 2002.

[9] G. Yıldırım, M. H. Sarwary, A. Al-Dahawi, O. Öztürk, A. Özgür, and M. Şahmaran, "Piezoresistive behavior of CF- and CNT-based reinforced concrete beams subjected to static flexural loading: shear failure investigation," *Construction and Building Materials*, vol. 168, pp. 266–279, 2018.

[10] A. Al-Dahawi, O. Öztürk, F. Emami, G. Yıldırım, and M. Şahmaran, "Effect of mixing methods on the electrical

properties of cementitious composites incorporating different carbon-based materials," *Construction and Building Materials*, vol. 104, pp. 160–168, 2016.

[11] V. C. Li, "On engineered cementitious composites (ECC)," *Journal of Advanced Concrete Technology*, vol. 1, no. 3, pp. 215–230, 2003.

[12] V. C. Li, C. Wu, S. Wang et al., "Interface tailoring for strain-hardening polyvinyl alcohol-engineered cementitious composites (PVA-ECC)," *ACI Materials Journal*, vol. 99, no. 5, pp. 463–472, 2002.

[13] H. Q. Xue and Z. C. Deng, "Study on durability of engineered cementitious composites," *Advanced Materials Research*, vol. 236–238, pp. 2688–2693, 2011.

[14] M. Şahmaran and V. C. Li, "Durability of mechanically loaded engineered cementitious composites under highly alkaline environments," *Cement and Concrete Composites*, vol. 30, no. 2, pp. 72–81, 2008.

[15] X. Huang, R. Ranade, W. Ni, and V. C. Li, "Development of green engineered cementitious composites using iron ore tailings as aggregates," *Construction and Building Materials*, vol. 44, pp. 757–764, 2013.

[16] J. Yu, J. Lin, Z. Zhang, and V. C. Li, "Mechanical performance of ECC with high-volume fly ash after sub-elevated temperatures," *Construction and Building Materials*, vol. 99, pp. 82–89, 2015.

[17] M. Şahmaran, E. Özbay, H. E. Yücel, M. Lachemi, and V. C. Li, "Frost resistance and microstructure of engineered cementitious composites: influence of fly ash and micro poly-vinyl-alcohol fiber," *Cement and Concrete Composites*, vol. 34, no. 2, pp. 156–165, 2012.

[18] M. Sahmaran and V. C. Li, "Durability properties of micro-cracked ECC containing high volumes fly ash," *Cementitious Concrete Research*, vol. 39, no. 11, pp. 1033–1043, 2009.

[19] B. Han, X. Yu, and J. Ou, "Multifunctional and smart carbon nanotube reinforced cement-based materials," *Nanotechnology in Civil Infrastructure*, pp. 1–47, 2011.

[20] V. W. J. Lin, M. Li, J. P. Lynch, and V. C. Li, "Mechanical and electrical characterization of self-sensing carbon black ECC," vol. 7983, pp. 1–12, 2011.

[21] A. Al-Dahawi, M. H. Sarwary, O. Öztürk et al., "Electrical percolation threshold of cementitious composites possessing self-sensing functionality incorporating different carbon-based materials," *Smart Materials and Structures*, vol. 25, no. 10, pp. 1–15, 2016.

[22] A. Al-Dahawi, G. Yıldırım, O. Öztürk, and M. Şahmaran, "Assessment of self-sensing capability of engineered cementitious composites within the elastic and plastic ranges of cyclic flexural loading," *Construction and Building Materials*, vol. 145, no. 1, pp. 1–10, 2017.

[23] S. Kumar, P. Kolay, S. Malla, and S. Mishra, "Effect of multiwalled carbon nanotubes on mechanical strength of cement paste," *Journal of Materials in Civil Engineering*, vol. 24, no. 1, pp. 84–91, 2012.

[24] B. M. Tyson, R. K. Abu Al-Rub, A. Yazdanbakhsh, and Z. Grasley, "A quantitative method for analyzing the dispersion and agglomeration of nano-particles in composite materials," *Composites Part B: Engineering*, vol. 42, no. 6, pp. 1395–1403, 2011.

[25] M. Li and V. C. Li, "Rheology, fiber dispersion, and robust properties of engineered cementitious composites," *Materials and Structures*, vol. 46, no. 3, pp. 405–420, 2013.

[26] M. A. Etman, S. S. Shebl, A. A. Mosallam, and M. A. EL-Dimerdash, "Effect of carbon nanotubes addition on mechanical properties of cement paste," *HBRC Journal*, vol. 7, no. 1, pp. 1–8, 2011.

[27] K. Gopalakrishnan, B. Birgisson, P. Taylor, and N. O. Attoh-Okine, *Nanotechnology in Civil Infrastructure*, Springer, Berlin, Germany, 2011.

[28] A. R. Sakulich and V. C. Li, "Nanoscale characterization of engineered cementitious composites (ECC)," *Cement and Concrete Research*, vol. 41, no. 2, pp. 169–175, 2011.

[29] H. Siad, M. Lachemi, M. Sahmaran, H. A. Mesbah, and K. A. Hossain, "Advanced engineered cementitious composites with combined self-sensing and self-healing functionalities," *Construction and Building Materials*, vol. 176, pp. 313–322, 2018.

[30] M. S. Sahmaran, H. E. Yücel, S. Demirhan, and C. V. Li, "Combined effect of aggregate and mineral admixtures on tensile ductility of engineered cementitious composites," *Journal of ACI Material*, vol. 109, no. 6, pp. 627–638, 2012.

[31] P. Xie, P. Gu, and J. J. Beaudoin, "Electrical percolation phenomena in cement composites containing conductive fibres," *Journal of Materials Science*, vol. 31, no. 15, pp. 4093–4097, 1996.

Research Article

A Coupling Electromechanical Cell-Based Smoothed Finite Element Method Based on Micromechanics for Dynamic Characteristics of Piezoelectric Composite Materials

Jianxiao Zheng [iD],[1] Zhishan Duan [iD],[1] and Liming Zhou [iD][2]

[1]*Yanta Road No. 13, School of Mechanical and Electrical Engineering, Xi'an University of Architecture and Technology, Xi'an 710055, Shaanxi, China*
[2]*Renmin Street No. 5988, School of Mechanical and Aerospace Engineering, Jilin University, Changchun 130022, Jilin, China*

Correspondence should be addressed to Jianxiao Zheng; zhengjianxiao1979@163.com

Coupling electromechanical cell-based smoothed finite element method (CSFEM) with the asymptotic homogenization method (AHM) is presented to overcome the overstiffness of FEM. This method could accurately simulate the dynamic responses and electromechanical coupling effects of piezoelectric composite material (PCM) structures. Firstly, the efficient performances for active compounds of round cross-section fibers are calculated based on AHM. Secondly, in the CSFEM, electromechanical multi-physic-field FEM is coupled with gradient smoothing technique. CSFEM returns the nearly exact stiffness of continuum structures, which auto discretes the elements in complex areas more readily and thus remarkably reduces the numerical errors. Static and dynamic characteristics of four PCM structures are investigated using CSFEM with AHM. Results are compared with analytical solution and those of FEM, which proves that CSFEM with AHM is more accurate and reliable than the standard FEM when solving problems of complex structures. Additionally, CSFEM could provide results of higher accuracy even using distorted meshes. Therefore, such method is a robust tool for analyzing mechanical properties of PCM structures.

1. Introduction

Piezoelectric composite materials (PCMs) could confirm between mechanical energy and electrical energy [1]. PCMs are made of piezoceramics and passive non-piezoelectric polymers [2, 3]. These composites possess superior properties owing to the most promising characteristics of components as well as various structures.

Because of the electromechanical effects, PCMs are more often used as sensors or actuators into noise, vibration, precision position control, energy harvesting, and structural health monitoring [4–6]. Thus, the electric-mechanical properties of PCMs were investigated widely. The heterogeneous media can be generally characterized by micromechanical models. Under such scenario, numerical or analytical ways were used to electromechanically characterize PCMs.

Some analytical approaches were presented to investigate PCMs, but the methods were limited by boundary conditions and loading cases [7, 8]. Moreover, single inclusion was applied into a piezoelectric material based on the micromechanical theory with the electromechanical solution [9–13]. Also, the asymptotic homogenization method (AHM) was developed to solve the effective coefficients of PCMs with the square fibers distribution [14, 15]. AHM can be used to calculate effective performances of structures made of hexagonal symmetrical and randomly distributed fibers [16, 17]. The effective elastic coefficients of periodic composites could be solved by an asymptotic method [18]. Otero et al. expressed the effective properties of reinforced PCMs in the closed form [19]. de Medeiros et al. studied the effective coefficients of PCMs made of circular or squared cross-sectional fibers based on AHM [20]. Viaño et al. derived a high-order asymptotic

expanding model of piezoelectric rods [21]. Le built an exact 2D theory based on the variation asymptotic method for functionally graded PCMs [22]. Fantoni et al. proposed a multifield AHM to analyze the periodic microstructured PCMs exposed to body force, charge density, and heat sources [23]. However, closed-form solutions which are very a valuable benchmark to issues concerning PCMs are often inaccessible except for relatively simple boundary and geometry conditions.

Among numerical approaches, researchers usually use the finite element model (FEM) to develop a specific representative volume element (RVE) for various physical problems, including piezoelectricity. Kar-Gupta and Venkatesh developed an FEM to evaluate how the fiber form affected the general piezoelectric characteristic of PCMs [24]. Jin et al. developed a micromechanical model based on linear stress strain relations and the stress amplification factor to determine the microstress under various mechanical loadings [25]. de Medeiros et al. compared the analytical model and FEM with RVEs in calculating the effective coefficients of PCMs [20]. Würkner et al. established a numerical model to estimate the effective indexes of unidirectional fiber-reinforced PCMs with rhombic fiber arrangement [26]. Mishra et al. extended FEM to evaluate the effective properties of PCMs with SU8 photoresist as the matrix reinforced by the vertically arrayed ZnO nanowires [27]. Bowen et al. discussed the effective properties of new PCMs based on ferroelectric PCR-7M ceramic [28]. Though most of the FEMs can interpolate displacement and electric potential as kinematic field indicators with satisfactory compatibility equations, these methods are often limited by overly stiffness, inaccuracy, and sensitivity to mesh distortion. These limitations can be overcome by hybrid and mixed finite elements [29–32]. Other contributions include drilling degree-of-freedom piezoelectric elements [33–35]. For details and review on FEM establishment for PCM analysis and modeling, refer to Reference [36]. So far, much research has been conducted to develop new special elements [12, 37]. However, the application of FEM is yet limited by the occurrence of mesh distortion.

To solve the problem of mesh distortion in FEM, Liu et al. presented a new smoothed FEM by incorporating the gradient smoothing technique (GST) into FEM for solid mechanics problems, based on the nodal integrated meshless methods [38–42]. The FEM employs standard Galerkin formulation in which the stiffness matrix is stiffened by the presumed displacement field [43]. In the smoothed FEM, the smoothed Galerkin weak form is used where GST softens the stiffness matrix through the softening effect. Theoretically, the smoothed FEM in the energy norm often creates a softer stiffness matrix than the FEM with the same background meshes [44, 45]. This unique ability endows smoothed FEM with many critical characteristics [46], such as the easier modeling, upper bound solution property [47], and even nearly perfect solutions in a norm [43, 48–52]. The softening effects enable smoothed FEM to process highly distorted meshes

and n-sided polygonal elements [45]. The smoothed FEM interpolates displacement according to the same lower standard mesh and evaluates the weak form based on the smoothing zones.

An ultraprecise hybrid smoothed FEM for the piezoelectric problem was designed using with the simplest three- and four-sided elements in 2D and 3D, respectively [53]. An edge-based smoothed FEM was proposed for static eigenvalue assessment of 2D piezoelectric structures [54]. An effective numerical method was presented to optimize and maximize the basic frequency of functionally graded carbon-nanotube-strengthened four-sided sheets [55]. On the commercial software ABAQUS, Bhowmick and Liu established a phase-field model based on cell-based smoothed FEM (CSFEM) to address the brittle fracturing in solids [56]. Pramod et al. developed the CSFEM with the Reissner's mixed variational theorem to analyze the static and free vibration of cross-ply sheet plates [57].

In this work, the dynamic characteristics on PCM structures were studied by using the technique based on the effective CSFEM with AHM. Longitudinal/transversal elastic, piezoelectric, and dielectric effective parameters of a piezoceramic fiber with an O-shaped geometrical section buried in a non-piezoelectric material were computed by AHM based on micromechanics. The CSFEM of PCM structures was presented by applying GST into the exit FEM for an electromechanical coupling field. Then, the equations of the dynamic responses under the multifield for PCM instruments were deduced. Finally, a bilayered PCM actuator and a PCM energy harvester based on micromechanics were calculated by CSFEM. Results of CSFEM were compared with those of FEM, which validated that CSFEM possessed the advantages of accuracy, convergence, and efficiency. Besides, CSFEM was insensitive to mesh distortion, which was very useful to analyze complex structures or large deformation problems. Therefore, CSFEM with AHM performed better than FEM.

This paper is organized as follows: Section 2 introduces the basic formulations for PCMs. Sections 3 and 4 describe the AHM based on micromechanics and CSFEM, respectively. Section 5 puts forward the modified Wilson-θ method. In Section 6, the bilayered PCM actuator and the PCMs energy harvester were elaborated. Section 7 gives the conclusions.

2. Basic Equations for PCMs

2.1. Geometry and Coordinate System.
The cross section of a PCM beam was a rectangle with length L, breadth b, and height h. Here, the continuum theory was used. The PCMs, cylindrical piezoceramic fibers, were buried in the epoxy substrate. The Cartesian coordinate system (x_1, x_2, x_3) and geometric parameters are illustrated in Figure 1.

2.2. Constitutive Equations.
The 3D linear constitutive equations, which can very accurately model the
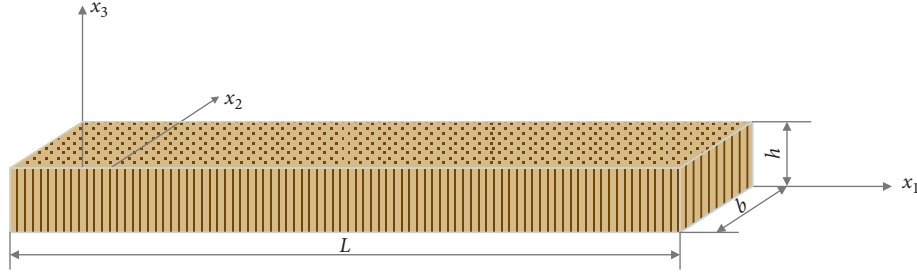
FIGURE 1: A PCMs beam: geometric parameters and Cartesian coordinate system.

electromechanical coupling behavior of PCMs, are polarized along the global coordinates as follows:

$$
\begin{bmatrix} \sigma_{11} \\ \sigma_{22} \\ \sigma_{33} \\ \sigma_{23} \\ \sigma_{13} \\ \sigma_{12} \end{bmatrix} = \begin{bmatrix} c_{11} & c_{12} & c_{13} & 0 & 0 & 0 \\ c_{12} & c_{22} & c_{23} & 0 & 0 & 0 \\ c_{13} & c_{23} & c_{33} & 0 & 0 & 0 \\ 0 & 0 & 0 & c_{44} & 0 & 0 \\ 0 & 0 & 0 & 0 & c_{55} & 0 \\ 0 & 0 & 0 & 0 & 0 & c_{66} \end{bmatrix} \begin{bmatrix} \varepsilon_{11} \\ \varepsilon_{22} \\ \varepsilon_{33} \\ 2\varepsilon_{23} \\ 2\varepsilon_{13} \\ 2\varepsilon_{12} \end{bmatrix}
$$

$$
- \begin{bmatrix} 0 & 0 & e_{31} \\ 0 & 0 & e_{32} \\ 0 & 0 & e_{33} \\ 0 & e_{24} & 0 \\ e_{15} & 0 & 0 \\ 0 & 0 & 0 \end{bmatrix} \begin{bmatrix} E_1 \\ E_2 \\ E_3 \end{bmatrix},
$$

(1)

$$
\begin{bmatrix} D_1 \\ D_2 \\ D_3 \end{bmatrix} = \begin{bmatrix} 0 & 0 & 0 & 0 & e_{15} & 0 \\ 0 & 0 & 0 & e_{24} & 0 & 0 \\ e_{31} & e_{32} & e_{33} & 0 & 0 & 0 \end{bmatrix} \begin{bmatrix} \varepsilon_{11} \\ \varepsilon_{22} \\ \varepsilon_{33} \\ 2\varepsilon_{23} \\ 2\varepsilon_{13} \\ 2\varepsilon_{12} \end{bmatrix}
$$

$$
+ \begin{bmatrix} \chi_{11} & 0 & 0 \\ 0 & \chi_{22} & 0 \\ 0 & 0 & \chi_{33} \end{bmatrix} \begin{bmatrix} E_1 \\ E_2 \\ E_3 \end{bmatrix},
$$

(2)

where σ_{ij} and ε_{kl} are the stress and infinitesimal strain tensors, respectively; E_i and D_i are electric field and electric displacement vector components, respectively; e_{ik}, c_{kl}, and χ_{ij} are the piezoelectric, elastic, and dielectric material constants, respectively.

In the PCM beam, equations (1) and (2) could be written in the matrix form:

$$
\boldsymbol{\sigma} = \mathbf{C}\boldsymbol{\varepsilon} - \mathbf{e}\mathbf{E},
$$
$$
\mathbf{D} = \mathbf{e}^{\mathrm{T}}\boldsymbol{\varepsilon} + \boldsymbol{\chi}\mathbf{E},
$$

(3)

where

$$
\boldsymbol{\sigma} = \begin{bmatrix} \sigma_{11} \\ \sigma_{33} \\ \sigma_{13} \end{bmatrix},
$$

$$
\mathbf{C} = \begin{bmatrix} c_{11} & c_{13} & 0 \\ c_{31} & c_{33} & 0 \\ 0 & 0 & c_{55} \end{bmatrix},
$$

$$
\mathbf{e} = \begin{bmatrix} 0 & e_{31} \\ 0 & e_{33} \\ e_{15} & 0 \end{bmatrix},
$$

$$
\mathbf{E} = \begin{bmatrix} E_1 \\ E_3 \end{bmatrix},
$$

$$
\boldsymbol{\varepsilon} = \begin{bmatrix} \varepsilon_{11} \\ \varepsilon_{33} \\ \varepsilon_{13} \end{bmatrix},
$$

$$
\mathbf{D} = \begin{bmatrix} D_1 \\ D_3 \end{bmatrix},
$$

$$
\boldsymbol{\chi} = \begin{bmatrix} \chi_{11} & 0 \\ 0 & \chi_{33} \end{bmatrix}.
$$

(4)

The balance law and Gauss' law underlie the description of the coupled field responses, and in the case of no body force and for quasistatic electromechanics, equations can be expressed as

$$
\sigma_{ji,j} = 0,
$$
$$
\sigma_{ji} = \sigma_{ij},
$$
$$
D_{i,i} = 0.
$$

(5)

The boundary conditions are as follows:
For the mechanical fields,

$$
u_i(t) = \overline{u}_i(t) \text{ on } \Gamma_u,
$$
$$
\sigma_{ij} n_j = \overline{\beta}_i(t) \text{ on } \Gamma_\beta,
$$
$$
\Gamma = \Gamma_u \cup \Gamma_\beta.
$$

(6)
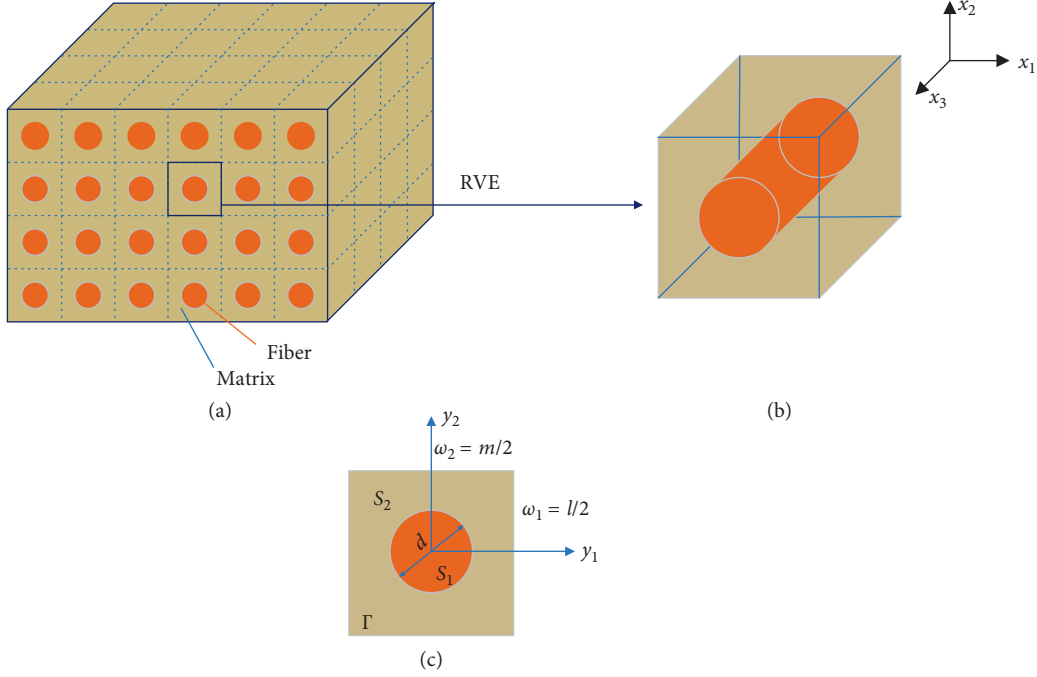
Figure 2: The geometric mode of PCMs: (a) structure, (b) representative volume element (RVE), and (c) transversal cross-section of the RVE.

For the electric fields,

$$\Phi(t) = \overline{\Phi}(t) \text{ on } \Gamma_p,$$
$$D_i n_i = \overline{Q}(t) \text{ on } \Gamma_b, \quad (7)$$
$$\Gamma = \Gamma_a \cup \Gamma_b,$$

where Γ, $\overline{u}_i(t)$, and $\overline{\Phi}(t)$ are the global boundary, displacement, and electrical potential, respectively; Γ_u, Γ_β, Γ_p, and Γ_q are the prescribed displacement, traction vector, normal component of the electric displacement vector, and electrical potential of Γ, respectively; $\overline{\beta}_i(t)$ and $\overline{Q}(t)$ are the surface load and surface density of free charge, respectively.

3. AHM

A fiber and matrix two-phase structure (Figure 2(a)) is defined by a composite body Ω and the axis x_3 parallel to the fibers. Straight reinforcement is periodically arranged. Hence, RVE could be illustrated in Figure 2(b). The periodic cell S has a squared transversal, which includes a circle of radius R (Figure 2(c)).

The phases are supposed to be homogeneous and electroelastically linear. Between the fiber and the matrix is the interface Γ, which is regarded as perfect. In the composite, the dimensions l and L are the fiber diameter and the center-to-center distance between two adjacent cylinders (fibers), respectively. Since $\varepsilon = l/L$ is far smaller than the dimension of RVE, two space scales the slow variable x and the fast variable $y = x/\varepsilon$, can be separated. The stress and strain tensors, electrical displacement vector, and electric potential are continuous across Γ or namely between phases. Thus, C_{kl}, e_{ik}, and χ_{ij} have piecewise constant roles in the periodic cells.

The first set of math issues has new physical relationships over Ω with mechanical ($\overline{C}$), piezoelectric ($\overline{e}$), and dielectric ($\overline{\chi}$) constant coefficients, which reflect the characteristics of a uniform medium Ω and are called the effective characteristics of PCMs (Figure 2). The coefficients $\overline{c}_{ijpq}$, $\overline{e}_{ipq}$, and $\overline{\chi}_{ip}$ could be computed using the equations in Reference [14].

4. Electromechanical CSFEM

4.1. Weak Formulation. The virtual work for a piezoelectric material with volume Ω and regular boundary surface Γ can be expressed as

$$\delta\Pi = \delta U - \delta W = -\int_\Omega \delta\overline{\varepsilon}^{\mathrm{T}} \boldsymbol{\sigma} d\Omega + \int_\Gamma \delta\mathbf{u}^{\mathrm{T}} \overline{\beta} d\Gamma$$
$$+ \int_\Omega \rho \delta\mathbf{u}^{\mathrm{T}} \ddot{\mathbf{u}} d\Omega + \int_\Omega \delta\overline{E}^{\mathrm{T}} \mathbf{D} d\Omega + \int_\Gamma \overline{Q} \delta\Phi d\Gamma = 0, \quad (8)$$

where ρ and δ are mass density and virtual quantity, respectively. Ω is divided into n_p elements, which contains N_n nodes, and the approximation displacement $\overline{u}$ and electrical potential $\overline{\Phi}$ for an FGPM problem can be expressed as

$$\overline{u} = \sum_{i=1}^{n_p} N_i^u u_i = \mathbf{N}_u \mathbf{u},$$
$$\overline{\Phi} = \sum_{i=1}^{n_p} N_i^\Phi \Phi_i = \mathbf{N}_\Phi \mathbf{\Phi}, \quad (9)$$

where $\mathbf{N}_u$ and $\mathbf{N}_\Phi$ are the shape functions of electromechanical CSFEM displacement and electrical potential, respectively.

A 4-node element is separated into four smoothing subdomains Ω_i^k. The nodes of field and edge/center smoothing, the edge Gaussian points, outer normal vector distribution, and the shape functions are shown in Figure 3.

At any point $\mathbf{x}^k$ in Ω_i^k, the smoothed form of strain $\overline{\varepsilon}(\mathbf{x}^k)$ and electric field $\overline{E}(\mathbf{x}^k)$ are

$$\overline{\varepsilon}(\mathbf{x}^k) = \int_{\Omega_i^k} \boldsymbol{\varepsilon}(\mathbf{x}) r(\mathbf{x} - \mathbf{x}^k) d\Omega, \tag{10}$$

$$\overline{E}(\mathbf{x}^k) = \int_{\Omega_i^k} \mathbf{E}(\mathbf{x}) r(\mathbf{x} - \mathbf{x}^k) d\Omega, \tag{11}$$

where $r(\mathbf{x} - \mathbf{x}^k)$ is the constant function:

$$r(\mathbf{x} - \mathbf{x}^k) = \begin{cases} 1/A_i^k, & \mathbf{x} \in \Omega_i^k, \\ 0, & \mathbf{x} \notin \Omega_i^k, \end{cases} \tag{12}$$

where

$$A_i^k = \int_{\Omega_i^k} d\Omega. \tag{13}$$

Substituting equation (12) in equations (10) and (11), we have

$$\overline{\varepsilon}(\mathbf{x}_k) = \frac{1}{A_i^k} \int_{\Gamma_i^k} \mathbf{n}_u^k \mathbf{u} d\Gamma, \tag{14}$$

$$\overline{E}(\mathbf{x}_k) = \frac{1}{A_i^k} \int_{\Gamma_i^k} \mathbf{n}_\Phi^k \boldsymbol{\Phi} d\Gamma, \tag{15}$$

where Γ_i^k is the boundary of Ω_i^k and $\mathbf{n}_u^k$ and $\mathbf{n}_\Phi^k$ are the outer normal vector matrices of the smoothing domain boundary:

$$\mathbf{n}_u^k = \begin{bmatrix} n_{x_1}^k & 0 \\ 0 & n_{x_3}^k \\ n_{x_3}^k & n_{x_1}^k \end{bmatrix},$$

$$\mathbf{n}_\Phi^k = \begin{bmatrix} n_{x_1}^k \\ n_{x_3}^k \end{bmatrix}. \tag{16}$$

Equations (14) and (15) can be newly expressed as

$$\overline{\varepsilon}(\mathbf{x}^k) = \sum_{i=1}^{n_e} \overline{B}_u^i(\mathbf{x}^k) \mathbf{u}_i,$$

$$\overline{E}(\mathbf{x}^k) = -\sum_{i=1}^{n_e} \overline{B}_\Phi^i(\mathbf{x}^k) \boldsymbol{\Phi}_i, \tag{17}$$

where n_e is the number of smoothing elements.

$$\overline{B}_u^i(\mathbf{x}^k) = \frac{1}{A_i^k} \int_{\Gamma^k} \begin{bmatrix} N_i^u n_{x_1}^k & 0 \\ 0 & N_i^u n_{x_3}^k \\ N_i^u n_{x_3}^k & N_i^u n_{x_1}^k \end{bmatrix} d\Gamma, \tag{18}$$

$$\overline{B}_\Phi^i(\mathbf{x}^k) = \frac{1}{A_i^k} \int_{\Gamma^k} \begin{bmatrix} N_i^\Phi n_{x_1}^k \\ N_i^\Phi n_{x_3}^k \end{bmatrix} d\Gamma, \tag{19}$$

At the Gaussian point $\mathbf{x}_b^G$, equations (18) and (19) become

$$\overline{B}_u^i(\mathbf{x}^k) = \frac{1}{A_i^k} \sum_{b=1}^{n_b} \begin{pmatrix} N_i^u(\mathbf{x}_b^G) n_{x_1}^k & 0 \\ 0 & N_i^u(\mathbf{x}_b^G) n_{x_3}^k \\ N_i^u(\mathbf{x}_b^G) n_{x_3}^k & N_i^u(\mathbf{x}_b^G) n_{x_1}^k \end{pmatrix} l_b^k, \tag{20}$$

$$\overline{B}_\Phi^i(\mathbf{x}^k) = \frac{1}{A_i^k} \sum_{b=1}^{n_b} \begin{pmatrix} N_i^\Phi(\mathbf{x}_b^G) n_{x_1}^k \\ N_i^\Phi(\mathbf{x}_b^G) n_{x_3}^k \end{pmatrix} l_b^k,$$

where l_b^k is the length of the smoothing boundary and n_b is the total number of boundaries in a subdomain. As the shape function varies linearly along each side of the subdomain, one Gauss point is enough for precise boundary integration [38].

The essential distinction between CSFEM and FEM is that FEM needs to construct the shape function matrix of the element, while CSFEM only needs to use the function at the Gaussian point of the smoothing element boundary and avoids the function derivatives, which reduces the continuity requirement of the shape function and improves the accuracy and convergence.

The dynamic model of the PCM electromechanical system can be deduced from the Hamilton rule as follows:

$$\overline{M}\ddot{\mathbf{q}} + \overline{K}\mathbf{q} = \overline{F}, \tag{21}$$

where

$$\overline{M} = \begin{bmatrix} \mathbf{M}_{uu} & 0 \\ 0 & 0 \end{bmatrix},$$

$$\ddot{q} = \begin{Bmatrix} \ddot{u} \\ \ddot{\Phi} \end{Bmatrix},$$

$$\overline{K} = \begin{bmatrix} \mathbf{K}_{uu} & \mathbf{K}_{u\Phi} \\ \mathbf{K}_{u\Phi}^T & \mathbf{K}_{\Phi\Phi} \end{bmatrix},$$

$$\mathbf{q} = \begin{Bmatrix} \mathbf{u} \\ \boldsymbol{\Phi} \end{Bmatrix}, \tag{22}$$

$$\overline{F} = \begin{Bmatrix} \mathbf{F} \\ \mathbf{Q} \end{Bmatrix},$$

$$\mathbf{M}_{uu} = \sum_e \mathbf{M}_{uu}^e,$$

$$\mathbf{M}_{uu}^e = \text{diag}\{m_1, m_1, m_2, m_2, m_3, m_3, m_4, m_4\},$$

where $m_i = p_i T$, A_i^k ($i = 1, 2, 3, 4$) is the mass of the i-th smoothing element related to node i, T is the smoothing element thickness, and p_i is the density of the Gaussian integration point of the i-th smoothing subdomain.
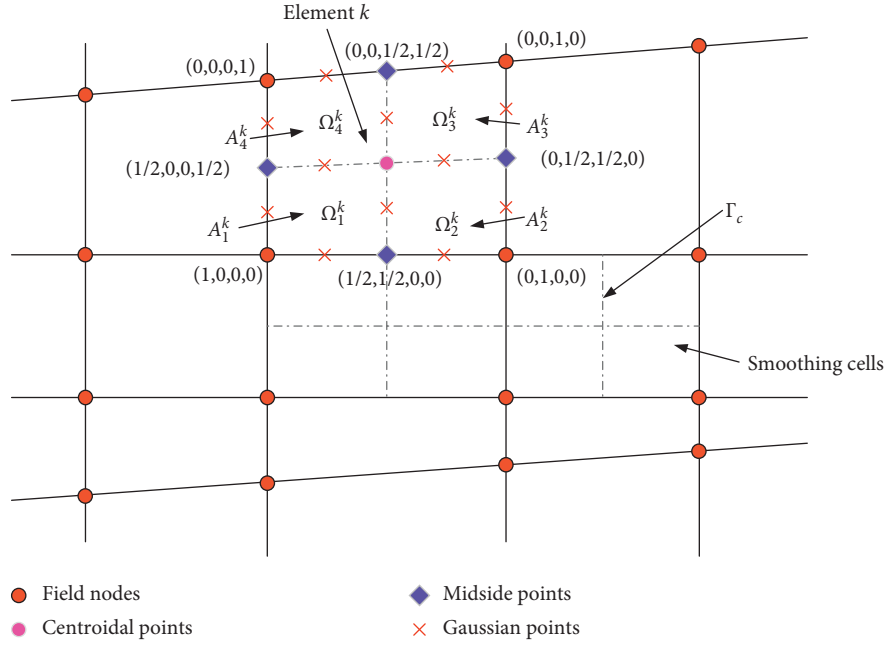
FIGURE 3: Smoothing subcells and the values of shape functions.

$$\mathbf{K}_{uu} = \sum_{i=1}^{n_c} \overline{B}_u^{i\mathrm{T}} \overline{CB}_u^i A_i^k,$$

$$\mathbf{K}_{u\Phi} = \sum_{i=1}^{n_c} \overline{B}_u^{i\mathrm{T}} \overline{e} \overline{B}_\Phi^i A_i^k,$$

$$\mathbf{K}_{\Phi\Phi} = -\sum_{i=1}^{n_c} \overline{B}_\Phi^{i\mathrm{T}} \overline{\chi} \overline{B}_\Phi^i A_i^k, \qquad (23)$$

$$\mathbf{F} = \int_{\Gamma_q} \mathbf{N}_u^{\mathrm{T}} \boldsymbol{\beta} d\Gamma,$$

$$\mathbf{Q} = \int_\Omega \mathbf{N}_\Phi^{\mathrm{T}} \overline{Q} d\Omega,$$

where $n_c = n_p \times n_e$.

5. Modified Wilson-θ Method

The modified Wilson-θ method is an important scheme and an implicit integral way to solve the dynamic system equations. If $\theta > 1.37$, the solution is unconditionally stable. The detailed procedures are shown as follows.

5.1. Initial Calculation

(1) Formulate generalized stiffness matrix $\overline{K}$, mass matrix $\overline{M}$

(2) Calculate initial values of $\mathbf{u}$, $\dot{u}$, $\ddot{u}$

(3) Select the time step Δt and the integral constant θ ($\theta = 1.4$)

$$a_0 = \frac{6}{(\theta \Delta t)^2},$$

$$a_1 = \frac{3}{(\theta \Delta t)},$$

$$a_2 = 2a_1,$$

$$a_3 = \frac{\theta \Delta t}{2},$$

$$a_4 = \frac{a_0}{\theta},$$

$$a_5 = -\frac{a_2}{\theta}, \qquad (24)$$

$$a_6 = 1 - \frac{3}{\theta},$$

$$a_7 = \frac{\Delta t}{2},$$

$$a_7 = \frac{\Delta t}{2},$$

$$a_8 = -\frac{\Delta t^2}{6}.$$

(4) Formulate an effective generalized stiffness matrix $\widetilde{K}$:
$\widetilde{K} = \overline{K} + a_0 \overline{M}$.

5.2. For Each Time Step

(1) Calculate the payload at time $t + \theta \Delta t$:

$$\overline{F}_{t+\theta \Delta t} = \overline{F}_t + \theta \left(\overline{F}_{t+\Delta t} - \overline{F}_t \right) + \overline{M} \left(a_0 \mathbf{q}_t + a_2 \dot{\mathbf{q}}_t + 2 \ddot{\mathbf{q}}_t \right). \tag{25}$$

(2) Calculate the generalized displacement at time $t + \theta \Delta t$:

$$\widetilde{K} \mathbf{u}_{t+\theta \Delta t} = \overline{F}_{t+\theta \Delta t}. \tag{26}$$

(3) Calculate the generalized acceleration, generalized speed, and generalized displacement at time $t + \Delta t$:

$$\ddot{\mathbf{u}}_{t+\Delta t} = a_4 \left(\mathbf{u}_{t+\theta \Delta t} - \mathbf{u}_t \right) + a_5 \dot{\mathbf{u}}_t + a_6 \ddot{\mathbf{u}}_t,$$
$$\dot{\mathbf{u}}_{t+\Delta t} = \dot{\mathbf{u}}_t + a_7 \left(\ddot{\mathbf{u}}_{t+\Delta t} + \ddot{\mathbf{u}}_t \right), \tag{27}$$
$$\mathbf{u}_{t+\Delta t} = \mathbf{u}_t + \Delta t \dot{\mathbf{u}}_t + a_8 \left(\ddot{\mathbf{u}}_{t+\Delta t} + 2 \ddot{\mathbf{u}}_t \right).$$

6. Numerical Results

6.1. A Singer-Player PCMs Strip. In this example to test the precision of CSFEM under mechanical and electrical boundary conditions, we used the shear deformation of a piezoelectric strip ($1 \times 1 \, \text{mm}^2$, thickness $t = 10 \, \mu\text{m}$) under compressive stress $\sigma_0 = 5 \, \text{N} \cdot \text{mm}^{-2}$ and applied voltage $V_0 = 1000 \, \text{V}$ (Figure 4). The PCMs, piezoceramic fibers (PZT-5A), were buried in the non-piezoelectric epoxy matrix. The material properties are shown in Table 1 [20]. A block of 10000 square cells (each cell $10 \times 10 \times 10 \, \mu\text{m}^3$) was used in the composite z with the specific fiber volume fraction of 55.55%. One part of the PCM structure ($60 \times 10 \times 40 \, \mu\text{m}^3$) is shown in Figure 5. The materials were polarized under the electric field set to the left and right edges, which resulted in shear strain. The boundary conditions were applied to the strip edges:

$$\Phi_{,z} (x, z = \pm h) = 0,$$
$$\sigma_{zz} (x, z = \pm h) = \sigma_0,$$
$$\sigma_{xz} (x = L, z) = 0,$$
$$\sigma_{xz} (x, z = \pm h) = 0,$$
$$\Phi (x = L, z) = -V_0, \tag{28}$$
$$\sigma_{xx} (x = L, z) = 0,$$
$$\Phi (x = 0, z) = V_0,$$
$$u (x = 0, z) = 0,$$
$$v (x = 0, z = 0) = 0.$$

The analytical solution to this problem is shown below [58]:

$$u = s_{13} \sigma_0 x,$$
$$v = \frac{d_{15} V_0 x}{h} + s_{33} \sigma_0 z, \tag{29}$$
$$\Phi = V_0 \left(1 - \frac{2x}{L} \right).$$
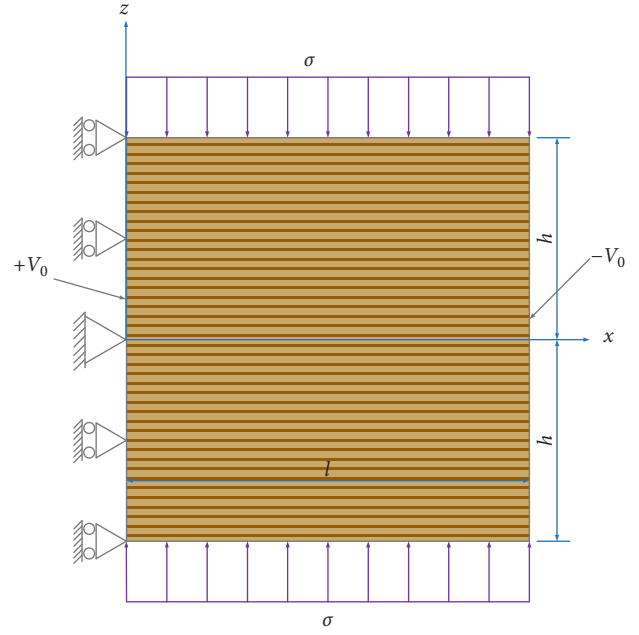
FIGURE 4: A singer-player PCMs strip under shear deformation.

It should be noted that all 11 effective coefficients in Table 2 were determined using AHM. CSFEM, FEM, and analytical solution were all based on AHM. Three meshes (each 10×10, including one with uniform elements and two with distorted elements) were analyzed by CSFEM (Figure 6). The α_{ir} is the irregularity factor that is assigned between 0.0 and 0.5 [38]. Meanwhile, 60×60 uniform elements were used by FEM. Figure 7 illustrates the CSFEM, FEM, and analytical horizontal displacement u_x at the central line ($z = 0$), while the vertical displacement u_z at $z = 0$ of the single-layer PCM strip is shown in Figure 8. The distributions of the electric potential Φ at $z = 0$ with FEM and the analytical solutions are demonstrated in Figure 9. Clearly, the displacements and electric potential computed by CSFEM match well with the analytical solutions and outperform those estimated by FEM for all three meshes, which suggested that CSFEM can recreate the linear behavior of the analytical solutions.

Moreover, the computation cost of CSFEM over PCMs in a homogenized structure surpasses that of FEM with a heterogeneous structure (Figure 10), but FEM costs more to reach the same precision. Thus, CSFEM clearly enhances the calculation efficiency.

A comparison of costs (computation time for the same accuracy) for the homogenized PCM structures indicates CSFEM takes much lower cost than traditional FEM.

6.2. A Cantilever PCMs Beam. The free vibrations on a cantilever PCM beam were calculated by CSFEM under the geometrical parameters of length $L = 20 \, \text{mm}$, width $H = 2 \, \text{mm}$, and plane stress (Figure 11). The PCMs, piezoceramic fibers (PZT-5A), were buried in the non-piezoelectric epoxy matrix. The material properties are shown in Table 3. A block of 16000 square cells was used in the composite z with the specific fiber volume fraction of

TABLE 1: Material constants for constituents of the PZT-5A and epoxy matrix.

Material constants	c_{11} (GPa)	c_{12} (GPa)	c_{13} (GPa)	c_{33} (GPa)	c_{44} (GPa)	c_{66} (GPa)	e_{13} (C/m^2)	e_{15} (C/m^2)	e_{33} (C/m^2)	χ_{11} (F/m)	χ_{33} (F/m)	ρ (kg/m^3)
Epoxy matrix	3.86	2.57	2.57	3.86	0.64	0.64	—	—	—	0.0797	0.0797	7500
PZt-5A	121.0	75.4	75.2	111.0	21.1	2.28	−5.4	12.3	15.8	8.11	7.35	7500
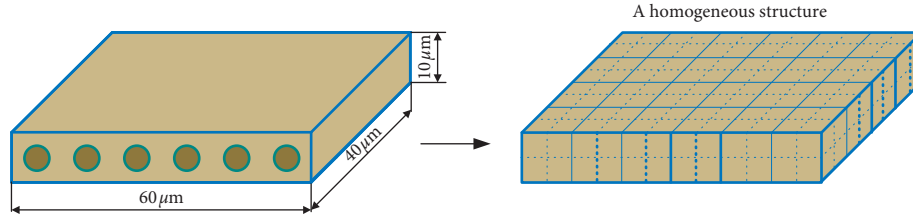
FIGURE 5: A part homogeneous model of the singer-player PCMs strip by AHM.

TABLE 2: The material properties of the singer-player PCMs strip were calculated by AHM.

Volume fraction	$\bar{c}_{11}$ (GPa)	$\bar{c}_{12}$ (GPa)	$\bar{c}_{13}$ (GPa)	$\bar{c}_{33}$ (GPa)	$\bar{c}_{44}$ (GPa)	$\bar{c}_{66}$ (GPa)	$\bar{e}_{15}$ (C/m^2)	$\bar{e}_{33}$ (C/m^2)	$\bar{e}_{13}$ (C/m^2)	$\bar{\chi}_{11}$ (nF/m)	$\bar{\chi}_{33}$ (nF/m)
0.5555	9.74292	5.54232	5.95557	35.11748	2.17285	2.1003	0.021904	10.879245	−0.251715	0.28018	4.27248

FIGURE 6: Typical irregular elements with irregularity factor α_{ir} = (a) 0.3 (I1) and (b) 0.5 (I2).

66.66%. The relevant boundary condition was $u_x = u_z = \Phi = 0$ at the clamped end.

The 11 effective coefficients estimated by AHM are shown in Table 3. The first 10 natural frequencies of the cantilever PCM beam with 100×10 uniform elements calculated by CSFEM (Figure 12) agree well with the solutions by FEM using 200×20 uniform elements. The CSFEM has higher accuracy than FEM. Figure 13 plots the first sixth-order modal shapes, which verify the correctness and validity of CSFEM.

6.3. A Bilayered PCMs Actuator.
In this example, the transient responses of a clamp-free bilayered PCM actuator ($L = 20$ mm, $b = 2$ mm, and layer width = 1 mm) exposed to triangular-wave load F (time period $T = 8$ s, and $F_0 = 5$ N) at point A were investigated (Figures 14 and 15). The actuator consisted of a lower PCM layer and an upper red copper layer, which were supposed to be well bonded. The PCMs (PZT-5A) were buried in the epoxy matrix. A block of 8000 square cells was used in the composite z with the specific fiber volume fraction of 44.44%. The red copper was featured by Young's modulus (E) = 108 GPa, Poisson ratio (ν) = 0.32, and volume density (ρ) = 8900 kg/m^3 (Table 2). The boundary condition of the actuator was $u_x = u_z = \Phi = 0$ (at the clamped end). The dynamic system equations were addressed by using the implicit integral Newmark scheme.
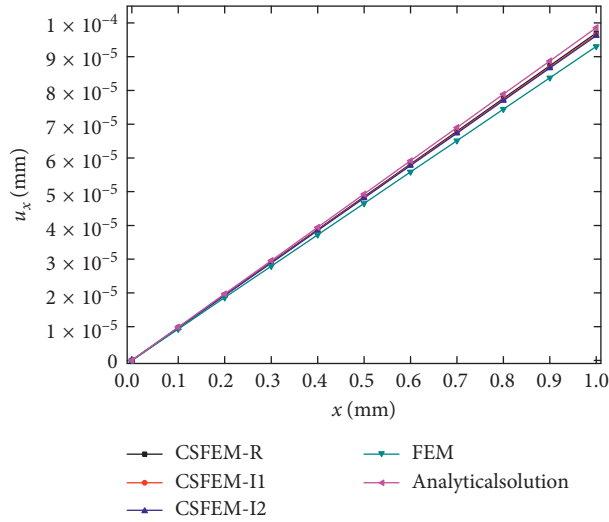
FIGURE 7: Variation of horizontal displacement u_x at the central line ($z = 0$) of the singer-player PCMs strip.
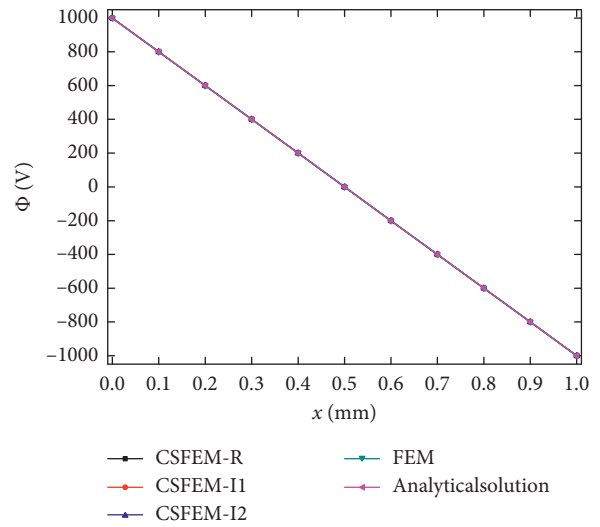
FIGURE 9: Variation of electric potential Φ at the central line ($z = 0$) of the singer-player PCMs strip.
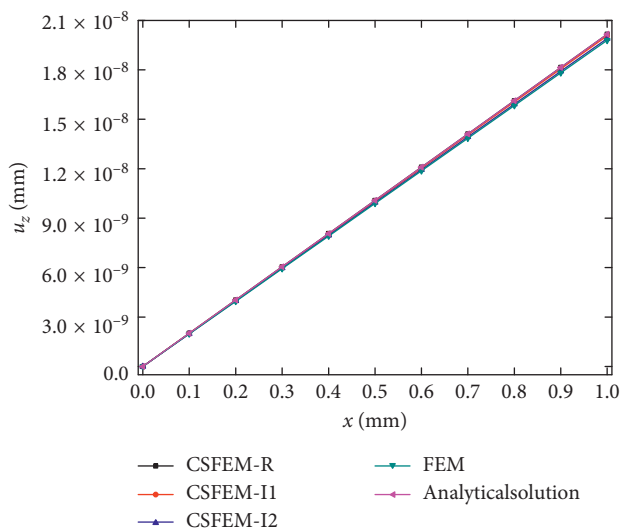
FIGURE 8: Variation of vertical displacement u_z at the central line ($z = 0$) of the singer-player PCMs strip.
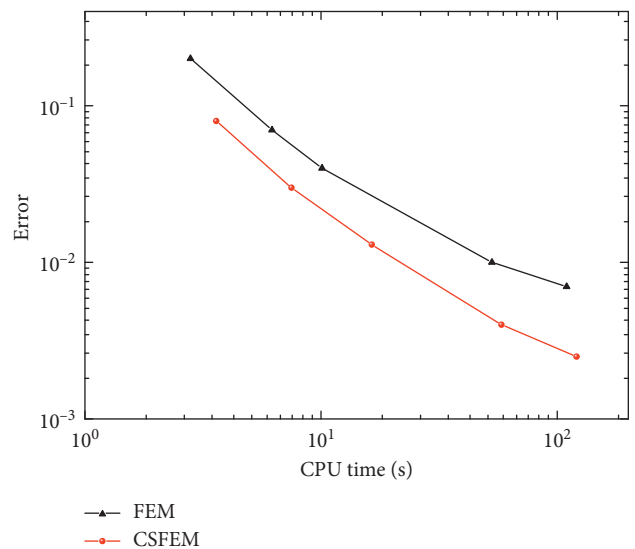
FIGURE 10: Computational cost by CSFEM and FEM.

The 12 effective coefficients calculated using AHM are shown in Table 4 ($\Delta t = 0.002$ s). The generalized displacements at points A and B calculated by CSFEM and FEM are shown in Figures 16–21. Clearly, the high agreement of the simulation results confirms the accuracy of CSFEM. CSFEM achieves higher precision by using fewer elements than FEM (40×4 VS 160×16 meshes). Thus, CSFEM is well feasible for dynamic analysis of PCM structures.

6.4. A PCMs Energy Harvester. The transient responses of a typical PCM energy harvester were investigated at points A and B (Figure 22). The mild steel was featured by $E = 210$ GPa, $\rho = 7800.0$ kg·m^{-3}, and $\nu = 0.3$, while red copper by $E = 108$ GPa, $\rho = 8900$ kg·m^{-3}, and $\nu = 0.32$ (Table 2). The PCMs (PZT-5A) were embedded in the epoxy matrix. A

block of 8000 square cells was used in the composite z with the specific fiber volume fraction of 55.55%. The boundary and initial conditions were the same as stated above. The sine-wave payload with 8 s and time step $\Delta t = 0.02$ s was applied (Figure 23). The background cells of quadrilateral elements for this harvester were first discretized (Figure 24). The implicit integral Newmark scheme was used to address dynamic system equations.

The 12 effective coefficients calculated using AHM are shown in Table 5. The dynamic responses of the PCM energy harvester were calculated by CSFEM in comparison with FEM (700 VS 5600 quadrilateral elements). The u_x, u_z, and Φ at points A and B are shown in Figures 25–30. Clearly, the CSFEM produced the generalized displacements closer to real solutions and thereby was proved to
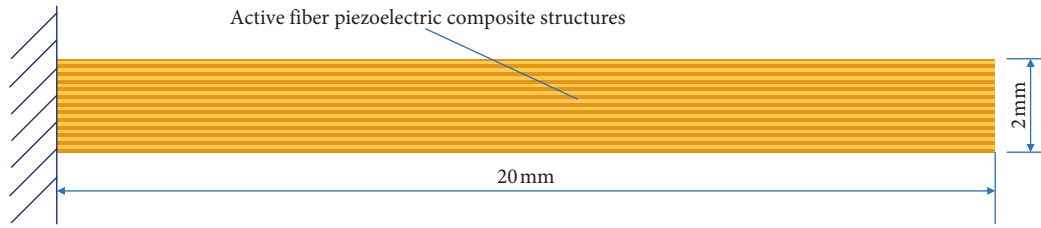
FIGURE 11: A cantilever PCMs beam.

TABLE 3: The material properties of the cantilever PCMs beam were calculated by AHM.

Volume fraction	$\bar{c}_{11}$ (GPa)	$\bar{c}_{12}$ (GPa)	$\bar{c}_{13}$ (GPa)	$\bar{c}_{33}$ (GPa)	$\bar{c}_{44}$ (GPa)	$\bar{c}_{66}$ (GPa)	$\bar{e}_{15}$ (C/m^2)	$\bar{e}_{33}$ (C/m^2)	$\bar{e}_{13}$ (C/m^2)	$\bar{\chi}_{11}$ (nF/m)	$\bar{\chi}_{33}$ (nF/m)	ρ (kg/m^3)
0.6666	13.27801	7.01985	7.87201	42.31662	3.18867	3.12908	0.052676	12.984637	-0.39420	0.42031	5.1058	7500
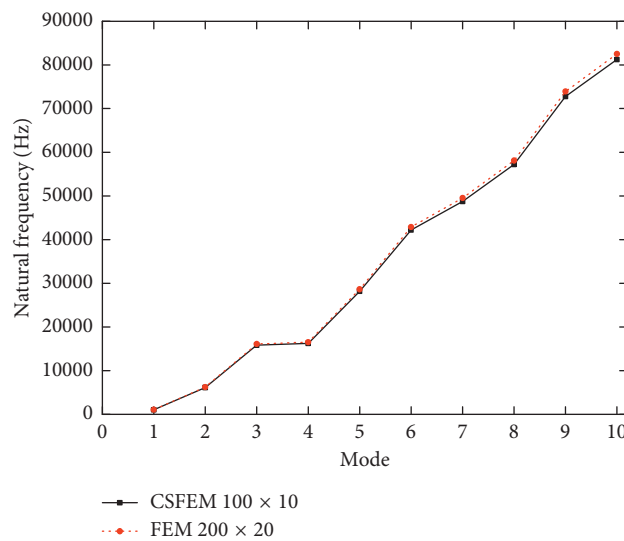
FIGURE 12: First 10 natural frequencies of the cantilever PCMs beam using CSFEM and FEM.
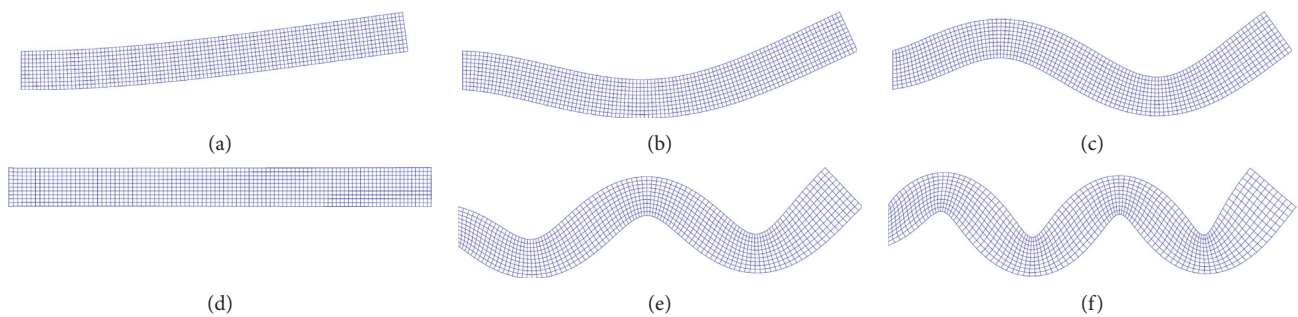
FIGURE 13: First 6 mode shapes of the cantilever PCMs beam by CSFEM and FEM. (a) Mode shape 1. (b) Mode shape 2. (c) Mode shape 3. (d) Mode shape 4. (e) Mode shape 5. (f) Mode shape 6.
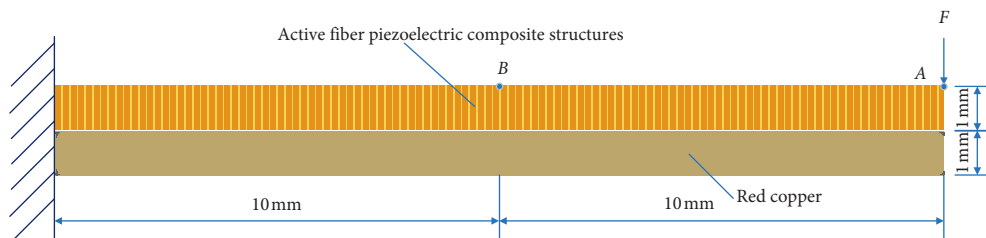
FIGURE 14: Geometry of the bilayered PCMs actuator.
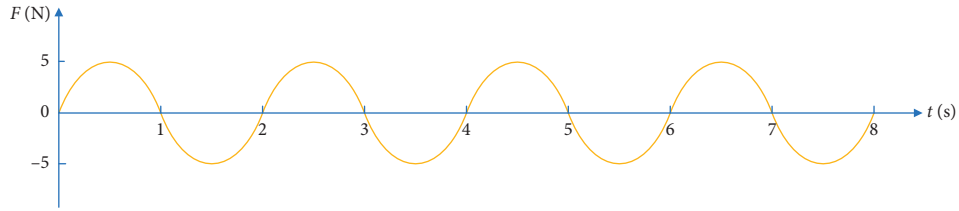
FIGURE 15: Sine-wave load at point A.

TABLE 4: The material properties of the bilayered PCMs actuator were calculated by AHM.

Volume fraction	$\bar{c}_{11}$ (GPa)	$\bar{c}_{12}$ (GPa)	$\bar{c}_{13}$ (GPa)	$\bar{c}_{33}$ (GPa)	$\bar{c}_{44}$ (GPa)	$\bar{c}_{66}$ (GPa)	$\bar{e}_{15}$ (C/m²)	$\bar{e}_{33}$ (C/m²)	$\bar{e}_{13}$ (C/m²)	$\bar{\chi}_{11}$ (nF/m)	$\bar{\chi}_{33}$ (nF/m)	ρ (kg/m³)
0.4444	7.61822	4.56846	4.77091	28.4779	1.61506	1.52487	0.010859	8.73225	-0.16364	0.20584	3.43606	7500
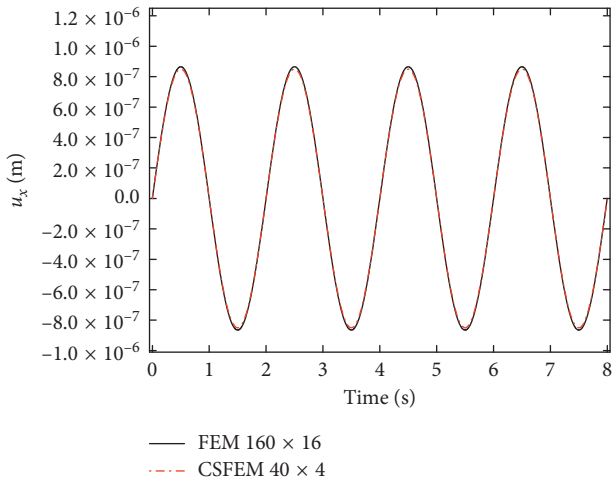
FIGURE 16: The variation of the displacement u_x at point A with respect to time.
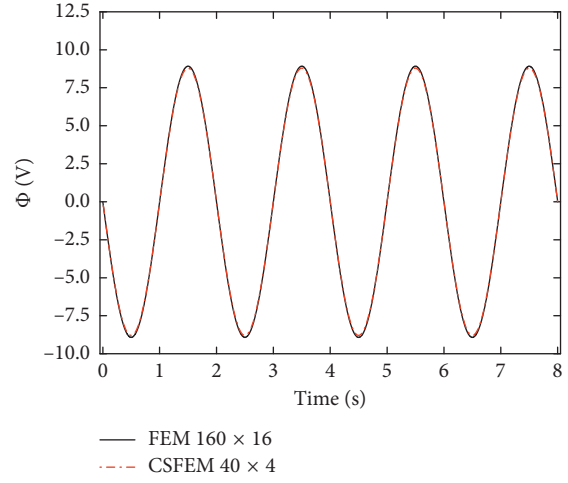
FIGURE 18: The variation of the electrical potential Φ at point A with respect to time.
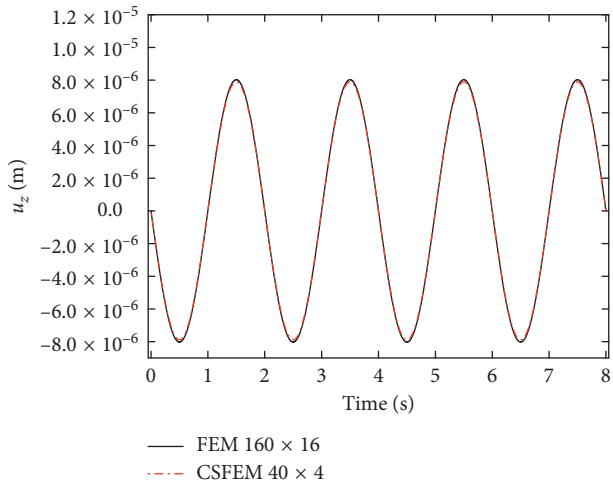
FIGURE 17: The variation of the displacement u_z at point A with respect to time.
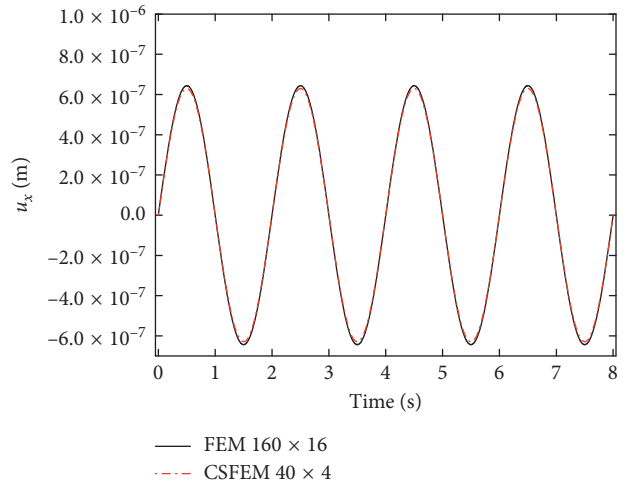
FIGURE 19: The variation of the displacement u_x at point B with respect to time.
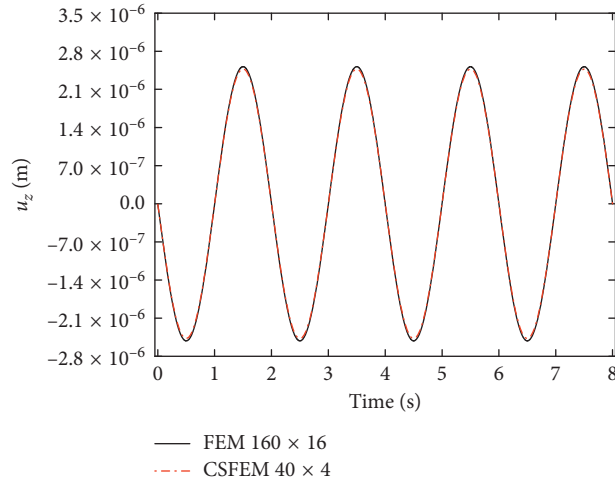
FIGURE 20: The variation of the displacement u_z at point A with respect to time.
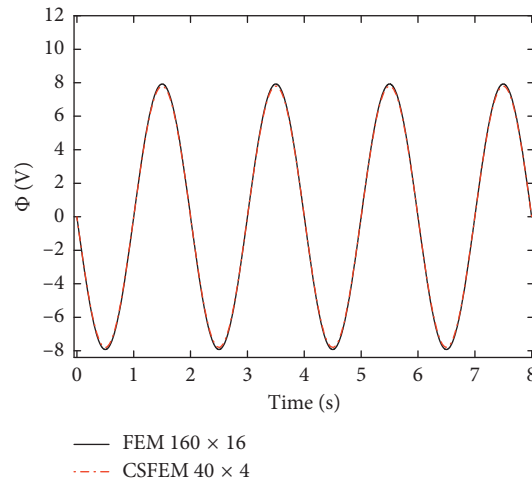
FIGURE 21: The variation of the electrical potential Φ at point A with respect to time.
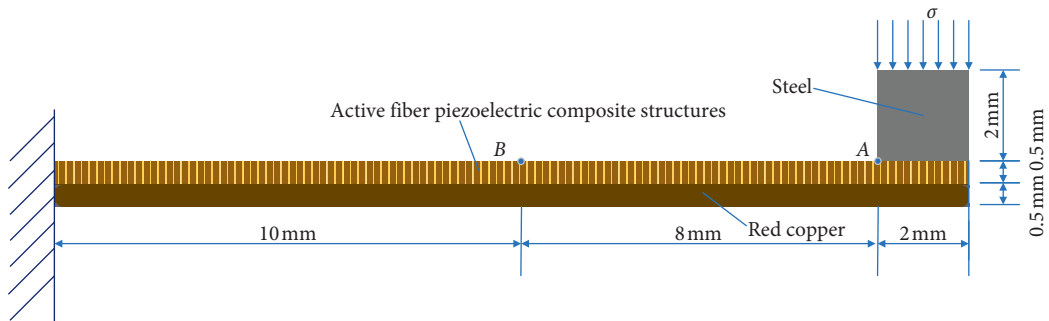
FIGURE 22: Geometry of PCMs energy harvester.
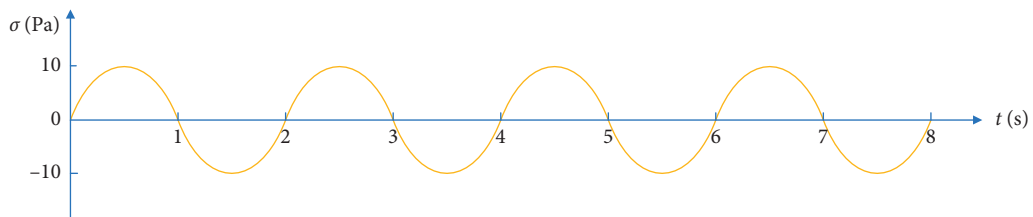
FIGURE 23: Sine-wave load at top surface of steel.

(a)

(b)
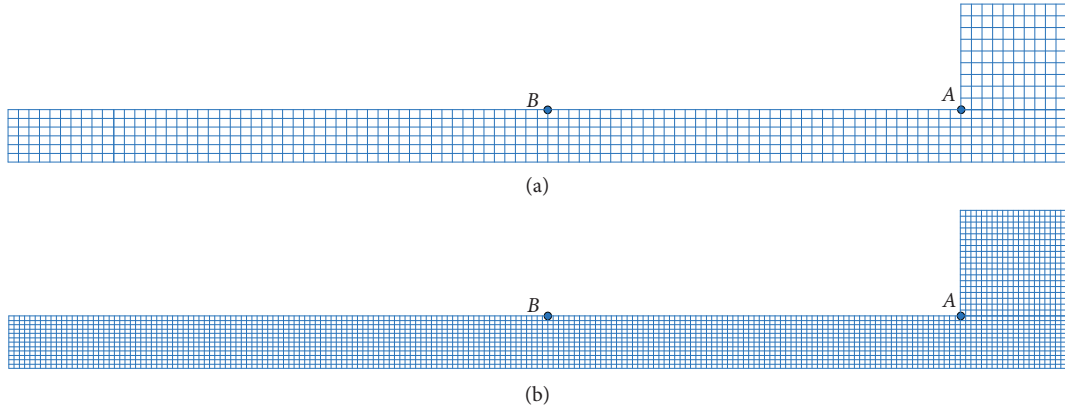
FIGURE 24: Discrete meshes of PCMs energy harvester. (a) Elements of CSFEM. (b) Elements of FEM.

TABLE 5: The material properties of the PCMs energy harvester were calculated using AHM.

Volume fraction	$\bar{c}_{11}$ (GPa)	$\bar{c}_{12}$ (GPa)	$\bar{c}_{13}$ (GPa)	$\bar{c}_{33}$ (GPa)	$\bar{c}_{44}$ (GPa)	$\bar{c}_{66}$ (GPa)	$\bar{e}_{15}$ (C/m^2)	$\bar{e}_{33}$ (C/m^2)	$\bar{e}_{13}$ (C/m^2)	$\bar{\chi}_{11}$ (nF/m)	$\bar{\chi}_{33}$ (nF/m)
0.5555	9.74292	5.54232	5.95557	35.11748	2.17285	2.1003	0.021904	10.879245	−0.251715	0.28018	4.27248

FIGURE 25: The variation of the displacement u_x of the PCMs energy harvester at point A with respect to time.
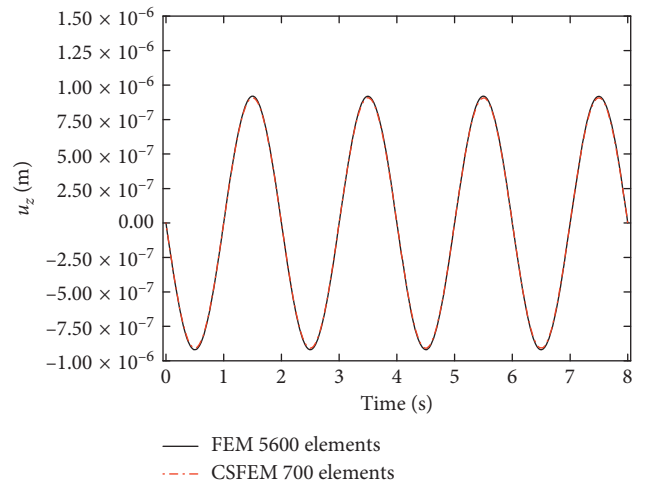
FIGURE 26: The variation of the displacement u_z of the PCMs energy harvester at point A with respect to time.

reduce the number of meshes and return more-accurate results.

7. Conclusions

The dynamic responses of PCM structures were investigated. Firstly, the effective properties of PCMs were calculated by AHM. Secondly, the effective CSFEM was established by applying gradient smoothing to calculate the electromechanical coupling field of FEM. Then, the equations for dynamic response computation over the multiphysics coupling field of PCMs were derived. Finally, a bilayered

PCM actuator and a PCM energy harvester were calculated by both CSFEM and FEM.

(i) CSFEM reduced the systematic stiffness of FEM and thereby enhanced the accuracy under the same element number. CSFEM took less computation time than FEM under the same accuracy.

(ii) CSFEM avoided the derivation of shape functions and reduced the requirement of form function continuity by simply converting area integral to boundary integral in the solution domain.

(iii) The practical bilayered PCM actuator and the PCM energy harvester were modeled by CSFEM,
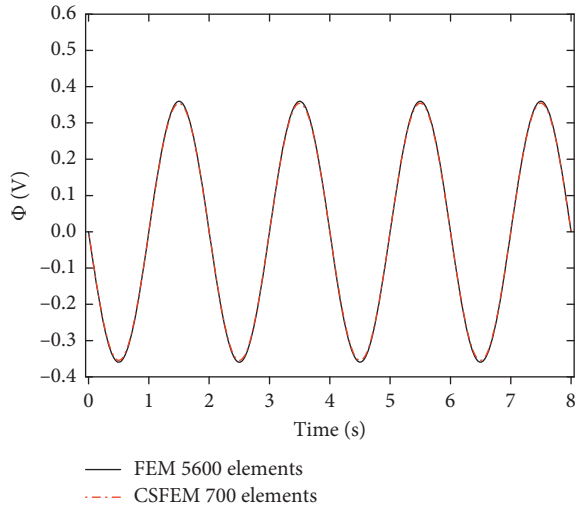
FIGURE 27: The variation of the electrical potential Φ of the PCMs energy harvester at point A with respect to time.
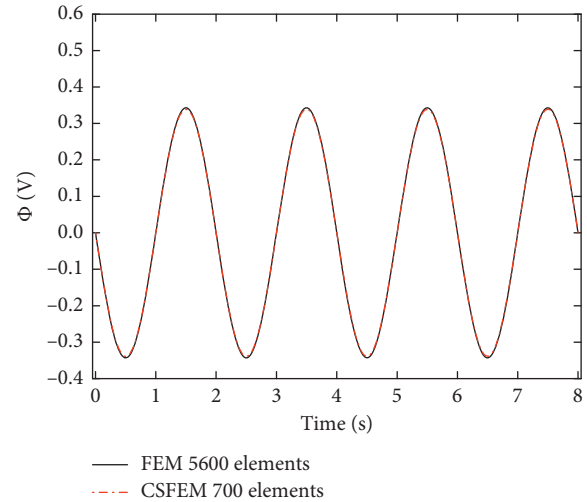
FIGURE 30: The variation of the electrical potential Φ of the PCMs energy harvester at point B with respect to time.

which outperformed FEM in calculating the transient responses by reducing the number of meshes.

Data Availability

The data used to support the findings of this study are included within the article.

Conflicts of Interest

The authors declare that they have no conflicts of interest.

Acknowledgments
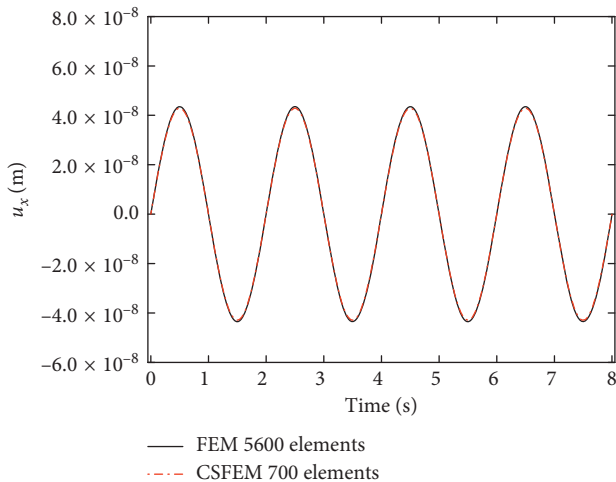
FIGURE 28: The variation of the displacement u_x of the PCMs energy harvester at point B with respect to time.

References

[1] X.-Q. Fang, J.-X. Liu, and V. Gupta, "Fundamental formulations and recent achievements in piezoelectric nanostructures: a review," *Nanoscale*, vol. 5, no. 5, pp. 1716–1726, 2013.

[2] P. Tan and L. Tong, "Micro-electromechanics models for piezoelectric-fiber-reinforced composite materials," *Composites Science and Technology*, vol. 61, no. 5, pp. 759–769, 2001.

[3] X. Wang, J. Zhou, J. Song, J. Liu, N. Xu, and Z. L. Wang, "Piezoelectric field effect transistor and nanoforce sensor based on a single ZnO nanowire," *Nano Letters*, vol. 6, no. 12, pp. 2768–2772, 2006.

[4] M. S. Azzouz, C. Mei, J. S. Bevan, and J. J. Ro, "Finite element modeling of MFC/AFC actuators and performance of MFC,"

FIGURE 29: The variation of the displacement u_z of the PCMs energy harvester at point B with respect to time.

Journal of Intelligent Material Systems and Structures, vol. 12, no. 9, pp. 601–612, 2001.

[5] Y. Qin, X. Wang, and Z. L. Wang, "Microfibre-nanowire hybrid structure for energy scavenging," *Nature*, vol. 451, no. 7180, pp. 809–813, 2008.

[6] C. Gui, J. Bai, and W. Zuo, "Simplified crashworthiness method of automotive frame for conceptual design," *Thin-walled Structures*, vol. 131, pp. 324–335, 2018.

[7] H. L. W. Chan and J. Unsworth, "Simple model for piezo-electric ceramic/polymer 1–3 composites used in ultrasonic transducer applications," *IEEE Transactions on Ultrasonics, Ferroelectrics and Frequency Control*, vol. 36, no. 4, pp. 434–441, 1989.

[8] W. A. Smith and B. A. Auld, "Modeling 1-3 composite pie-zoelectrics: thickness-mode oscillations," *IEEE Transactions on Ultrasonics, Ferroelectrics and Frequency Control*, vol. 38, no. 1, pp. 40–47, 1991.

[9] B. Wang, "Three-dimensional analysis of a flat elliptical crack in a piezoelectric material," *International Journal of Engineering Science*, vol. 30, no. 6, pp. 781–791, 1992.

[10] M. L. Dunn and M. Taya, "Micromechanics predictions of the effective electroelastic moduli of piezoelectric composites," *International Journal of Solids and Structures*, vol. 30, no. 2, pp. 161–175, 1993.

[11] T. Chen, "Piezoelectric properties of multiphase fibrous composites: some theoretical results," *Journal of the Mechanics and Physics of Solids*, vol. 41, no. 11, pp. 1781–1794, 1993.

[12] A. Benjeddou, "Advances in piezoelectric finite element modeling of adaptive structural elements: a survey," *Computers & Structures*, vol. 76, no. 1–3, pp. 347–363, 2000.

[13] Y. Benveniste and G. J. Dvorak, "Uniform fields and universal relations in piezoelectric composites," *Journal of the Mechanics and Physics of Solids*, vol. 40, no. 6, pp. 1295–1312, 1992.

[14] R. Rodríguez-Ramos, F. J. Sabina, R. Guinovart-Díaz, and J. Bravo-Castillero, "Closed-form expressions for the effective coefficients of a fiber-reinforced composite with transversely isotropic constituents–I. Elastic and square symmetry," *Mechanics of Materials*, vol. 33, no. 4, pp. 223–235, 2001.

[15] J. Bravo-Castillero, R. Guinovart-Díaz, F. J. Sabina, and R. Rodríguez-Ramos, "Closed-form expressions for the effective coefficients of a fiber-reinforced composite with transversely isotropic constituents–II. Piezoelectric and square symmetry," *Mechanics of Materials*, vol. 33, no. 4, pp. 237–248, 2001.

[16] R. Guinovart-Díaz, J. Bravo-Castillero, R. Rodríguez-Ramos, R. Martínez-Rosado, F. Serranía, and M. Navarrete, "Modeling of elastic transversely isotropic composite using the asymptotic homogenization method. Some comparisons with other models," *Materials Letters*, vol. 56, no. 6, pp. 889–894, 2002.

[17] I. Sevostianov and M. Kachanov, "Plasma-sprayed ceramic coatings: anisotropic elastic and conductive properties in relation to the microstructure; cross-property correlations," *Materials Science and Engineering: A*, vol. 297, no. 1-2, pp. 235–243, 2001.

[18] I. V. Andrianov, V. V. Danishevs'kyy, and D. Weichert, "Asymptotic determination of effective elastic properties of composite materials with fibrous square-shaped inclusions," *European Journal of Mechanics—A/Solids*, vol. 21, no. 6, pp. 1019–1036, 2002.

[19] J. A. Otero, J. Bravo-Castillero, R. Guinovart-Díaz, R. Rodríguez-Ramos, and G. A. Maugin, "Analytical expressions of effective constants for a piezoelectric composite reinforced with square cross-section fibers," *Archives of Mechanics*, vol. 55, no. 4, pp. 357–371, 2003.

[20] R. de Medeiros, R. Rodríguez-Ramos, R. Guinovart-Díaz, J. Bravo-Castillero, J. A. Otero, and V. Tita, "Numerical and analytical analyses for active fiber composite piezoelectric composite materials," *Journal of Intelligent Material Systems and Structures*, vol. 26, no. 1, pp. 101–118, 2014.

[21] J. M. Viaño, C. Ribeiro, J. Figueiredo, and Á. Rodríguez-Arós, "A high order model for piezoelectric rods: an asymptotic approach," *International Journal of Solids and Structures*, vol. 81, pp. 294–310, 2016.

[22] K. C. Le, "An asymptotically exact theory of functionally graded piezoelectric shells," *International Journal of Engineering Science*, vol. 112, pp. 42–62, 2017.

[23] F. Fantoni, A. Bacigalupo, and M. Paggi, "Multi-field asymptotic homogenization of thermo-piezoelectric materials with periodic microstructure," *International Journal of Solids and Structures*, vol. 120, pp. 31–56, 2017.

[24] R. Kar-Gupta and T. A. Venkatesh, "Electromechanical response of 1–3 piezoelectric composites: a numerical model to assess the effects of fiber distribution," *Acta Materialia*, vol. 55, no. 4, pp. 1275–1292, 2007.

[25] K.-K. Jin, H. Yuanchen Huang, Y.-H. Lee, and H. Sung Kyu Ha, "Distribution of micro stresses and interfacial tractions in unidirectional composites," *Journal of Composite Materials*, vol. 42, no. 18, pp. 1825–1849, 2008.

[26] M. Würkner, H. Berger, and U. Gabbert, "On numerical evaluation of effective material properties for composite structures with rhombic fiber arrangements," *International Journal of Engineering Science*, vol. 49, no. 4, pp. 322–332, 2011.

[27] N. Mishra, B. Krishna, R. Singh, and K. Das, "Evaluation of effective elastic, piezoelectric, and dielectric properties of SU8/ZnO nanocomposite for vertically integrated nano-generators using finite element method," *Journal of Nanomaterials*, vol. 2017, Article ID 1924651, 14 pages, 2017.

[28] C. R. Bowen, V. Y. Topolov, Y. Zhang, and A. A. Panich, "1–3-type composites based on ferroelectrics: electromechanical coupling, figures of merit, and piezotechnical energy-harvesting applications," *Energy Technology*, vol. 6, no. 5, pp. 813-814, 2018.

[29] A. A. Cannarozzi and F. Ubertini, "Some hybrid variational methods for linear electroelasticity problems," *International Journal of Solids and Structures*, vol. 38, no. 15, pp. 2573–2596, 2001.

[30] K. Y. Sze and Y. S. Pan, "Hybrid finite element models for piezoelectric materials," *Journal of Sound and Vibration*, vol. 226, no. 3, pp. 519–547, 1999.

[31] K. Y. Sze and L. Q. Yao, "Modelling smart structures with segmented piezoelectric sensors and actuators," *Journal of Sound and Vibration*, vol. 235, no. 3, pp. 495–520, 2000.

[32] K. Y. Sze, X.-M. Yang, and L.-Q. Yao, "Stabilized plane and axisymmetric piezoelectric finite element models," *Finite Elements in Analysis and Design*, vol. 40, no. 9-10, pp. 1105–1122, 2004.

[33] C. S. Long, P. W. Loveday, and A. A. Groenwold, "Planar four node piezoelectric elements with drilling degrees of freedom," *International Journal for Numerical Methods in Engineering*, vol. 65, no. 11, pp. 1802–1830, 2006.

[34] C. W. Lim and C. W. H. Lau, "A new two-dimensional model for electro-mechanical response of thick laminated piezoelectric actuator," *International Journal of Solids and Structures*, vol. 42, no. 20, pp. 5589–5611, 2005.

[35] R. Zemčík, R. Rolfes, M. Rose, and J. Teßmer, "High-performance four-node shell element with piezoelectric

coupling for the analysis of smart laminated structures," *International Journal for Numerical Methods in Engineering*, vol. 70, no. 8, pp. 934–961, 2007.

[36] M. Jaroslav, "Smart materials and structures-a finite element approach-an addendum: a bibliography (1997–2002)," *Modelling and Simulation in Materials Science and Engineering*, vol. 11, no. 5, pp. 707–704, 2003.

[37] E. Carrera and M. Boscolo, "Classical and mixed finite elements for static and dynamic analysis of piezoelectric plates," *International Journal for Numerical Methods in Engineering*, vol. 70, no. 10, pp. 1135–1181, 2007.

[38] X. Y. Cui, G. Wang, and G. Y. Li, "A nodal integration axisymmetric thin shell model using linear interpolation," *Applied Mathematical Modelling*, vol. 40, pp. 2720–2742, 2016.

[39] X. Y. Cui, X. Hu, G. Wang, and G. Y. Li, "An accurate and efficient scheme for acoustic-structure interaction problems based on unstructured mesh," *Computer Methods in Applied Mechanics and Engineering*, vol. 317, pp. 1122–1145, 2017.

[40] Y. H. Bie, X. Y. Cui, and Z. C. Li, "A coupling approach of state-based peridynamics with node-based smoothed finite element method," *Computer Methods in Applied Mechanics and Engineering*, vol. 331, pp. 675–700, 2018.

[41] L. Zhou, S. Ren, G. Meng, X. Li, and F. Cheng, "A multiphysics node-based smoothed radial point interpolation method for transient responses of magneto-electro-elastic structures," *Engineering Analysis with Boundary Elements*, vol. 101, pp. 371–384, 2019.

[42] L. Zhou, B. Nie, S. Ren, R. Liu, X. Li, and B. Xue, "Coupling magneto-electro-elastic cell-based smoothed radial point interpolation method for static and dynamic characterization of MEE structures," *Acta Mechanica*, vol. 230, no. 5, pp. 1641–1662, 2019.

[43] X. Hu, X. Y. Cui, Q. Y. Zhang, G. Wang, and G. Y. Li, "The stable node-based smoothed finite element method for analyzing acoustic radiation problems," *Engineering Analysis with Boundary Elements*, vol. 80, pp. 142–152, 2017.

[44] P. Phung-Van, T. Nguyen-Thoi, T. Le-Dinh, and H. Nguyen-Xuan, "Static and free vibration analyses and dynamic control of composite plates integrated with piezoelectric sensors and actuators by the cell-based smoothed discrete shear gap method (CS-FEM-DSG3)," *Smart Materials and Structures*, vol. 22, no. 9, article 095026, 2013.

[45] W. Zeng and G. R. Liu, "Smoothed finite element methods (S-FEM): an overview and recent developments," *Archives of Computational Methods in Engineering*, vol. 25, no. 2, pp. 397–435, 2018.

[46] J. Yue, G.-R. Liu, M. Li, and R. Niu, "A cell-based smoothed finite element method for multi-body contact analysis using linear complementarity formulation," *International Journal of Solids and Structures*, vol. 141-142, pp. 110–126, 2018.

[47] X. B. Hu, X. Y. Cui, Z. M. Liang, and G. Y. Li, "The performance prediction and optimization of the fiber-reinforced composite structure with uncertain parameters," *Composite Structures*, vol. 164, pp. 207–218, 2017.

[48] L. Zhou, M. Li, G. Meng, and H. Zhao, "An effective cell-based smoothed finite element model for the transient responses of magneto-electro-elastic structures," *Journal of Intelligent Material Systems and Structures*, vol. 29, no. 14, pp. 3006–3022, 2018.

[49] L. M. Zhou, G. W. Meng, F. Li, and H. Wang, "Cell-based smoothed finite element method-virtual crack closure technique for a piezoelectric material of crack," *Mathematical Problems in Engineering*, vol. 2015, Article ID 371083, 10 pages, 2015.

[50] L. Zhou, S. Ren, C. Liu, and Z. Ma, "A valid inhomogeneous cell-based smoothed finite element model for the transient characteristics of functionally graded magneto-electro-elastic structures," *Composite Structures*, vol. 208, pp. 298–313, 2019.

[51] L. Zhou, M. Li, Z. Ma et al., "Steady-state characteristics of the coupled magneto-electro-thermo-elastic multi-physical system based on cell-based smoothed finite element method," *Composite Structures*, vol. 219, pp. 111–128, 2019.

[52] X. Y. Cui, X. B. Hu, and Y. Zeng, "A copula-based perturbation stochastic method for fiber-reinforced composite structures with correlations," *Computer Methods in Applied Mechanics and Engineering*, vol. 322, pp. 351–372, 2017.

[53] E. Li, Z. C. He, L. Chen, B. Li, X. Xu, and G. R. Liu, "An ultra-accurate hybrid smoothed finite element method for piezoelectric problem," *Engineering Analysis with Boundary Elements*, vol. 50, pp. 188–197, 2015.

[54] H. Nguyen-Xuan, G. R. Liu, T. Nguyen-Thoi, and C. Nguyen-Tran, "An edge-based smoothed finite element method for analysis of two-dimensional piezoelectric structures," *Smart Materials and Structures*, vol. 18, no. 6, article 065015, 2009.

[55] T. Vo-Duy, T. Truong-Thi, V. Ho-Huu, and T. Nguyen-Thoi, "Frequency optimization of laminated functionally graded carbon nanotube reinforced composite quadrilateral plates using smoothed FEM and evolution algorithm," *Journal of Composite Materials*, vol. 52, no. 14, pp. 1971–1986, 2018.

[56] S. Bhowmick and G. R. Liu, "A phase-field modeling for brittle fracture and crack propagation based on the cell-based smoothed finite element method," *Engineering Fracture Mechanics*, vol. 204, pp. 369–387, 2018.

[57] A. L. N. Pramod, S. Natarajan, A. J. M. Ferreira, E. Carrera, and M. Cinefra, "Static and free vibration analysis of cross-ply laminated plates using the Reissner-mixed variational theorem and the cell based smoothed finite element method," *European Journal of Mechanics—A/Solids*, vol. 62, pp. 14–21, 2017.

[58] R. R. Ohs and N. R. Aluru, "Meshless analysis of piezoelectric devices," *Computational Mechanics*, vol. 27, no. 1, pp. 23–36, 2001.

Research Article

Prediction of Mechanical Strength of Fiber Admixed Concrete Using Multiple Regression Analysis and Artificial Neural Network

S. Karthiyaini [iD],[1] **K. Senthamaraikannan** [iD],[2] **J. Priyadarshini,**[3] **Kamal Gupta,**[1] **and M. Shanmugasundaram** [iD][1]

[1]*School of Mechanical and Building Sciences, Vellore Institute of Technology-Chennai Campus, Chennai-600127, Tamilnadu, India*
[2]*Department of Civil and Architectural Engineering, Al Musanna College of Technology, Muladdah Musanna, Oman*
[3]*School of Computing Science and Engineering, Vellore Institute of Technology-Chennai Campus, Chennai-600127, Tamilnadu, India*

Correspondence should be addressed to M. Shanmugasundaram; shanmugaresearch@gmail.com

The present study is to compare the multiple regression analysis (MRA) model and artificial neural network (ANN) model designed to predict the mechanical strength of fiber-reinforced concrete on 28 days. The model uses the data from early literatures; the data consist of tensile strength of fiber, percentage of fiber, water/cement ratio, cross-sectional area of test specimen, Young's modulus of fiber, and mechanical strength of control specimen, and these were used as the input parameters; the respective strength attained was used as the target parameter. The models are created and are used to predict compressive, split tensile, and flexural strength of fiber admixed concrete. These models are evaluated through the statistical test such as coefficient of determination (R^2) and root mean squared error (RMSE). The results show that these parameters produce a valid model through both MRA and ANN, and this model gives more precise prediction for the fiber admixed concrete.

1. Introduction

Concrete is considered to be the fundamental and an important material in construction industry. Maintaining and testing the quality and behavior of concrete is the challenge faced by the industries in recent times. Also, the modeling of materials through regression tools and AI tools is recently increasing due to its accurate prediction and evaluation. The concrete as generally known for its good compressive behavior is made to behave well under tension and flexure through addition of fiber additives. The general tensile and flexural strength enhancements are made through addition of fibers made up of various materials with different physical and chemical properties. The addition of fibers made up of various materials changes the behavior of cement-based composites and enhances the toughness, tension resistance, and flexural resistance [1–9]. These fibers act at various levels in altering the mechanical behavior of concrete and thus defy the rules framed for its tensile and flexural

performance, making it hard to predict. The major factors that act in enhancing the tensile and flexural strength are fiber distribution and its physical parameters. In recent years, analyzing the concrete properties through prediction modeling is gaining importance due to its accuracy and effectiveness in real-time application. These concrete models were presumed to predict the strength development through certain factors which are used as input parameters. This prediction facilitates in making decision on concrete mix and material selection [10–15]. But there is a challenge when creating a model of concrete for predicting tensile strength and flexural strength, as an effective prediction model is not created through parameters which were used for predicting the compressive strength [16–18]. The challenge on accuracy in prediction increases in fiber admixed concrete while predicting tensile strength and flexural strength; this is due to the fiber properties and its distribution.

In this study, the predictive model was created through multiple regression analysis (MRA) and artificial neural

network (ANN). The fiber properties were used as parameters along with basic concrete and fiber parameters with single target system, and the model is tested through statistical tools for its performance.

2. Prediction Modeling and Testing

The model created here is for fiber-reinforced concrete; the data set was collected for steel fiber, polypropylene fiber, hybrid fiber, glass fiber, and basalt fiber from early studies. The actual compressive strength, split tensile strength, and flexural strength are taken as the target values based on the following parameters which are used as input parameters:

  (1) Tensile strength of fiber (F)
  (2) Percentage of fiber (P)
  (3) Water/cement ratio (R)
  (4) Cross-sectional area of test specimen (A)
  (5) Young's modulus of fiber (Y)
  (6) Mechanical strength of control specimen (S)

Based on the input parameter and target values, the output was generated through ANN and MRA, and these output values were compared with target (actual) values. The types of fibers and its respective literature source are presented in Table 1. The active compressive strength data set has 5 columns and 252 rows (5×252) of input data and 1 column and 252 rows (1×252) of target data. The active split tensile strength data set has 5 columns and 119 rows (5×119) of input data and 1 column and 119 rows (1×119) of target data. The active flexural strength data set has 5 columns and 150 rows (5×150) of input data and 1 column and 150 rows (1×150) of target data. The target data for compressive strength, split tensile strength, and flexural strength were used in both the MRA and ANN model as separate target in this study. This single target system was used due to the usage of cross-sectional area of test specimens as one of the parameters, and it was known that the shape of the specimens varies with different mechanical strengths.

2.1. Prediction Model and Its Statistical Test.
Two prediction models, artificial neural network (ANN) and multiple regression analysis (MRA), are used in this study to predict the compressive strength, split tensile strength, and flexural strength of fiber-reinforced concrete (FRC).

2.2. Artificial Neural Network (ANN).
The ANN prediction model is programmed through MATLAB with two hidden layers, 15 neurons in each hidden layer and one output layer with dependent variable as compressive strength, split tensile strength, and flexural strength. Among all the data, approximately 70%, 15%, and 15% has been considered for training, testing, and validation, respectively. The Levenberg–Marquardt (LM) algorithm is used for training due to its robustness and speed. Layered feed-forward networks have been used in this algorithm, in which the neurons are arranged in layers. Here, signals are sent forward, and errors are propagated backwards.

2.3. Multiple Regression Analysis (MRA).
In this study, the linear-type multiple regression analysis modeling is carried out using MS excel. The coefficients of regression are calculated by considering 95% confidence level; hence, the error tolerance level is limited to maximum of 5%. For a given input variable, the calculated probability value (p value) is considered to be significant, if and only if its value is less than 0.05. Through the regression analysis, the following coefficients presented in Table 2 were found and substituted in linear multiple regression equation (equation (1)):

$$\text{output} = I + C_1 F + C_2 P + C_3 R + C_4 A + C_5 Y + C_6 S. \quad (1)$$

2.4. Statistical Test.
The performance of the ANN and MRA prediction for the mechanical behavior was tested through the statistical methods. The tests involved are coefficient of determination (R^2) and root mean squared error (RMSE). The coefficient of determination is presented in equation (2). This can be obtained from the comparative chart of predicted compressive strength vs. experimental compressive strength. The accuracy of the predictions of a network was quantified by the root of the mean squared error difference (RMSE), between the experimented and the predicted values, and the procedure of finding RMSE is presented in equation (3):

$$R^2 = 1 - \frac{\text{sum of squares of residuals}}{\text{sum of sqaures of predicted values}}, \quad (2)$$

$$\text{RMSE} = \sqrt{\frac{1}{n} \sum_{i=1}^{n} (ACST - PCST)^2}. \quad (3)$$

3. Results and Discussion

The effectiveness and the acceptance of prediction models are based upon the ability of the model to predict the output. In this study, the models were designed to predict the mechanical behavior (mechanical strength) of FRC based on input parameters, and two methods of predictions, ANN and MRA, are used. The prediction models are validated through coefficient of determination (R^2) and root mean squared error (RMSE) and are consolidated in Table 3.

The MRA and ANN prediction of the compressive strength value is plotted with respect to the actual compressive strength and presented in Figures 1 and 2, respectively. The MRA prediction has the coefficient of determination R^2 as 0.93 which is almost an acceptable value, whereas the ANN has an R^2 value of 1 which indicates that the ANN model is accurate. The RMSE of the MRA model is 7.23 MPa, and the ANN model is 0.14 MPa which demonstrates that error in the MRA model is large and cannot be relied upon for predicting the compressive strength.

The MRA and ANN prediction model plot for split tensile strength with respect to its actual value is presented in Figures 3 and 4, respectively. The R^2 value for the MRA model is 0.87 and ANN model is 0.94. The RMSE for the

TABLE 1: Range of parameters in data base for prediction model.

Type of fiber	Tensile strength of fiber in MPa	Percentage addition of fiber	Water/binder ratio	Area of specimen tested for compression in mm²	Data range for prediction model					
					Area of specimen tested for tension in mm²	Area of specimen tested for flexure in mm²	Compression strength in MPa	Split tensile strength in MPa	Flexural strength in MPa	Elastic modulus of fiber in MPa
Steel fiber [19–27]	1000–2800	0.025–2.000	0.15–0.5	1600–22500	22500–62832	25200–90000	38.2–146.3	3.23–8.95	3.5–20.2	22830–60.477.26846
Polypropylene fiber [18, 24, 28–34]	320–1200	0.0001–2.000	0.30–0.64	1600–22500	22500–141372	40000–79500	12.7–97.5	1.98–7.98	3–12.02	17818.53–49371.04
Hybrid fiber [35, 36]	450–1200	0.200–2.000	0.38–0.50	7850–17671	—	25200–40000	27.01–73.22	—	4.31–11.3	18460–42784.34
Glass fiber [15, 37–48]	1500–3750	0.100–0.300	0.2–0.71	380–141371	648–141371.67	10000–50000	14–75.82	1.07–7.1	3.39–10.1	3680–43537.34
Basalt fiber [23, 49–52]	3400–4600	0.015–12.450	0.4–0.5	7850–14137	22500–62831.85	24000–92720	29.13–85.78	2.37–4.59	3.9–10.8	26986–44415

TABLE 2: Multiple regression analysis coefficients.

MRA coefficients	Coefficients for compressive strength	Coefficients for split tensile strength	Coefficients for flexural strength
I	−2.083944795	2.864487059	7.214539466
C_1	0.000669227	5.24726×10^{-05}	-4.23499×10^{-05}
C_2	1.097340646	0.81644571	0.513456489
C_3	−31.43416778	−6.912788644	−13.36882713
C_4	-5.56151×10^{-05}	8.71841×10^{-06}	1.9284×10^{-05}
C_5	0.001154844	4.70901×10^{-05}	2.60556×10^{-05}
C_6	0.569536979	0.475257898	0.551752286

TABLE 3: Statistical test conducted on prediction models.

Predicted parameters	MRA		ANN	
	R^2	RMSE	R^2	RMSE
Compression strength	0.93	7.23	1.00	0.14
Split tensile strength	0.87	0.70	0.94	0.42
Flexural strength	0.92	0.99	0.94	0.79
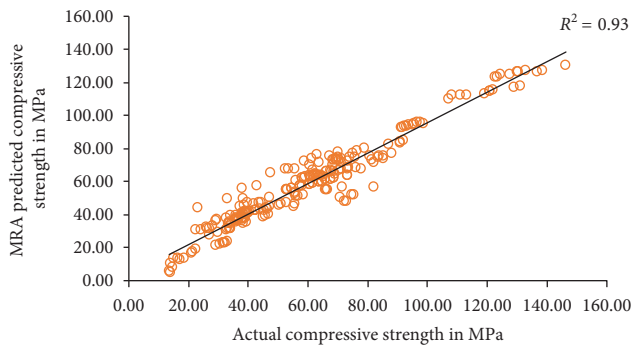
FIGURE 1: Actual vs. MRA predicted value for compressive strength.
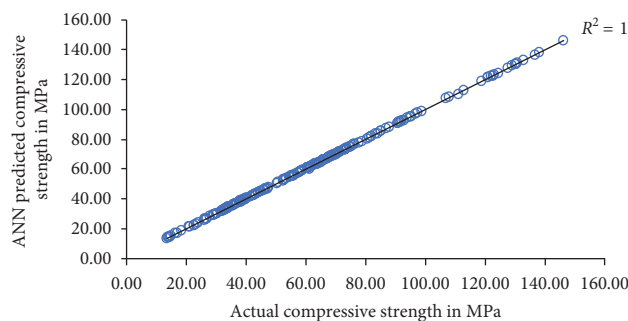
FIGURE 2: Actual vs. ANN predicted value for compressive strength.

FIGURE 3: Actual vs. MRA predicted value for split tensile strength.
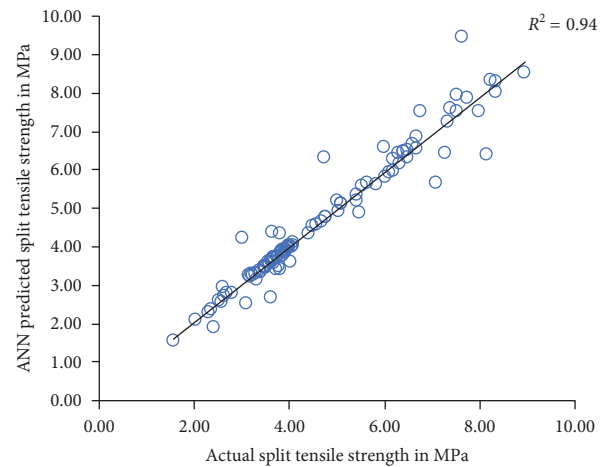
FIGURE 4: Actual vs. ANN predicted value for split tensile strength.

MRA model is 0.70 MPa and ANN is 0.42 MPA. The statistical validation of the split tensile strength model shows that both the MRA model and ANN model are in acceptable limit; even though ANN shows more accuracy than MRA, the mathematical model is also predicting the split tensile strength in par with the ANN model. From Figure 3, it is observed that the MRA model predicts to a high accuracy until actual split tensile strength is 4 MPa, after which the scatter plots were deviating from the actual trend line. From Figure 4, it is observed that the ANN prediction is accurate until the actual strength is 7.5 MPa, after which the scattered plot almost does not fit the trend line.

The MRA and ANN prediction model plot for flexural strength with respect to its actual value is presented in Figures 5 and 6, respectively. The R^2 value for MRA and ANN was 0.92 and 0.94, respectively, which has similar validation value. The RMSE value of the MRA model is 0.99 MPa and ANN model is 0.79 MPa. Both the MRA and ANN were having similar model behavior in terms of statistical validation and graphical representation through Figures 5 and 6. The prediction is accurate in both MRA and ANN models until the actual flexural strength is 9 MPa after which the scattered plot is observed for both models. But there were fitted plots for the MRA model at higher actual flexural strength which lies between 13 MPa and 14 MPa. This higher-order flexural strength fitness towards the trend line was not observed in the ANN model. The observation indicates that flexural strength prediction using MRA and ANN model has effectiveness, and more accurate prediction is rendered in both models. Through the three strength aspects, it was observed that the MRA gains its accurateness in predicting split tensile and flexural strength. The ANN predicts compressive strength to the maximum possible accuracy, and the prediction of split tensile strength and
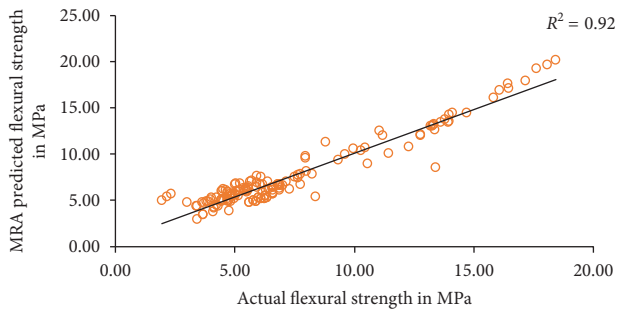
FIGURE 5: Actual vs. MRA predicted value for flexural strength.
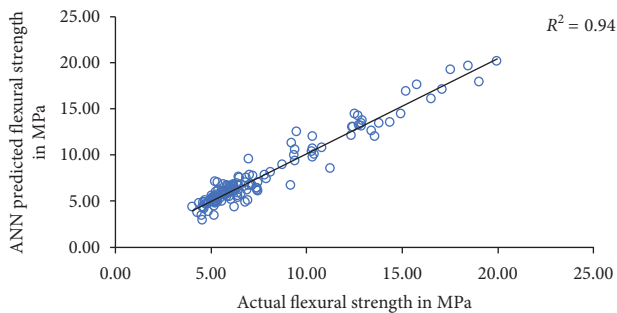
FIGURE 6: Actual vs. ANN predicted value for flexural strength.

flexural strength was also of higher accuracy. Though the fibers have various factors on influencing the strength development in concrete, the prediction models MRA and ANN are accurate by its output values. The ANN even though has its advantage of higher accuracy over MRA model; the performance of the MRA model is also efficient. The contribution of fiber properties in the prediction model proved to be effective and also gives more preciseness to the model. Earlier models that uses other parameters such as quantity of cement, admixtures, coarse aggregate, fine aggregate, and water were not able to perform well in prediction of tensile and flexural properties [53]; this limitation was overcome by the current model, where both the MRA and ANN model performs well with the given factors. Thus, both current models can predict the complete mechanical behavior of fiber admixed concrete with high precision.

4. Conclusion

This study investigated the feasibility of modeling a predictive analysis through earlier study data, converting the unstructured factors to possible structured parameters and using those in creating the MRA model and ANN model. Also, the effectiveness of these models is tested using statistical tools such as R^2 and RMSE. The compressive strength model shows that ANN has efficient prediction model with R^2 value in unity. The MRA model has R^2 value of 0.93, but the error difference is 7.23 MPa which is very high for a predictive model. The MRA model of split tensile strength and flexural strength shows high efficiency; even though the R^2 values are lesser than the compressive model, the performance of models is relatively strong. The ANN model for

split tensile and flexural strength has similar statistical valuation. The MRA model shows more robustness while predicting the flexural strength, than the split tensile strength. Also, it is noted that the MRA model performs well in split tensile and flexural strength prediction and is validated through the R^2 and RMSE values. The MRA performs well similar to that of ANN and achieves half its effectiveness, except in compressive strength prediction. The study concludes that the fiber properties contribute high to the prediction model, thus increasing the models' performance.

Data Availability

The data supporting this work are available from previously reported studies and datasets, which have been cited. The processed data used to support the findings of this study are available from the corresponding author upon request.

Conflicts of Interest

The authors declare no conflicts of interest.

References

[1] X. Lu and C.-T. T. Hsu, "Behavior of high strength concrete with and without steel fiber reinforcement in triaxial compression," *Cement and Concrete Research*, vol. 36, no. 9, pp. 1679–1685, 2006.

[2] V. F. P. Dutra, S. Maghous, and A. C. Filho, "A homogenization approach to macroscopic strength criterion of steel fiber reinforced concrete," *Cement and Concrete Research*, vol. 44, pp. 34–45, 2013.

[3] P. S. Song and S. Hwang, "Mechanical properties of high-strength steel fiber-reinforced concrete," *Construction and Building Materials*, vol. 18, no. 9, pp. 669–673, 2004.

[4] M. L. Allan and L. E. Kukacka, "Strength and durability of polypropylene fibre reinforced grouts," *Cement and Concrete Research*, vol. 25, no. 3, 1995.

[5] B. Chen and J. Liu, "Residual strength of hybrid-fiber-reinforced high-strength concrete after exposure to high temperatures," *Cement and Concrete Research*, vol. 34, no. 6, pp. 1065–1069, 2004.

[6] C. S. Poon, Z. H. Shui, and L. Lam, "Compressive behavior of fiber reinforced high-performance concrete subjected to elevated temperatures," *Cement and Concrete Research*, vol. 34, no. 12, pp. 2215–2222, 2004.

[7] Y. Ding, C. Azevedo, J. B. Aguiar, and S. Jalali, "Study on residual behaviour and flexural toughness of fibre cocktail reinforced self compacting high performance concrete after exposure to high temperature," *Construction and Building Materials*, vol. 26, no. 1, 2011.

[8] A. Avci, H. Arikan, and A. Akdemir, "Fracture behavior of glass fiber reinforced polymer composite," *Cement and Concrete Research*, vol. 34, no. 3, pp. 429–434, 2004.

[9] I. Curosu, V. Mechtcherine, and O. Millon, "Effect of fiber properties and matrix composition on the tensile behavior of strain-hardening cement-based composites (SHCCs) subject to impact loading," *Cement and Concrete Research*, vol. 82, pp. 23–35, 2016.

[10] I. B. Topçu and M. Sarıdemir, "Prediction of compressive strength of concrete containing fly ash using artificial neural networks and fuzzy logic," *Computational Materials Science*, vol. 41, no. 3, pp. 305–311, 2008.

[11] N. Al-Mutairi, M. Terro, and A.-L. Al-Khaleefi, "Effect of recycling hospital ash on the compressive properties of concrete: statistical assessment and predicting model," *Building and Environment*, vol. 39, no. 5, pp. 557–566, 2004.

[12] M. A. Kewalramani and R. Gupta, "Concrete compressive strength prediction using ultrasonic pulse velocity through artificial neural networks," *Automation in Construction*, vol. 15, no. 3, pp. 374–379, 2006.

[13] R. Siddique, P. Aggarwal, and Y. Aggarwal, "Prediction of compressive strength of self-compacting concrete containing bottom ash using artificial neural networks," *Advances in Engineering Software*, vol. 42, no. 10, pp. 780–786, 2011.

[14] Z. H. Duan, S. C. Kou, and C. S. Poon, "Prediction of compressive strength of recycled aggregate concrete using artificial neural networks," *Construction and Building Materials*, vol. 40, pp. 1200–1206, 2013.

[15] H. I. Erdal, O. Karakurt, and E. Namli, "High performance concrete compressive strength forecasting using ensemble models based on discrete wavelet transform," *Engineering Applications of Artificial Intelligence*, vol. 26, no. 4, pp. 1246–1254, 2013.

[16] A. Nazari and S. Riahi, "Computer-aided prediction of the ZrO_2 nanoparticles' effects on tensile strength and percentage of water absorption of concrete specimens," *Journal of Materials Science & Technology*, vol. 28, no. 1, pp. 83–96, 2012.

[17] M. Baena, A. Turon, L. Torres, and C. Miàs, "Experimental study and code predictions of fibre reinforced polymer reinforced concrete (FRP RC) tensile members," *Composite Structures*, vol. 93, no. 10, pp. 2511–2520, 2011.

[18] H. Fathi, T. Lameie, M. Maleki, and R. Yazdani, "Simultaneous effects of fiber and glass on the mechanical properties of self-compacting concrete," *Construction and Building Materials*, vol. 133, pp. 443–449, 2017.

[19] S. Yehia, A. Douba, O. Abdullahi, and S. Farrag, "Mechanical and durability evaluation of fiber-reinforced self-compacting concrete," *Construction and Building Materials*, vol. 121, pp. 120–133, 2016.

[20] M. Mastali and A. Dalvand, "Fresh and hardened properties of self-compacting concrete reinforced with hybrid recycled steel—polypropylene fiber," *Journal of Materials in Civil Engineering*, vol. 29, no. 6, article 04017012, 2017.

[21] W.-C. Liao, W. Perceka, and E.-J. Liu, "Compressive stress-strain relationship of high strength steel fiber reinforced concrete," *Journal of Advanced Concrete Technology*, vol. 13, no. 8, pp. 379–392, 2015.

[22] C. D. Atis, O. Karahan, K. Ari, Ö. C. Sola, C. Bilim, and F. Ash, "Relation between strength properties (flexural and compressive) and abrasion resistance of fiber (steel and polypropylene) reinforced fly ash concrete," *Journal of Materials in Civil Engineering*, vol. 21, no. 8, pp. 402–408, 2009.

[23] M. Z. N. Khan, Y. Hao, H. Hao, and F. U. A. Shaikh, "Mechanical properties of ambient cured high strength hybrid steel and synthetic fibers reinforced geopolymer composites," *Cement and Concrete Composites*, vol. 85, pp. 133–152, 2018.

[24] J. J. Li, C. J. Wan, J. G. Niu, L. F. Wu, and Y. C. Wu, "Investigation on flexural toughness evaluation method of steel fiber reinforced lightweight aggregate concrete," *Construction and Building Materials*, vol. 131, pp. 449–458, 2017.

[25] A. Caggiano, S. Gambarelli, E. Martinelli, N. Nisticò, and M. Pepe, "Experimental characterization of the post-cracking response in hybrid steel/polypropylene fiber-reinforced concrete," *Construction and Building Materials*, vol. 125, pp. 1035–1043, 2016.

[26] M. Hsie, C. Tu, and P. S. Song, "Mechanical properties of polypropylene hybrid fiber-reinforced concrete," *Materials Science and Engineering: A*, vol. 494, no. 1-2, pp. 153–157, 2008.

[27] L. Shan and L. Zhang, "Experimental study on mechanical properties of steel and polypropylene fiber-reinforced concrete," *Applied Mechanics and Materials*, vol. 584–586, pp. 1355–1361, 2014.

[28] H. Mohammadhosseini, A. S. M. Abdul Awal, and J. B. Mohd Yatim, "The impact resistance and mechanical properties of concrete reinforced with waste polypropylene carpet fibres," *Construction and Building Materials*, vol. 143, pp. 147–157, 2017.

[29] M. G. Alberti, A. Enfedaque, and J. C. Gálvez, "Fibre reinforced concrete with a combination of polyolefin and steel-hooked fibres," *Composite Structures*, vol. 171, pp. 317–325, 2017.

[30] S. Fallah and M. Nematzadeh, "Mechanical properties and durability of high-strength concrete containing macro-polymeric and polypropylene fibers with nano-silica and silica fume," *Construction and Building Materials*, vol. 132, pp. 170–187, 2017.

[31] M. Hassani Niaki, A. Fereidoon, and M. Ghorbanzadeh Ahangari, "Experimental study on the mechanical and thermal properties of basalt fiber and nanoclay reinforced polymer concrete," *Composite Structures*, vol. 191, pp. 231–238, 2018.

[32] A. M. Alhozaimy, P. Soroushian, and F. Mirza, "Mechanical properties of polypropylene fiber reinforced concrete and the effects of pozzolanic materials," *Cement and Concrete Composites*, vol. 18, no. 2, pp. 85–92, 1996.

[33] V. Afroughsabet and T. Ozbakkaloglu, "Mechanical and durability properties of high-strength concrete containing steel and polypropylene fibers," *Construction and Building Materials*, vol. 94, pp. 73–82, 2015.

[34] S. Iqbal, A. Ali, K. Holschemacher, and T. A. Bier, "Mechanical properties of steel fiber reinforced high strength lightweight self-compacting concrete (SHLSCC)," *Construction and Building Materials*, vol. 98, pp. 325–333, 2015.

[35] G. M. Ren, H. Wu, Q. Fang, and J. Z. Liu, "Effects of steel fiber content and type on static mechanical properties of UHPCC," *Construction and Building Materials*, vol. 163, pp. 826–839, 2018.

[36] P. Iyer, S. Y. Kenno, and S. Das, "Mechanical properties of fiber-reinforced concrete made with basalt filament fibers," *Journal of Materials in Civil Engineering*, vol. 27, no. 11, article 04015015, 2015.

[37] V. R. Sivakumar, O. R. Kavitha, G. Prince Arulraj, and V. G. Srisanthi, "An experimental study on combined effects of glass fiber and Metakaolin on the rheological, mechanical, and durability properties of self-compacting concrete," *Applied Clay Science*, vol. 147, pp. 123–127, 2017.

[38] S. Ahmad, A. Umar, and A. Masood, "Properties of normal concrete, self-compacting concrete and glass fibre-reinforced self-compacting concrete: an experimental study," *Procedia Engineering*, vol. 173, pp. 807–813, 2017.

[39] S. T. Tassew and A. S. Lubell, "Mechanical properties of glass fiber reinforced ceramic concrete," *Construction and Building Materials*, vol. 51, pp. 215–224, 2014.

[40] A. B. Kizilkanat, N. Kabay, V. Akyüncü, S. Chowdhury, and A. H. Akça, "Mechanical properties and fracture behavior of basalt and glass fiber reinforced concrete: an experimental study," *Construction and Building Materials*, vol. 100, pp. 218–224, 2015.

[41] M. Khan and M. Ali, "Use of glass and nylon fibers in concrete for controlling early age micro cracking in bridge decks," *Construction and Building Materials*, vol. 125, pp. 800–808, 2016.

[42] A. Hanif, P. Parthasarathy, Z. Lu, M. Sun, and Z. Li, "Fiber-reinforced cementitious composites incorporating glass cenospheres - mechanical properties and microstructure," *Construction and Building Materials*, vol. 154, pp. 529–538, 2017.

[43] M. E. Arslan, "Effects of basalt and glass chopped fibers addition on fracture energy and mechanical properties of ordinary concrete: CMOD measurement," *Construction and Building Materials*, vol. 114, pp. 383–391, 2016.

[44] T. A. Söylev and T. Özturan, "Durability, physical and mechanical properties of fiber-reinforced concretes at low-volume fraction," *Construction and Building Materials*, vol. 73, pp. 67–75, 2014.

[45] R. M. Novais, J. Carvalheiras, M. P. Seabra, R. C. Pullar, and J. A. Labrincha, "Effective mechanical reinforcement of inorganic polymers using glass fibre waste," *Journal of Cleaner Production*, vol. 166, pp. 343–349, 2017.

[46] T. Simões, H. Costa, D. Dias-da-Costa, and E. Júlio, "Influence of fibres on the mechanical behaviour of fibre reinforced concrete matrixes," *Construction and Building Materials*, vol. 137, pp. 548–556, 2017.

[47] G. B. Maranan, A. C. Manalo, B. Benmokrane, W. Karunasena, and P. Mendis, "Evaluation of the flexural strength and serviceability of geopolymer concrete beams reinforced with glass-fibre-reinforced polymer (GFRP) bars," *Engineering Structures*, vol. 101, pp. 529–541, 2015.

[48] W. H. Kwan, M. Ramli, and C. B. Cheah, "Flexural strength and impact resistance study of fibre reinforced concrete in simulated aggressive environment," *Construction and Building Materials*, vol. 63, pp. 62–71, 2014.

[49] J. Branston, S. Das, S. Y. Kenno, and C. Taylor, "Mechanical behaviour of basalt fibre reinforced concrete," *Construction and Building Materials*, vol. 124, pp. 878–886, 2016.

[50] U. Larisa, L. Solbon, and B. Sergei, "Fiber-reinforced concrete with mineral fibers and nanosilica," *Procedia Engineering*, vol. 195, pp. 147–154, 2017.

[51] T. Ayub, N. Shafiq, and S. U. Khan, "Compressive stress-strain behavior of HSFRC reinforced with basalt fibers," *Journal of Materials in Civil Engineering*, vol. 28, article 06015014, 2016.

[52] M. Abdulhadi and Liaoning University of Technology, Jinzhou, "A comparative study of basalt and polypropylene fibers reinforced concrete on compressive and tensile behavior," *International Journal of Engineering Trends and Technology*, vol. 9, no. 6, pp. 295–300, 2014.

[53] M. F. M. Zain, H. B. Mahmud, A. Ilham, and M. Faizal, "Prediction of splitting tensile strength of high-performance concrete," *Cement and Concrete Research*, vol. 32, no. 8, pp. 1251–1258, 2002.

Research Article

Effect of Calcium Carbonate Whisker and Fly Ash on Mechanical Properties of Cement Mortar under High Temperatures

Li Wang,[1] **Hongliang Zhang** ⬭**,**[1] **Bendong Zhao,**[2] **and Yang Gao**[1]

[1]*Key Laboratory for Special Area Highway Engineering of Ministry of Education, Chang'an University, Xi'an, Shaanxi, China*
[2]*CCCC First Highway Consultants Co. Ltd., Xi'an, Shaanxi, China*

Correspondence should be addressed to Hongliang Zhang; zhliang0105@163.com

Calcium carbonate ($CaCO_3$) whisker, as a new type of microfibrous material, has been extensively used in the reinforcement of cementitious materials. However, the combined effect of $CaCO_3$ whisker and fly ash on mechanical properties of cementitious materials under high temperatures was still unknown. In this study, the coupling effect of $CaCO_3$ whisker, and fly ash on mechanical properties of the cement was investigated. Two sets of cement mortars were fabricated, including $CaCO_3$ whisker-based mortar which contained 0 wt.%, 5 wt.%, 10 wt.%, 15 wt.%, and 20 wt.% $CaCO_3$ whisker as cement substitution and $CaCO_3$ whisker-based fly ash mortar which contained 30 wt.% fly ash in addition to 0 wt.%, 5 wt.%, 10 wt.%, 15 wt.%, and 20 wt.% $CaCO_3$ whisker as cement substitution. Mass loss, compressive strength, and flexural strength of these two sets of specimens before and after being subjected to high temperatures of 200°C, 400°C, 600°C, 800°C, and 1000°C were measured. Based on the results of the aforementioned tests, load-deflection test was performed on the specimen which exhibited the superior performance to further study its mechanical behavior after exposure to high temperatures. Moreover, microstructural analysis, such as mercury intrusion porosimetry (MIP) and scanning electron microscopy (SEM), was conducted to reveal the damage mechanism of high temperature and to illustrate the combined effect of $CaCO_3$ whisker and fly ash on high-temperature resistance of the cement. Results showed that fly ash could improve the high-temperature performance of $CaCO_3$ whisker-based mortar before 600°C and limit the loss of strength after 600°C.

1. Introduction

Fire is one of the fatal threats which seriously affect human life, property security, and economic development in the world. Concrete, as a widely used key material in the construction of infrastructural facilities, is noncombustible and performs well when exposed to high temperatures because the components of it, such as cement and aggregates, are chemically inert. However, the physical and chemical deteriorations of cementitious materials due to moisture loss and decomposition of hydrated products at high temperatures may result in the generation of cracks and the loss to mechanical strengths of concrete, finally lead to the structural damage [1]. Therefore, it is crucial to investigate the mechanical performance of concrete at elevated temperatures and enhance the mechanical properties of concrete, which can also provide references for engineers to select concrete of good fire resistance.

As is well known, concrete is a brittle material which has low flexural strength, and in practice, a variety of fibrous materials, such as steel, carbon, polymer, and natural fibers, are often employed to enhance its toughness [2–5]. The whisker is a new type of microfibrous, single-crystal material which has tiny diameter and large aspect ratio, and therefore, it possesses both the characteristics of fillers and fibers. In addition, the atomic arrangement of the whisker is highly ordered, so theoretically its strength is close to that of intact crystal. And above all, whiskers often have excellent thermostability with high decomposition temperature around 800°C which makes them a suitable reinforcement for composite materials not only to enhance

mechanical properties but also to improve high-temperature resistance performance. Whiskers can be categorized as organic and inorganic whiskers, and organic whisker such as cellulosic whisker is frequently used for reinforcing the polymer materials [6, 7]. With respect to inorganic whisker, calcium carbonate whisker [8–12], calcium sulphate whisker [13], zinc oxide whisker [14], silicon carbide whisker [15], and potassium titanate whisker [16] are commonly used, and among which, $CaCO_3$ whisker has the most extensive application in the reinforcement of cementitious materials. Previous studies have shown that $CaCO_3$ whisker has the capacity to improve the mechanical strength and enhance the flexural toughness of cementitious materials. Cao et al. conducted a series of researches on the application of $CaCO_3$ whisker in cementitious materials, and they found that, with the incorporation of $CaCO_3$ whisker, mechanical properties of cement pastes were improved before the temperature was up to 600°C while a deteriorated phenomenon was observed at 600–1000°C [8, 9]. They also discovered that, at ambient temperature, $CaCO_3$ whisker significantly improved the flexural strength of cement mortar, and the optimum dosage was 10% [10]. Moreover, they indicated that the rheological properties of mortars containing $CaCO_3$ whisker complied with the Bingham model and with the whisker content of 1.5%, and mortars exhibited the uniform distribution [11]. Yang et al. reported that $CaCO_3$ whisker with the addition of 10% could remarkably enhance the tensile strength of cement paste, and the constitutive relationship of the stress-strain curve of $CaCO_3$ whisker-reinforced cement pastes and toughening mechanism of $CaCO_3$ whisker were illustrated as well [12]. On the other hand, the microsize of $CaCO_3$ whisker enables the combined use of it with various large-sized fibers in order to achieve the multiscale cracking resistance of cementitious materials [17–21].

Moreover, as global warming continues, environmental protection should be taken into consideration prior to the construction of concrete structures. However, during the manufacturing of cement, environmental problem associated with huge emissions of greenhouse gases, mainly carbon dioxide (CO_2), has raised concern for sustainable development, based on the fact that the production of every tonne of ordinary Portland cement (OPC) releases an equivalent amount of CO_2 into the atmosphere [22]. In addition, with the development of urbanization, the accompanying high demand for cement will make the environmental problem increasingly severe, and measures should be taken to reduce the energy consumption and curb the emission of CO_2 during the fabrication of cement. In consideration of sustainability and energy conservation, one of the effective measures to reduce the consumption of cement is to replace part of the cement with supplementary cementitious materials (SCMs), such as fly ash, silica fume, and granulated blast furnace slag, and other waste materials [23].

Fly ash, as one of the most important SCMs, is a by-product of coal power stations and therefore using it as cement substitution not only reduce the production of cement but also provide an efficient method for disposal of

waste material compared with other conventional disposal methods. Silicon dioxide (SiO_2) and aluminium oxide (Al_2O_3), as main chemical compositions of fly ash, can react with calcium hydroxide (CH) produced during cement hydration to form calcium silicate hydrate (CSH) and calcium aluminate hydrate (CAH), thereby densifying the paste and achieving higher strength and better durability, which is known as pozzolanic effect of fly ash. Generally, the cement replacement by fly ash is limited to be around 15%–30% by mass of the total binding material. Previous studies have pointed out the superiority of fly ash when it is moderately incorporated into cementitious materials as cement replacement. In particular, the mechanical strength of fly ash concrete after exposure to high temperatures is still comparatively advantageous, although the overall strength of concrete decreases with the increase in maximum temperature. The study of Ibrahim et al. has demonstrated that, after exposure to high temperatures of up to 700°C, mechanical properties of mortars were enhanced when 25% of cement was replaced by fly ash [24]. Tanyildizi and Coskun reported that, under high temperatures of up to 800°C, mechanical strengths of concrete were improved through substituting up to 30% of cement with fly ash [1]. Soleimanzadeh and Othuman found that the flexural strength of foamed concrete containing 30% FA was higher than the ordinary concrete after exposure to high temperatures of up to 600°C [25].

To the best of our knowledge, the combined effect of $CaCO_3$ whisker and fly ash on mechanical properties of cementitious materials after exposure to elevated temperatures has not been reported. Better understanding this knowledge could extend the application of $CaCO_3$ whisker and facilitate the utilization of fly ash, thereby lowering the amount of other expensive fibers, reducing the overall cost of concrete projects, and promoting the sustainable development. In the current study, systematic experiments, including mass loss test, compressive strength test, flexural strength test, and load-deflection curve test, were carried out to study the influence of $CaCO_3$ whisker and fly ash on properties of cement mortars before and after exposure to high temperatures of 200°C, 400°C, 600°C, 800°C, and 1000°C. Meanwhile, the effect of $CaCO_3$ whisker on the high-temperature performance of cement mortars was also examined as a reference to see whether fly ash could have a positive influence on the high-temperature performance of $CaCO_3$ whisker-based cement mortar and thus promoting the sustainable development. Furthermore, the deterioration mechanism of high temperatures and the interaction mechanism of $CaCO_3$ whisker and fly ash with the cement were explored by MIP and SEM.

2. Materials and Experiments

2.1. Raw Materials. Raw materials used in this study include cement, fly ash, $CaCO_3$ whisker, and natural river sand. Cement was OPC 42.5 that met the requirements of ASTM C150 specification [26]. Fly ash was class F fly ash that met the requirements of ASTM C618 specification [27]. $CaCO_3$ whisker that has a high tensile strength of 3–6 GPa and high

elastic modulus of 410–710 GPa was used in this study. The diameter and aspect ratio of it was in the range of 5–10 μm and 10–30, respectively, as shown in Figure 1. The chemical compositions of the cement, the fly ash, and the whisker, provided by suppliers, are presented in Table 1. The sand used in this study was natural river sand with a fineness modulus of 2.7. In order to maintain a favorable workability, polycarboxylic-type water-reducing agent that met the requirements of ASTM C494-type F specification [28] was also used in this study.

2.2. Specimen Preparation. In order to investigate the mechanical properties and microstructural mechanism of cement mortars containing $CaCO_3$ whisker and fly ash, different types of specimens were prepared. Cement, natural river sand, and water were used in all the mortar mixtures, along with $CaCO_3$ whisker and fly ash in specific mixtures. To be exact, cement mortars were classified into two sets, which were $CaCO_3$ whisker-based mortar and $CaCO_3$ whisker-based fly ash mortar. The first set was $CaCO_3$ whisker-based mortar which contained OPC and different contents of $CaCO_3$ whisker (e.g., 0 wt.%, 5 wt.%, 10 wt.%, 15 wt.%, and 20 wt.%) as the binder, while the second set was $CaCO_3$ whisker-based fly ash mortar which was fabricated with OPC and 30 wt.% fly ash as a fixed substitution of cement in addition to 0 wt.%, 5 wt.%, 10 wt.%, 15 wt.%, and 20 wt.% $CaCO_3$ whisker. Therefore, a total number of ten mortar mixtures were designed in this study. It should be noted that, for all the mixtures, a constant water-to-binder ratio of 0.4, binder-to-sand ratio of 1 : 2.75, and a total cementitious material content of 500 kg/m^3 were used. Details of the mix proportions are listed in Table 2.

With respect to specimen fabrication, raw materials, such as cement, $CaCO_3$ whisker, fly ash, and sand, according to the corresponding mix proportions, were mixed together for 3 min by an electrically driven mixer before adding the mixing water. Then, 70% of the mixing water was added to the mixture and mixed for another 3 min. Thereafter, the water-reducing agent together with the rest of the mixing water was added, and the mixture was mixed for 1 min to ensure the homogeneity and uniformity of it. The mixture was subsequently placed into stainless steel molds and vibrated on a vibration machine for 2 min to achieve a desirable compactness. And after 24 h of curing, the molded mortar specimens were removed from the molds and left to continue curing for 27 d under a temperature of 20°C and a relative humidity of 95% until the testing day. Cubic specimens of 50 × 50 × 50 mm were prepared for the test of compressive strength and prismatic specimens of 40 × 40 × 160 mm were prepared for the tests of flexural strength and load-deflection curve.

2.3. Heating Regimes. High temperatures of 200°C, 400°C, 600°C, 800°C, and 1000°C were selected in this investigation, and these high temperatures were achieved through using an electrically heated furnace which covered a temperature range of 20–1000°C and a constant heating rate of 10°C/min. When the prescribed temperature was reached, the

temperature of the furnace was kept constantly for 1 h so as to ensure the thermal steady state [29]. Thereafter, the specimens were cooled down naturally to room temperature and were subsequently subjected to the associated tests including mass loss test and mechanical tests so as to evaluate their high-temperature resistance capacity.

2.4. Mass Loss. The evaporation of moisture and decomposition of hydration products of cement paste under high temperature will lead to the mass change of cement mortar, which is an important indicator to deteriorations of cement mortar after exposure to high temperature. Therefore, the mass of mortar specimens before and after exposure to various high temperatures was recorded prior to the mechanical property test to calculate the mass loss during the heating process. It should be noted that, before exposure to high temperatures, specimens were put into a drying oven for 24 h at 100°C.

2.5. Mechanical Properties. The compressive strength of cubic specimens before and after exposure to different high temperatures was obtained through operating a hydraulic testing machine according to ASTM C109 [30]. The flexural behavior of prismatic specimens before and after exposure to different high temperatures was also evaluated in accordance with ASTM C348 [31] and ASTM C1609 [32]. Triplicate specimens were tested for each parameter, and the average values were recorded.

In this investigation, the mortar specimen that exhibited the optimal high-temperature resistance based on the results of the mechanical experiments was selected as the optimal specimen for further microstructural analysis, together with the ordinary specimen C0 which contained only OPC as the binder for comparison.

2.6. Pore Size Distribution. There is a general agreement that the mechanical properties of a material are closely related to its microstructure [33]. Therefore, it is an effective method to evaluate the degradations of specimens after being subjected to high temperatures through pore structure analysis. In accordance with ISO 15901-1 [34], mercury intrusion porosimetry (MIP) was employed to assess the porosity and pore size distribution of the ordinary specimen and the optimal specimen before and after exposure to varying high temperatures (e.g., 200°C, 400°C, 600°C, 800°C, and 1000°C).

2.7. SEM Analysis. The microscopic images of the ordinary specimen and the optimal specimen before and after exposure to different high temperatures were also acquired by scanning electron microscopy (SEM) analysis. The specimens should be coated with gold to be conductive prior to the test.

3. Results and Discussion

3.1. Mass Loss. When exposed to various high temperatures, the mass of a substance will be altered due to different

(a)   (b)
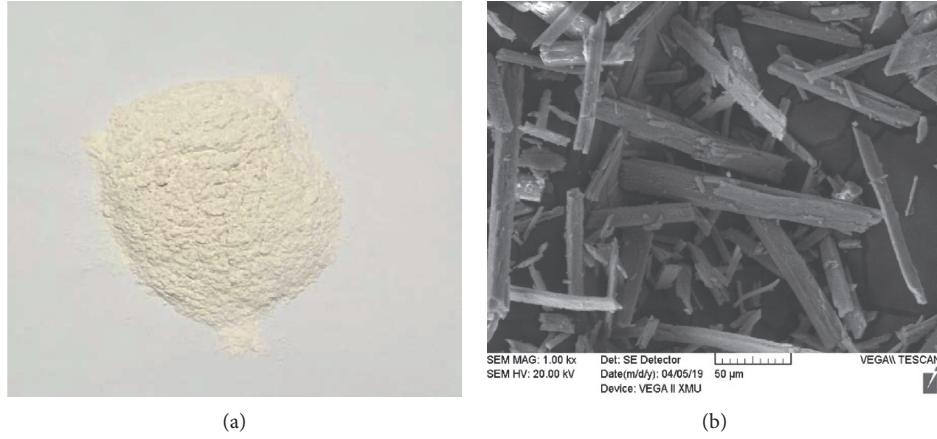
FIGURE 1: (a) Macroscopic and (b) microscopic images of $CaCO_3$ whisker.

TABLE 1: Chemical compositions of raw materials (wt.%).

Oxides	CaO	SiO_2	Al_2O_3	Fe_2O_3	MgO	SO_3	CO_2	Na_2O	K_2O	LOI
Cement	59.42	19.93	4.88	4.31	2.02	2.80	—	1.14	0.82	4.68
Fly ash	4.86	61.43	22.60	5.45	1.04	0.16	—	0.72	1.23	2.51
Whisker	54.93	0.29	0.11	0.07	2.14	0.31	42.07	—	—	—

TABLE 2: Mix proportions of mortars.

Set	Mix proportions	W/b	Cement (kg/m³)	$CaCO_3$ whisker (kg/m³)	Fly ash (kg/m³)	Sand (kg/m³)	Water (kg/m³)	Superplasticizer (L/m³)
	C0 (control)	0.4	500	0	0	1375	200	0.37
	C5	0.4	475	25	0	1375	200	0.43
1	C10	0.4	450	50	0	1375	200	0.47
	C15	0.4	425	75	0	1375	200	0.54
	C20	0.4	400	100	0	1375	200	0.59
	C0F30	0.4	350	0	150	1375	200	0.23
	C5F30	0.4	325	25	150	1375	200	0.25
2	C10F30	0.4	300	50	150	1375	200	0.28
	C15F30	0.4	275	75	150	1375	200	0.31
	C20F30	0.4	250	100	150	1375	200	0.39

Note: C and F represent $CaCO_3$ whisker and fly ash, respectively.

thermal stability of its components. As a result, the mass variation is a direct index of the deterioration of the material after exposure to high temperature. Previous investigations have indicated that the mass loss of the cementitious material after exposure to high temperatures is mainly due to the evaporation of physically bounded water (80–150°C), the dehydration of C-S-H, AFm, and AFt (≤350°C), the decomposition of CH (400–550°C), and the decarbonation of $CaCO_3$ (≥600°C) [35]. The mass loss of $CaCO_3$ whisker-based specimens is presented in Figure 2, and it is discovered that the mass loss for all the specimens regardless of without or with fly ash exhibited an upward trend with the increase in maximum temperature.

With respect to $CaCO_3$ whisker-based mortar specimens, as shown in Figure 2(a), the mass loss increased with the increase in temperature, and for all the specimens, the mass loss reached the maximum at 1000°C. It is interesting to notice that, before 600°C, the mass loss between different

types of specimens after exposure to a specific temperature was not obvious, while between 600 and 1000°C, the mass loss increased with the increase in $CaCO_3$ whisker content. This phenomenon is mainly attributed to the high thermal stable temperature of $CaCO_3$ whisker of about 800°C; therefore, when the temperature is lower than 600°C, the decomposition of $CaCO_3$ whisker will not take place, while when the temperature is in the range of 600–1000°C, the mass loss is mainly due to the decomposition of $CaCO_3$ whisker, and the more the $CaCO_3$ whisker, the higher the mass loss.

Regarding $CaCO_3$ whisker-based fly ash specimens, as shown in Figure 2(b), the mass loss of them was slightly higher than that of corresponding specimens without fly ash, regardless of the variation in high temperatures. One possible reason may be that the moderate incorporation of fly ash into the cement mortar can improve the water-retaining property of cement mortar [36]. However, the mass loss of

(a)

(b)
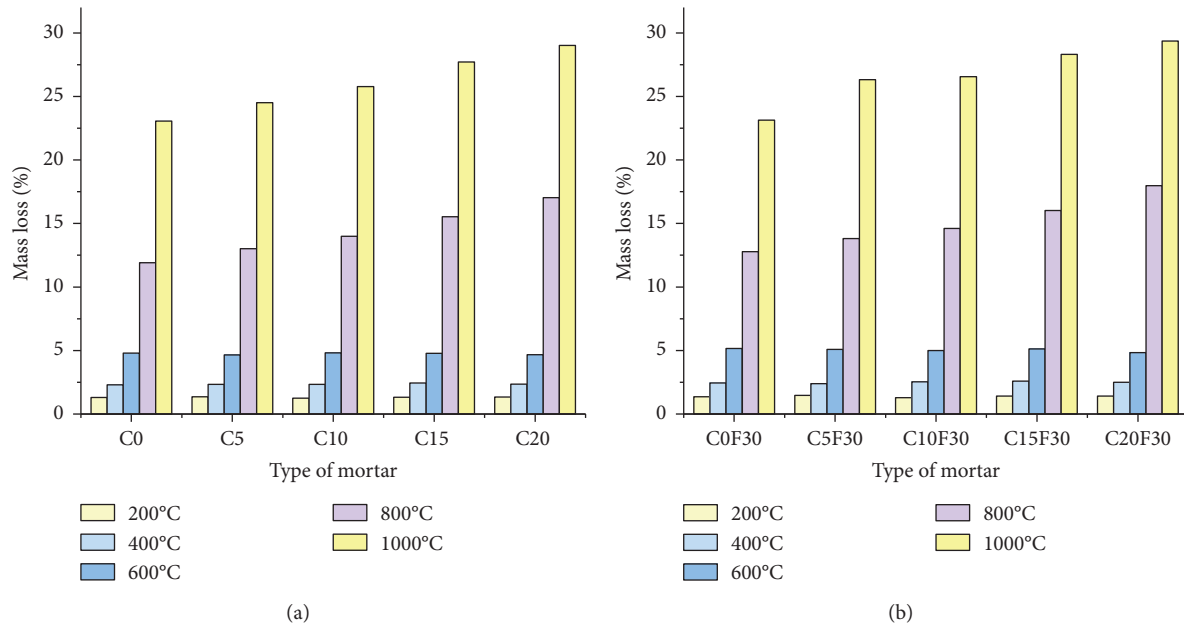
FIGURE 2: Mass loss of (a) $CaCO_3$ whisker-based specimens and (b) $CaCO_3$ whisker-based fly ash specimens after exposure to various temperatures.

specimens after being subjected to high temperature is mainly due to the evaporation of moisture; as a result, the presence of fly ash could lead to an increase in mass loss.

In general, exposure to high temperature will lead to the moisture loss of the mortar specimen which is mainly due to the evaporation of bound water and the dehydration of hydration products, and the mass loss increased with the increase in temperature. In addition, a larger $CaCO_3$ whisker content could lead to a higher mass loss when the temperature was between 600 and 1000°C.

3.2. Mechanical Properties. After measuring the mass of $CaCO_3$ whisker-based specimens before and after exposure to high temperatures, the mechanical properties of those specimens were immediately evaluated. The compressive strength and flexural strength of $CaCO_3$ whisker-based specimens are displayed in Figures 3 and 4, respectively. It is noticed that, although different temperatures had different effects on the mechanical strength of mortar specimens, the maximum strength was achieved when the temperature reached to 400°C for all the specimens.

Before exposure to high temperatures, both the compressive strength and flexural strength of $CaCO_3$ whisker-based specimen were improved rapidly with the increase in $CaCO_3$ whisker content until this content was up to 10 wt.%; thereafter, the strength enhancement was negatively correlated with the increase in $CaCO_3$ whisker content, as shown in Figures 3(a) and 4(a). The reason why the strength decreased when the $CaCO_3$ whisker content was over 10 wt.% may be related to the aggregation of $CaCO_3$ whisker, which leads to the generation of a heterogeneous microstructure, thereby lowering the overall strength of $CaCO_3$ whisker-based specimen [13]. In addition, the increase in $CaCO_3$ whisker content may result in a relatively weak bond

between cement paste and $CaCO_3$ whisker, and thus reducing the strength of $CaCO_3$ whisker-based specimen. Numerous studies have demonstrated that there is a critical fiber content for whisker-reinforced composites and a higher content of whisker leads to a lower strength [14–16]. Similar trend was observed in the strength of the $CaCO_3$ whisker-based fly ash specimen. However, a slight reduction was found in the strength of $CaCO_3$ whisker-based specimen when 30 wt.% fly ash was used as partial replacement of cement, as shown in Figures 3(b) and 4(b). Take C0 and C0F30 for example, with the incorporation of fly ash, the 28d strength of C0 decreased by 3.9% and 4.6% for compressive strength and flexural strength, respectively. This is because that the reduction in cement content will result in less production of hydration products, such as C-S-H which is the most important contributor to the strength of cement paste. Besides, the pozzolanic reaction of fly ash is a slow process which is only beneficial to the long-term strength development of cement paste; as a consequence, the 28 d strength of $CaCO_3$ whisker-based specimens exhibited a slight decline with the incorporation of fly ash [37].

After exposure to 200°C, the compressive strength of $CaCO_3$ whisker-based specimen was approximately the same with the strength at 20°C, while for $CaCO_3$ whisker-based fly ash specimen, the compressive strength showed a slight increase. Furthermore, an evident improvement was observed in the compressive strength of all the specimens when exposed to 400°C, and C10F30 had the highest compressive strength at 400°C, with the strength increased by 23.8% compared with the unheated C10F30. Relatively lower improvements were found in the compressive strength of C0 and C10 at 400°C, which were 16.2% and 18.4%, respectively, indicating that the presence of fly ash had a positive effect on the compressive strength of $CaCO_3$ whisker-based specimens. The improvement in strength is
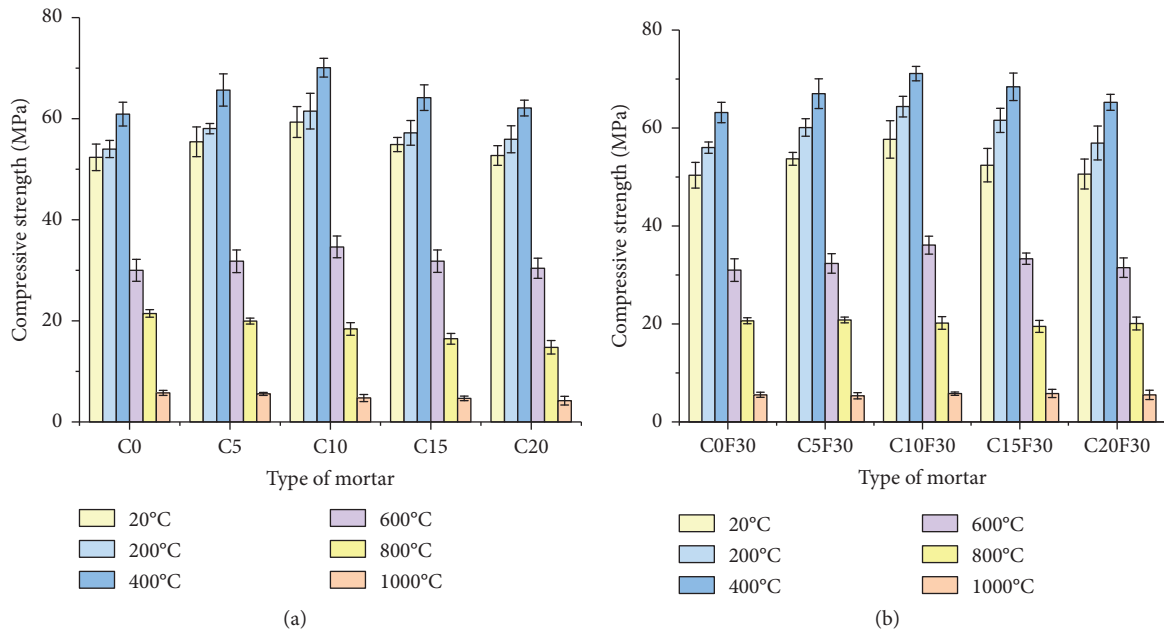
FIGURE 3: Compressive strength of (a) CaCO$_3$ whisker-based specimens and (b) CaCO$_3$ whisker-based fly ash specimens before and after exposure to various temperatures.
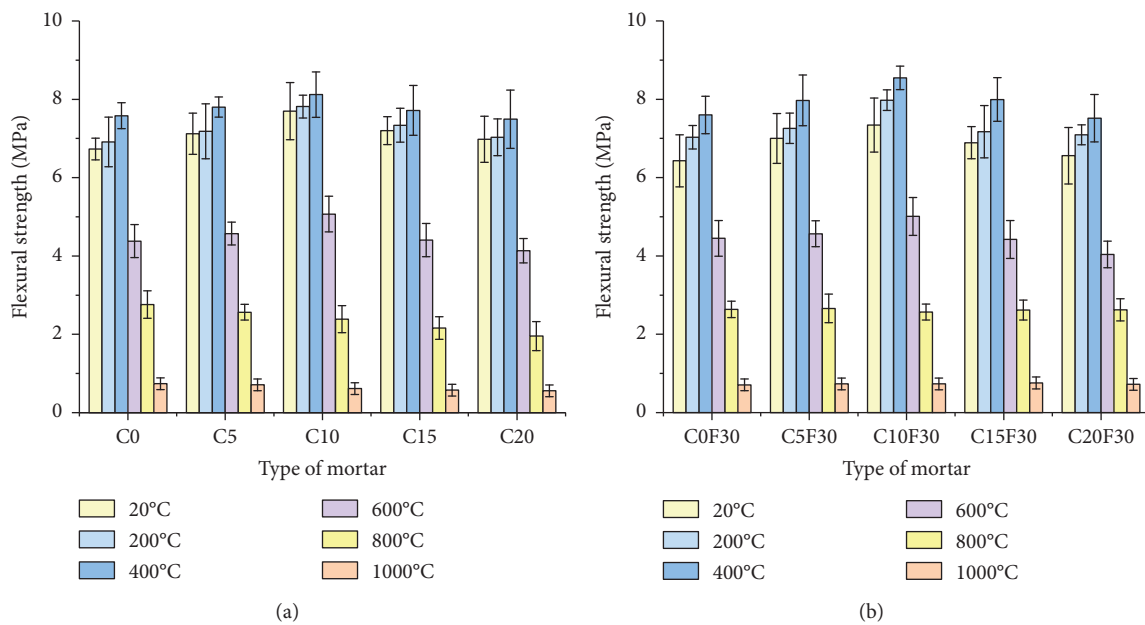
FIGURE 4: Flexural strength of (a) CaCO$_3$ whisker-based specimens and (b) CaCO$_3$ whisker-based fly ash specimens before and after exposure to various temperatures.

likely due to the acceleration in cement hydration at high temperatures. Cement hydration process will proceed at a higher speed with the increase in temperature, and meanwhile, high temperature will promote more generation of high-density C-S-H which has excellent high-temperature resistance [38]. In addition, the pozzolanic reaction of fly ash will be speeded up as well, leading to the rehydration of dissociated CH and the formation of additional C-S-H [39]. With regards to the flexural strength, the enhancement was

not obvious, and the flexural strength of C10F30 at 400°C increased by 15.9% compared with that of the unheated C10F30. The reason may lie in the fact that the loss of moisture increases the porosity of the mortar specimen and then cause the generation of microcracks which has an undesirable impact on the flexural strength of the specimen, while the bridge connection effect of CaCO$_3$ whisker between microcracks partially offsets the negative effect brought about by high temperature exposure [8, 9].

When the temperature further increased to 600°C, both the compressive strength and flexural strength of $CaCO_3$ whisker-based specimens showed a remarkable decrease, and the reason may be that the combined effect of moisture loss and decomposition of CH increases the porosity of the specimen and makes the microstructure of the specimen coarser and at the same time, weakens the bond between whiskers and cement paste; therefore, the strength of $CaCO_3$ whisker-based specimens declined accordingly. It is worth noting that, although both the compressive strength and flexural strength of all the $CaCO_3$ whisker-based specimens reduced significantly at 600°C, the strength of fly ash specimens still had comparative advantage in high-temperature resistance, which indicated that fly ash could improve the high-temperature resistance of $CaCO_3$ whisker-based specimens.

Exposure to 800°C led to a sharp decrease in both compressive strength and flexural strength of specimens, which is mainly due to the decomposition of $CaCO_3$ and CSH at about 800°C [37]. Therefore, the reduction in strength was more severe when more $CaCO_3$ whisker was contained in the specimen, since the decomposition of $CaCO_3$ whisker results in an even looser microstructure of the specimen. However, specimens with fly ash still had a higher strength than those without fly ash. Similarly, the strength of the specimen continued to degrade when the temperature increased to 1000°C, leading to a further deterioration in strength.

To sum up, the incorporation of $CaCO_3$ whisker could improve both compressive strength and flexural strength of mortar specimens when the temperature was less than 600°C, and the optimal dosage of it was 10 wt.%. At 800°C and 1000°C, the strength of specimens rapidly decreased with the increase in $CaCO_3$ whisker content; therefore, the specimens with $CaCO_3$ whisker exhibited lower strength than C0. The presence of fly ash enhanced the high-temperature performance of $CaCO_3$ whisker-based specimens before 600°C and limited the loss of strength after 600°C. According to the results, the ordinary mortar (C0) and the mortar containing 10 wt.% $CaCO_3$ whisker and 30 wt.% fly ash (C10F30) were selected to perform the load-deflection test and the microscopic tests to explore the mechanism behind.

3.3. Load-Deflection Curve. Load-deflection curves of the ordinary mortar and the mortar containing 10 wt.% $CaCO_3$ whisker and 30 wt.% fly ash before and after exposure to different high temperatures were measured through the three-point bending test, and the results are presented in Figure 5. There are three stages in the load-deflection curve, including linear stage, nonlinear stage, and a softening stage. In the linear stage, the load increases with the increase in the deflection, representing that cracks do not extend, while in the nonlinear stage, cracks begin to propagate, and in the softening stage, the load decreases with the increase in the deflection, representing that cracks expand rapidly [40].

It is examined that the maximum load of both C0 and C10F30 increased with the increase in temperature until a maximal value was reached at 400°C, while the maximum load of the two specimens dropped rapidly after being exposed to 600–1000°C. Although the maximum load of the two specimens decreased at 600°C, the maximum load of C10F30 was still higher than that of C0, which is mainly due to the fact that $CaCO_3$ whisker can not only reinforce the specimen but also bridge microcracks in the specimen. Besides, the slope of the load-deflection curve of C10F30 in the linear stage before 600°C was a little bigger than that of C0, indicating that the flexural stiffness of C10F30 was higher than that of C0. Meanwhile, it is also worthy to note that the maximum deflection of C10F30 was a little larger than that of C0 before 600°C, demonstrating that the addition of $CaCO_3$ whisker and fly ash could improve the deformability and toughness of the specimen. This may be attributed to the fact that $CaCO_3$ whisker itself has high tensile strength, and the incorporation of $CaCO_3$ whisker can improve the flexural behavior of the specimen. Nevertheless, the improvement in flexural toughness was not remarkable, which can be attributed to the tiny size of whiskers, and this may be the reason to encourage the combined use of $CaCO_3$ whiskers with other large-sized fibers, so as to improve the multiscale cracking resistance of cementitious materials.

The significant decline in the maximum load of C10F30 and C0 at 800°C pointed out that the decomposition of $CaCO_3$ and CSH at this temperature range had a negative effect on the strength of specimens, and microstructural analysis will make an explanation about the change in mechanical performance. With regards to the slope of the load-deflection curve in the linear stage at 800°C, it can be examined that the slope of C10F30 was almost the same with that of C0, suggesting that the two specimens had the same flexural stiffness after exposure to 800°C. The reason may be that the addition of fly ash can enable the generation of high-density CSH which is high-temperature resistant since the decomposition of $CaCO_3$ takes place at this temperature. Similarly, the flexural stiffness of the two specimens at 1000°C experienced a further decline.

3.4. Pore Size Distribution. The pore size distribution of the ordinary mortar and the mortar containing 10 wt.% $CaCO_3$ whisker and 30 wt.% fly ash before and after exposure to different high temperatures were obtained through utilizing MIP method, as presented in Figure 6. It is found from the results that, before exposure to high temperatures, the porosity of C10F30 showed a slight increase in comparison with C0. This may be linked to the fact that the addition of $CaCO_3$ whisker may result in some additional pores in the interface between mortar matrix and whiskers, thereby leading to an increase in the porosity. In addition, the anhydrous fly ash may also cause an increase in porosity. It is worthy to note that, compared with C0, the volume of harmless pore (<20 nm) and few-harm pore (20–50 nm) in C10F30 was higher, and meanwhile, the volume of harmful pore (50–200 nm) was lower, which may be the reason why C10F30 with a larger porosity had higher mechanical
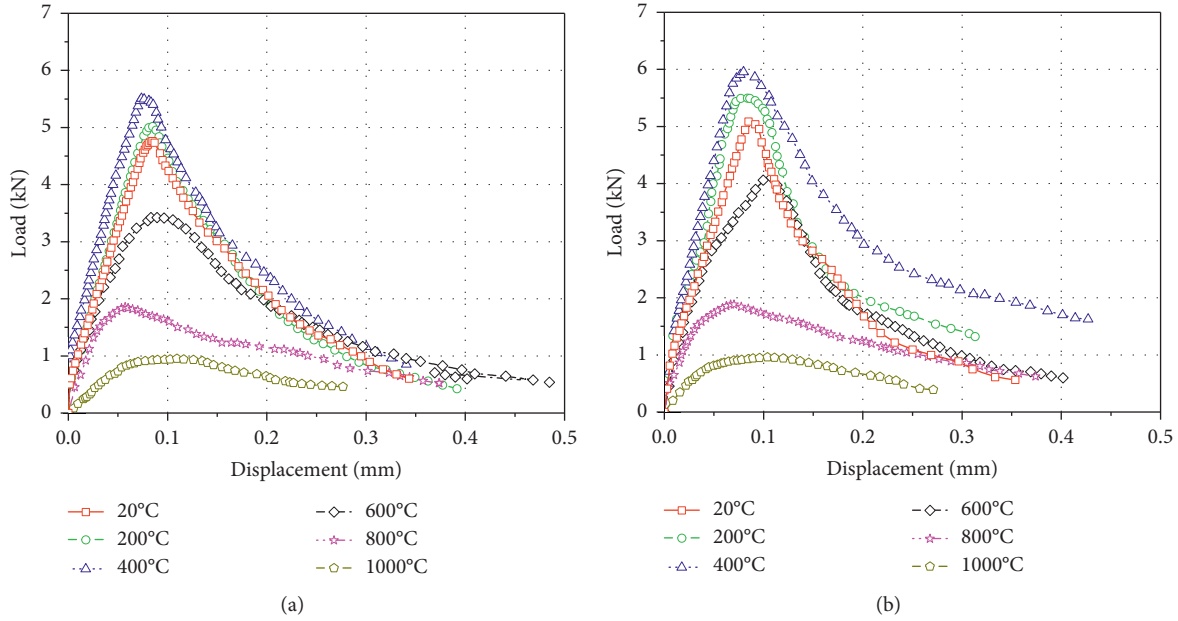
FIGURE 5: Load-deflection curves of (a) C0 and (b) C10F30 before and after exposure to various temperatures.
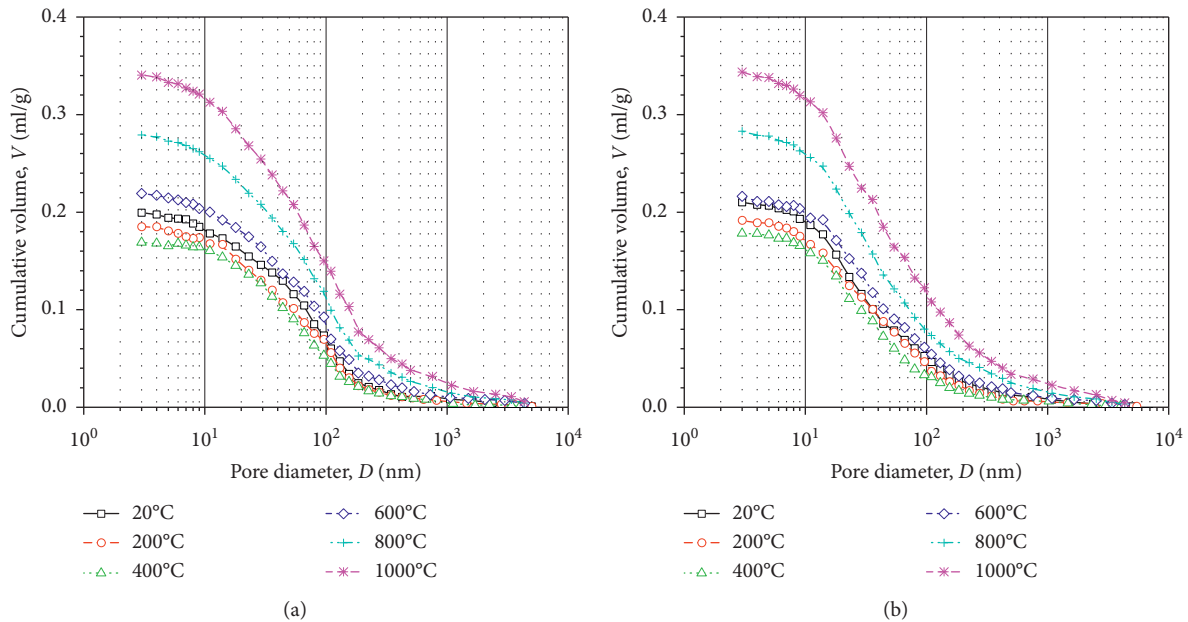
FIGURE 6: Pore size distribution of (a) C0 and (b) C10F30 before and after exposure to various temperatures.

strength compared with C0, for the incorporation of $CaCO_3$ whisker and fly ash refined pore distribution in the specimen.

When exposed to 200°C, C0 kept approximately the same porosity compared with the specimen unheated, while the porosity of C10F30 experienced a slight reduction. This phenomenon can be attributed to the fact that the increase in temperature had a positive influence on the rehydration of cement, and the pozzolanic reaction of fly ash was also stimulated by the high temperature, which

enables CH to react with the main components of fly ash, such as SiO_2 and Al_2O_3, to form C-S-H and C-A-H. Therefore, the overall porosity of the specimens showed a decrease.

Similarly, the porosity of both C0 and C10F30 showed a further reduction after exposure to 400°C. High temperature may induce the generation of a large number of microcracks due to different thermal expansion coefficients of hydration products, while the presence of microfibrous $CaCO_3$ whisker may bridge these cracks, thus refining the pore size

(a)

(b)

(c)

(d)

(e)

(f)
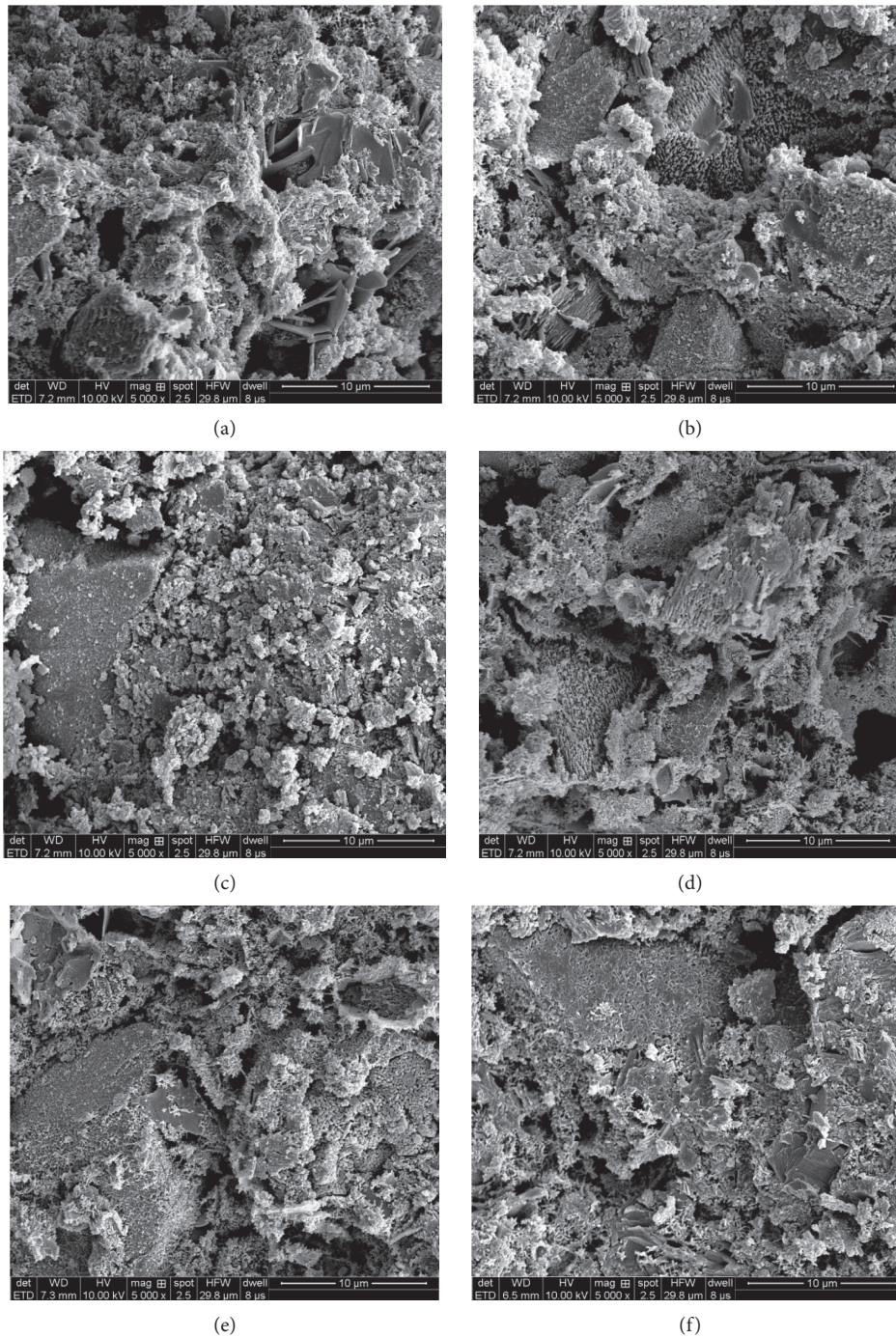
FIGURE 7: Microscopic images of C0 before and after exposure to different temperatures: (a) 20°C, (b) 200°C, (c) 400°C, (d) 600°C, (e) 800°C, and (f) 1000°C.

distribution and enhance the toughness of the specimen. Furthermore, the filler effect of $CaCO_3$ whisker can also densify the microstructure of the mortar due to the good compatibility between them. This may be the reason why C10F30 exhibited a superior high-temperature resistance in terms of mechanical strength compared with C0, since the mechanical strength of the specimen is closely linked with its porosity and pore size distribution.

The overall porosity of both C0 and C10F30 increased after being subjected to 600°C, with the reduction in volume of harmless pores and the increase in volume of harmful pores. The decomposition of CH, together with loss of moisture in this temperature range, increased the porosity of the two specimens, and the reason why C10F30 still maintain the superior mechanical strength compared with C0 is most likely due to the combined effect of $CaCO_3$

(a)

(b)

(c)

(d)

(e)

(f)
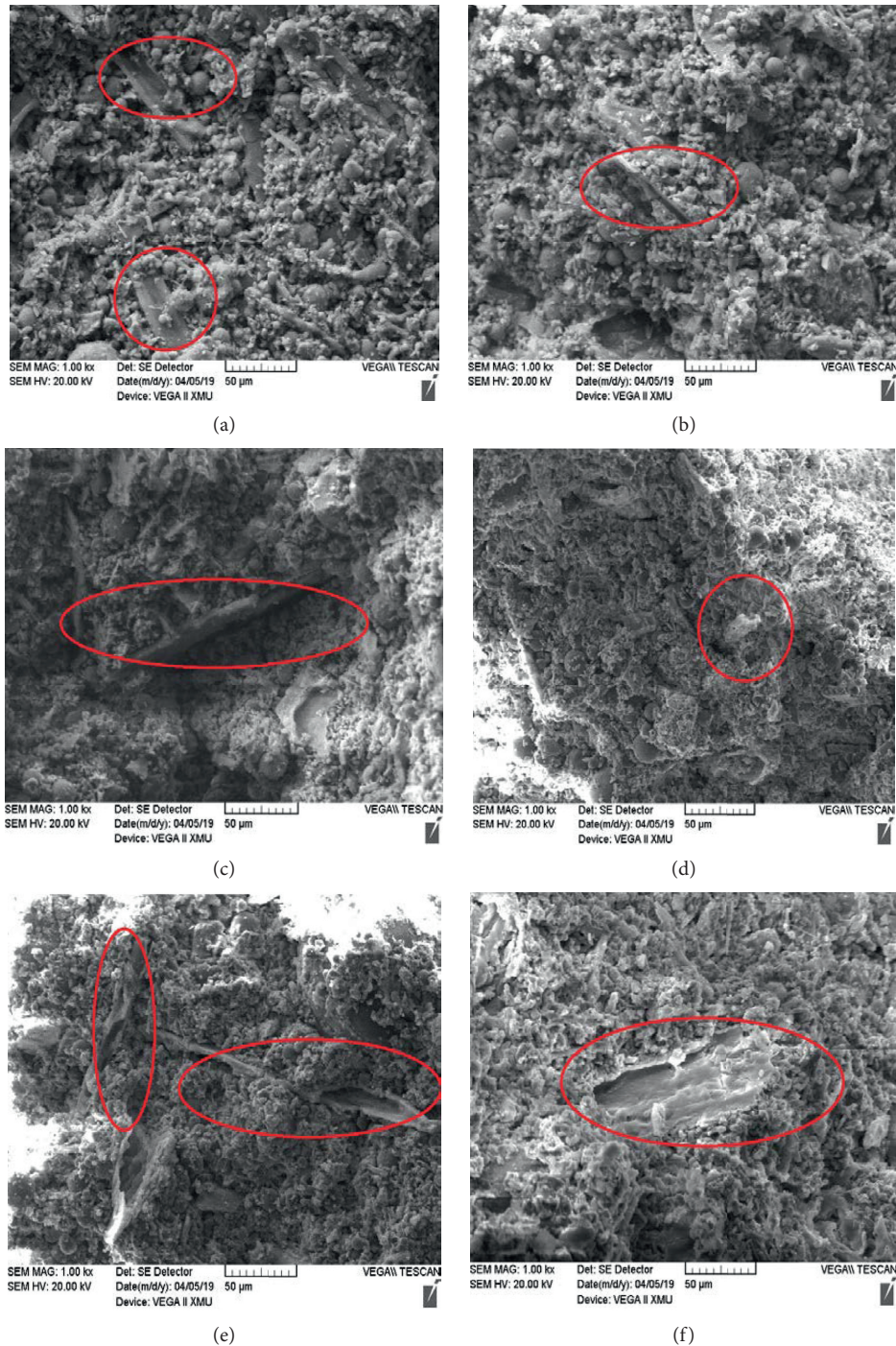
FIGURE 8: Microscopic images of C10F30 before and after exposure to different temperatures ($CaCO_3$ whiskers are marked in the red circle): (a) 20°C, (b) 200°C, (c) 400°C, (d) 600°C, (e) 800°C, and (f) 1000°C.

whisker to bridge the microcracks and fly ash to proceed the pozzolanic reaction with CH and free lime [41].

The porosity of C10F30 and C0 increased dramatically after exposure to 800°C and 1000°C, because more hydration products, such as $CaCO_3$ and CSH, will be disintegrated, resulting in a much coarser microstructure of the specimen. Meanwhile, although $CaCO_3$ whisker decomposed in this temperature range, the porosity of C10F30 was almost equal

to C0, the reason may be that fly ash enables the generation of thermostable hydration products [41].

3.5. SEM Analysis. Microscopic images of the ordinary mortar and the mortar containing 10 wt.% $CaCO_3$ whisker and 30 wt.% fly ash before and after exposure to different high temperatures are presented in Figures 7 and 8. The scale

for Figure 7 is $10 \mu m$, while Figure 8 has a scale of $50 \mu m$ in order to examine the behavior of $CaCO_3$ whisker better.

The microstructural images of C0 before and after exposure to high temperatures of 200°C, 400°C, 600°C, 800°C, and 1000°C are shown in Figure 7. As seen in Figure 7(a), hydration products such as CH and C-S-H were distributed in C0, and the microstructure of C0 was not very dense. However, after exposure to 200°C, more C-S-H was generated due to the further hydration of cement, and the similar trend was discovered in Figure 7(c) when C0 was heated to 400°C. After exposure to 600°C, the microstructure of C0 became coarser, and microcracks were found in the specimen. The even looser microstructures after 800°C and 1000°C in Figures 7(e) and 7(f) represented the deterioration of the specimen under high temperature, which was in agreement with the results of mechanical strength tests and porosity test.

Figure 8 shows microstructural images of C10F30 before and after exposure to high temperatures of 200°C, 400°C, 600°C, 800°C, and 1000°C. It can be seen from Figure 8(a) that spherical fly ash particles and $CaCO_3$ whiskers were uniformly distributed in the specimen, demonstrating that the pozzolanic reaction of fly ash is a slow process, and there is still much unreacted fly ash at 28 d of curing. When C10F30 was subjected to high temperature of 200°C, the microstructure of the specimen became denser which was proved by the improvement in mechanical strength. The morphology of C10F30 after exposure to 400°C indicated that the further reaction of fly ash made the microstructure of C10F30 become even more compact, with fewer unreacted fly ash particles left in the specimen. Besides, microcracks were observed in the specimen and the presence of $CaCO_3$ whiskers restrained the propagation of these microcracks, as shown in Figure 8(c). Therefore, the strength of C10F30 after being subjected to 400°C was higher with the incorporation of $CaCO_3$ whisker and fly ash. After exposure to 600°C, C10F30 exhibited a porous and coarse microstructure due to the decomposition of CH and further moisture loss, while the $CaCO_3$ whisker pullout, as presented in Figure 8(d), demonstrated the reinforcing effect of $CaCO_3$ whisker on the mechanical properties of the specimen. With the increasing temperature to 800°C, $CaCO_3$ whisker was almost disintegrated, as shown in Figure 8(e), with the thin shell of whiskers left in the specimen. And at 1000°C, $CaCO_3$ whiskers were totally disintegrated, and the changes in microstructures agreed with the variations in mechanical strength. It can also be found that C10F30 had a relatively compact microstructure than C0 when the temperature exceeded 600°C.

4. Conclusion

The objective of the current study is to investigate the combined effect of $CaCO_3$ whisker and fly ash on cement mortars before and after exposure to varying high temperatures and evaluate the high-temperature resistance of different types of mortars. Conclusions drawn from the experimental results were listed as follows:

(1) High-temperature exposure caused the increase in mass loss for all the $CaCO_3$ whisker-based mortars, regardless of without or with fly ash, and the mass loss increased with the increase in maximum temperature. $CaCO_3$ whisker-based fly ash mortars exhibited a slight increase in mass loss in comparison with their corresponding mortars without fly ash.

(2) Before exposure to high temperatures, the mechanical strength of $CaCO_3$ whisker-based mortars was enhanced with the increasing dosage of $CaCO_3$ whisker, while the mechanical strength showed a downward trend when the $CaCO_3$ whisker content was more than 10 wt.%. The incorporation of fly ash led to a slight decrease in mechanical strength of mortars.

(3) With respect to $CaCO_3$ whisker-based specimens, they reached their maximum strength after exposure to 400°C, while the strength of them decreased notably when exposed to 600°C. At 800°C and 1000°C, the strength of these specimens exhibited a further decrease, and due to the decomposition of $CaCO_3$ whisker, specimens with more $CaCO_3$ whisker had the lower strength.

(4) With respect to $CaCO_3$ whisker-based fly ash specimens, in spite of a slight decrease in the strength at 20°C, the strength of them at 200°C and 400°C was even higher than that of corresponding specimens without fly ash. And after exposure to 600°C, the residual strength was still higher, indicating that the high-temperature resistance of $CaCO_3$ whisker-based mortar was improved due to the presence of fly ash. Although the decomposition of $CaCO_3$ whisker took place at 800°C and 1000°C, the strength of fly ash specimens was almost the same with C0.

(5) Compared with C0, C10F30 exhibited superior mechanical properties after exposure to different temperatures.

(6) With the incorporation of $CaCO_3$ whisker and fly ash, the flexural stiffness and flexural toughness of the specimen were improved before 600°C.

(7) Although the total porosity of C10F30 at 20°C increased, the overall pore distribution was refined compared with C0. There was an evident decline in pore volume of mortars when exposed to 400°C, but exposure to temperatures higher than 600°C resulted in a significant increase in pore volume.

(8) Microscopic images showed that the filler effect and crack-bridging effect of $CaCO_3$ whisker, together with the acceleration in pozzolanic reaction of fly ash at high temperatures, made C10F30 possess preferable high-temperature resistance capacity, which could be reflected in the results of mechanical tests.

Data Availability

The data used to support the findings of this study are available from the corresponding author upon request.

Conflicts of Interest

The authors declare that they have no conflicts of interest.

Acknowledgments

References

[1] H. Tanyildizi and A. Coskun, "The effect of high temperature on compressive strength and splitting tensile strength of structural lightweight concrete containing fly ash," *Construction and Building Materials*, vol. 22, no. 11, pp. 2269–2275, 2008.

[2] O. Düğenci, T. Haktanir, and F. Altun, "Experimental research for the effect of high temperature on the mechanical properties of steel fiber-reinforced concrete," *Construction and Building Materials*, vol. 75, pp. 82–88, 2015.

[3] H. Tanyildizi and Y. Yonar, "Mechanical properties of geopolymer concrete containing polyvinyl alcohol fiber exposed to high temperature," *Construction and Building Materials*, vol. 126, pp. 381–387, 2016.

[4] M. Rangelov, S. Nassiri, L. Haselbach, and K. Englund, "Using carbon fiber composites for reinforcing pervious concrete," *Construction and Building Materials*, vol. 126, pp. 875–885, 2016.

[5] S. Nasir, M. Ayoub, S. Zafar et al., "Experimental study on comparison of strength properties of natural waste fiber (Coir and Jute) reinforced concrete," *Journal of Applied and Emerging Sciences*, vol. 7, pp. 105–110, 2018.

[6] Y. Wang, X. Cao, L. Zhang et al., "Effects of cellulose whiskers on properties of soy protein thermoplastics," *Macromolecular Bioscience*, vol. 6, no. 7, pp. 524–531, 2006.

[7] J. Bras, M. L. Hassan, C. Bruzesse, E. A. Hassan, N. A. El-Wakil, and A. Dufresne, "Mechanical, barrier, and biodegradability properties of bagasse cellulose whiskers reinforced natural rubber nanocomposites," *Industrial Crops and Products*, vol. 32, no. 3, pp. 627–633, 2010.

[8] M. Cao, X. Ming, H. Yin, and L. Li, "Influence of high temperature on strength, ultrasonic velocity and mass loss of calcium carbonate whisker reinforced cement paste," *Composites Part B: Engineering*, vol. 163, pp. 438–446, 2019.

[9] M. Cao, L. Li, H. Yin, and X. Ming, "Microstructure and strength of calcium carbonate ($CaCO_3$) whisker reinforced cement paste after exposed to high temperatures," *Fire Technology*, 2019.

[10] M. Cao, C. Zhang, H. Lv, and L. Xu, "Characterization of mechanical behavior and mechanism of calcium carbonate whisker-reinforced cement mortar," *Construction and Building Materials*, vol. 66, pp. 89–97, 2014.

[11] M. Cao, L. Xu, C. Zhang et al., "Rheology, fiber distribution and mechanical properties of calcium carbonate ($CaCO_3$) whisker reinforced cement mortar," *Composites Part A: Applied Science and Manufacturing*, vol. 90, pp. 662–669, 2016.

[12] Y. Yang, S. Fu, X. Li et al., "Mechanical attributes of uniaxial compression for calcium carbonate whisker reinforced oil well cement pastes," *Advances in Materials Science and Engineering*, vol. 2017, Article ID 2939057, 13 pages, 2017.

[13] X. Cheng, Q. Dong, Z. Li et al., "High-temperature mechanical properties of $CaSO_4$ whiskers reinforced high alumina cement," *Magazine of Concrete Research*, vol. 70, pp. 1–13, 2018.

[14] M. Li, S. Deng, Y. Yu, J. Jin, Y. Yang, and X. Guo, "Mechanical properties and microstructure of oil well cement stone enhanced with Tetra-needle like ZnO whiskers," *Construction and Building Materials*, vol. 135, pp. 59–67, 2017.

[15] M. Li, M. He, Y. Yu, S. Deng, and X. Guo, "Mechanical properties and microstructure of oil-well cement stone enhanced with submicron SiC whiskers," *Journal of Adhesion Science and Technology*, vol. 33, no. 1, pp. 50–65, 2019.

[16] X. Cheng, Q. Dong, Z. Li, X. Guo, and W. Duan, "Influence of potassium titanate whisker on the mechanical properties and microstructure of calcium aluminate cement for in situ combustion," *Journal of Adhesion Science and Technology*, vol. 32, no. 4, pp. 343–358, 2018.

[17] M. Li, Y. Yang, M. Liu, X. Guo, and S. Zhou, "Hybrid effect of calcium carbonate whisker and carbon fiber on the mechanical properties and microstructure of oil well cement," *Construction and Building Materials*, vol. 93, pp. 995–1002, 2015.

[18] M. Li, M. Liu, Y. Yang, Z. Li, and X. Guo, "Mechanical properties of oil well cement stone reinforced with hybrid fiber of calcium carbonate whisker and carbon fiber," *Petroleum Exploration and Development*, vol. 42, no. 1, pp. 104–111, 2015.

[19] M. Cao, C. Zhang, Y. Li et al., "Using calcium carbonate whisker in hybrid fiber-reinforced cementitious composites," *Journal of Materials in Civil Engineering*, vol. 27, no. 4, article 04014139, 2014.

[20] M. Cao, L. Xu, and C. Zhang, "Rheological and mechanical properties of hybrid fiber reinforced cement mortar," *Construction and Building Materials*, vol. 171, pp. 736–742, 2018.

[21] Y. Yang and Y. Deng, "Mechanical properties of hybrid short fibers reinforced oil well cement by polyester fiber and calcium carbonate whisker," *Construction and Building Materials*, vol. 182, pp. 258–272, 2018.

[22] M. S. Imbabi, C. Carrigan, and S. McKenna, "Trends and developments in green cement and concrete technology," *International Journal of Sustainable Built Environment*, vol. 1, no. 2, pp. 194–216, 2012.

[23] E. Benhelal, G. Zahedi, E. Shamsaei, and A. Bahadori, "Global strategies and potentials to curb CO_2 emissions in cement industry," *Journal of Cleaner Production*, vol. 51, pp. 142–161, 2013.

[24] R. K. Ibrahim, R. Hamid, and M. R. Taha, "Fire resistance of high-volume fly ash mortars with nanosilica addition," *Construction and Building Materials*, vol. 36, pp. 779–786, 2012.

[25] S. Soleimanzadeh and M. M. A. Othuman, "Influence of high temperatures on flexural strength of foamed concrete containing fly ash and polypropylene fiber," *International Journal of Engineering*, vol. 26, no. 2, pp. 117–126, 2013.

[26] ASTM (American Society for Testing and Materials), "C150: standard specification for Portland cement," in *Annual Book of ASTM*, ASTM, West Conshohocken, PA, USA, 2001.

[27] ASTM (American Society for Testing and Materials), *C618: Standard Specification for Coal Fly Ash and Raw or Calcined Natural Pozzolan for Use in Concrete*, ASTM, West Conshohocken, PA, USA, 2012.

[28] ASTM (American Society for Testing and Materials), *C494: TYPE F: Standard Specification for Chemical Admixtures for Concrete*, ASTM, West Conshohocken, PA, USA, 2001.

[29] S. Donatello, C. Kuenzel, A. Palomo, and A. Fernández-Jiménez, "High temperature resistance of a very high volume

fly ash cement paste," *Cement and Concrete Composites*, vol. 45, pp. 234–242, 2014.

[30] ASTM (American Society for Testing and Materials), *C109/C109M-16a: Standard Test Method for Compressive Strength of Hydraulic Cement Mortars (Using 2-in. or [50-mm] Cube Specimens)*, ASTM, West Conshohocken, PA, USA, 2016.

[31] ASTM (American Society for Testing and Materials), *C348–18: Standard Test Method for Flexural Strength of Hydraulic-Cement Mortars*, ASTM, West Conshohocken, PA, USA, 2018.

[32] ASTM (American Society for Testing and Materials), *C1609/C1609M-12: Standard Test Method for Flexural Performance of Fiber-Reinforced Concrete (Using Beam with Third-Point Loading)*, ASTM, West Conshohocken, PA, USA, 2012.

[33] M.-H. Zhang and H. Li, "Pore structure and chloride permeability of concrete containing nano-particles for pavement," *Construction and Building Materials*, vol. 25, no. 2, pp. 608–616, 2011.

[34] BS ISO, *Pore Size Distribution and Porosity of Solid Materials by Mercury Porosimetry and Gas Adsorption*, BS ISO, 15901-1, London, UK, 2005.

[35] S. Bahafid, S. Ghabezloo, M. Duc, P. Faure, and J. Sulem, "Effect of the hydration temperature on the microstructure of Class G cement: C-S-H composition and density," *Cement and Concrete Research*, vol. 95, pp. 270–281, 2017.

[36] N. Khurram, K. Khan, M. U. Saleem, M. N. Amin, and U. Akmal, "Effect of elevated temperatures on mortar with naturally occurring volcanic ash and its blend with electric arc furnace slag," *Advances in Materials Science and Engineering*, vol. 2018, Article ID 5324036, 11 pages, 2018.

[37] A. M. Rashad, "An exploratory study on high-volume fly ash concrete incorporating silica fume subjected to thermal loads," *Journal of Cleaner Production*, vol. 87, pp. 735–744, 2015.

[38] M. J. DeJong and F.-J. Ulm, "The nanogranular behavior of C-S-H at elevated temperatures (up to 700°C)," *Cement and Concrete Research*, vol. 37, no. 1, pp. 1–12, 2007.

[39] M. H. Beigi, J. Berenjian, O. Lotfi Omran, A. Sadeghi Nik, and I. M. Nikbin, "An experimental survey on combined effects of fibers and nanosilica on the mechanical, rheological, and durability properties of self-compacting concrete," *Materials & Design*, vol. 50, pp. 1019–1029, 2013.

[40] S. Djaknoun, E. Ouedraogo, and A. Ahmed Benyahia, "Characterisation of the behaviour of high performance mortar subjected to high temperatures," *Construction and Building Materials*, vol. 28, no. 1, pp. 176–186, 2012.

[41] O. Karahan, "Transport properties of high volume fly ash or slag concrete exposed to high temperature," *Construction and Building Materials*, vol. 152, pp. 898–906, 2017.

Research Article

Mechanical Properties of Polypropylene Macrofiber-Reinforced Concrete

Zhishu Yao [iD],[1] **Xiang Li** [iD],[1] **Cao Fu,**[1] **and Weipei Xue** [iD][1,2,3]

[1]*School of Civil Engineering and Architecture, Anhui University of Science and Technology, Huainan 232001, China*
[2]*Post-doctoral Research Station of Safety Science and Engineering, Anhui University of Science and Technology, Huainan 232001, China*
[3]*Safety Science and Engineering Postdoctoral Research Workstation, China Coal Mine Construction Group Co. Ltd., Hefei 230000, China*

Correspondence should be addressed to Xiang Li; lixiang6897@126.com

To economically and reasonably solve the difficult problem of mine shaft support subject to complex geological conditions, we studied the mechanical properties of polypropylene macrofiber-reinforced concrete (PPMFRC). First, we selected test raw materials through an investigation and comparison of technical parameters. Second, using a preparation test, we obtained the composition of reference concrete of PPMFRC for the mine shaft lining structure, and test specimens were manufactured according to relevant test technical regulations. Finally, the mechanical properties of the specimens were compared, and the results show that the compressive, flexural, and tensile strengths of PPMFRC were increased by approximately 3%, 30%, and 20%, respectively, for mixtures with polypropylene macrofibers. The fracture toughness of PPMFRC was between 0.26 and 0.35, and the fracture energy was between 382.7 N/m and 485.6 N/m, which is significantly higher than that of plain concrete. The test results show that PPMFRC is an ideal material for the lining structure of a mine shaft under complex geological conditions, and we have provided technical parameters for engineering applications.

1. Introduction

To exploit deep underground mineral resources, vertical shafts must be constructed in the stratum to transport minerals, personnel, materials, equipment, ventilation, etc. A wellbore maintains stability because of a shaft lining structure close to its inner wall. In the past, plain concrete was primarily used for the lining. However, with the increase of mining depth, the engineering geological and hydrological conditions of the strata through which the wellbore passed became more complex. Meanwhile, the concrete used in the shaft lining was subjected to compressive stress, tensile stress, etc. Hence, the concrete cracked easily. Further, when subjected to underground pressure water, the cracks caused fracture and expansion, which seriously affected the safe use of the shaft. Thus, concrete for deep shaft lining required not only high compressive strength, but also high tensile strength, flexural strength, crack resistance, and permeability resistance. A few

scholars developed shaft lining structures made of steel fiber and steel skeleton-reinforced concrete, and these new types of reinforced concrete were successfully applied to engineering practices [1–4]. Nevertheless, through engineering applications, they were considered expensive and easily corroded. Therefore, it is necessary to find a new material for the shaft lining structure.

Polypropylene macrofiber is a fiber with diameter and length exceeding 0.1 and 40 mm, respectively, and it is developed from polypropylene and polyethylene, which are the main raw materials. When the polypropylene macrofibers in concrete reach a certain level, they behave in a manner similar to steel fibers. Thus, the fibers are also referred to as "imitation steel fibers" [5–7]. Polypropylene macrofibers have many advantages such as high tensile strength, corrosion resistance, good chemical stability, strong bonding strength with concrete, and easy construction. However, few researchers have investigated the

application of polypropylene macrofiber-reinforced concrete (PPMFRC) to underground structures. To economically and feasibly solve the difficult supporting problems of mine shaft lining structures under complex conditions, PPMFRC was prepared and its mechanical properties were studied.

2. Materials and Preparation

2.1. Materials

2.1.1. Cement. In this study, Conch P.II 52.5 Portland cement, with the specific surface area 389 m^2/kg, was selected. Its initial and final setting times were 145 and 199 min, respectively, and the cement was qualified as stable. Its 3 d compressive and flexural strengths were 25.7 and 4.6 MPa, respectively, and its 28 d compressive strength and flexural strength were 55.8 and 7.3 MPa, respectively.

2.1.2. Aggregate. Sand from Huaihe River was selected as the fine aggregate with a fineness module of 2.9 and saturated surface drying density of 2580 kg/m^3. Basalt gravel was selected as the coarse aggregate with a particle size of less than 25 mm and saturated surface drying density of 2720 kg/m^3.

2.1.3. Plasticizer. This study used the high-performance water-reducing agent NF produced by Anhui Huaihe Chemical Co., Ltd.; its water reducing rate is greater than 30%.

2.1.4. Admixture. Furthermore, this study used slag, with a specific surface area greater than 350 m^2/kg, produced by Anhui Hefei Qingya Building Material Co., Ltd. The microsilicon powder produced by Shanxi Dongyi Ferroalloy Factory was selected. Its specific surface area was greater than 18000 m^2/kg.

2.1.5. Fiber. The polypropylene macrofiber produced by Hangzhou Jianqing Fiber Company was selected (Figure 1). The parameters of the fiber are listed in Table 1.

2.2. Mixture Composition and Preparation. Existing studies have generally used concrete with a standard cubic compressive strength of 60 MPa (C60) for shaft lining structures, and thus, C60 was taken as the design value of concrete strength in this test. The composition of the reference concrete for the test was then obtained from an orthogonal test (Table 2).

Four groups of specimens were needed for each test. One group comprised plain concrete specimens; these were considered to be reference concrete. The other three groups were PPMFRC specimens containing 0.5%, 1.0%, and 1.5% (volume fraction) fibers. The four groups were named A-0, A-0.5, A-1.0, and A-1.5, respectively. Each group had three specimens whose shapes and sizes corresponding to each test are shown in Figure 2.

Figure 1: Polypropylene macrofibers.

Table 1: Characteristic parameters of polypropylene macrofiber.

Length (mm)	Equivalent diameter (mm)	Length-diameter ratio	Density (kg/m^3)	Tensile strength (MPa)
55	0.85	≥65	0.91	≥450

Table 2: Composition of reference concrete (kg·m^{-3}).

Cement	Sand	Gravel	Water	Admixture	Slag	Silica fume
400	667.2	1088.5	164.3	7.2	105	25

The sequence for mixing the PPMFRC was as follows. First, cement, aggregate, and admixture were dry-mixed in a concrete mixer for 2 min. Second, polypropylene macrofibers were added and the mixture was stirred for 2 min. Then, NF water reducer was dissolved in 60% water and poured into the mixer for 3 min. Finally, the remaining 40% of the water was poured into the mixer and stirred for 3 min.

Specimens were poured and vibrated onanHZJ-0.8 concrete shaking table until slurry was discharged. After shaping, the surface was immediately covered with impervious film and the specimens in molds were placed in an ambient temperature of 20°C for 24 h. Then, the specimens were demolded and placed in a YH-40 standard curing box (20 ± 2°C, 95% humidity) for 28 d.

2.3. Experimental Methods and Facilities. In the experiment, the WAW2000B universal testing machine developed by SFMIT was used, and the load and displacement were recorded using the Test Master software [8, 9]. After all specimens were removed from the standard maintenance box, they were wiped clean with a dry cloth, and then they were placed in the dry equipment and corrected according to the specifications. An anticracking net cover was installed around the test machine to ensure safety.

In the compressive strength test, loading rate was controlled between 0.08 and 0.10 MPa/s. When the specimen was close to failure and began to deform sharply, we stopped adjusting the throttle of the testing machine until failure occurred.
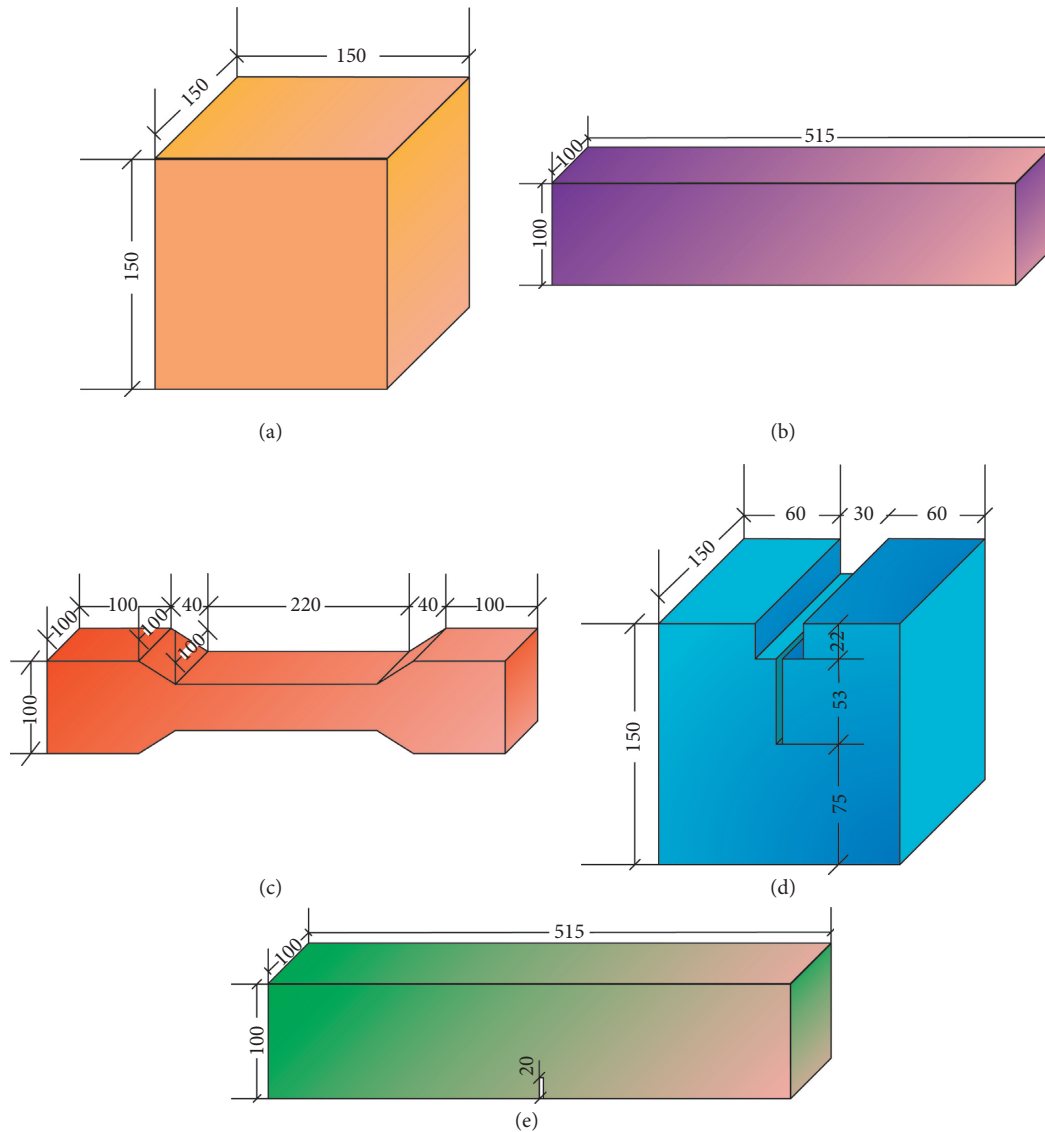
FIGURE 2: Shapes and sizes of specimens in different tests in millimetres: (a) compressive strength test specimen; (b) flexural strength test specimen; (c) uniaxial tensile test specimen; (d) wedged split tensile test specimen; (e) bending test specimen.

In the flexural strength test, the loading rate was controlled between 0.08 and 0.10 MPa/s. Using the flexural test device, two equal loads were simultaneously applied at three points of the specimen span. The loading diagram is shown in Figure 3.

In the uniaxial tensile test, a pair of special fixtures (Figure 4) matching the size of the test specimen were used, and the loading rate was controlled at 1.2 mm/min. To reduce the effects of eccentric load, the articulated ring was welded to the outer end of the upper fixture and greased to improve articulation effects.

In the wedged split tensile test, the loading rate was controlled at 0.3 mm/min using a step-by-step continuous loading method. The splitting and pulling device (Figure 5) was clamped into the wide slot cut in advance in to the specimen. The clamp extensometer was installed to monitor the V value of the crack. The time from the beginning of loading to fracturing of specimens was 30–50 min. When the

specimen approached failure, the loading speed was reduced and the test process was maintained at as table level. Finally, the F-V curve for the test was obtained.

In the bending test, a 20 mm crack was cut into the center of the lower surface for specimen. The loading speed was controlled at 0.025 mm/min, and a clamp extensometer was installed to monitor the crack deflection. When the material approached failure, the loading speed was reduced appropriately. Finally, the F-δ curve (load-deflection curve) for the three-point bending notched beam was obtained.

3. Results and Discussion

3.1. Compressive Strength Test. Vertical load was recorded using Test Master measurement and control software, and the peak values were labeled. The numerical values were accurate to 0.1 MPa. Normally, the average value of three specimens is taken as the strength value of the group of

FIGURE 3: Specimen dimensions and loading manner of the flexural test.

FIGURE 4: Special fixtures used in the uniaxial tensile test.

FIGURE 5: Loading manner of wedged split tensile test: (a) uniformly distributed load; (b) vertical pressure transfer device; (c) horizontal pressure transfer device; (d) displacement direction; (e) specimen.

compressive strength testing. The test results are listed in Table 4:

$$f_f = 0.85 \frac{F_{zmax} l}{b h^2}, \tag{1}$$

where f_f is the flexural strength (MPa), 0.85 is the dimension conversion coefficient, F_{zmax} is the peak load (kN), l is the span between supports (mm), h is the section height (mm), and b is the section weight (mm).

Figure 6 shows that before the ultimate flexural strength of plain concrete was reached, the curves basically coincided and linearity was evident. Then, different curves began to show different trends. After reaching the peak value, the stress of plain concrete decreased rapidly. Although the concrete had residual strength, it was completely destroyed in a short time and brittle failure was very evident. Over time, PPMFRC materials with different fiber dosages continued to bear loads. PPMFRC reached its ultimate strength and was destroyed at 210 s, which was nearly 30 s longer than the duration for plain concrete. Additionally, the decline rate of PPMFRC was slower than that of plain concrete. When the fiber content was 1.0%, PPMFRC had the highest flexural strength. Therefore, 1.0% can be used as the best volume fraction for flexural strength.

3.3. Uniaxial Tensile Strength Test. We found that most of the fibers were pulled out of the material. Meanwhile, a few fibers were not pulled out; however, they were instead broken because of the strong bond between the fibers and the concrete matrix. When the concrete cracked, the bonding force between the fibers and the concrete matrix played a key role. Then, most of the fibers were pulled out. However, a few fibers having a high bonding force with the

specimens. However, if the difference between the maximum value and the minimum value of the three measurements exceeds 15% of the median value, the maximum value and the minimum value are discarded, and the median value is taken as the compressive strength value of the group of specimens. If the difference between the maximum and the median value and the minimum and the median value exceeds 15% of the median values, the test results for the specimen group are invalid. The test results are listed in Table 3.

Table 3 shows that the compressive strength of PPMFRC increased with increasing fiber ratios. For fiber ratios of 1.0% and 1.5%, the strength increased by 3.4%. It shows that the addition of polypropylene macrofibers improves the compressive strength of concrete; however, the range is limited. The best volume ratio to improve the compressive strength of PPMFRC can be selected as 1.0%.

3.2. Flexural Strength Test. Flexural strength was calculated from peak load. Because the specimen sizes were nonstandard, the flexural strength results had to be converted (formula 1). The numerical value was accurate to 0.1 MPa. The strength determination method was the same as that in

TABLE 3: Compressive strength test results.

Group	Compressive strength (MPa)	Increase range (%)
A-0	64.3	0
A-0.5	66.2	3.0
A-1.0	66.5	3.4
A-1.5	66.5	3.4

TABLE 4: Flexural strength test results.

Group	Flexural strength (MPa)	Increase range (%)
A-0	5.8	0
A-0.5	6.8	17.2
A-1.0	7.5	29.3
A-1.5	7.3	25.9
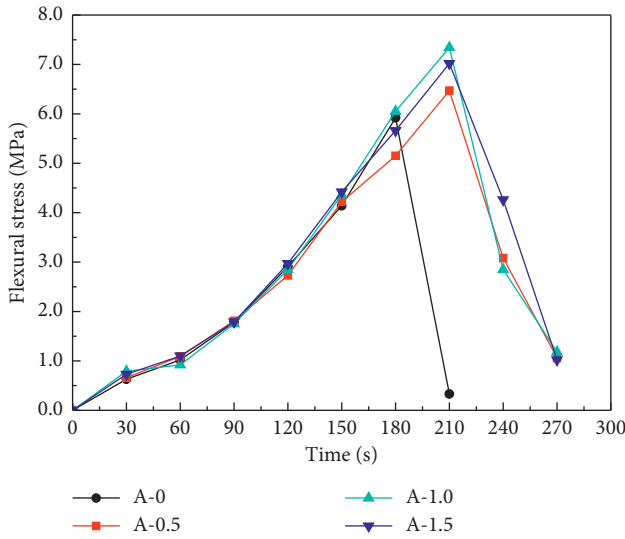
FIGURE 6: Relationship between flexural stress and time.

concrete matrix were not pulled out, and their tensile strength resisted overall fracturing.

Because of the randomness of the distribution of coarse aggregate and fibers in the concrete, the distribution of original defects such as cracks and voids in the concrete was also random (Figure 7). The internal randomness caused the strength and stress distributions to different in various sections of specimens; thus, no evident specimen failure was observed. The fracture surfaces for some specimens were near the middle of the specimens. However, the fracture surfaces for the other specimens were only approximately 110–140 mm away from the clamp opening.

During testing, a few specimens cracked on the one side, and then on the other side, the cracks eventually expand to the interior and break through. Most of the specimens cracked initially on one side, with the cracks gradually expanding to the interior and ultimately penetrating the damage. This phenomenon was mainly owing to a certain degree of eccentric tension after the first initial cracking in most specimens, which resulted in the crack extending inward along one side.

Table 5 shows that, with increase in fiber content, both the ultimate tensile strength and peak strain increased.

FIGURE 7: Fractured specimens after the uniaxial tensile test.

When the dosage was 1.5%, the ultimate tensile strength was 21.4% higher than that of plain concrete. In the stage prior to the 70–80% peak values, the stress-strain relationship was linear elastic. In this stage, the microcracks were relatively smaller and their influence was weak. With increasing stress, microcracks gradually began to expand, which affected the stress area of the specimen, making residual stress increase and further increasing failure trends.

3.4. Wedged Split Tensile Test. Draw F-V curve (vertical load-displacement of crack opening curve) (Figure 8) and calculate initial fracture toughness $K_{\mathrm{IC}}^{\mathrm{ini}}$, instability fracture toughness $K_{\mathrm{IC}}^{\mathrm{un}}$, effective crack length a_{c}, fracture energy G_{f}, and tensile strength f:

$$K_{\mathrm{IC}}^{\mathrm{ini}} = \frac{F_{\mathrm{HQ}} \times 10^{-3}}{t\sqrt{h}} f(\alpha),$$

$$K_{\mathrm{IC}}^{\mathrm{un}} = \frac{F_{\mathrm{HS}} \times 10^{-3}}{t\sqrt{h}} f(\alpha),$$

$$a_{\mathrm{c}} = (h + h_0)\left[1 - \sqrt{\frac{13.18}{(tEV_{\mathrm{c}}/F_{\mathrm{HS}}) + 0.16}}\right] - h_0, \quad (2)$$

$$G_{\mathrm{f}} = \frac{W}{th},$$

$$f = \frac{6F_{\mathrm{ZS}}y}{th^2} + \frac{F_{\mathrm{ZS}}}{th},$$

where F_{HQ} is the horizontal load of initial fracture (kN), F_{HS} is the horizontal load of instability fracture (kN), t is the ligament thickness (mm), h is the ligament height (mm), h_0 is the thickness of cutter edge thin steel plate of clamp extension meter (mm), a_0 is the initial length of crack (mm), E is the modulus of elasticity (GPa), $c_i = V_i/F_i$, is the reciprocal slope of straight line segment in curve ascent (mm/kN), $\alpha = \alpha_{\mathrm{c}}/h$, $f(\alpha) = 3.675[1 - 0.12(\alpha - 0.45)](1 - \alpha)^{-3/2}$, V_{c} is the critical value of crack opening displacement (mm), W is the work done by vertical load, envelope area of F-V curve (J), and y is the distance from the ligament center to the horizontal loading point (mm) [10]. The test and calculation results are listed in Table 6.

TABLE 5: Uniaxial tensile test results.

Group	Uniaxial tensile strength (MPa)	Increase range (%)	Peak strain ($\times 10^{-6}$)
A-0	2.8	0	117.63
A-0.5	3.1	10.7	124.63
A-1.0	3.2	14.3	145.41
A-1.5	3.4	21.4	152.34
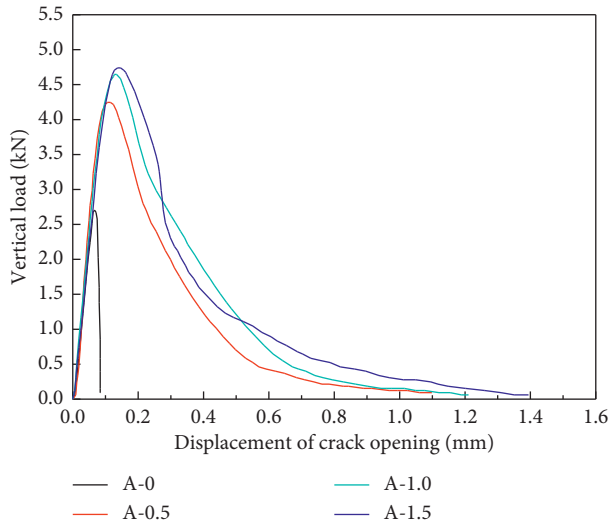
FIGURE 8: Relationship between vertical load and displacement of crack opening.

The failure modes of concrete can be clearly observed from Figure 9. The matrix of plain concrete is completely split and divided into two parts. The brittle failure mode is evident. Under the same stress, PPMFRC with 1.5% fiber content exhibits microcracks but no evident damage, and the effects of fiber crack prevention are evident.

3.5. Bending Test. According to the load, deflection, and crack opening displacement measured by the test, $F\text{-}\delta$ curve (vertical load-deflection) is drawn, and the fracture toughness K_{IC} and fracture energy G_f are calculated:

$$K_{IC} = \frac{6Y M_{\max} \sqrt{a_0}}{t h^2},$$

$$G_f = \frac{A_0 + m_g \delta_{\max}}{A_{lig}},$$

$$(3)$$

where $Y(l/h) = 1.93 - 3.07(l/h) + 14.53(l/h)^2 - 25.11(l/h)^3 + 25.8(l/h)^4$ is the shape factor, $M_{\max}$ is the sum of the maximum load and the bending moment produced by the dead-weight of the beam (N/m), a_0 is the notch depth (mm), A_0 is the envelope area of $F\text{-}\delta$ curve (mm^2), m_g is the deadweight of support section of concrete beam (kN), $\delta_{\max}$ is the deformation of beams at final failure (mm), and A_{lig} is the ligament area (mm^2). The meaning of other parameters is consistent with that of the penetration splitting test. The test and calculation results are listed in Table 7.

Figure 10 shows that there are only two stages in plain concrete: elastic and failure stages. The brittle failure characteristics are evident. PPMFRC has evident elastic-plastic characteristics, which can be divided into the elastic, deflection stable development, deflection instability, and failure stages. In the elastic stage, the curve is linear and the fibers and concrete bear the load together. In the stable development stage of deflection, when the ultimate load reaches 70–80%, the curve slows, the matrix cracks begin to propagate slowly, and the fibers across the cracks begin to play a role in delaying the crack propagation speed until it reaches a peak value. Macroscopic cracks begin to appear near the peak load. In the deflection instability stage, after reaching peak stress, the curve is steep, because the specimen reaches its ultimate strength and destructs. The bearing capacity decreases sharply; however, the deflection changes little. In the damage stage, the fibers show strong crack resistance, with little change in the bearing capacity of the specimens. The deflection continues to develop until the specimens are destroyed, reflecting the high toughness of PPMFRC.

With increasing fiber content, the ultimate strength loads and peak deflection increase. The fiber volume fraction has an evident effect on bending resistance, and fracture energy also increases. The value is between 382.7 and 485.6 N/m. This occurs mainly because the fibers connect the cracks and span between them. When the microcracks expand, the fibers effectively alleviate the stress concentrations of the cracks and prevent the cracks from expanding. The numerical results show that the fracture energy is significantly increased. In addition to overcoming the resistance of the concrete matrix itself, the external load also must overcome the bond stress between the fibers and the matrix, as well as the tensile strength of the fibers themselves.

4. Conclusion

(1) The flexural strength, tensile strength, fracture toughness, and fracture energy of PPMFRC were evidently higher than those of plain concrete. However, the compressive strength of PPMFRC was only slightly higher than that of plain concrete.

(2) For a fiber content of 1.0%, the flexural strength of PPMFRC was 29.3% higher than that of plain concrete. With increase in fiber content, the uniaxial tensile strength and wedged split tensile strength of PPMFRC were improved. At a fiber content of 1.5%, the uniaxial tensile strength was highest, and it was 21.4% higher than that of plain concrete.

(3) With increasing fiber content, the fracture energy of PPMFRC was improved. When the fiber content was 0.5–1.5%, the fracture toughness of PPMFRC was 0.26–0.35 and the fracture energy was 382.7–485.6 N/m. Thus, the crack resistance of the PPMFRC is evidently better than that of plain concrete.

TABLE 6: Wedged split tensile test results.

Group	Wedged split tensile strength (MPa)	Increase range (%)	V_c (μm)	a_c (μm)	K_{ini} (MPa/$\sqrt{m}$)	K_{IC}^{un} (MPa/$\sqrt{m}$)	G_f (N/m)
A-0	2.4	0	63.69	81.13	0.54	1.48	89.06
A-0.5	3.4	41.7	84.51	112.25	0.61	1.48	122.10
A-1.0	3.8	58.3	96.90	136.19	0.68	1.61	153.89
A-1.5	3.9	62.5	122.65	167.08	0.70	1.70	174.84

(a)   (b)
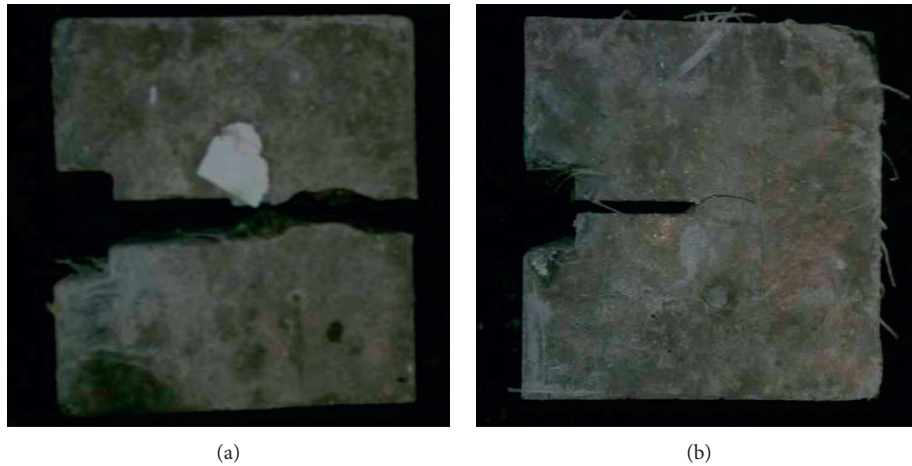
FIGURE 9: Specimens damaged by the wedged split tensile test: (a) plain concrete; (b) PPMFRC of 1.5% polypropylene macrofibers content.

TABLE 7: Bending test results.

Group	Ultimate bearing load (kN)	Increase range (%)	Peak deflection (mm)	K_{IC} (MPa/m$^{1/2}$)	G_f (N/m)
A-0	10.0	0	0.1340	0.25	279.2
A-0.5	10.6	6.0	0.2096	0.26	382.7
A-1.0	12.4	24.0	0.3221	0.31	429.5
A-1.5	14.0	40.0	0.6118	0.35	485.6
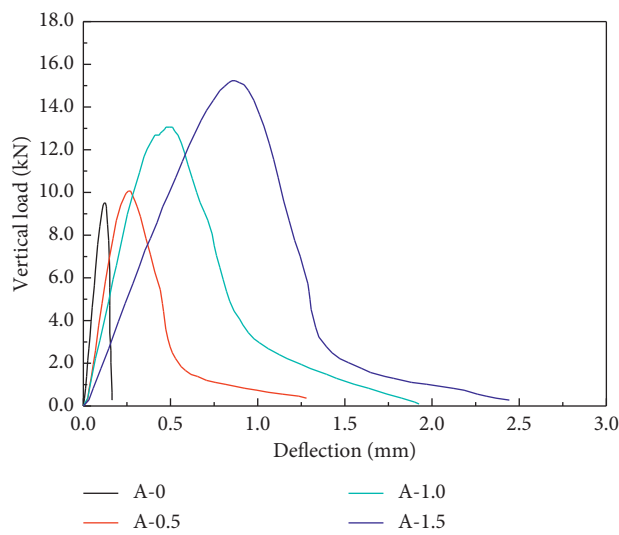
FIGURE 10: Relationship between vertical load and deflection.

(4) Both the F-V and F-δ curves exhibited the brittleness characteristics of plain concrete and the elastic-plastic characteristics of PPMFRC, and they indicated the evident anticracking and toughening effects of the fibers.

Data Availability

The data used to support the findings of this study are included within the article.

Conflicts of Interest

The authors declare that they have no conflicts of interest.

Acknowledgments

References

[1] Z. S. Yao, H. Cheng, and X. B. Ju, "Research and application of high strength steel fiber concrete compound shaft lining with inner steel plate in deep alluvium shaft repair," *Journal of China Coal Society*, vol. 42, no. 9, pp. 2295–2301, 2007.

[2] T. Han, W. H. Yang, Y. L. Ren, and Z. J. Yang, "Numerical and experimental model studies of the horizontal bearing properties of shaft lining of encased steel or steel fiber reinforced, high strength concrete," *Journal of China University of Mining & Technology*, vol. 41, no. 2, pp. 205–211, 2012.

[3] M. S. Wei, L. S. Li, Q. P. Zheng, and Q. A. Ding, "Comparative study of evaluate method for toughness factor of steel fiber reinforced concrete (SFRC)," *Building Structure*, vol. 37, no. 12, pp. 90–92, 2007.

[4] S. Z. Qi and W. H. Yang, "Study of mechanical characteristics of high strength steel fiber reinforced concrete shaft lining with inner steel plate," *Coal Engineering*, vol. 48, no. 3, pp. 103–106, 2016.

[5] Y.-z. Bi, D.-l. Zhang, and J.-h. Hu, "Application of modified polypropylene (crude) fibers concrete to strengthen the support structures in deep mine roadway," *Journal of Coal Science and Engineering (China)*, vol. 18, no. 4, pp. 379–384, 2012.

[6] Z. Z. Sun and Q. W. Xu, "Microscopic, physical and mechanical analysis of polypropylene fiber reinforced concrete," *Materials Science and Engineering*, vol. 527, no. 1-2, pp. 198–204, 2009.

[7] A. A. Ramezanianpour, M. Esmaeili, S. A. Ghahari, and M. H. Najafi, "Laboratory study on the effect of polypropylene fiber on durability, and physical and mechanical characteristic of concrete for application in sleepers," *Construction and Building Materials*, vol. 44, pp. 411–418, 2013.

[8] China Standards Publication, *Standard for Test Method of Mechanical Properties or Plain Concrete, GB/T50081-2002*, Standard Press of China, Beijing, China, 2002.

[9] China Standards Publication, *Technical Specification for Application of Fiber Reinforced Concrete, JG/T 221-2010*, Standard Press of China, Beijing, China, 2010.

[10] S. L. Xu, "The calculation approaches of double-K fracture parameters of concrete and a possible coding standard test method for determine them," *Journal of China Three Gorges University (Natural Sciences)*, vol. 24, no. 1, pp. 1–8, 2002.

Research Article

Estimating the Tensile Strength of Ultrahigh-Performance Fiber-Reinforced Concrete Beams

In-Hwan Yang [ID],[1] **Changbin Joh** [ID],[2] **and The Quang Bui**[1]

[1]*Kunsan National University, Department of Civil Engineering, Kunsan, Jeonbuk 54150, Republic of Korea*
[2]*Korea Institute of Civil Engineering and Building Technology, Structural Engineering Research Institute, Goyang, Gyeonggi 10223, Republic of Korea*

Correspondence should be addressed to In-Hwan Yang; ihyang@kunsan.ac.kr

The tensile behavior of ultrahigh-performance fiber-reinforced concrete (UHPFRC) depends on the dispersion and orientation of steel fibers within the concrete matrix. The uneven dispersion of randomly oriented steel fibers in concrete may cause differences in the tensile behavior between material testing specimens and beams. Therefore, in this study, the tensile behavior was investigated by fitting the analysis result of the moment-curvature curve to the experimental result of a UHPFRC beam. To this end, three UHPFRC mixtures with different compressive strengths were fabricated to test the material properties and flexural behavior of UHPFRC beams. Both a single type of steel fiber and a combination of steel fiber types were used with volume fractions of 1.0% and 1.5%, respectively, in the three mixtures. Based on the design recommendations, the material properties of UHPFRC were modeled. The results ultimately show that by fitting the analysis results to the experimental results of the moment-curvature curves, the tensile strength of UHPFRC beams can be reasonably estimated.

1. Introduction

Concrete is a brittle material with a low tensile strength; furthermore, increasing the compressive strength of concrete will increase its brittleness. The advent of ultrahigh-performance fiber-reinforced concrete (UHPFRC) represents the outcome of continuous research to improve the performance of high-strength concrete under tension. Following the improvements in its mechanical properties, UHPFRC has become suitable for many applications requiring long spans, such as in stadia, bridges, and docks. Therefore, many researchers have conducted numerous studies to explore the tensile and flexural behaviors of UHPFRC [1–6]. For example, uniaxial tensile tests were performed by Boulay et al. [7] and Wile et al. [8] to investigate the tensile behavior of UHPFRC, while Su et al. [9] and Mertol et al. [10] conducted a series of bending beam tests to study the flexural behavior of UHPFRC. In addition, Li et al. [11] examined the influences of UHPFRC and high-strength reinforcement on the flexural behavior of

reinforced concrete beams. The findings of these studies revealed that the use of UHPFRC increases the overall performance of a beam relative to the use of high-strength concrete.

The most important factor affecting the tensile behavior of UHPFRC is the inclusion of steel fiber. The addition of steel fiber to UHPFRC makes it more ductile, increases its strength, and improves its resistance to cracking [12–16]. The results of a study performed by Ren et al. [17] indicated that the flexural strength, load carrying capacity, energy absorption capacity, fracture toughness, and fracture energy increased significantly with increasing steel fiber content. Moreover, Yoo et al. [18] investigated the effects of four different fiber volume fractions on the mechanical and fracture properties of UHPFRC; their results showed that an increase in the fiber volume fraction increased the flexural strength of notched beams. Subsequently, to investigate the flexural behavior of steel fiber-reinforced concrete beams under both quasistatic and impact loads, Yoo et al. [19] used four different fiber volume contents ranging from 0% to

2.0% and concluded that the inclusion of a large quantity of steel fibers would enhance the flexural strength, deflection capacity, and toughness of the beams.

However, the orientation and distribution of steel fiber in a concrete matrix are random; unfortunately, this randomness can considerably affect the flexural response of a UHPFRC beam. Consequently, many researchers have attempted to control the orientation and distribution of steel fibers in UHPFRC members. For instance, Abrishambaf et al. [20] and Kang and Kim [21] quantified the effect of the fiber orientation on the tensile behavior of UHPFRC and concluded that the fiber orientation significantly affects the tensile behavior of UHPFRC, especially its deflection-hardening behavior. According to the studies of Yang et al. [22] and Kang and Kim [21], in which two different methods for emplacing concrete were adopted, steel fiber orientation is influenced by the method utilized to place UHPFRC. In addition, Al-Mattarneh [23] determined the concentration, dispersion, and orientation of steel fibers in concrete by using a surface electromagnetic sensor. Furthermore, Nunes et al. [24] estimated the tensile strength of thirty-six UHPFRC layers with varying fiber contents and fiber orientation distributions based on a comparison of magnetic measurements and experimental results.

Therefore, the objective of this study is to estimate the tensile behavior of UHPFRC beams subjected to flexure. The experimental parameters included the compressive strength of UHPFRC and the volume content of a combination of steel fibers. Target compressive strengths of 120, 150, and 180 MPa were considered for the UHPFRC; moreover, both a single type of steel fiber and a combination of steel fiber types with volume fractions of 1.0% and 1.5%, respectively, were used in this study. The material behavior of UHPFRC was modeled based on material testing results, and flexural tests were carried out on nine UHPFRC beams. Finally, the tensile strength of the UHPFRC beams was estimated by fitting the analysis results with the testing results of the moment-curvature curves.

2. Material Properties of UHPFRC

2.1. Mixing Proportions.
In this study, the UHPFRC mixtures included straight steel fibers at volume fractions of 1.0% and 1.5%. Ordinary Portland cement (OPC) was used as the cementitious material, and fine aggregate with a diameter of 0.5 mm or less was used. The water-binder ratios (w/b) were 0.18 and 0.22, and a polycarboxylic acid-based high-performance water-reducing agent with a density of 1.01 was used to ensure workability with a low water-binder ratio. In addition, filler and zirconium were also used in the UHPFRC mixtures.

Three fiber-reinforced concrete mixtures, namely, FRC120, FRC150, and FRC180, were fabricated, where the number in each mixture label represents the target compressive strength of the resultant concrete. A single type of straight fiber with a length of 19.5 mm was used in the FRC120 mixture at a volume fraction of 1.0%, while a combination of fibers was utilized in the FRC150 and

FRC180 mixtures at a volume fraction of 1.5%. The combination of fibers used in the FRC150 and FRC180 mixtures constituted 0.5% straight fibers with a length of 16.5 mm and 1.0% straight fibers with a length of 19.5 mm. The straight fibers had a diameter of 0.2 mm, a unit weight of 7500 kg/m³, and a tensile strength of 2500 MPa. The detailed mixing proportions are given in Table 1.

2.2. Compressive Behavior of UHPFRC.
The compressive strength of UHPFRC was obtained through compressive testing on cylindrical specimens with a height of 200 mm and a diameter of 100 mm. Three linear variable displacement transducers (LVDTs) were installed around the cylindrical specimens to measure the displacement during the loading step. The stress-strain curve of the UHPFRC was calculated by using the load-displacement relationship, which was obtained from the compressive strength test. In addition, the modulus of elasticity was calculated from the UHPFRC stress-strain curve [25].

The mean compressive strengths of the FRC120, FRC150, and FRC180 specimens were 133.7, 148.8, and 181.2 MPa, respectively. In addition, the mean elastic moduli of the FRC120, FRC150, and FRC180 specimens were 40150, 43220, and 45140 MPa, respectively.

2.3. Tensile Behavior of UHPFRC.
To evaluate the tensile behavior of UHPFRC, including its postcracking behavior, prismatic specimens of each mixture were fabricated and tested. The prismatic specimens, which had a height of 100 mm, a width of 100 mm, and a length of 400 mm, had a notch with a depth of 10 mm cut into the tensile zone. The crack mouth opening displacement (CMOD) was measured by using a clip gauge attached to both edges of the notch.

A three-point loading test was performed to obtain the tensile behavior of the UHPFRC. The clear span length between the specimen supports was 300 mm, and the load was measured during its application. To measure the deflections of the prismatic specimens, three LVDTs were attached at the midheight of each specimen. The experimental setup for measuring the CMOD of the prismatic specimens is shown in Figure 1. The load-CMOD relationship curves of the FRC120, FRC150, and FRC180 specimens are shown in Figure 2.

2.4. Modeling the Material Properties of UHPFRC.
The UHPFRC stress-strain relationship was modeled based on the current design recommendations [26]. Based on the compressive stress-strain test results of the cylindrical specimens, the compressive stress-strain relationship was modeled as a linear curve by using the maximum compressive strength and elastic modulus; a linear shape was chosen because the experimental results showed an approximately linear relationship between the compressive stress and strain.

The tensile behavior of the UHPFRC can be estimated by performing an inverse analysis based on the testing results of

TABLE 1: Mixing proportions of the UHPFRC.

Mixture	w/b	W	Binders			S	F	Steel fiber	
			OPC	Zr	BFS			Fiber volume content, V_f (%)	Diameter, D_f (mm)
FRC120	0.22	209	770	58	135	847	231	1.0 = 1.0 (19.5 mm)	0.2
FRC150	0.18	180	788	99	99	867	236	1.5 = 1.0 (19.5 mm) + 1.0 (16.5 mm)	0.2
FRC180	0.18	178	783	196	—	862	235	1.5 = 1.0 (19.5 mm) + 1.0 (16.5 mm)	0.2

OPC: ordinary Portland cement; Zr: zirconium; BFS: blast-furnace slag; S: sand; F: filler; W: water.

FIGURE 1: CMOD test setup.

the load-CMOD relationship curve. Accordingly, the tensile stress-CMOD relationship was derived from the load-CMOD relationship through inverse analysis, after which the tensile stress-strain curve was obtained from the tensile stress-CMOD relationship. The tensile strengths of the FRC120, FRC150, and FRC180 mixtures estimated from the load-CMOD relationship were 7.21, 9.07, and 7.76 MPa, respectively; these results show that the tensile strength of the FRC180 mixture was less than that of the FRC150 mixture. At the beginning of the test, it was expected that the tensile strength of UHPFRC would increase with the compressive strength; however, this is not consistent with the tensile test results. The tensile and compressive stress-strain relationships are shown in Figure 3. The equations for the characteristic points of the curve are as follows:

$$\varepsilon_{el} = \frac{f_{ctk,el}}{E_{cm}}, \tag{1}$$

where ε_{el} is the elastic tensile strain corresponding to the characteristic elastic tensile strength, $f_{ctk,el}$ is the characteristic elastic tensile strength, and E_{cm} is the mean elastic modulus of the UHPFRC.

$$\varepsilon_{peak} = \frac{w_{0.3}}{l_c} + \frac{f_{ctk,el}}{E_{cm}},$$
$$\varepsilon_{1\%} = \frac{w_{1\%}}{l_c} + \frac{f_{ctk,el}}{E_{cm}}. \tag{2}$$

where ε_{peak} is the equivalent strain corresponding to the local peak in the postcracking phase or to a crack width equal to 0.3 mm if there is no peak, and $w_{0.3}$ represents the crack opening width corresponding to 0.3 mm. $\varepsilon_{1\%}$ is the equivalent strain corresponding to a crack width of $0.01H$; $w_{1\%} = 0.01H$, where H denotes the height of the prismatic specimen; and l_c is the characteristic length expressed as $l_c = 2h/3$, where h is the depth of the cross section of the beam.

$$\varepsilon_{lim} = \frac{l_f}{4l_c}, \tag{3}$$

where ε_{lim} is the ultimate strain beyond which the effect of fiber is no longer taken into account in the ultimate limit state and l_f is the length of the steel fiber.

The compressive stress-strain relationships for the FRC120, FRC150, and FRC180 mixtures are shown in Figure 4, and those simulated for each mixture are represented by the solid lines in Figure 5. The values of the characteristic points are listed in Table 2.

3. Bending Test of UHPFRC Beams

3.1. Bending Test Setup. A total of nine beams with rectangular cross-sectional dimensions of 200×250 mm and a length of 3300 mm were fabricated and tested. Figure 6 shows the beam dimensions and reinforcement details. The main experimental variables of the test beams were the compressive strength of the concrete and the reinforcement ratio (i.e., rebar ratio) of the beams; these variables are listed in Table 3. Three different types of UHPFRC with compressive strengths of 120, 150, and 180 MPa were cast with different rebar ratios, which ranged between 0.59 and 1.19%. The constant moment region was 600 mm long; in this region, stirrups were not used while they were placed in the shear spans. All beams were reinforced by stirrups with a diameter of 10 mm at a spacing of 150 mm to avoid shear failure at both shear spans.

The beams were tested under a four-point loading system, as shown in Figure 7. The load was applied by a hydraulically operated actuator and a spread beam. A pair of steel supports was utilized with a support placed at either end of the beams separated by a clear span of 3000 mm. The distance between the two loading points was 600 mm, and the displacement control of the load was maintained at a rate of 1.5 mm/min.

Three LVDTs were placed within the constant moment region of each beam to measure the deflection during the test. To obtain the strain of both the concrete and the rebar, electrical resistance strain gauges were also attached to each beam. The strain in the concrete was measured by five strain gauges attached on the sides of the beams at the midspan, and the strain in the rebar was measured by four strain gauges attached on the surface of the rebar.

3.2. Bending Test Results. The cracking and failure patterns of the UHPFRC beams are shown in Figure 8. The beams began to crack initially in the constant moment region, and

(a) FRC120 specimens

(b) FRC150 specimens

(c) FRC180 specimens
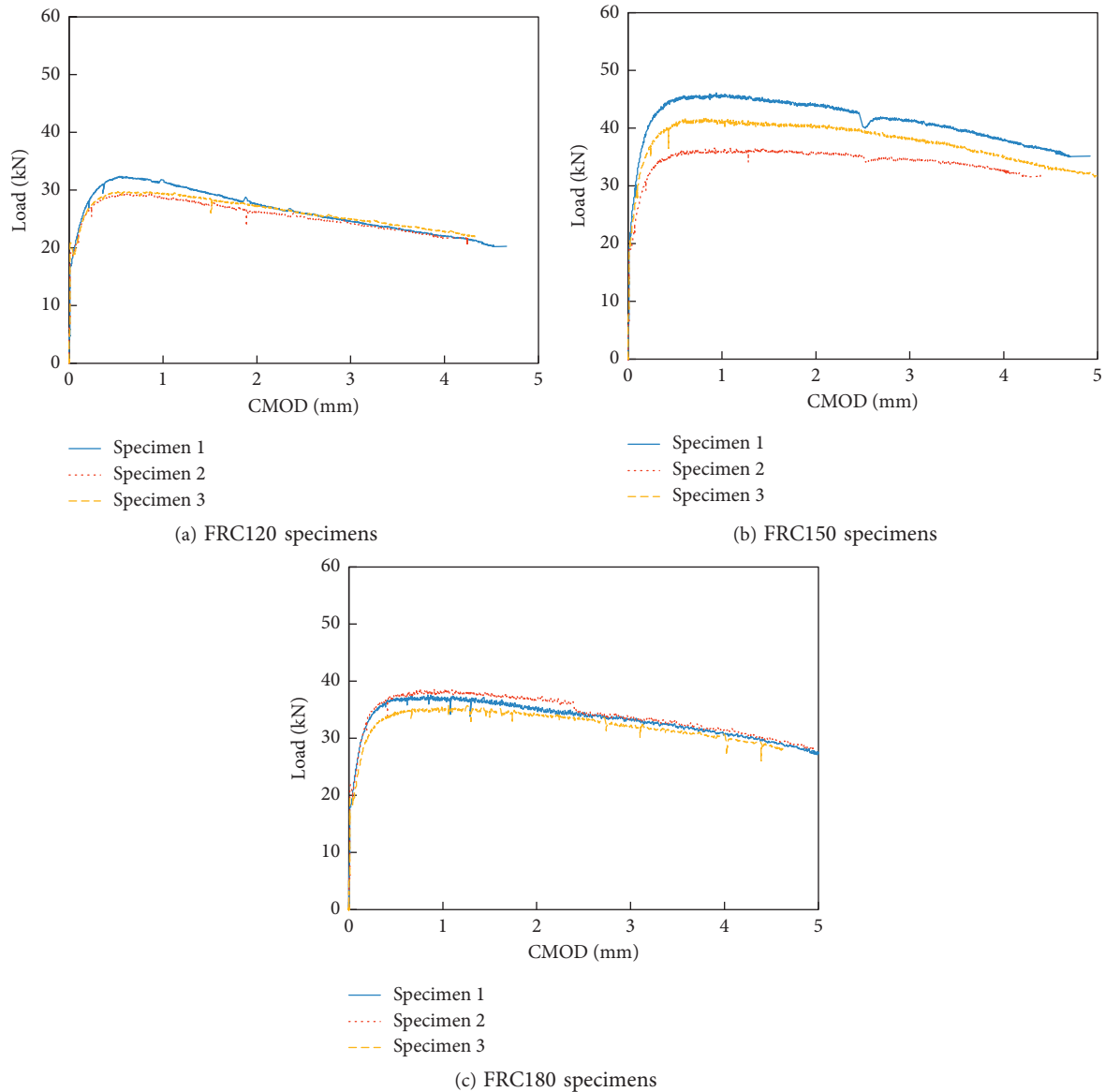
Figure 2: Load-CMOD relationship curves.

more cracks formed between the existing cracks as the load increased. The cracks were well distributed throughout the constant moment region at a low loading level, and more cracks formed in the shear spans at a higher loading level. After the peak load was reached, a single crack from the existing cracks within the constant moment region significantly widened and developed into a localized major crack, as shown in Figure 8. The localization of cracking within the constant moment region can cause bridging cracks to weaken and eventually form a plastic hinge. Moreover, the experimental results showed that steel fibers were pulled out of the matrix at the ultimate state.

The load-deflection curves of the beams with different rebar ratios are shown in Figure 9, and the bending test results of the beams are also shown in detail in Table 4. With regard to the beams with a rebar ratio of 0.59% (R2), the peak loads of the FRC120-R2, FRC150-R2, and FRC180-R2

beams were 66.7, 76.0, and 111.5 kN, respectively. The FRC180-R2 beam exhibited a greater peak load than the other beams. With regard to the beams with a rebar ratio of 0.89% (R3), the peak loads of the FRC120-R3, FRC150-R3, and FRC180-R3 beams were significantly different from each other. The highest peak load of 131.3 kN was obtained for the FRC180-R3 beam, while the peak loads of the FRC120-R3 and FRC150-R3 beams were 123.3 and 118.6 kN, respectively. With regard to the beams with a rebar ratio of 1.19% (R4), the FRC180-R4 beam exhibited a peak load of 147.2 kN, which was greater than that of the other beams; the peak loads of the FRC120-R4 and FRC150-R4 beams were 127.3 and 139.9 kN, respectively. For each rebar ratio, the peak loads of the FRC180 beams were greater than those of the FRC120 and FRC150 beams. Therefore, the bending strength of UHPFRC beams is considerably affected by the compressive strength of the concrete.

(a) Compression

(b) Tension
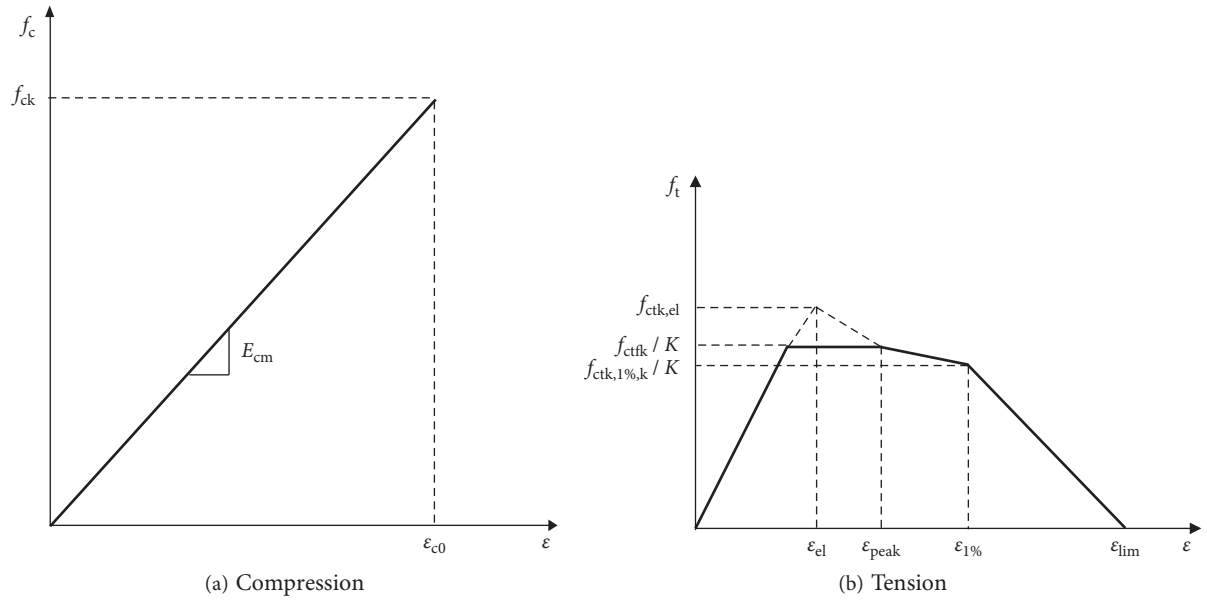
FIGURE 3: Stress-strain relationships.
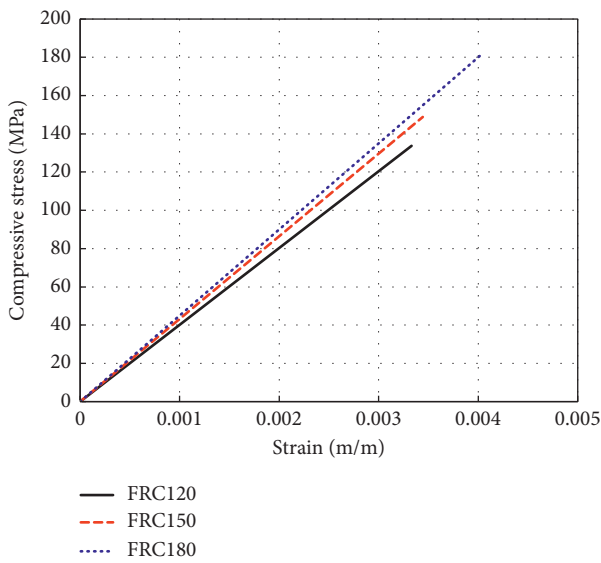
FIGURE 4: Modeling of the compressive behavior of UHPFRC.

With regard to the beams with a rebar ratio of 0.59% (R2), the deflections at the ultimate states of the FRC120-R2, FRC150-R2, and FRC180-R2 beams were 22.2, 17.9, and 17.8 mm, respectively. The deflection of the FRC120-R2 beam was greater than that of the other beams, and the deflections at the ultimate states of the FRC150-R2 and FRC180-R2 beams were similar. With regard to the beams with a rebar ratio of 0.89% (R3), the deflections at the ultimate states of the FRC120-R3, FRC150-R3, and FRC180-R3 beams were 20.9, 34.6, and 21.2 mm, respectively. At the ultimate state, the FRC150-R3 beam showed the greatest deflection and the deflections of the FRC120-R3 and FRC180-R3 beams were similar. With regard to the beams with a rebar ratio of 1.19% (R4), the ultimate deflection of the

FRC150-R4 beam was the greatest. Therefore, the deflection at the ultimate state of a UHPFRC beam is not directly affected by the compressive strength of UHPFRC, while the bending strength of a UHPFRC beam is approximately proportionally affected by the compressive strength of concrete.

The load-deflection relationship of a beam subjected to bending depends on the curvature along the axis of the beam. In a low-loading state, because the widths of the cracks in the constant moment region are small and uniform, the curvature in this region is relatively uniform; this results in deflection, which depends on the constant curvature. However, if a major crack forms, the curvature in the constant moment region will no longer be uniform; thus, the midspan deflection of the beam will not depend on the constant curvature. As shown in Figure 8, a major crack appeared in all the test beams. Therefore, the experimental results of the midspan deflection at the ultimate state did not show an obvious trend with the compressive strength of UHPFRC.

4. Estimating the Tensile Behavior of UHPFRC Beams

4.1. Method for Predicting the Bending Moment-Curvature Relationship. In this study, a sectional analysis was performed by using a multilayer section to predict the bending strength of UHPFRC beams. The cross section of the test beam is divided into several layers along the height, and it is assumed that the compression and tensile strain are both linear throughout the cross section. The compressive strain at the top layer and the tensile strain at the bottom layer of the cross section are calculated by using two variables: the cross-sectional curvature (φ) and the distance from the top layer to the neutral axis (c).

(a) FRC120 series

(b) FRC150 series

(c) FRC180 series
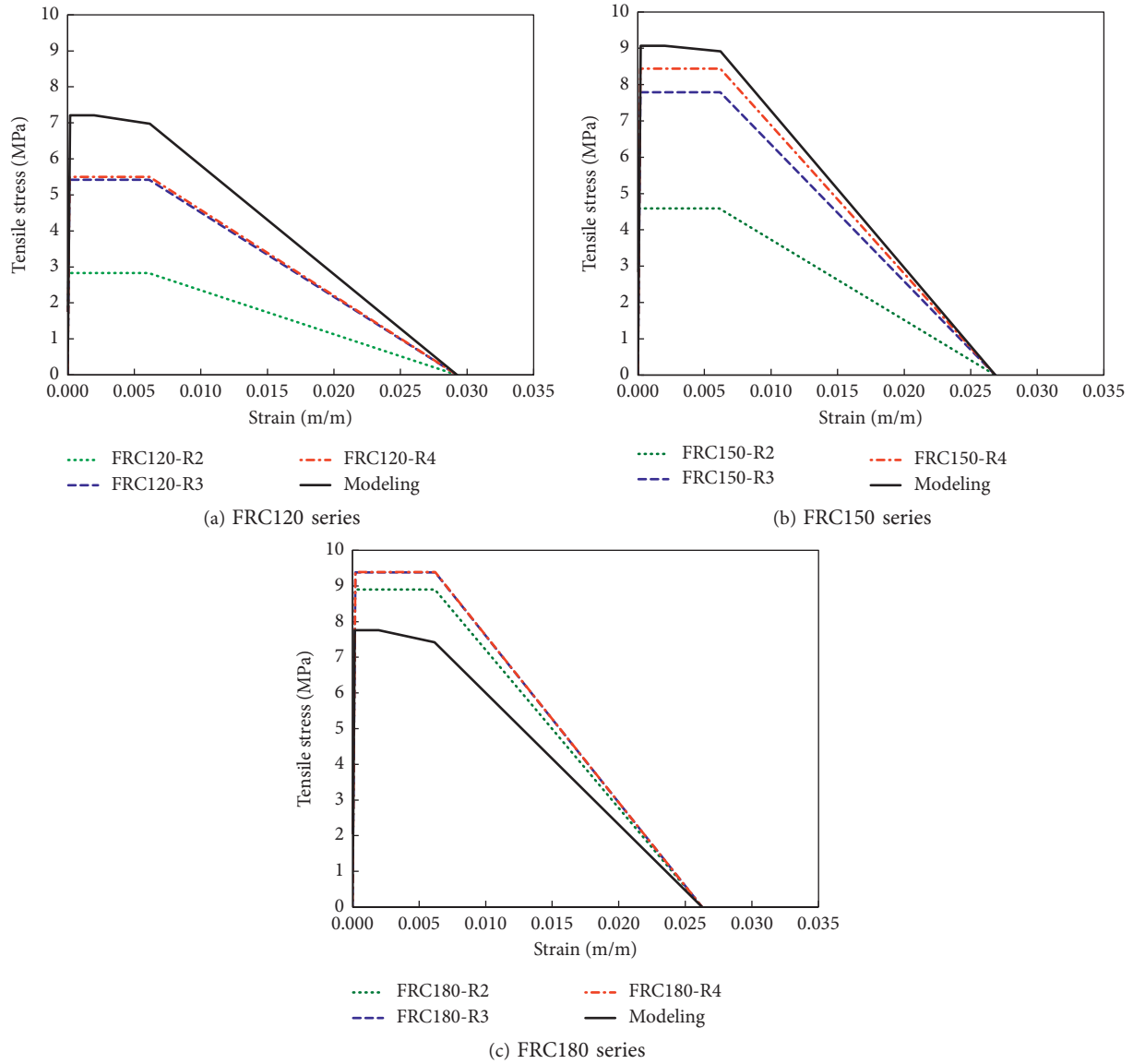
Figure 5: Modeling and estimation of the tensile behavior of UHPFRC.

Table 2: Material modeling of the UHPFRC.

| Mixture | Compressive behavior | | | Tensile behavior | | | | | |
	f_{ck} (MPa)	ε_{c0}	E_{cm} (MPa)	f_{ctfk} (MPa)	$f_{ctf,1\%,k}$ (MPa)	ε_{el}	ε_{peak}	$\varepsilon_{1\%}$	ε_{lim}
FRC120	133.7	0.0033	40,150	7.21	6.98	0.00018	0.00198	0.00618	0.02925
FRC150	148.8	0.0034	43,220	9.07	9.07	0.00021	0.00201	0.00621	0.02685
FRC180	181.2	0.0040	45,140	7.76	7.76	0.00017	0.00197	0.00617	0.02625

The terms in the table are shown in Figure 3.

The compressive strain at the top face and the tensile strain at the bottom face are calculated as follows:

$$\varepsilon_{top} = c\varphi,$$
$$\varepsilon_{bottom} = (h - c)\varphi, \quad (4)$$

where h is the beam height.

After the strains in the top and bottom layers are determined, the strain in the other layers can be obtained, as shown in Figure 10, because the strain distribution is assumed to be linear throughout the cross section. Then, the stress of each layer can be obtained from the material model. In addition, the force of each layer is determined based on the stress of the UHPFRC in each layer and the stress of the steel rebar. The sum of the forces
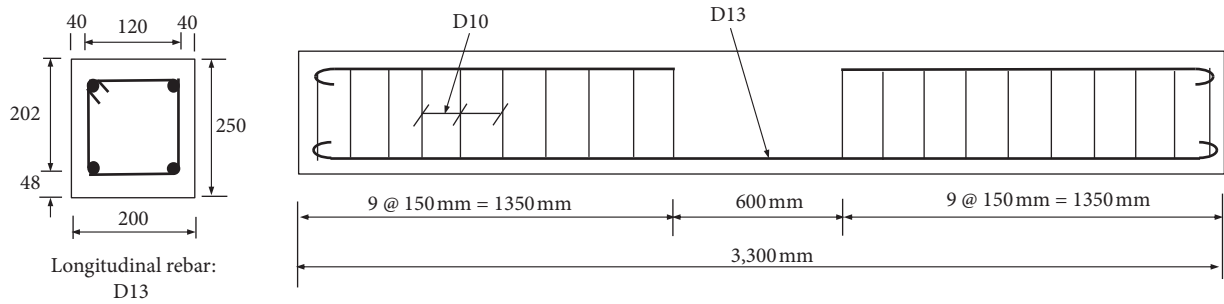
FIGURE 6: Dimensions of the beam.

TABLE 3: Details of the beams.

| Beams | Target compressive strength (MPa) | Mean compressive strength (MPa) | Fiber volume content, V_f (%) | Beam dimensions | | | Rebar | | | |
				Width of section, b (mm)	Height of section, h (mm)	Effective depth of beam, a (mm)	Number	Area, A_s (mm^2)	Rebar ratio, ρ (%)	Yielding strength, f_y (MPa)
FRC120-R2				200	250	213.5	2-D13	258	0.59	420
FRC120-R3	120	133.7	1.0	200	250	213.5	3-D13	387	0.89	420
FRC120-R4				200	250	213.5	4-D13	516	1.19	420
FRC150-R2				200	250	213.5	2-D13	258	0.59	420
FRC150-R3	150	148.8	1.5	200	250	213.5	3-D13	387	0.89	420
FRC150-R4				200	250	213.5	4-D13	516	1.19	420
FRC180-R2				200	250	213.5	2-D13	258	0.59	420
FRC180-R3	180	181.2	1.5	200	250	213.5	3-D13	387	0.89	420
FRC180-R4				200	250	213.5	4-D13	516	1.19	420
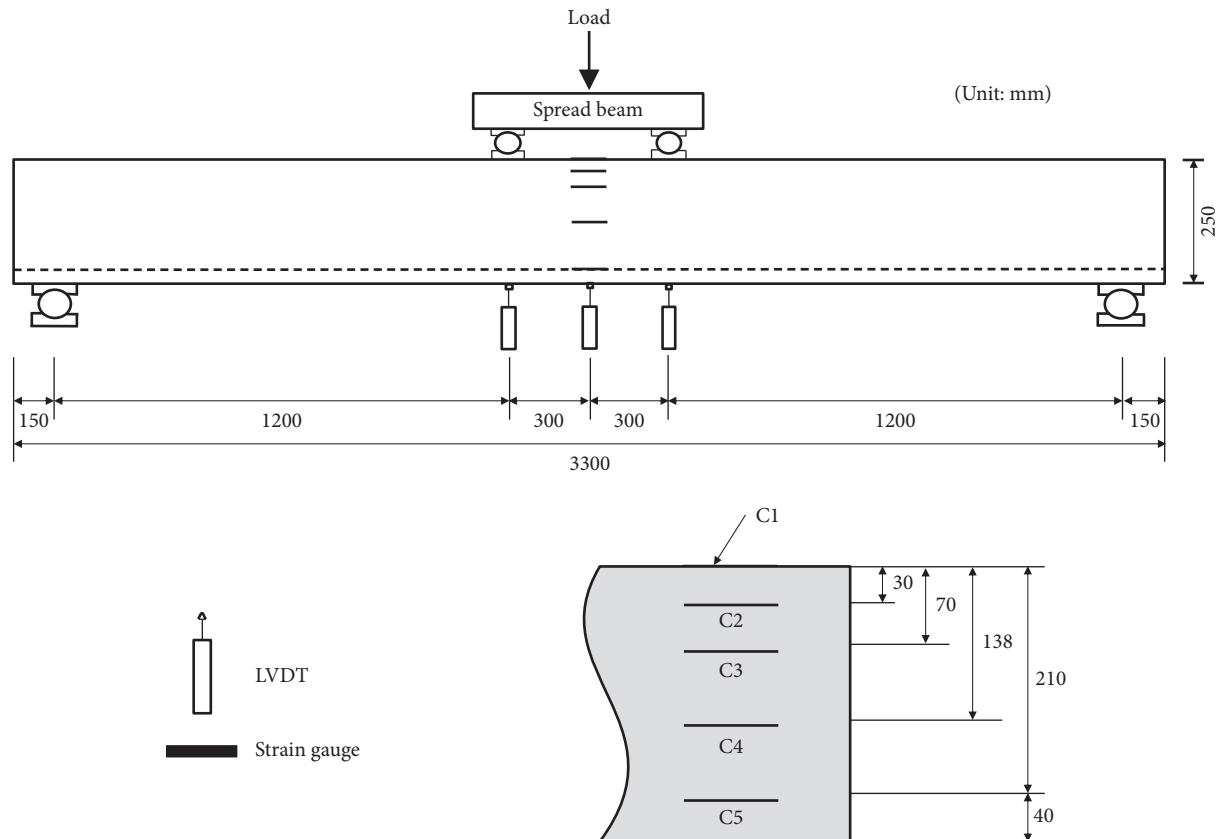
FIGURE 7: Instrumentation used for the flexural tests of the beams.

FRC120-R2 beam   FRC180-R2 beam

(a) Rebar ratio of 0.59% (R2)

FRC120-R3 beam   FRC180-R3 beam

(b) Rebar ratio of 0.89% (R3)

FRC120-R4 beam   FRC180-R4 beam

(c) Rebar ratio of 1.19% (R4)
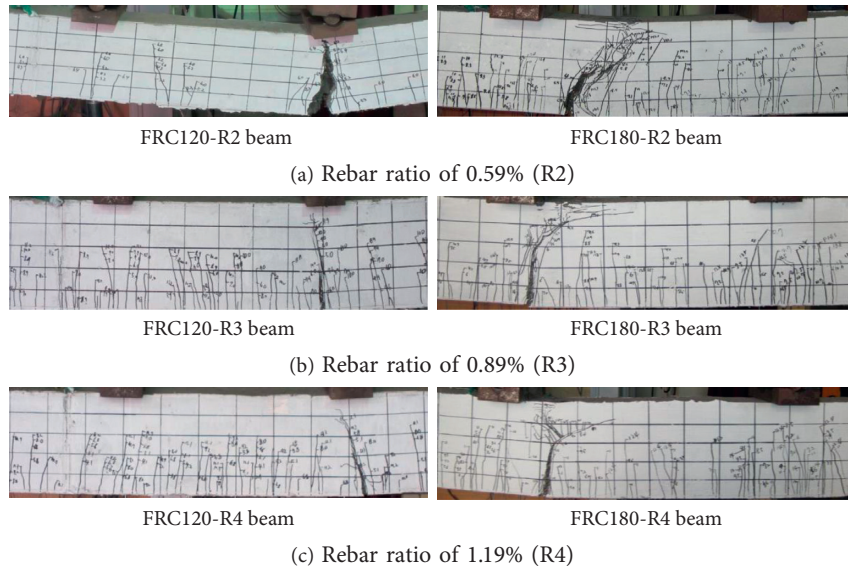
FIGURE 8: Cracking and failure of the UHPFRC beams.

(a) Rebar ratio of 0.59% (R2)

(b) Rebar ratio of 0.89% (R3)

(c) Rebar ratio of 1.19% (R4)
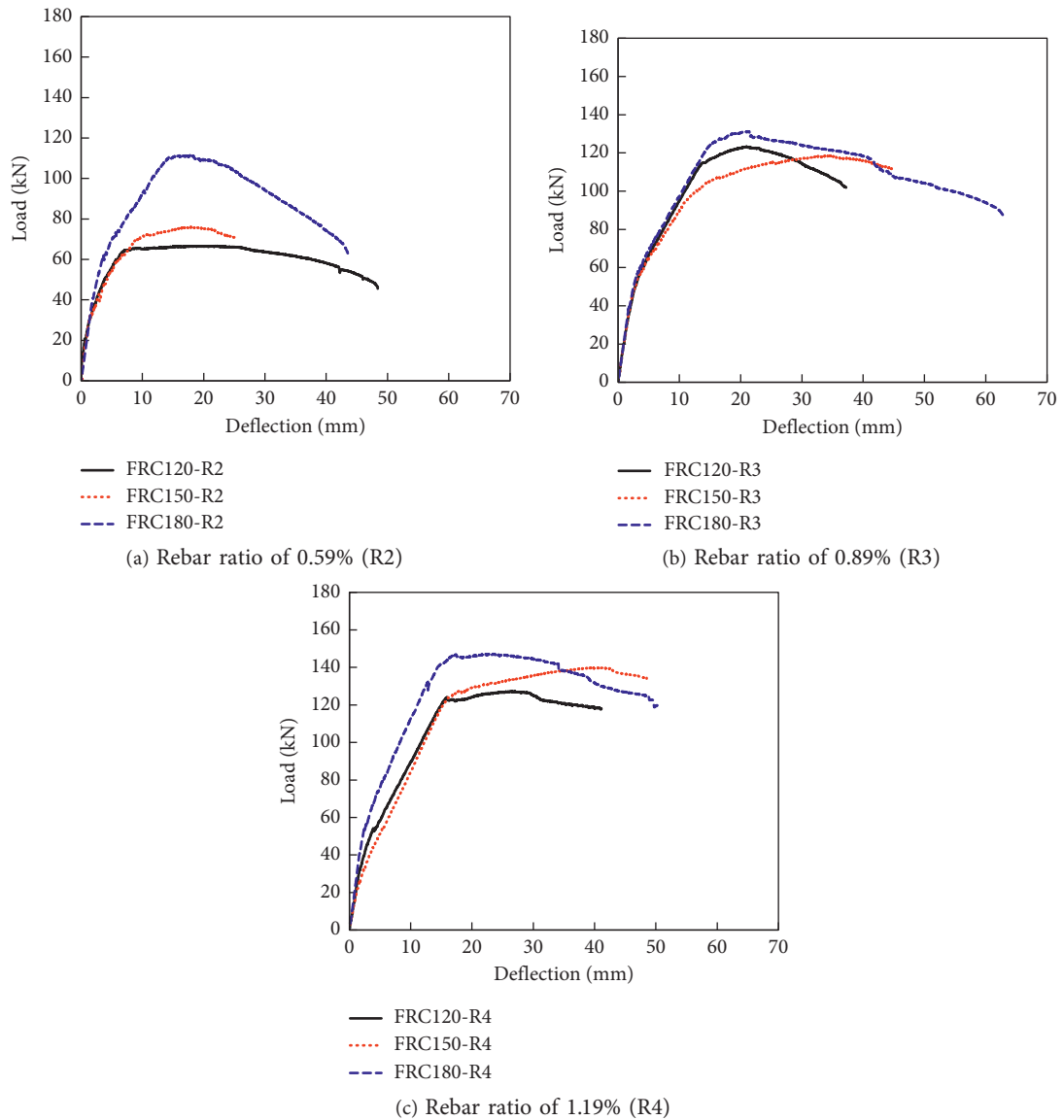
FIGURE 9: Load-deflection relationship curves.

TABLE 4: Experimental results of the beams.

Beams	Initial cracking stage			Yielding stage			Ultimate stage		
	Initial cracking load, P_{cr} (kN)	Initial cracking moment, M_{cr} (kN·m)	Initial cracking deflection, Δ_{cr} (mm)	Yielding load, P_y (kN)	Yielding moment, M_y (kN·m)	Yielding deflection, Δ_y (mm)	Ultimate load, P_u (kN)	Ultimate moment, M_u (kN·m)	Ultimate deflection, Δ_u (mm)
FRC120-R2	32.0	19.2	4.1	63.5	38.1	6.7	66.7	40.0	22.2
FRC120-R3	60.1	36.1	4.0	117.2	70.3	15.3	123.3	74.0	20.9
FRC120-R4	54.6	32.8	4.2	123.8	74.3	15.8	127.3	76.4	26.4
FRC150-R2	41.0	24.6	2.5	71.5	42.9	11.0	76.0	45.6	17.9
FRC150-R3	48.4	29.0	2.6	107.7	64.6	31.7	118.6	71.2	34.6
FRC150-R4	44.1	26.5	3.8	123.9	74.3	16.1	139.9	83.9	39.5
FRC180-R2	41.1	24.7	1.9	105.3	63.2	12.8	111.5	66.9	17.8
FRC180-R3	40.8	24.5	1.8	122.0	73.2	14.4	131.3	78.8	21.2
FRC180-R4	41.0	24.6	1.7	126.9	76.1	12.0	147.2	88.3	25.5

(a) Cross section　(b) Strain distribution　(c) Stress distribution　(d) Equilibrium of forces
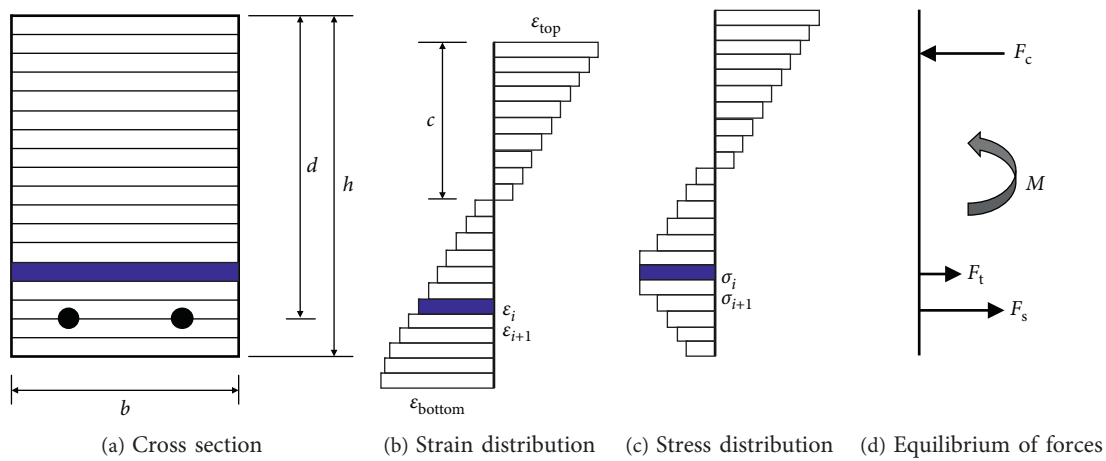
FIGURE 10: Strain compatibility and equilibrium forces in sectional analysis.

for each section should satisfy the equilibrium condition. When the forces throughout the cross section are in equilibrium, the bending moment can finally be determined.

4.2. Prediction of the Bending Capacity and Estimation of the Tensile Strength of UHPFRC Beams.

To predict the bending behavior of UHPFRC beams, two analytical approaches were used in this study. In the first approach, which is shown schematically in Figure 11, the tensile properties obtained from the CMOD test results were used as the input for the sectional analysis to obtain the moment-curvature relationship, after which the analysis result of the moment-curvature curve was compared with the experimental result. Comparisons of the analysis results and experimental results for the moment-curvature relationships are shown in Figures 12–14, in which the relationships between the moment and curvature obtained from the beam tests are plotted using the strain measurements from the beam surface. The measured strain profile along the beam height can be used to determine the curvature. However, individual strain measurements became unreliable after the crack observed at the surface of the concrete beam widened; consequently, not all curvatures are shown in the moment-curvature relationships.

The analysis result of the bending moment of the FRC120-R2 beam overestimated the experimental result, as shown in Figure 12; the ratio of the analysis result to the experimental result for the bending strength is 1.54, as shown in Table 5. Meanwhile, the analysis results of the bending strengths of the FRC120-R3 and FRC120-R4 beams were slightly greater than the experimental results; thus, the ratios of the analysis results to the test results for these two beams are 0.99 and 1.10, respectively.

For the FRC150 beam series, the analysis result of the bending moment of the FRC150-R2 beam overestimated the test result greatly; thus, the ratio of the analysis result to the experimental result for the bending strength is 1.46. Meanwhile, the analysis results of the bending moments of the FRC150-R2 and FRC150-R3 beams were in good agreement with the experimental results; thus, the ratios of the analysis results to the experimental results are 1.06 and 1.01, respectively.

In contrast to the FRC120 and FRC150 beam series, the analysis results of the FRC180 beam series were underestimated. The analysis results of the bending strengths of the FRC180-R2, FRC180-R3, and FRC180-R4 beams were less than the corresponding experimental results, with analytical-experimental result ratios of 0.92, 0.90, and 0.92, respectively.

(a) Approach I   (b) Approach II
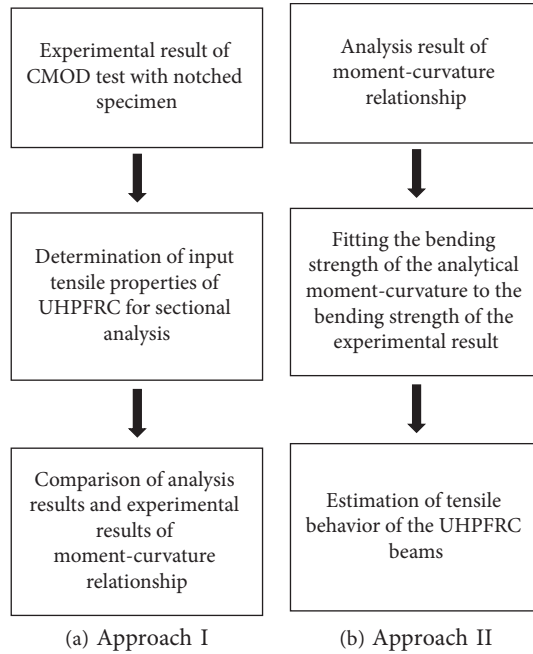
FIGURE 11: Approaches for estimating the tensile behavior of a UHPFRC beam.

(a) FRC120-R2 beam   (b) FRC120-R3 beam

(c) FRC120-R4 beam
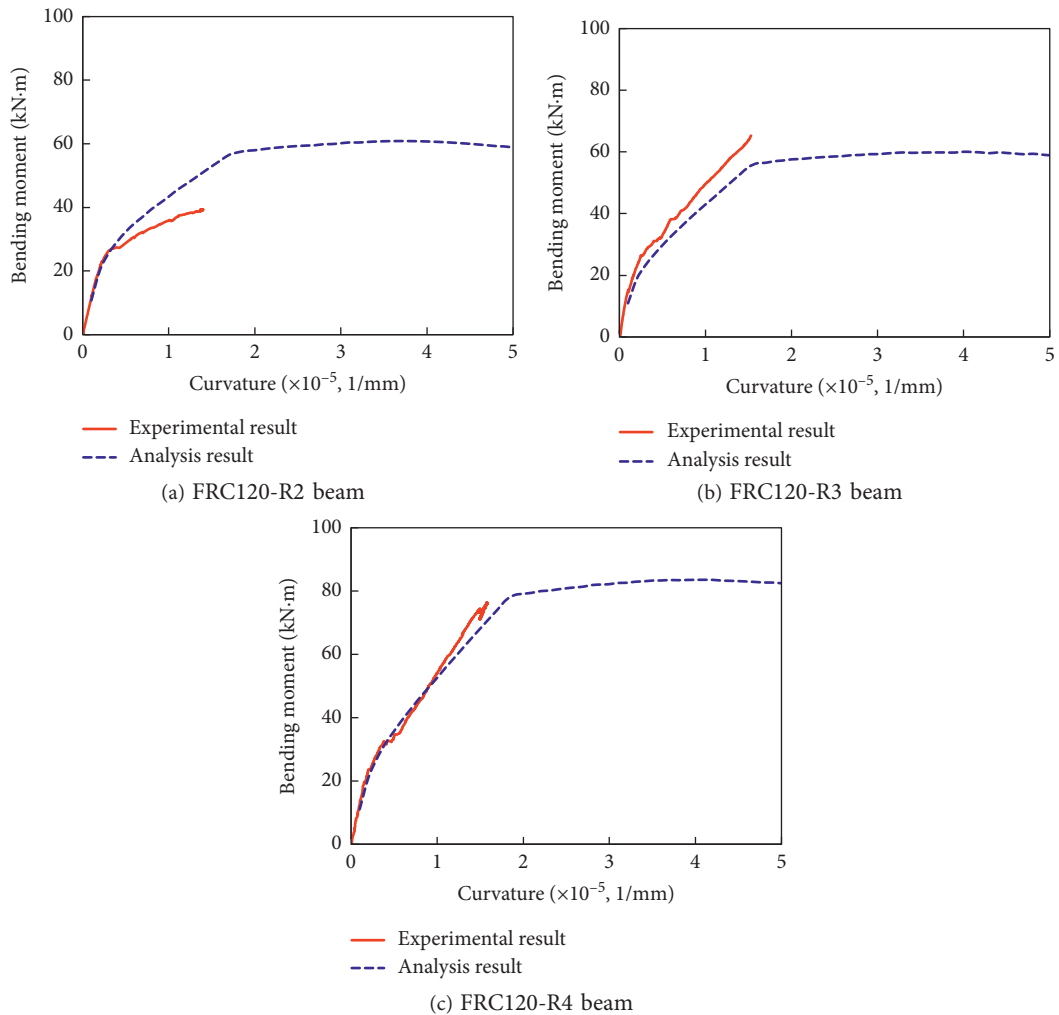
FIGURE 12: Prediction of moment-curvature curves (FRC120 series beams).

(a) FRC150-R2 beam

(b) FRC150-R3 beam

(c) FRC150-R4 beam
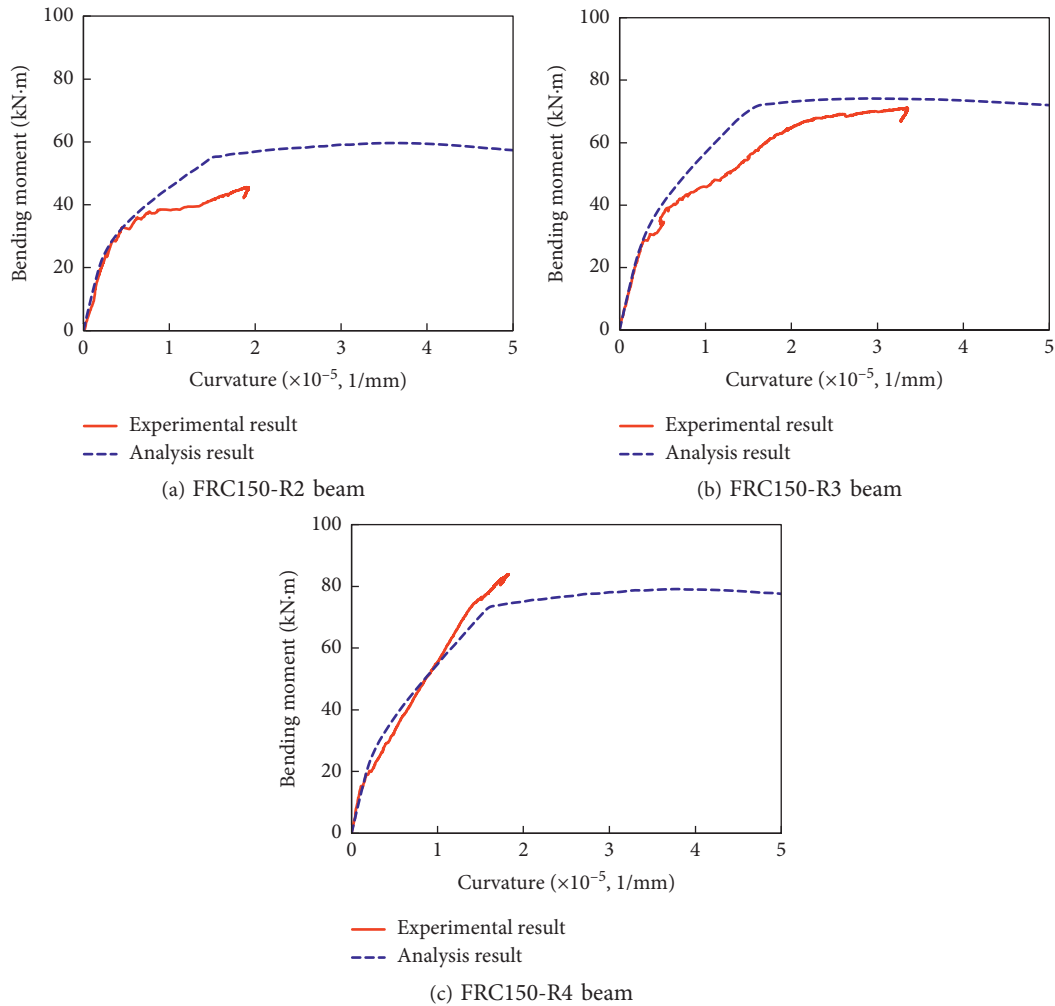
Figure 13: Prediction of moment-curvature curves (FRC150 series beams).

The most important parameter for predicting the bending moment-curvature curve of UHPFRC is the tensile strength. It is well known that an accurate prediction of the bending strength of a UHPFRC beam is dependent on the tensile strength of the UHPFRC. The deviation of the analysis result from the experimental result of the bending strength may primarily be due to the difference between the tensile strength obtained from the material test with the notched specimen and the actual tensile strength of the test beam.

Therefore, a second approach was employed to estimate the actual tensile strength of each test beam. In the second approach, a sectional analysis was performed for the moment-curvature curve to ensure that the bending strength of the analytical moment-curvature curve was in good agreement with that of the experimental result. The fitting of the bending strengths from the analytical moment-curvature curves and from the experimental work is illustrated in Figures 15–17.

The tensile strength of UHPFRC is a major parameter influencing the bending capacity of a UHPFRC beam. If the bending strength of the analysis result is almost identical to the experimental result, the tensile properties used as input for the sectional analysis can be assumed to be the actual tensile properties for the test beam.

The tensile strengths obtained from the material testing with the notched specimens and estimated by fitting the bending strengths of the analytical moment-curvature curves to the experimental result (shown in Figures 15–17) are listed in Table 5. The findings reveal that the tensile strength obtained from the material testing is different from the tensile strength estimated by fitting the moment-curvature curves between the analysis and experimental results. For example, for the FRC120 and FRC150 beam series, the tensile strength obtained from the tensile test of the notched UHPFRC specimens was greater than that estimated by fitting the bending strength determined from the analytical moment-curvature curve to that determined experimentally.

From the test of the notched prismatic specimen, the tensile strength of the FRC120 beam series was 7.21 MPa, while the estimated tensile strengths of the FRC120-R2, FRC120-R3, and FRC120-R4 beams were 2.83, 5.42, and 5.50 MPa, respectively. The tensile strength of the FRC150 beam series obtained from the test on the prismatic specimen was 9.07 MPa, while the estimated tensile strengths of the FRC150-R2, FRC150-R3, and FRC150-R4 beams were 4.59, 7.79, and 8.44 MPa, respectively. Meanwhile, the tensile strength of the

(a) FRC180-R2 beam

(b) FRC180-R3 beam

(c) FRC180-R4 beam
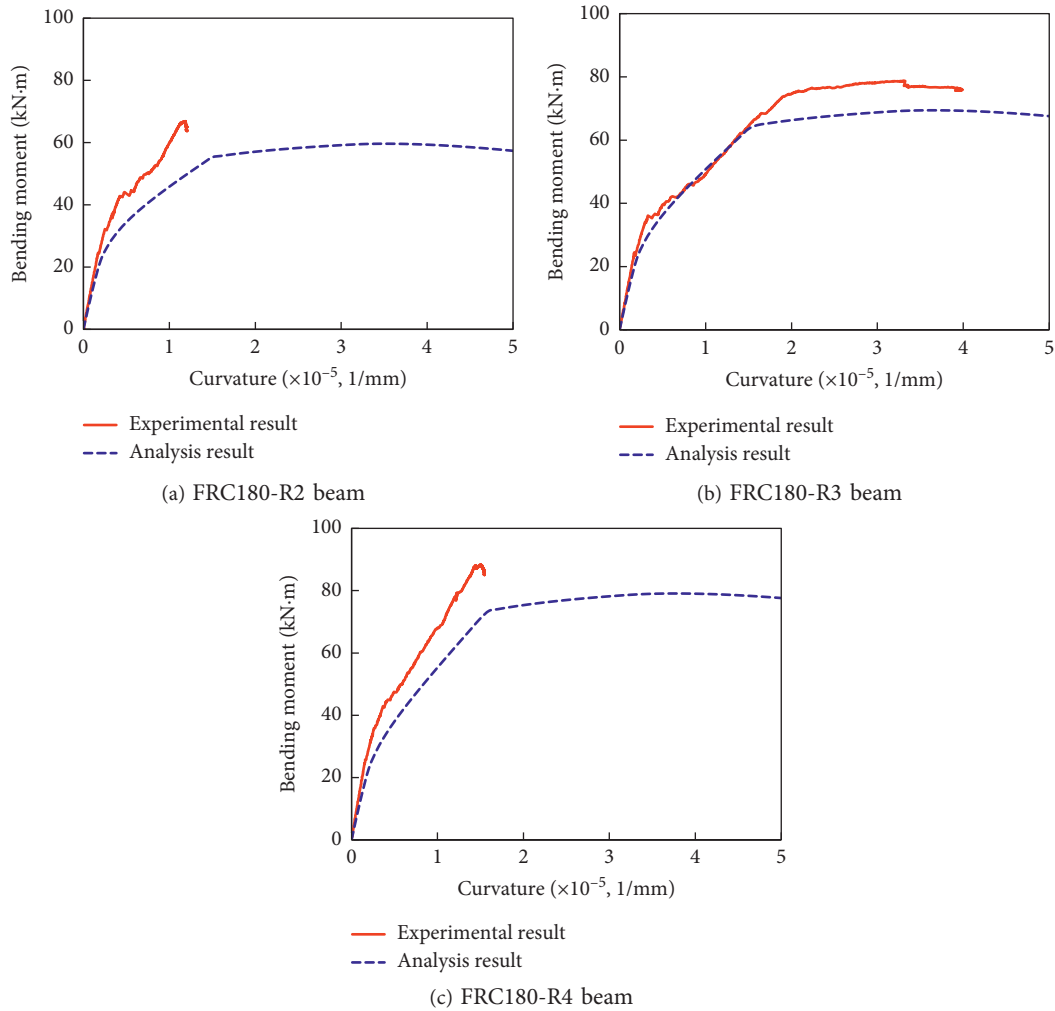
Figure 14: Prediction of moment-curvature curves (FRC180 series beams).

Table 5: Analysis results.

Beams	Tensile strength (MPa)		Bending strength (kN·m)		Ratio (2)/(1)	Difference between tensile strengths* (%)
	CMOD test result ($f_{t,test}$)	Estimation from curve fitting ($f_{t,estimation}$)	Beam test result (1)	Prediction using the tensile strength from the CMOD test (2)		
FRC120-R2	7.21	2.83	40.0	61.7	1.54	154.8
FRC120-R3	7.21	5.42	74.0	73.0	0.99	33.0
FRC120-R4	7.21	5.50	76.4	84.4	1.10	31.1
FRC150-R2	9.07	4.59	45.6	66.6	1.46	97.6
FRC150-R3	9.07	7.79	71.2	75.8	1.06	16.4
FRC150-R4	9.07	8.44	83.9	85.0	1.01	7.5
FRC180-R2	7.76	8.90	66.9	61.5	0.92	12.8
FRC180-R3	7.76	9.38	78.8	71.2	0.90	17.3
FRC180-R4	7.76	9.39	88.3	80.9	0.92	17.4

*Difference between the tensile strength obtained from the material test and that estimated by fitting the moment-curvature curves.

FRC180 beam series obtained from the tensile test was 10% less than that estimated by fitting the moment-curvature curve.

5. Conclusions

An experimental study on the flexural behavior of UHPFRC is presented in this study, and the tensile strength of UHPFRC beams is estimated by fitting the analysis result of the moment-curvature curve to the experimental result of the bending strength. Based on the experimental and analysis results, the following conclusions can be made:

(1) The width of one of the well-distributed cracks in the constant moment zone was significantly widened, and the crack became localized. The localization of

(a) FRC120-R2 beam

(b) FRC120-R3 beam

(c) FRC120-R4 beam
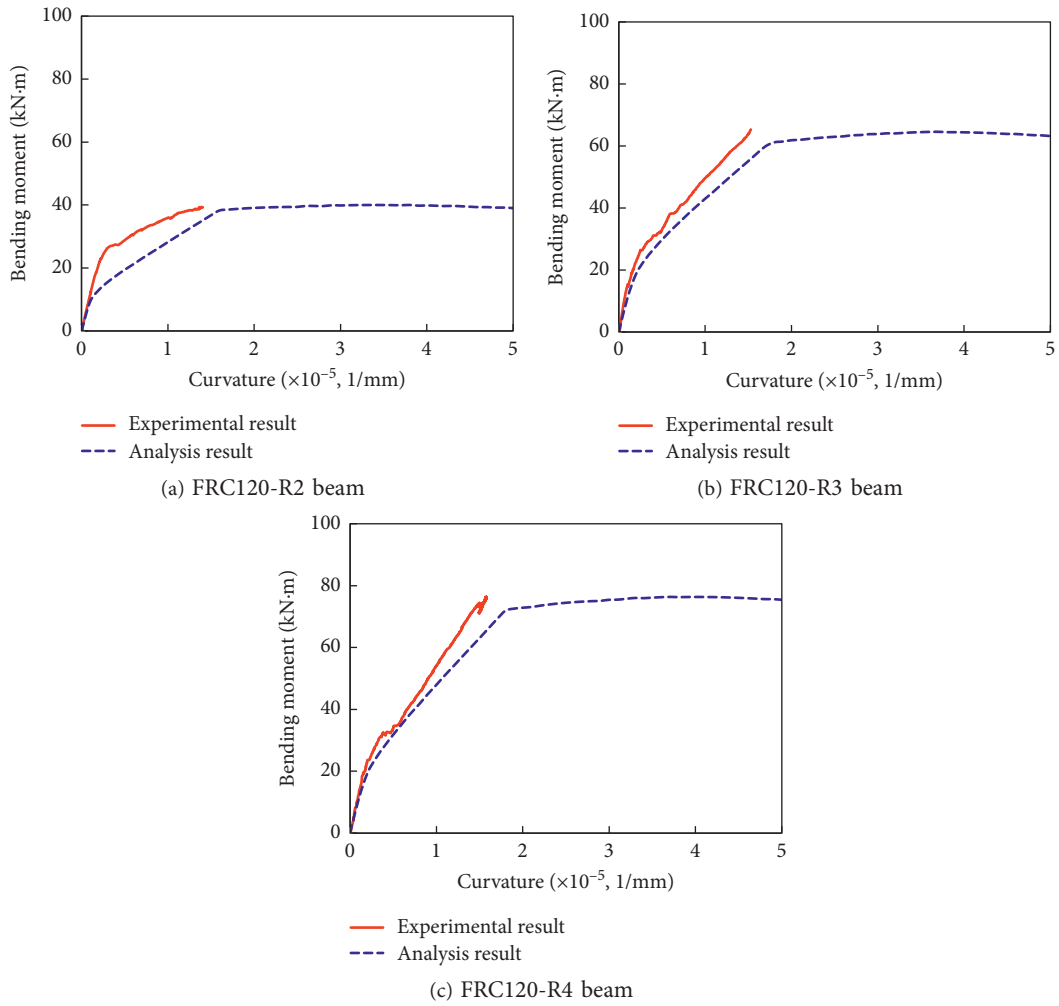
FIGURE 15: Fitting of moment-curvature curves between the experimental and analysis results (FRC120 series beams).

(a) FRC150-R2 beam

(b) FRC150-R3 beam
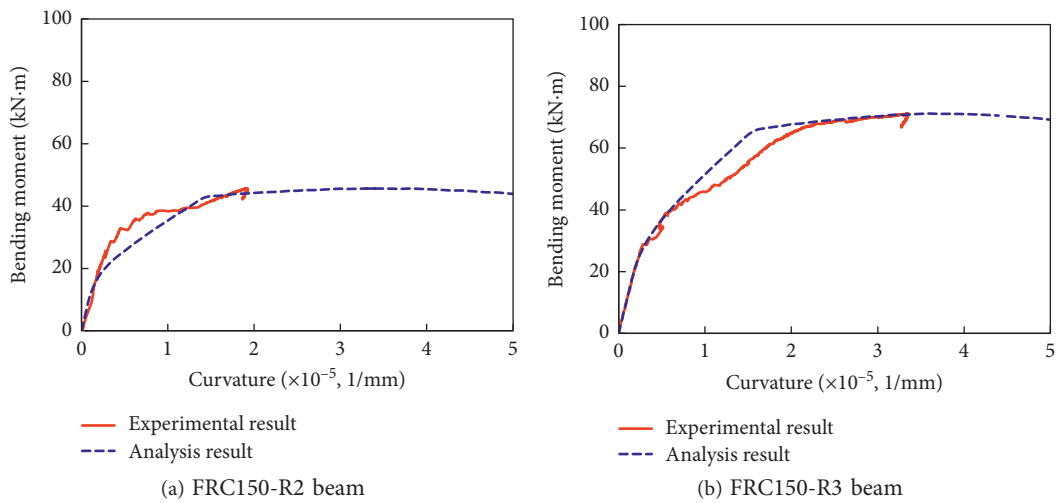
FIGURE 16: Continued.

(c) FRC150-R4 beam
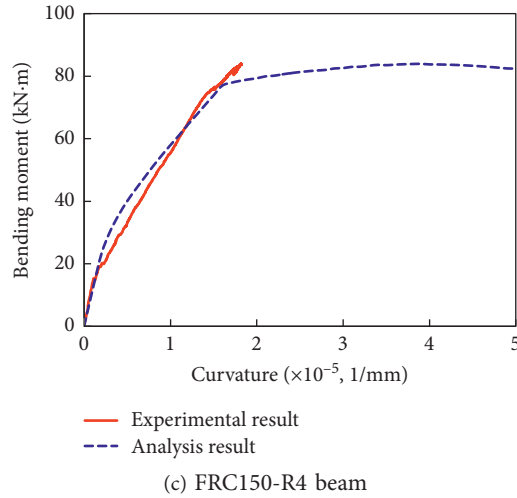
FIGURE 16: Fitting of moment-curvature curves between the experimental and analysis results (FRC150 series beams).

(a) FRC180-R2 beam

(b) FRC180-R3 beam

(c) FRC180-R4 beam
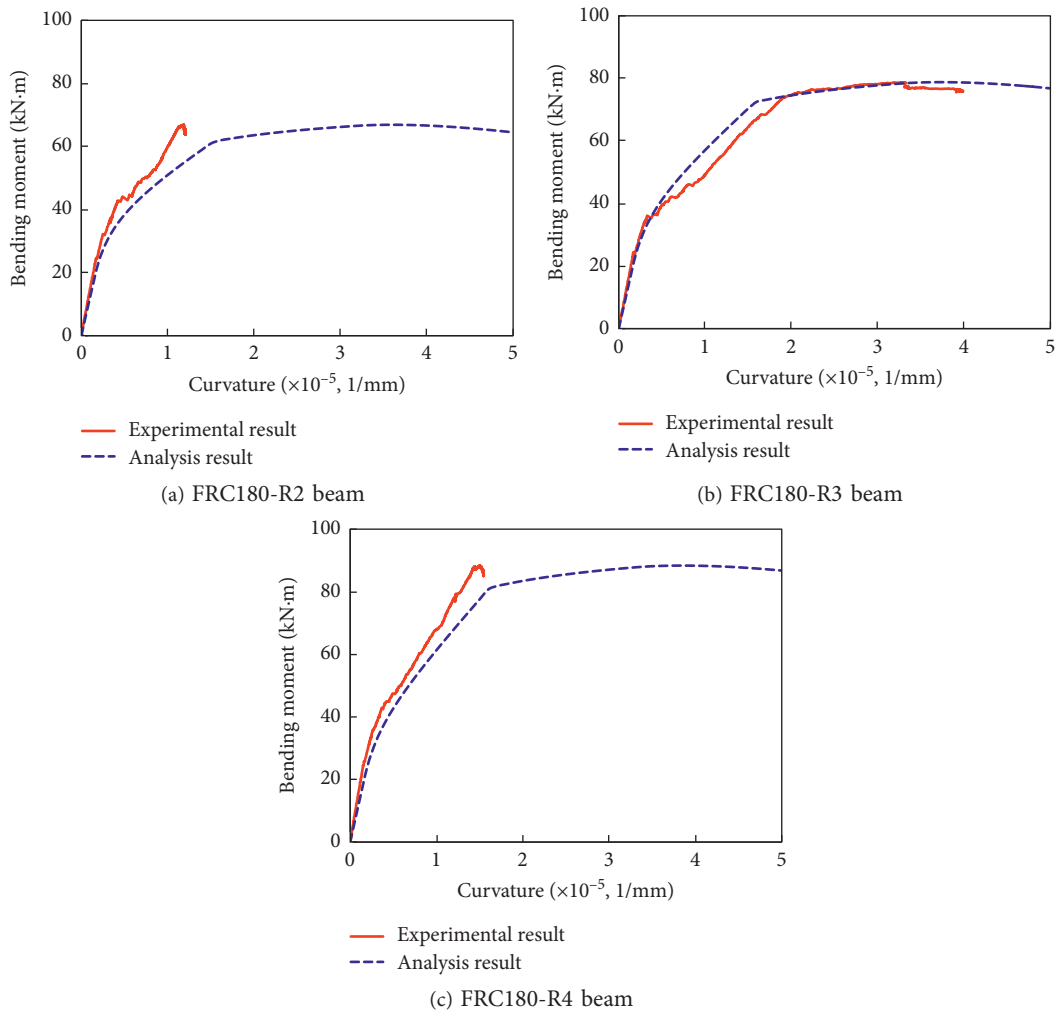
FIGURE 17: Fitting of moment-curvature curves between the experimental and analysis results (FRC180 series beams).

cracks within the constant moment region caused the bridging effect to weaken, and steel fibers were eventually pulled out of the matrix in the region of localized cracking.

(2) The bending strengths of the FRC150 and FRC180 beam series were greater than those of the FRC120 beam series, indicating that the flexural strength of the UHPFRC beams increased with the steel fiber content.

(3) The bending strength obtained from the sectional analysis using the material test result was compared with the beam test result. This comparison showed that the bending strengths of several beams differed from the corresponding test results, thereby indicating that the tensile strength obtained from the material test would be significantly different from that estimated from the beam test results. The estimated tensile strengths of the FRC120-R2, FRC120-R3, and FRC120-R4 beams were 60.7, 24.8, and 23.7% less than the tensile strength obtained from the material test, respectively. Similarly, the estimated tensile strengths of the FRC150-R2, FRC150-R3, and FRC150-R4 beams were 49.4, 14.1, and 6.9% less than the tensile strength obtained from the material test, respectively. Meanwhile, the estimated tensile strengths obtained from the FRC180 beam series were 14.7~21.0% greater than the tensile strength obtained from the material test.

(4) The tensile strengths of the UHPFRC beams were estimated reasonably by fitting the analysis results of the moment-curvature curve to the beam test results. The estimated tensile strength of the UHPFRC increased with its compressive strength.

Data Availability

The data used to support the findings of this study are available from the corresponding author upon request.

Conflicts of Interest

The authors declare that they have no conflicts of interest.

Acknowledgments

References

[1] S. H. Park, D. J. Kim, G. S. Ryu, and K. T. Koh, "Tensile behavior of ultra high performance hybrid fiber reinforced concrete," *Cement and Concrete Composites*, vol. 34, no. 2, pp. 172–184, 2012.

[2] S.-T. Kang, Y. Lee, Y.-D. Park, and J.-K. Kim, "Tensile fracture properties of an ultra high performance fiber reinforced concrete (UHPFRC) with steel fiber," *Composite Structures*, vol. 92, no. 1, pp. 61–71, 2010.

[3] S. Pyo, S. El-Tawil, and A. E. Naaman, "Direct tensile behavior of ultra high performance fiber reinforced concrete (UHP-FRC) at high strain rates," *Cement and Concrete Research*, vol. 88, pp. 144–156, 2016.

[4] A. M. T. Hassan, S. W. Jones, and G. H. Mahmud, "Experimental test methods to determine the uniaxial tensile and compressive behaviour of ultra high performance fibre reinforced concrete (UHPFRC)," *Construction and Building Materials*, vol. 37, pp. 874–882, 2012.

[5] Q. Chunxiang and I. Patnaikuni, "Properties of high-strength steel fiber-reinforced concrete beams in bending," *Cement and Concrete Composites*, vol. 21, no. 1, pp. 73–81, 1999.

[6] A. N. Dancygier and Z. Savir, "Flexural behavior of HSFRC with low reinforcement ratios," *Engineering Structures*, vol. 28, no. 11, pp. 1503–1512, 2006.

[7] C. Boulay, P. Rossi, and J. L. Tailhan, "Uniaxial tensile test on a new cement composite having a hardening behaviour," in *Proceeding of the sixth RILEM symposium in fibre-reinforced concretes (FRC)*, BEFIB, Varenna, Italy, September 2004.

[8] K. Wile, S. E. Tawil, and A. E. Naaman, "Properties of strain hardening ultra-high performance fiber reinforced concrete (UHP-FRC) under direct tensile loading," *Cement and Concrete Composites*, vol. 48, pp. 53–66, 2014.

[9] J. Z. Su, B. C. Chen, and Q. W. Huang, "Experimental studies on the flexural behavior of UHPC beams," in *Proceeding of the AFGC-ACI-fib-RILEM Int. Symposium on Ultra-High Performance Fibre-Reinforced Concrete*, UHPFRC, Montpellier, France, October 2017.

[10] H. C. Mertol, E. Baran, and H. J. Bello, "Flexural behavior of lightly and heavily reinforced steel fiber concrete beams," *Construction and Building Materials*, vol. 98, pp. 185–193, 2015.

[11] Y. Li, C. Guertin-Normoyle, O. Algassem, and H. Aoude, "Effects of ultra-high performance fibre reinforced concrete and high-strength steel on the flexural behaviour of reinforced concrete beams," in *Proceeding of the AFGC-ACI-fib-RILEM Int. Symposium on Ultra-High Performance Fibre-Reinforced Concrete*, UHPFRC, Montpellier, France, October 2017.

[12] Z. Wu, C. Shi, W. He, and L. Wu, "Effects of steel fiber content and shape on mechanical properties of ultra high performance concrete," *Construction and Building Materials*, vol. 103, pp. 8–14, 2016.

[13] M. Singh, A. H. Sheikh, M. S. Mohamed Ali, P. Visintin, and M. C. Griffith, "Experimental and numerical study of the flexural behaviour of ultra-high performance fibre reinforced concrete beams," *Construction and Building Materials*, vol. 138, pp. 12–25, 2017.

[14] G. G. K. Reddy and P. Ramadoss, "Flexural behavior of ultra-high performance steel fiber reinforced concrete: a state of the art review," *International Journal of Engineering Technology Science and Research*, vol. 4, pp. 2394–3386, 2017.

[15] S. Abbas, M. L. Nehdi, and M. A. Saleem, "Ultra-high performance concrete: mechanical performance, durability, sustainability and implementation challenges," *International Journal of Engineering Technology Science and Research*, vol. 10, no. 3, pp. 271–295, 2017.

[16] Y. Kusumawardaningsih, E. Fehling, M. Ismail, and A. A. M. Aboubakr, "Tensile strength behavior of UHPC and UHPFRC," *Procedia Engineering*, vol. 125, pp. 1081–1086, 2015.

[17] G. M. Ren, H. Wu, Q. Fang, and J. Z. Liu, "Effects of steel fiber content and type on static mechanical properties of UHPCC," *Construction and Building Materials*, vol. 163, pp. 826–839, 2018.

[18] D.-Y. Yoo, J.-H. Lee, and Y.-S. Yoon, "Effect of fiber content on mechanical and fracture properties of ultra high performance fiber reinforced cementitious composites," *Composite Structures*, vol. 106, pp. 742–753, 2013.

[19] D.-Y. Yoo, Y.-S. Yoon, and N. Banthia, "Flexural response of steel-fiber-reinforced concrete beams: effects of strength, fiber content, and strain-rate," *Cement and Concrete Composites*, vol. 64, pp. 84–92, 2015.

[20] A. Abrishambaf, M. Pimentel, and S. Nunes, "Influence of fibre orientation on the tensile behaviour of ultra-high performance fibre reinforced cementitious composites," *Cement and Concrete Research*, vol. 97, pp. 28–40, 2017.

[21] S.-T. Kang and J.-K. Kim, "Investigation on the flexural behavior of UHPCC considering the effect of fiber orientation distribution," *Construction and Building Materials*, vol. 28, no. 1, pp. 57–65, 2012.

[22] I. H. Yang, C. B. Joh, and B. S. Kim, "Structural behavior of ultra-high performance concrete beams subjected to bending," *Engineering Structure*, vol. 32, no. 11, p. 3487, 2010.

[23] H. Al-Mattarneh, "Electromagnetic quality control of steel fiber concrete," *Construction and Building Materials*, vol. 73, pp. 350–356, 2014.

[24] S. Nunes, M. Pimentel, F. Ribeiro, P. Milheiro-Oliveira, and A. Carvalho, "Estimation of the tensile strength of UHPFRC layers based on non-destructive assessment of the fibre content and orientation," *Cement and Concrete Composites*, vol. 83, pp. 222–238, 2017.

[25] B. A. Graybeal, "Compressive behavior of ultra-high-performance fiber-reinforced concrete," *ACI Materials Journal*, vol. 104, no. 2, pp. 146–152, 2007.

[26] AFGC-SETRA, *Ultra High Performance Fibre-Reinforced, Recommendations*, AFGC, Paris, France, Revised edition, 2013.

Research Article

Analysis of Hydration and Optimal Strength Combinations of Cement-Limestone-Metakaolin Ternary Composite

Xiao-Yong Wang ⓘD

Department of Architectural Engineering, Kangwon National University, Chuncheon-Si, Republic of Korea

Correspondence should be addressed to Xiao-Yong Wang; wxbrave@kangwon.ac.kr

Metakaolin (MK) is an aluminosilicate pozzolan material and can contribute to property development of concrete due to the pozzolanic reaction. Limestone (LS) powder presents the dilution effect, nucleation effect, and chemical effect on hydration of cement. When metakaolin and limestone are used together, due to the additional chemical reaction between the aluminum phase in MK and limestone, the synergetic benefit can be achieved. This study presents a hydration model for cement-limestone-metakaolin ternary blends. Individual reactions of cement, metakaolin, and limestone are simulated separately, and the interactions among cement hydration, limestone reaction, and metakaolin reaction are considered through the contents of calcium hydroxide and capillary water. The hydration model considers the pozzolanic reaction of metakaolin, chemical and physics effects of limestone, and synergetic effect between metakaolin and limestone. Furthermore, the gel-space ratio of hydrating concrete is calculated using reaction degrees of binders and concrete mixtures. The strength development of ternary blends is evaluated using the gel-space ratio. Based on parameter analysis, the synergetic effect on strength development is shown and the optimal combinations of cement-limestone-metakaolin ternary blends are determined.

1. Introduction

Metakaolin is increasingly used in modern concrete industry. The addition of metakaolin can make many advantages on the performance of concrete. Metakaolin can enhance workability and finishing ability, increase compressive and flexural strength, and reduce chloride permeability. However, metakaolin-blended binary concrete has some drawbacks. As the replacement level of cement by metakaolin increases, an increased amount of superplasticizer is necessary to reach the required consistency. The material cost of the metakaolin is higher than that of cement. To avoid these drawbacks, the substitution level of cement by metakaolin is generally lower than 25%. Summarily, the benefits of metakaolin, such as mechanical performance and extended service life, may overcome its negative effect. Metakaolin is a very promising supplementary cementitious material for the concrete industry [1, 2].

Limestone powder can improve the workability, reduce the bleeding, and reduce the amount of CO_2 emission of the concrete industry. The price of limestone is much lower than

that of metakaolin. The addition of limestone lowers the late-age strength of concrete. When limestone and metakaolin are used together, the pozzolanic reaction of metakaolin can contribute to concrete late-age strength. In addition, metakaolin has a high aluminum content which can react with limestone, form carboaluminate phases, and increase solid volume and strength of concrete. This is the synergetic effect of ternary concrete. While metakaolin or limestone is added individually, the synergetic effect cannot be achieved. In summary, when using metakaolin- and limestone ternary-blended concrete, the economic benefit and strength benefit can be achieved [1, 2].

Many experimental studies have been done about workability, mechanical, and durability aspects of cement-limestone-metakaolin ternary blends. Vance et al. [3] reported that, for cement-limestone-metakaolin ternary blends, the yield stress reduces as the limestone content increases. This is because of the particle packing, water demand, and interparticle spacing and contacts. Vance et al. [4] found that the synergetic effect of limestone and MK incorporation can improve early-age properties and

maintain late-age properties of concrete. Alvarez et al. [5] presented that combined mixtures of limestone and MK enhance compressive strength compared with 100% Portland cement concrete. Ramezanianpour and Hooton [6] presented that carboaluminate hydrates are formed for cement-limestone-MK ternary blends, and there is an optimum level of limestone in terms of the maximum strength and minimum porosity. Perlot et al. [7] reported that ternary-blended mix presents a real benefit for carbonation durability performances due to the refinement of the pore structure. Sotiriadis et al. [8] reported that the use of MK in the limestone cement concrete retards and inhibits deterioration due to the sulfate attack and improves its durability.

Compared with abundant experimental studies, the theoretical models about cement-limestone-metakaolin ternary blends are very limited. Antoni et al. [9] made the thermodynamic model for cement-limestone-metakaolin ternary blends and present phase assemblage for different combinations of binders. Shi et al. [10, 11] presented the thermodynamic model for carbonation and chloride ingression of cement-limestone-metakaolin ternary blends. Changes in phase assemblages and total porosities due to carbonation and chloride exposure are evaluated [10, 11]. The thermodynamic models [9–11] mainly focus on the chemical aspect of ternary blends, such as the phase assemblages of hydrated concrete and reaction products between concrete and ingression ions. However, limited works was done about mechanical aspects, such as the evaluation of strength development and optimal combinations of binders of ternary blends [9–11].

Optimal combinations of binders of ternary blends are an interesting topic for concrete manufacture and construction company. This study presents a blended hydration model for ternary blends considering the synergetic effect between limestone and MK. The strength development of ternary blends is evaluated using reaction degrees of binders and gel-space ratios. Based on parameter analysis, the optimal combinations of cement-limestone-metakaolin ternary blends are determined.

2. Hydration Model and Strength Model for Ternary Blends

2.1. Hydration Model.
For MK- and limestone-blended concrete, the hydration of cement, the reaction of MK, and reaction of limestone coexist. In this study, we simulate the hydration of cement, MK, and limestone, respectively. Meanwhile, the interactions among cement hydration, metakaolin reaction, and limestone reaction are considered through the contents of capillary water and calcium hydroxide in hydrating blends.

2.1.1. Cement Hydration Model.
The hydration of cement can be described using a kinetic model shown in our former studies [12]. The degree of hydration α can be calculated as $\alpha = \int_0^t (d\alpha/dt)dt$, where t is the time and $d\alpha/dt$ is the rate of hydration, which can be determined as follows:

$$\frac{d\alpha}{dt} = f(B, C, \text{De}, \text{kr}) * \lambda_1 * \lambda_2, \tag{1}$$

where B and C are the rate-determining coefficients in the initial dormant period, De is the reaction parameter in the diffusion-controlled period, kr is the reaction parameter in the phase boundary-controlled period, λ_1 considers the reduction of the hydration rate due to development of microstructure, and λ_2 considers the reduction of hydration rate due to the consumption of capillary water ($\lambda_2 = W_{\text{cap}}/W_0$, where W_{cap} is the amount of capillary water and W_0 is the amount of water in concrete mixtures).

The kinetic processes involved in cement hydration, such as the initial dormant process, phase boundary reaction process, and diffusion process, are considered in the cement hydration model. The input variables of the cement hydration model are cement compound compositions, Blaine surface of cement, concrete mixing proportions, and curing conditions. The values of hydration parameters B, C, De, and kr can be determined using cement compound compositions. Furthermore, the reaction degree of cement can be calculated automatically using hydration parameters B, C, De, and kr. The effect of curing temperature on cement hydration is considered using Arrhenius law [12]. For high-strength concrete, the water-to-cement ratio is low, and the hydration rate is significantly lowered due to the reduction of capillary water [13, 14]. This effect is considered using capillary water concentration λ_2. Summarily, the proposed cement hydration model is valid for concrete with different strength levels, different types of Portland cement, and different curing conditions [12].

2.1.2. MK Reaction Model.
The reaction process of MK also consists of the initial dormant process, phase boundary reaction process, and diffusion process, which is similar with the processes involved in hydration of cement [15]. On the contrary, MK is a pozzolanic material. The reaction rate of the pozzolanic reaction is dependent on the amount of calcium hydroxide in blends [16, 17]. Considering the kinetic reaction processes and the essence of MK as the pozzolanic material, Wang [15] proposed that the reaction equation of MK can be written as follows:

$$\frac{d\alpha_{\text{MK}}}{dt} = f(B_{\text{MK}}, C_{\text{MK}}, \text{De}_{\text{MK}}, \text{kr}_{\text{MK}}) * \frac{\text{CH}(t)}{P}, \tag{2}$$

where α_{MK} is the reaction degree of MK, $d\alpha_{\text{MK}}/dt$ is the reaction rate of MK, B_{MK} and C_{MK} are reaction parameters of MK in the dormant period, De_{MK} is the reaction parameter of MK in the diffusion-controlled period, kr_{MK} is the reaction parameter of MK in the phase boundary-controlled period, $\text{CH}(t)$ is the content of calcium hydroxide in blends, and P is the content of MK in concrete mixtures. The verifications of the MK reaction model are available in our former study [15]. An integrated hydration-strength-durability model for MK-blended concrete is proposed for evaluating the reaction degrees of binders, strength development, and chloride penetrability [15].

2.1.3. Limestone Reaction Model. The addition of limestone powder presents the dilution effect, nucleation effect, and chemical effect on hydration of cement. In this study, dilution effect is considered through the amount of capillary water, nucleation effect is considered through a nucleation effect indicator, and chemical effect is considered through a logarithm function with multiple modification factors [18, 19].

The hydration products of cement can form on the surface of limestone powder. This is called as the nucleation effect. The nucleation effect indicator of limestone powder can be written as follows [2]:

$$L_r = \frac{LS_0 * S_{LS}}{C_0 * S_C}, \tag{3}$$

where L_r is the limestone nucleation effect indicator; LS_0 and C_0 are the mass of limestone and cement in mixing proportions, respectively; and S_{LS} and S_C are the Blaine surface area of limestone powder and cement, respectively.

In our former study [2], based on the experimental results of hydration degree of cement in cement-limestone binary blends, Wang and Luan [2] proposed that the nucleation effect of limestone powder can be described as follows:

$$k_{rLS} = k_r (1 + 1.2L_r), \tag{4}$$

$$D_{eLS} = D_e (1 + 1.2L_r), \tag{5}$$

where k_{rLS} is the updated phase boundary reaction coefficient in cement-limestone blends, 1.2 is enhancing coefficients of k_r [2], D_{eLS} is the updated diffusion coefficient in cement-limestone blends, and 1.2 is enhancing coefficients of D_e [2].

Until now, the experimental results about the reaction degree of limestone are very limit. Tentatively, Wang and Luan [2] proposed an empirical model with multi-modification factors for analyzing the reaction degree of limestone. The empirical model considers the effects of various factors on the chemical reaction of limestone, such as limestone replacement ratios, mineral admixtures additions, limestone fineness, cement fineness, water-to-binder ratio, and curing temperature. The empirical model for the limestone reaction is shown as follows:

$$\alpha_{LS1} = 0.0087 \ln(t) - 0.0265, \quad t > 21 \text{ hours}, \tag{6}$$

$$\alpha_{LS} = \alpha_{LS1} * m_1 * m_2 * m_3 * m_4 * m_5 * m_6, \tag{7}$$

where α_{LS1} is the reaction degree of limestone in a reference mixture. This reference mixture is Portland cement, and limestone binary blends with a water-to-binder ratio 0.5 and 20% limestone addition cured at 20°C. m_1 considers the effect of limestone replacement ratios on the reaction degree of limestone, m_2 considers the effect of limestone fineness, m_3 considers the effect of cement fineness, m_4 considers the effect of MK addition, m_5 considers the effect of the water-to-binder ratio, and m_6 considers the effect of the curing temperature. Table 1 shows the summary of influencing factors of the limestone reaction. As limestone replacement ratio increases,

reaction degree of LS decreases. While fineness of limestone, fineness of cement, MK addition, and water to binder ratio increase, the reaction degree of LS increases. Especially, for modification factor $m_4 = 1 + (Al_{MK} \alpha_{MK} P / Al_C \alpha C_0)$, where Al_{MK} is the aluminum content in MK, Al_C is the aluminum content in cement, $Al_{MK} \alpha_{MK} P$ in the numerator is reacted aluminum content from the MK reaction, and $Al_C \alpha C_0$ in denominator is the reacted aluminum content from the cement reaction. Because the aluminum content in MK is much higher than that in cement, the addition of MK can significantly improve the reactivity of limestone. The factor m_4 considers the synergetic effect of limestone and MK. A higher aluminum content and a higher reactivity of MK are effective to enhance the reactivity of limestone.

Summarily, this study considers the dilution effect, nucleation effect, and chemical effect of limestone additions. The enhancement of limestone reactivity due to the addition of metakaolin is considered through a modification factor. The influences of other factors, such as limestone replacement ratio, fineness of binders, and water-to-binder ratios, are also considered in the limestone reaction model.

2.1.4. Interaction Model among Cement, Metakaolin, and Limestone. In this study, the interactions among cement hydration, metakaolin reaction, and limestone reaction are considered through the contents of capillary water and calcium hydroxide. Maekawa et al. [13] proposed that, as 1 g cement hydrates, 0.4 g capillary water will be consumed. Dunster et al. [20] proposed that, as 1 g metakaolin reacts, 0.55 g capillary water will be consumed. Bentz [21] proposed that, as 1 g limestone reacts, 1.62 g capillary water will be consumed. For hydrating cement-metakaolin-limestone ternary blends, the content of capillary water can be determined as follows:

$$W_{cap} = W_0 - 0.4 * C_0 * \alpha - 0.55 * \alpha_{MK} * P \\ - 1.62 * LS_0 * \alpha_{LS}, \tag{8}$$

where $0.4 * C_0 * \alpha$, $0.55 * \alpha_{MK} * P$, and $1.62 * LS_0 * \alpha_{LS}$ are the contents of consumed water from cement hydration, metakaolin reaction, and limestone reaction, respectively [13, 20, 21]. The consumption of capillary water from the 1 g limestone reaction is much higher than those of cement and metakaolin. This is because the reaction products of limestone powder are monocarboaluminate and ettringite which contains abundant water.

For hydrating cement-metakaolin-limestone ternary blends, the content of calcium hydroxide can be determined as follows:

$$CH(t) = RCH_{CE} * C_0 * \alpha - v_{MK} * \alpha_{MK} * P, \tag{9}$$

where RCH_{CE} means the mass of CH produced from the hydration of 1 unit mass of cement and v_{MK} means the mass of CH consumed from the reaction of 1 unit mass of metakaolin [15]. $RCH_{CE} * C_0 * \alpha$ is the mass of CH produced from cement hydration. $v_{MK} * \alpha_{MK} * P$ is the mass of CH consumed from the metakaolin reaction.

TABLE 1: Summary of influencing factors of the limestone reaction.

Factor	Equation	Influencing trend
Limestone replacement ratios	$m_1 = 0.2/(LS_0/(C_0 + LS_0))$	As the limestone replacement ratio increases, α_{LS} decreases
Fineness of limestone	$m_2 = 1.0131 - 0.0144 * d_{LS}$, where d_{LS} is an average diameter of limestone	As fineness of limestone increases, α_{LS} increases
Fineness of cement	$m_3 = 0.55(S_C/S_{C1}) + 0.45$, where S_{C1} is the Blaine surface of cement used in the reference study	As fineness of cement increases, α_{LS} increases
Metakaolin additions	$m_4 = 1 + (Al_{MK}\alpha_{MK}P/Al_C\alpha C_0)$	As the MK addition increases, α_{LS} increases
Water-to-binder ratios	$m_5 = \alpha/\alpha_{0.5}$, where $\alpha_{0.5}$ is the reaction degree of cement in the reference study	As water-to-binder ratio increases, α_{LS} increases
Curing temperature	$m_6 = 1$	Curing temperature does not present significant influence on α_{LS}

Summarily, the effect of cement hydration, metakaolin reaction, and limestone reaction on the contents of capillary water and calcium hydroxide is considered. The capillary water content can be used for the cement hydration model (equation (1)), and the calcium hydroxide content can be used for the metakaolin reaction model (equation (2)). In addition, because the blended hydration model has considered the interactions among cement, metakaolin, and limestone reactions, the coefficients of the hydration model do not vary with different mixtures. When the mixtures change from one to another, the coefficients of the hydration model are constant.

2.2. Strength Development Model.

The gel-space ratio denotes the ratio of the volume of binder hydration products to the sum of volume of hydrated binders and capillary pore. For cement-metakaolin-limestone blends, 1 ml hydrated cement, 1 ml reacted metakaolin, and 1 ml reacted limestone occupy 2.06 ml of space [16, 22], 2.52 ml space [16, 22], and 4.1 ml space, respectively. Reacted products of 1 ml limestone can occupy much higher space that those of cement (4.1 vs. 2.06). This is due to the development of ettringite and monocarboaluminate from the limestone reaction. Considering the reactions of cement, metakaolin, and limestone, the gel-space ratio of cement-metakaolin-limestone ternary-blended cement can be determined as follows:

$$x_c = \frac{2.06(1/\rho_C)\alpha C_0 + 2.52(1/\rho_{MK})\alpha_{MK}P + 4.1(1/\rho_{LS})\alpha_{LS}LS_0}{(1/\rho_C)\alpha C_0 + (1/\rho_{MK})\alpha_{MK}P + (1/\rho_{LS})\alpha_{LS}LS_0 + W_0},$$ (10)

where ρ_C, ρ_{MK}, and ρ_{LS} are densities of cement, metakaolin, and limestone powder, respectively.

According to Powers' strength theory, the compressive strength of hydrating concrete can be evaluated using the gel-space ratio as follows:

$$f_c(t) = Ax_c^n,$$ (11)

where $f_c(t)$ is the concrete compressive strength, A is the intrinsic strength of concrete, and n is the strength exponent.

For cement-metakaolin-limestone blends, cement, metakaolin, and limestone will affect the intrinsic strength of concrete and strength exponent. We assume that the intrinsic strength of concrete A and strength exponent n is proportional to the weight fractions of cement, metakaolin, and limestone in the mixing proportion as follows:

$$A = a1 * \frac{C_0}{C_0 + P + LS_0} + a2 * \frac{P}{C_0 + P + LS_0} + a3 * \frac{LS_0}{C_0 + P + LS_0},$$ (12)

$$n = b1 * \frac{C_0}{C_0 + P + LS_0} + b2 * \frac{P}{C_0 + P + LS_0} + b3 * \frac{LS_0}{C_0 + P + LS_0},$$ (13)

where coefficients $a1$, $a2$, and $a3$ in equation (12) represent the contributions of cement, metakaolin, and limestone to the intrinsic strength of concrete, respectively, and the units of $a1$, $a2$, and $a3$ are MPa; the coefficients $b1$, $b2$, and $b3$ in equation (13) represent the contributions of cement, metakaolin, and limestone to the strength exponent, respectively. For neat Portland cement concrete without limestone or metakaolin, the strength of concrete only pertains to $a1$ and $b1$. For metakaolin-blended binary concrete without limestone, the strength of concrete pertains to coefficients $a1$, $a2$, $b1$, and $b2$. For ternary-blended concrete, the strength of concrete pertains to coefficients $a1$, $a2$, $a3$, $b1$, $b2$, and $b3$. These coefficients $a1$, $a2$, $a3$, $b1$, $b2$, and $b3$ do not change for various mixing proportions of concrete.

The flowchart of calculation is proven in Figure 1. Each time step, the response levels of cement, metakaolin, and limestone powder are calculated by utilizing ternary-blended hydration model. The quantity of CH and capillary water are based on using reaction levels of binders and concrete mixtures. In addition, the gel-space ratio of hydrating concrete is decided, thinking about the contributions from reactions of cement, metakaolin, and limestone reactions. By utilizing Powers' strength theory, the compressive strength of hardening concrete is calculated.

3. Verifications of Proposed Models

3.1. Verification of Hydration Model.

Experimental results from Antoni et al. [9] are used to verify the proposed blended hydration model and strength development model.
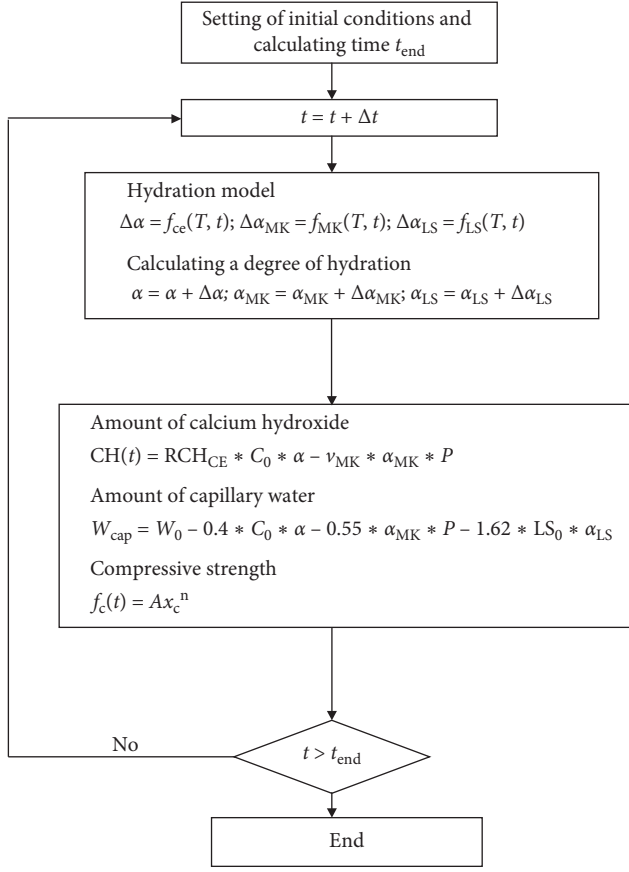
FIGURE 1: Flowchart of simulation.

TABLE 2: Chemical compositions of binders.

	Cement (%)	Limestone (%)	Metakaolin (%)
SiO_2	21.01	0.04	50.62
Al_2O_3	4.63	0.06	46.91
Fe_2O_3	2.60	0.05	0.38
CaO	64.18	56.53	0.02
MgO	1.82	0.10	0.09
SO_3	2.78	-	0.08
Na_2O	0.20	0.04	0.28
K_2O	0.94	0.04	0.18
TiO_2	0.14	0.03	1.29
Others	0.44	0.02	0.16
Loss on ignition (LOI)	1.26	43.09	0.00
Total	100.0	100.0	100.0

TABLE 3: Mixing proportions of specimens [9].

	Cement (%)	Limestone (%)	Metakaolin (%)
PC	100	0	0
LS15	85	15	0
MK30	70	0	30
B15	85	5	10
B30	70	10	20
B45	55	15	30
B60	40	20	40

Antoni et al. [9] measured the reaction degrees of binder and compressive strength of cement-MK-LS ternary-blended concrete. The chemical compositions of cement, metakaolin, and limestone are shown in Table 2. The mixing proportions are shown in Table 3. Paste specimens with a water-to-binder ratio of 0.4 were used for measuring reaction degree of binders. Mortar specimens with a water-to-binder ratio of 0.5 were used for measuring compressive strength. For cement-limestone binary blends, the replacement ratio of limestone was 15%, while for cement-metakaolin binary blends, the replacement ratio of metakaolin was 30%. For ternary-blended specimens, the sum of limestone and metakaolin ranged from 15% to 60%, and the mass ratio of metakaolin to limestone was fixed as 2. The reaction degrees and strength were measured at the ages of 1, 7, 28, and 90 days.

The input parameters of the ternary-blended cement hydration model are concrete mixtures, curing temperature, and compound compositions and Blaine surface areas of binders. By using the blended cement hydration model, the reaction degree of MK and LS is calculated and shown in Figure 2.

As shown in Figure 2(a), the sequences of the reaction degree of MK from higher to lower are B15 > B30 > MK30 > B45 > B60. This can be explained using the MK reaction model (equation (2)). As shown in equation (2), the reaction degree of MK mainly depends on the mass ratio of cement to MK. As the ratio of cement to MK increases, the activation effect from cement hydration is enhanced, and reaction degree of MK increases. The mass ratios of cement to MK were 8.5, 3.5, 2.33, 1.83, and 1 in the mixtures of B15, B30, MK30, B45, and B60, respectively. The orders of reaction degree of MK are consistent with the mass ratios of cement to MK.

As shown in Figure 2(b), the sequences of reaction degree of limestone from higher to lower are B15 > B30 > B45 > B60. The proposed ternary-blended hydration model can reflect this trend of reaction degree of LS. In this study, the mass ratio of MK to LS in ternary blends is constant, and the difference of the reaction degree of LS is mainly due to the variations of the cement-to-limestone ratio. The mass ratios of cement to LS were 17, 7, 3.66, and 2 in the mixtures of B15, B30, B45, and B60, respectively. As the mass ratio of cement to LS decreases, the reaction degree of LS also decreases (parameter m_1 of equation (7)). The trend of the reaction degree of LS is consistent with the mass ratio of cement to LS. In addition, the reaction degree of LS at 1 day is almost zero. This also agrees with our analysis. As shown in equation (6), we assumed that the reaction of LS starts after 21 hours. Furthermore, the reactivity of LS is very low. At the age of 90 days, the reaction degree of LS for B15 is 12% which is much lower than cement.

Figure 3 shows the parameter analysis of the hydration model. Figure 3(a) shows the reaction degree of LS in cement-LS binary blends. As limestone replacement ratio increases, the reaction degree of limestone decreases. Similar to the contents shown in Figure 3(a), Aqel and Panesar [23]
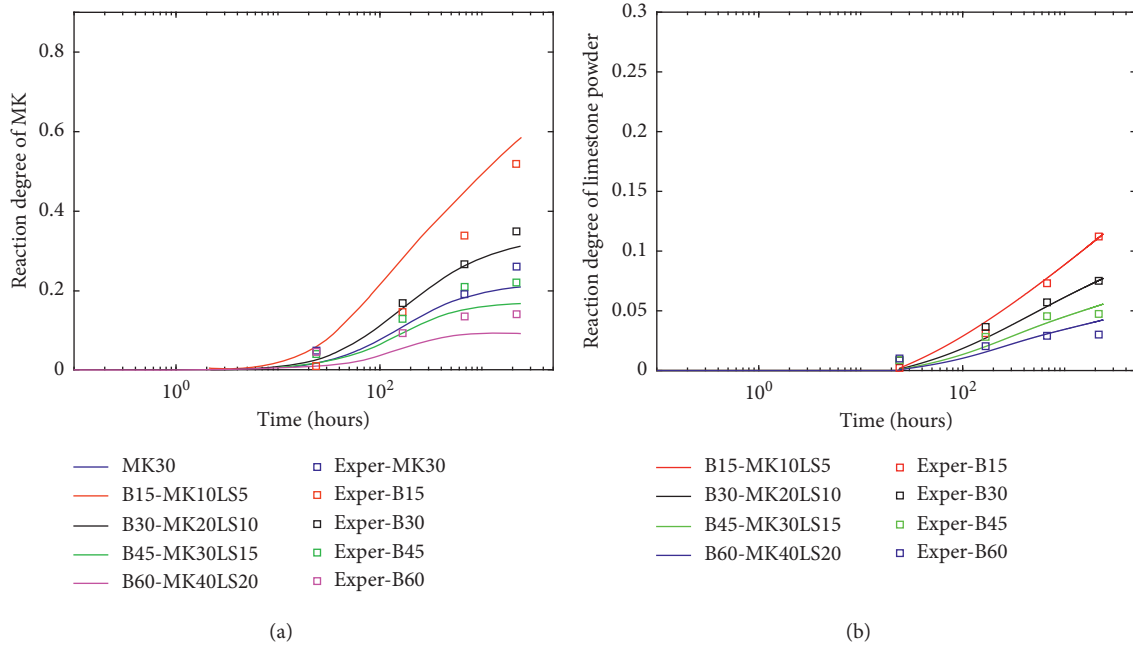
FIGURE 2: Verification of the hydration model: (a) reaction degree of MK; (b) reaction degree of LS.

also found the reactivity of limestone will be lower with the increasing of limestone content.

Figure 3(b) shows the reaction degree of MK in cement-MK binary blends. As MK replacement ratio increases, the activation effect from cement hydration becomes weaker, and the reaction degree of MK decreases. Similar to the contents shown in Figure 3(b), Poon et al. [24] also found similar results that the reaction degree of MK will be lower as the content of MK increases.

Figure 3(c) shows the effect of MK additions on the reaction degree of LS. The addition of MK presents the twofold effect on reaction of LS. First, when MK is added to replace partial cement in the mixtures, the mass ratio of cement to LS decreases which will lower the reaction degree of LS (this is considered through parameter m_1 of equation (7)). However, the aluminum content in MK (46%) is about ten times of the aluminum content in cement (4.6%). The addition of MK will enhance the reaction of LS (this is considered through parameter m_4 of equation (7)). Because the enhancing effect is much more significant than the lowering effect, the addition of MK can increase the reaction degree of limestone (shown in Figure 3(c)). Similar to the contents shown in Figure 3(c), many researchers [4, 9] also experimentally found that reactivity of limestone can be improved due to MK addition.

Figure 3(d) shows the effect of metakaolin and limestone contents on the reaction degree of cement. When metakaolin and limestone are used to replace partial cement, the reaction degree of cement is improved due to the dilution effect and nucleation effect (the dilution effect is considered through parameter λ_2 in equation (1), and the nucleation effect is considered through equations (4) and (5)). Similar to the contents shown in Figure 3(d), Lam et al. [25] also found that the addition of mineral admixtures can improve the reaction degree of cement.

3.2. Verification of Strength Development Model. By using the cement-MK-LS ternary-blended hydration model, the gel-space ratio of hydrating concrete can be calculated (equation (10)). Furthermore, based on the strength of concrete at different ages, the values of strength coefficients of $a1$, $a2$, and $a3$ and $b1$, $b2$, and $b3$ can be calibrated ($a1 = 140$ MPa, $a2 = 258$ MPa, $a3 = 120$ MPa, $b1 = 3.85$, $b2 = 1.13$, and $b3 = 1.34$). These coefficients do not vary with concrete mixtures. The values of $a1$ and $b1$ relate to cement hydration, the values of $a2$ and $b2$ relate to the metakaolin reaction, and the values of $a3$ and $b3$ relate to the limestone reaction. For cement-metakaolin binary blends, the development of strength relates to $a1$, $a2$, $b1$, and $b2$. For cement-limestone binary blends, the development of strength relates to $a1$, $a3$, $b1$, and $b3$. For cement-metakaolin-limestone ternary blends, the development of strength relates to $a1$, $a2$, $a3$, $b1$, $b2$, and $b3$. The analyzed results of compressive strength are shown in Figure 4. The analysis results generally agree with experimental results. At the ages of 28 days, the B15 concrete (cement 85% + metakaolin 10% + limestone 5%) has a highest strength than other mixtures. This may be because of the synergetic effect of metakaolin and limestone.

Because the strength coefficients of strength evaluation equation are constants for different concrete mixtures, we can make parameter analysis for different concrete mixtures. Figure 5(a) shows the strength development of cement-limestone binary blends. At the early age, due to the nucleation effect, the strength of limestone blends concrete shows higher strength than control concrete. While at late ages, due to the dilution effect, the strength of limestone blends concrete is lower than control concrete. As the contents of limestone increases from 10% to 20%, the late-age strength decreases. The trend shown in Figure 5(a) agrees with Bonavetti et al.'s [19] studies about strength development of limestone-blended concrete.
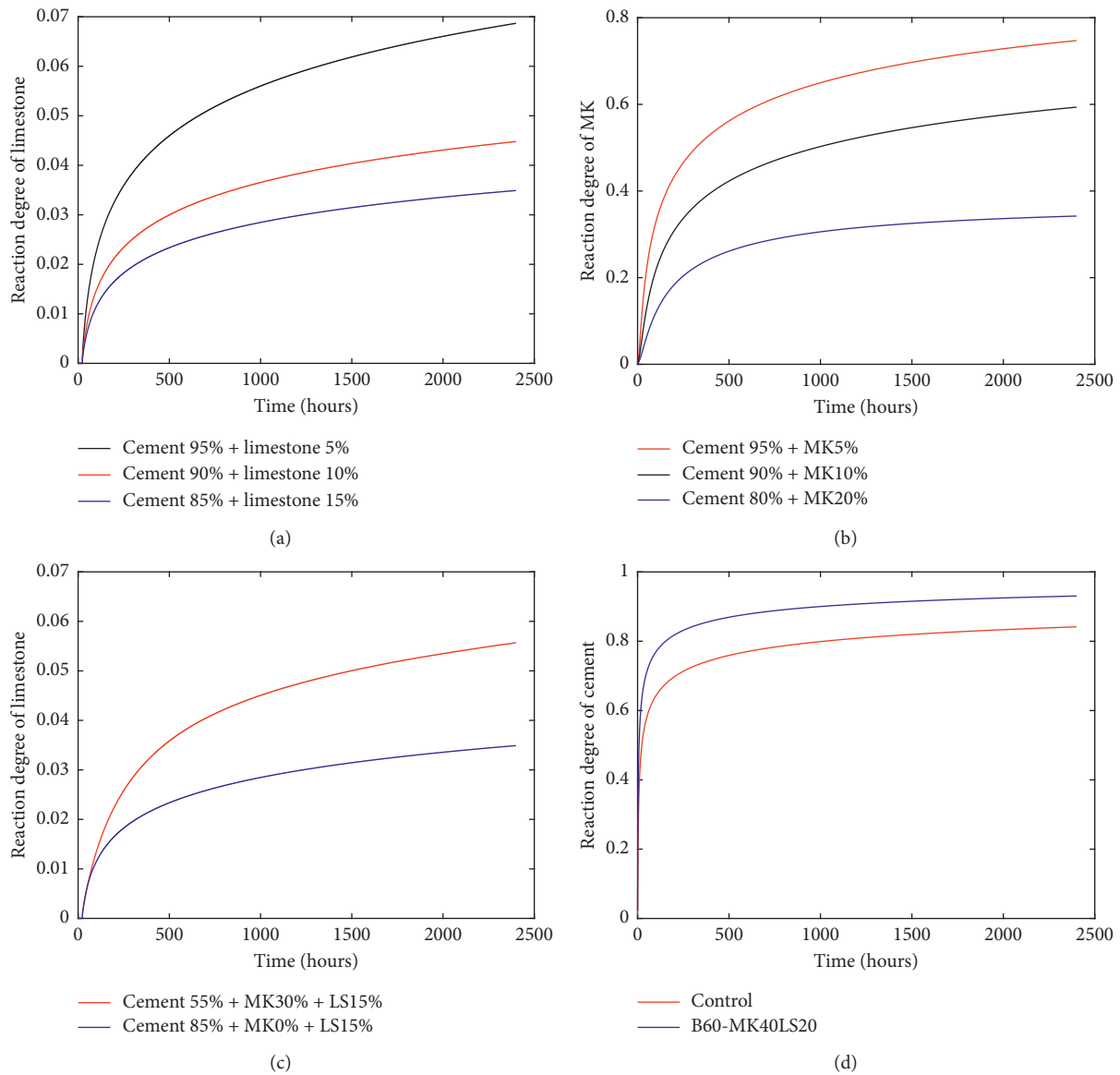
FIGURE 3: Parameter analysis of reaction degree of binders: (a) effect of limestone contents on the reaction degree of limestone; (b) effect of metakaolin contents on the reaction degree of metakaolin; (c) effect of metakaolin contents on the reaction degree of limestone; (d) effect of metakaolin and limestone contents on the reaction degree of cement.

Figure 5(b) shows the strength development of cement-metakaolin binary blends. Metakaolin-blended concrete has a higher strength than control concrete. As the contents of metakaolin increases from 5% to 10%, the strength also increases. The trend shown in Figure 5(b) agrees with Poon et al.'s [24] studies about strength development of metakaolin-blended concrete.

Damidot et al. [26] studies the strength development of 70% cement + 30% clay-limestone ternary blends. The sum of clay and limestone was fixed as 30%, and the weight fraction of clay/(clay + limestone) ranges from 0 to 100% [26]. Damidot et al. [26] found that, at the age of 28 days, the mix with 70% metakaolin has the highest strength than other mixes. This is because of the synergetic effect of limestone and metakaolin [26]. Based on the proposed strength development in this study, we make parameter analysis of

strength development for 70% cement + 30% clay-limestone ternary blends. In our analysis, the sum of clay and limestone is also fixed as 30%, the weight fractions of clay/(clay + limestone) are given as 0, 25%, 50%, 75%, and 100%, and the ages of parameter analysis are 1.5 days, 3 days, 28 days, and 90 days, respectively. The results of parameter analysis are shown in Figures 6(a)–6(d). As shown in Figure 6(a), at the age of 1.5 days, the strength of blended concrete is higher than base Portland cement. This is because of the nucleation effect of limestone. While as shown in Figures 6(b)–6(d), at the age of 3 days, 28 days, and 90 days, when the mk/(mk + limestone) equals to zero (the content of metakaolin is zero, and binder consists of 30% limestone and 70% cement), the strength of limestone-blended concrete is lower than base Portland cement. This is because of the dilution effect of limestone. While for other mk/

(a)

(b)

(c)

MK 10% limestone 5%

(d)

MK 20% limestone 10%

(e)

MK 30% limestone 20%

(f)
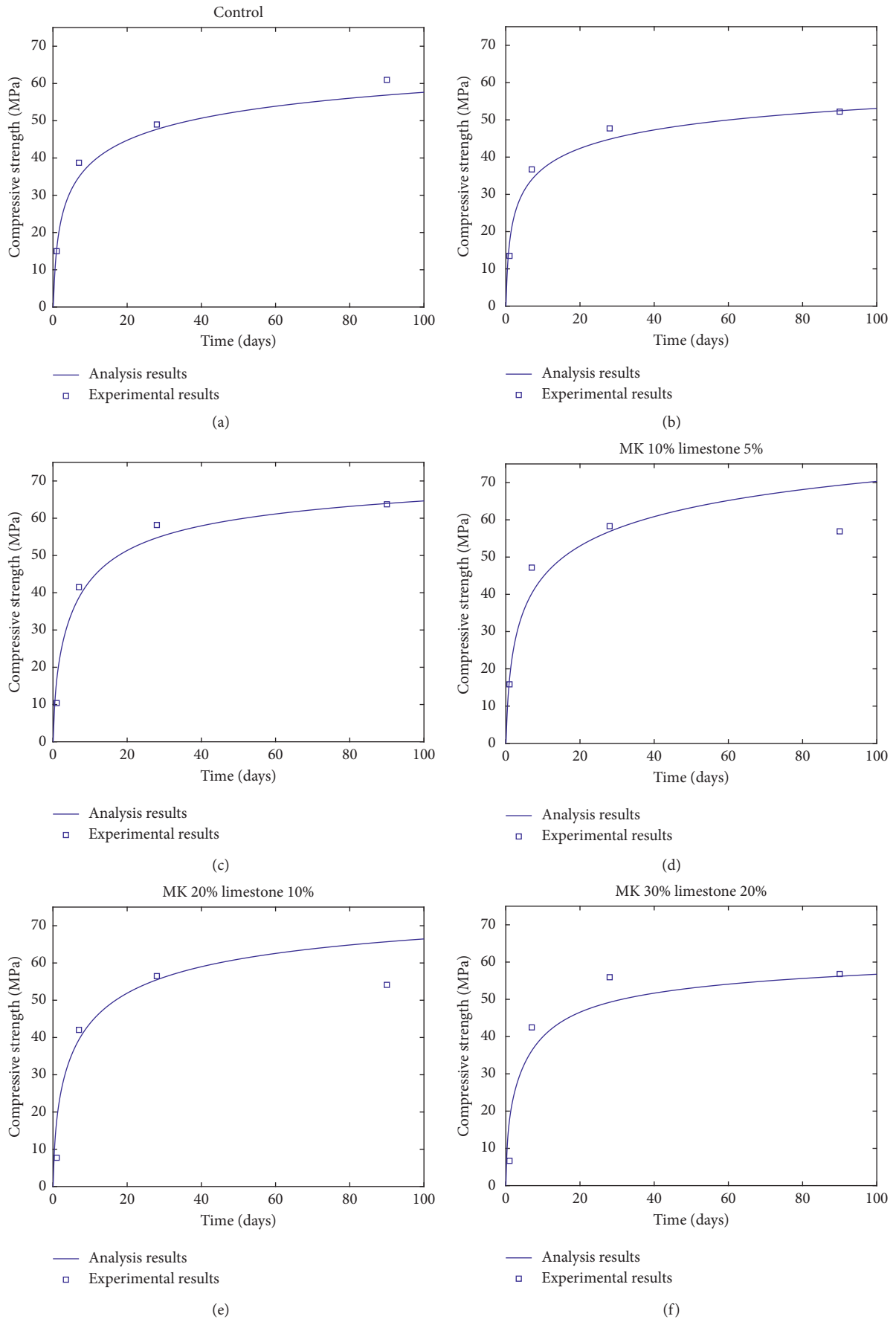
Figure 4: Continued.

(g)
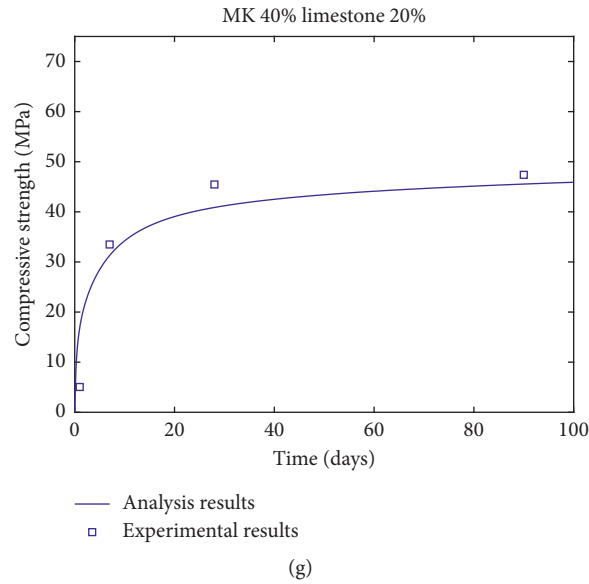
FIGURE 4: Analysis of compressive strength: (a) PC; (b) LS15; (c) MK30; (d) B15; (e) B30; (f) B45; (g) B60.

(a)

(b)
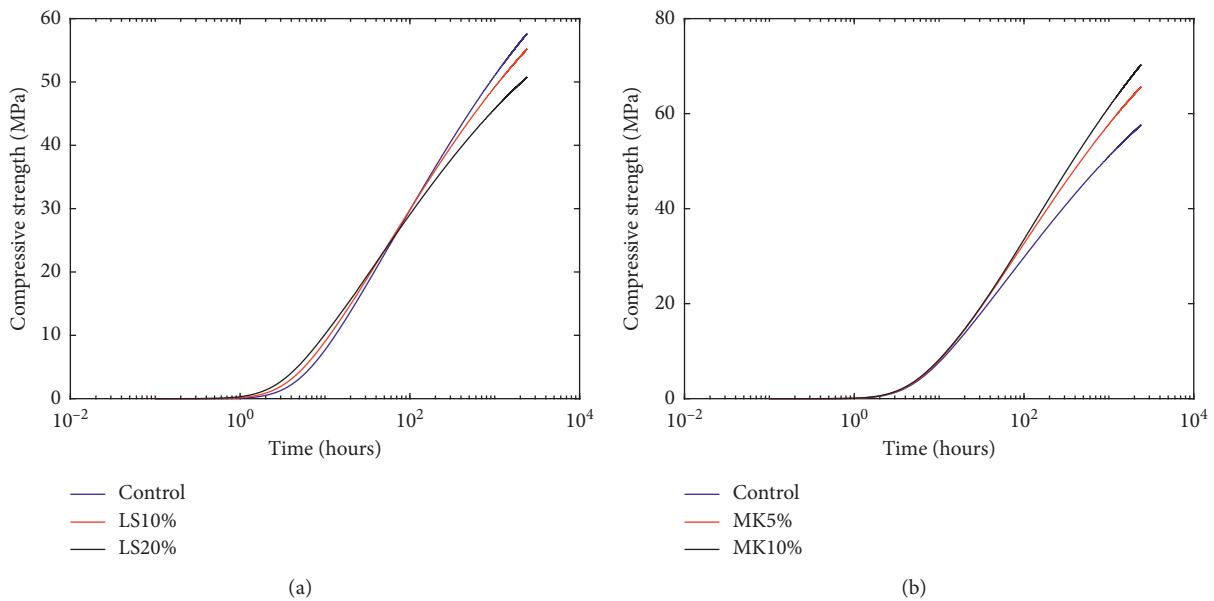
FIGURE 5: Effect of LS and MK on strength development: (a) cement-LS binary blends; (b) cement-MK binary blends.

(mk + limestone) ratios of 25%, 50%, 75%, and 100%, because the reaction of metakaolin can contribute to the strength, the strength of blended concrete is higher than base Portland cement.

At the age of 1.5 days, 3 days, 28 days, and 90 days, the optimum weight fractions of clay/(clay + limestone) are 25%, 50%, 75%, and 75%, respectively (shown in Figures 6(e)). Our analysis result about optimum weight fraction of clay/(clay + limestone) is similar to that of Damidot et al. [26] studies. In addition, our analysis shows that, at the ages of 1.5 days, 3 days, 28 days, and 90 days, the optimum weight fraction of limestone/(clay + limestone) is 75%, 50%, 25%, and 25%, respectively. It means that, at the early age, limestone is effective to improve the strength of concrete (this is because of

the nucleation effect of limestone), and at the late age, metakaolin is effective to improve the strength of concrete (this is because of the pozzolanic reaction of metakaolin).

In Figure 6, the sum of metakaolin and limestone is fixed as 30%. To find the optimum combinations of cement, metakaolin, and limestone, we make much wider parameter analysis. In this wider parameter analysis, the sum of metakaolin and limestone is not a fixed value. The contents of metakaolin vary from 0 to 30%, and the contents of limestone vary from 0 to 20%. The analysis results of isoline of strength are shown in Figures 7(a)–7(d). At the early age 1.5 days, the concrete with a higher limestone content and a lower metakaolin content has highest strength (shown in Figure 7(a)), while at the late

(a)

(b)

(c)

(d)

(e)
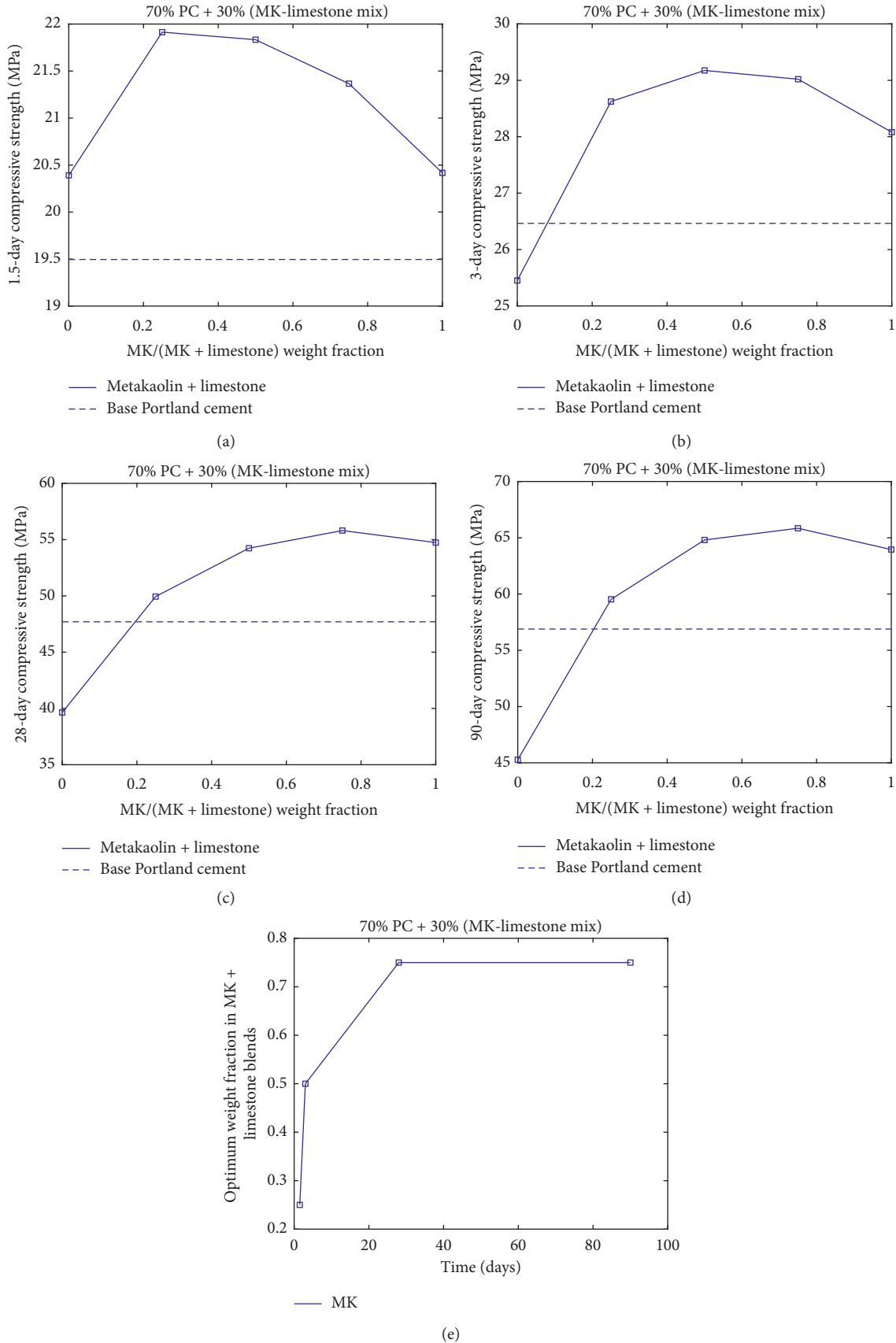
FIGURE 6: Synergetic effect of cement-MK-LS ternary blends (MK + LS = 30%): (a) 1.5 days; (b) 3 days; (c) 28 days; (d) 90 days, (e) optimum fractions of MK.
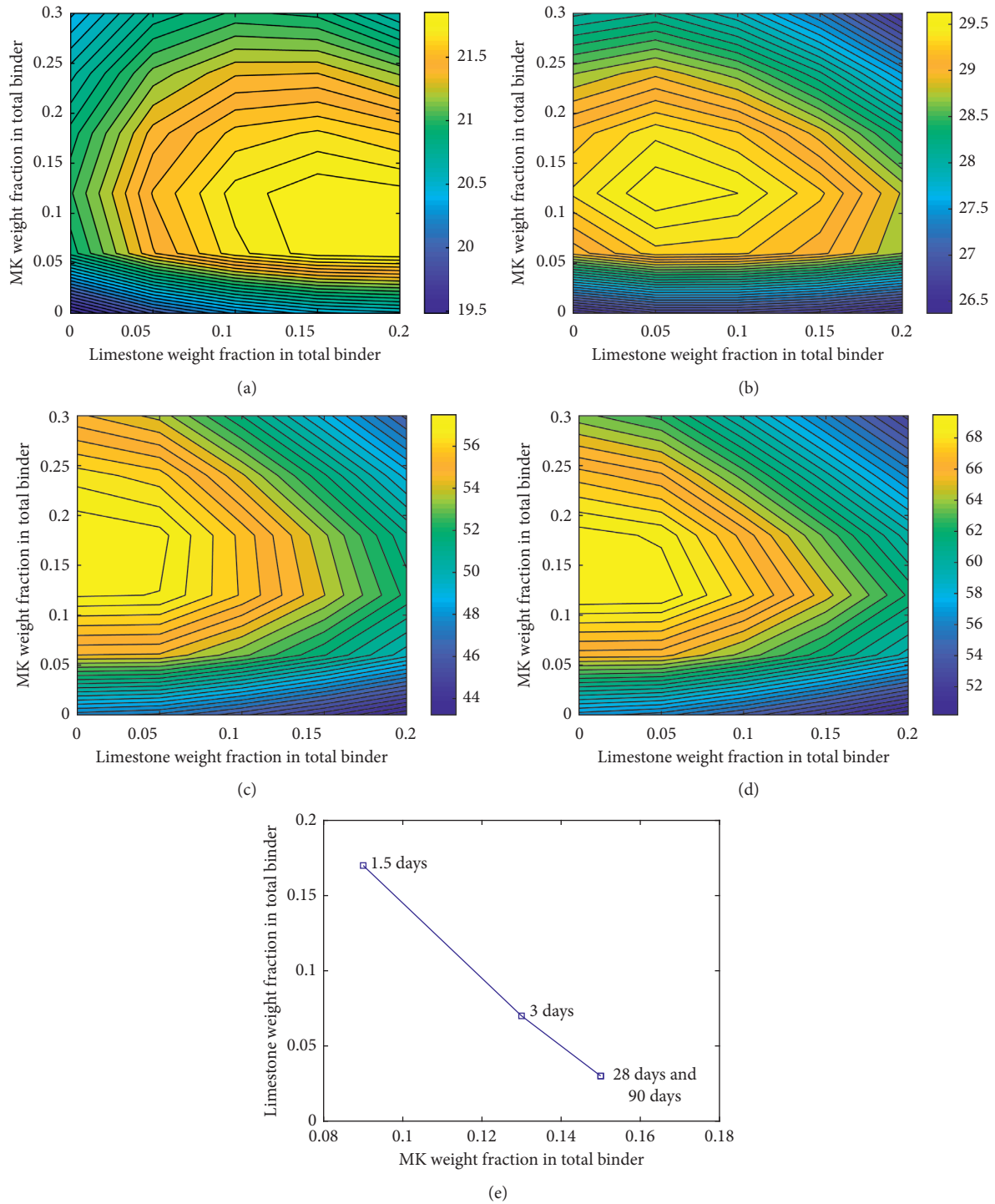
FIGURE 7: Analysis of optimum MK and LS combinations: (a) 1.5 days; (b) 3 days; (c) 28 days; (d) 90 days; (e) optimum MK and LS combinations at different ages.

age of 90 days, the concrete with a higher metakaolin content and a lower limestone content has highest strength (shown in Figure 7(d)). In other words, to achieve the highest strength of cement-metakaolin-limestone ternary blends, the optimum combination of metakaolin and limestone is dependent on ages. From the early age to late age, the optimum combinations change shift from high limestone-low metakaolin zone to low limestone-high metakaolin zone (shown in Figure 7(e)).

4. Conclusions

This study presents an integrated hydration-strength model for cement-limestone-metakaolin ternary blends.

First, a cement hydration model, a metakaolin reaction model, and a limestone reaction model are proposed in the ternary-blended hydration model. Pozzolanic reaction of metakaolin, chemical and physics effect of limestone, and synergetic effect between metakaolin and limestone are detailed considered in the ternary-blended hydration model. Moreover, the interactions among cement hydration, limestone reaction, and metakaolin reaction are considered through the contents of calcium hydroxide and capillary water. The coefficients of the hydration model do not change for various concrete mixtures.

Second, based on the hydration model, the gel-space ratio of hydrating blends is calculated considering the contributions from the reactions of cement, metakaolin, and limestone. Furthermore, the strength development of ternary blends is evaluated using the gel-space ratio. The coefficients of the strength model do not change for various concrete mixtures. Based on parameter analysis, the synergetic effect on strength development is shown, and the optimal combinations of cement-limestone-metakaolin ternary blends are determined. From the early age to late age, the optimum combinations of ternary blends shift from high limestone-low metakaolin zone to low limestone-high metakaolin zone.

Data Availability

The data used to support the findings of this study are included within the article.

Conflicts of Interest

The author declares that there are no conflicts of interest regarding the publication of this paper.

Acknowledgments

References

[1] X.-Y. Wang, "Modeling of hydration, compressive strength, and carbonation of Portland-limestone cement (PLC) concrete," *Materials*, vol. 10, no. 2, pp. 115–131, 2017.

[2] X. Y. Wang and Y. Luan, "Modeling of hydration, strength development, and optimum combinations of cement-slag-limestone ternary concrete," *International Journal of Concrete Structures and Materials*, vol. 12, no. 1, pp. 193–206, 2018.

[3] K. Vance, A. Kumar, G. Sant, and N. Neithalath, "The rheological properties of ternary binders containing Portland cement, limestone, and metakaolin or fly ash," *Cement and Concrete Research*, vol. 52, pp. 196–207, 2013.

[4] K. Vance, M. Aguayo, T. Oey, G. Sant, and N. Neithalath, "Hydration and strength development in ternary portland cement blends containing limestone and fly ash or metakaolin," *Cement and Concrete Composites*, vol. 39, pp. 93–103, 2013.

[5] G. L. Alvarez, A. Nazari, A. Bagheri, J. G. Sanjayan, and C. De Lange, "Microstructure, electrical and mechanical properties of steel fibres reinforced cement mortars with partial metakaolin and limestone addition," *Construction and Building Materials*, vol. 135, pp. 8–20, 2017.

[6] A. M. Ramezanianpour and R. D. Hooton, "A study on hydration, compressive strength, and porosity of Portland-limestone cement mixes containing SCMs," *Cement and Concrete Composites*, vol. 51, pp. 1–13, 2014.

[7] C. Perlot, P. Rougeau, and S. Dehaudt, "Slurry of metakaolin combined with limestone addition for self-compacted concrete: application for precast industry," *Cement and Concrete Composites*, vol. 44, pp. 50–57, 2013.

[8] K. Sotiriadis, E. Nikolopoulou, S. Tsivilis, A. Pavlou, E. Chaniotakis, and R. N. Swamy, "The effect of chlorides on the thaumasite form of sulfate attack of limestone cement concrete containing mineral admixtures at low temperature," *Construction and Building Materials*, vol. 43, pp. 156–164, 2013.

[9] M. Antoni, J. Rossen, F. Martirena, and K. Scrivener, "Cement substitution by a combination of metakaolin and limestone," *Cement and Concrete Research*, vol. 42, no. 12, pp. 1579–1589, 2012.

[10] Z. Shi, M. R. Geiker, K. De Weerdt et al., "Role of calcium on chloride binding in hydrated Portland cement-metakaolin-limestone blends," *Cement and Concrete Research*, vol. 95, pp. 205–216, 2017.

[11] Z. Shi, B. Lothenbach, M. R. Geiker et al., "Experimental studies and thermodynamic modeling of the carbonation of Portland cement, metakaolin and limestone mortars," *Cement and Concrete Research*, vol. 88, pp. 60–72, 2016.

[12] X.-Y. Wang and H.-S. Lee, "Modeling the hydration of concrete incorporating fly ash or slag," *Cement and Concrete Research*, vol. 40, no. 7, pp. 984–996, 2010.

[13] K. Maekawa, R. Chaube, and T. Kishi, *Modelling of Concrete Performance: Hydration, Microstructure and Mass Transport*, CRC Press, London, UK, 1999.

[14] K. van Breugel, *Simulation of Hydration and Formation of Structure in Hardening Cement-Based Materials*, Delft University Press, Delft, Netherlands, 1997.

[15] X.-Y. Wang, "Analysis of hydration-mechanical-durability properties of metakaolin blended concrete," *Applied Sciences*, vol. 7, no. 10, pp. 1087–1102, 2017.

[16] V. G. Papadakis, "Experimental investigation and theoretical modeling of silica fume activity in concrete," *Cement and Concrete Research*, vol. 29, no. 1, pp. 79–86, 1999.

[17] Y. Elakneswaran, E. Owaki, S. Miyahara, M. Ogino, T. Maruya, and T. Nawa, "Hydration study of slag-blended cement based on thermodynamic considerations," *Construction and Building Materials*, vol. 124, pp. 615–625, 2016.

[18] T. Vuk, V. Tinta, R. Gabrovšek, and V. Kaučič, "The effects of limestone addition, clinker type and fineness on properties of Portland cement," *Cement and Concrete Research*, vol. 31, no. 1, pp. 135–139, 2001.

[19] V. Bonavetti, H. Donza, G. Menéndez, O. Cabrera, and E. F. Irassar, "Limestone filler cement in low w/c concrete: a rational use of energy," *Cement and Concrete Research*, vol. 33, no. 6, pp. 865–871, 2003.

[20] A. M. Dunster, J. R. Parsonage, and M. J. K. Thomas, "The pozzolanic reaction of metakaolinite and its effects on Portland cement hydration," *Journal of Materials Science*, vol. 28, no. 5, pp. 1345–1350, 1993.

[21] D. P. Bentz, "Modeling the influence of limestone filler on cement hydration using CEMHYD3D," *Cement and Concrete Composites*, vol. 28, no. 2, pp. 124–129, 2006.

[22] B. Pichler, C. Hellmich, J. Eberhardsteiner et al., "Effect of gel-space ratio and microstructure on strength of hydrating cementitious materials: an engineering micromechanics approach," *Cement and Concrete Research*, vol. 45, pp. 55–68, 2013.

[23] M. Aqel and D. K. Panesar, "Hydration kinetics and compressive strength of steam-cured cement pastes and mortars containing limestone filler," *Construction and Building Materials*, vol. 113, pp. 359–368, 2016.

[24] C.-S. Poon, L. Lam, S. C. Kou, Y.-L. Wong, and R. Wong, "Rate of pozzolanic reaction of metakaolin in high-performance cement pastes," *Cement and Concrete Research*, vol. 31, no. 9, pp. 1301–1306, 2001.

[25] L. Lam, Y. L. Wong, and C. S. Poon, "Degree of hydration and gel/space ratio of high-volume fly ash/cement systems," *Cement and Concrete Research*, vol. 30, no. 5, pp. 747–756, 2000.

[26] D. Damidot, B. Lothenbach, D. Herfort, and F. P. Glasser, "Thermodynamics and cement science," *Cement and Concrete Research*, vol. 41, no. 7, pp. 679–695, 2011.

Research Article

Estimation of Minimum Torsional Reinforcement of Reinforced Concrete and Steel Fiber-Reinforced Concrete Members

Hyunjin Ju [iD],[1] **Sun-Jin Han**,[2] **Dichuan Zhang**,[3] **Jong Kim** [iD],[4] **Wei Wu**,[5] **and Kang Su Kim** [iD][6]

[1]Post-Doctoral Research Fellow, Department of Civil Engineering and Natural Hazards,
  University of Natural Resources and Life Sciences, Feistmantelstrasse 4, 1180 Vienna, Austria
[2]Ph.D. Candidate, Department of Architectural Engineering, University of Seoul, 163 Seoulsiripdaero, Dongdaemun-gu,
  Seoul 02504, Republic of Korea
[3]Assistant Professor, Department of Civil and Environmental Engineering, School of Engineering, Nazarbayev University,
  53 Kabanbay Batyr Ave., Astana 010000, Kazakhstan
[4]Professor, Department of Civil and Environmental Engineering, School of Engineering, Nazarbayev University,
  53 Kabanbay Batyr Ave., Astana 010000, Kazakhstan
[5]Professor, Department of Civil Engineering and Natural Hazards, University of Natural Resources and Life Sciences,
  Feistmantelstrasse 4, 1180 Vienna, Austria
[6]Professor, Department of Architectural Engineering, University of Seoul, 163 Seoulsiripdaero, Dongdaemun-gu,
  Seoul 02504, Republic of Korea

Correspondence should be addressed to Kang Su Kim; kangkim@uos.ac.kr

Received 31 December 2018; Accepted 10 February 2019; Published 10 March 2019

Guest Editor: Doo-Yeol Yoo

The current code specifies a minimum torsional reinforcement ratio to prevent possible brittle failure after torsional cracking in concrete members. However, since there are many researches, in which even the concrete members with the minimum torsional reinforcement fail to secure sufficient reserved strength after torsional cracking, continuous research needs to be carried out. Accordingly, in the authors' previous research, a minimum torsional reinforcement ratio was proposed based on the reserved strength concept and was extended to the steel fiber-reinforced concrete members in order to suggest the minimum fiber factor as the minimum torsional reinforcement ratio. In the present study, a pure torsion test was carried out on reinforced concrete and steel fiber-reinforced concrete members after a brief introduction on the above, and the proposed model was verified based on the test results. The test results of six torsional specimens were compared with those of the proposed model, and it was found that the proposed model provides a reasonable evaluation on the torsional failure mode of the specimen according to the reserved strength ratio.

1. Introduction

With the development of construction materials and concrete engineering, concrete members are becoming increasingly irregular and slender. Therefore, the importance of torsional design is increasing, although it was not considered important in the design of concrete structures [1, 2]. As in the case of flexural and shear design of concrete members, the minimum torsional reinforcement should be determined by the torsion design to prevent brittle failure of the members after the occurrence of torsional cracking. However, based on the minimum torsional reinforcement ratio presented in the current structural standards [3–6], the reserved strength of members subjected to torsion is often evaluated to be on the unsafe side [7]. In addition, the current structural standards fail to consider the correlation between transverse and longitudinal reinforcement or fail to offer the minimum longitudinal reinforcement for torsion in most cases.

In a previous research [8], authors proposed a minimum torsional reinforcement ratio to ensure sufficient reserved strength exceeding the torsional cracking strength (T_{cr}) by introducing the reserved strength factor (λ). Both the longitudinal and transverse reinforcement ratios were considered in the proposed method. In addition, the

authors proposed a minimum torsional reinforcement requirement not only for reinforced concrete (RC) members but also for steel fiber-reinforced concrete (SFRC) members using the minimum fiber factor (F_{min}) and suggested an integrated approach for both RC and SFRC members. In the present study, the proposed minimum torsional reinforcement ratio of the RC and SFRC members was introduced briefly, and the proposed model was verified through experimental research on a total of six torsional specimens.

2. Minimum Torsional Reinforcement

2.1. Reinforced Concrete (RC) Members. In the previous research [8], the minimum amount of torsional reinforcement was derived with the reserved strength concept, in which the ultimate torsional strength (T_n) should be larger than certain strength related to cracking strength (λT_{cr}). The torsional cracking strength (T_{cr}) of the reinforced concrete member was provided based on the existing experimental results [9, 10]. In addition, for the torsional strength (T_n), the ACI318 code [3] was used. The torsional strength can be expressed with either transverse or longitudinal reinforcement from the equilibrium condition of forces in the space truss model [8], and with the relation between T_n and λT_{cr}, the minimum amount of torsional reinforcement in transverse and longitudinal directions was derived. If the reinforcement amount is expressed by reinforcement ratio and the ratios in two directions (ρ_t and ρ_l) are added together, the total minimum torsional reinforcement ratio ($\rho_{tot,min}$) is derived as follows:

$$\rho_{tot,min} = 0.34\sqrt{f'_c}\,\frac{A_{cp}}{A_0}\,\frac{p_h}{p_{cp}}\left(\frac{f_{yt}\cot\theta + f_{yl}\tan\theta}{f_{yt}f_{yl}}\right), \quad (1)$$

where f'_c is the compressive strength of concrete (MPa), A_{cp} is the area enclosed by the outer perimeter in the concrete section, A_0 is the cross-sectional area closed by shear flow, p_h is the centerline perimeter of the outermost closed transverse stirrup, p_{cp} is the outer perimeter length of the concrete section, f_{yt} is the yield stress of transverse torsional reinforcement, and f_{yl} is the yield strength of longitudinal torsional reinforcement. The reserved strength factor (λ) was determined to secure a reserved strength greater than 35% based on the results of existing experiments [8]. Also, in equation (1), $\tan\theta$ can be calculated by $\sqrt{\rho_t f_{yt}/(\rho_l f_{yl})}$ [11], which is limited to $0.3 \sim 3$ [8]. If either one of the longitudinal and transverse reinforcement requirements is determined in design, the minimum torsional reinforcement requirement in the other direction can be determined using equation (1) and $\tan\theta$.

2.2. Steel Fiber-Reinforced Concrete Members. In recent years, studies have been actively conducted to incorporate steel fibers to replace the complicated reinforcement details of RC members or the minimum reinforcement requirement [1, 7, 12–20]. In the previous research of the authors [8], equation (1) was extended to suggest the minimum amount of torsional reinforcement, which is suitable for SFRC members to which the minimum fiber factor (F_{min}) is introduced.

According to the thin-walled tube theory [21], because steel fibers near the center of the cross section of the SFRC member contribute little to torsional moment resistance, the steel fibers only within the effective thickness (t_d) were assumed to be effective to resist torsional moment [22]. With the effective thickness, the effective volume fraction of the steel fibers was also derived [8] and the steel fibers resisting torsion within the effective thickness were simply assumed to be evenly distributed in the transverse and longitudinal directions. These can be regarded as the equivalent reinforcement ratios of the steel fibers that resist in the transverse and longitudinal directions, that is, ρ_t^f and ρ_l^f.

Since steel fibers exhibit a very high tensile strength, the maximum stress is determined by the bond stress between the fiber and the concrete [19]. Therefore, the maximum stress of the steel fiber (σ_{max}^{sf}) was calculated by the bond strength between the steel fiber and the surrounding concrete as follows [8]:

$$\sigma_{max}^{sf} = 0.41\tau_{uf}\frac{F}{V_f}, \quad (2)$$

where τ_{uf} is the ultimate bond stress, which is $2.5f_{ct}$ [23], f_{ct} is the tensile strength of concrete ($0.33\sqrt{f'_c}$) [24], and V_f is the fiber volume fraction. In addition, F represents the fiber factor considering the geometry and volume fraction of the steel fibers and can be calculated as $l_f V_f \alpha_f/d_f$, where l_f and d_f are the length and diameter of a fiber, respectively, and α_f is the bond factor according to the type of steel fiber [25].

The previous research [8] found that, in the case of SFRC members with reinforcing bars, the sum of the torsional reinforcing bar and steel fibers should meet the minimum torsional reinforcement ratio represented in equation (1). In other words, if the equivalent reinforcement ratio based on the sum of reinforcement ratios for reinforcing bars ($\rho_{tot}^{rebar} = \rho_l + \rho_t$) and steel fiber-reinforcement ratio ($\rho_{tot}^{sf} = \rho_t^f + \rho_l^f$) is greater than equation (1), a sufficient reserved strength can be secured against the torsional load. Thus, the relationship ρ_{tot}^{rebar}, ρ_{tot}^{sf}, and $\rho_{tot,min}$ of equation (1) is expressed by the following equation:

$$\rho_{tot}^{rebar} + \rho_{tot}^{sf}\frac{\sigma_{max}^{sf}}{(f_{yt} + f_{yl})/2} \geq \rho_{tot,min}. \quad (3)$$

Therefore, in the form of the required minimum fiber factor, F_{min} is derived as follows:

$$F_{min} = 1.5\left(\rho_{tot,min} - \rho_{tot}^{rebar}\right)\frac{f_{yt} + f_{yl}}{\xi\sqrt{f'_c}}. \quad (4)$$

In case equation (4) gives a negative value, it means that steel fibers to ensure the reserved strength is not necessary. Additionally, for the SFRC members without reinforcing bars, $\rho_{tot}^{rebar} = 0$, the minimum fiber factor (F_{min}) can be calculated by substituting equation (1) into $\rho_{tot,min}$ and replacing the yield strengths (f_{yt} and f_{yl}) with the maximum stresses of the steel fibers (σ_{max}^{sf}) of equation (2).

3. Experimental Program

3.1. Details of Test Specimens. In the present study, a pure torsion test was conducted on a total of six test specimens, as shown in Table 1, and the proposed equations for calculating the minimum torsional reinforcement requirements (i.e., equations (1) and (4)) were verified based on the test results. The main variables of the test specimens include compressive strength of concrete (f_c'), longitudinal reinforcement ratio (ρ_l), transverse reinforcement ratio (ρ_t), and incorporation of steel fibers. As shown in Figure 1, the length of each specimen was 3,000 mm, the cross-sectional width and height were 350 mm and 500 mm, respectively, and the net cover thickness was 20 mm. In addition, the measurement section in which torsional failure was induced is the center of the member, and stirrups were placed densely in other sections to prevent failure. As summarized in Table 1, D13, D16, and D19 steel bars were used in the test specimens, and the average yield strengths of each rebar were 489.8 MPa, 467.5 MPa, and 500.4 MPa, respectively. In addition, the transverse reinforcement ratios of the specimens (ρ_t) ranged from 0.34% to 0.91%, the longitudinal reinforcement ratios (ρ_l) from 0.43% to 0.98%, and the total reinforcement ratios (ρ_{tot}) from 0.77% to 1.89%. Also, the $\rho_t f_{yt}/\rho_l f_{yl}$ ratio of all specimens was designed to be less than 1.0, considering the details of reinforcing bars placed in typical structures.

Of the six test specimens, steel fibers were mixed in the MTF25-0.77 and MTF25-N specimens. The MTF25-0.77 specimen has the same cross-sectional details as those of the MT30-0.77 specimen, which is an RC member. The MTF25-N specimen is a member in which only longitudinal reinforcement is placed without transverse reinforcement. The steel fiber volume fraction (V_f) of the SFRC specimen was 2.0%, and a hook-shaped steel fiber with a diameter (d_f) of 0.5 mm, a length (l_f) of 30 mm, and a tensile strength of 1,200 MPa was used in the test specimen.

Table 2 shows the mix proportion of the concrete in the test specimens. Portland cement type I and coarse aggregates with a maximum size of 25 mm were used. The concrete compressive strengths (f_c') of the MT30 series, MT40 series, and MTF25 series were 29.3, 40.3, and 24.0 MPa, respectively. The MTF25 series specimens were originally designed with the same mix proportion as the MT30 series specimens. However, it was estimated that their compressive strengths were somewhat lower due to the fiber balling phenomenon during concrete placement [26].

3.2. Test Setup and Measurements. Figure 2 shows the details of torsional loading and displacement measurements. As shown in Figures 2(a) and 2(c), a frame was fixed at a point 300 mm away from the right end of the test specimen. As shown in Figures 2(a), and 2(b) at a point 300 mm away from the left end, a 600 mm long torsion arm was installed to introduce a torsional moment (T). Moreover, as shown in Figure 2(c), rollers were installed in the upper and lower parts at the right end to release the longitudinal restraints, while an arc bearing was placed at the lower part of the left end of the test specimen so that torsional rotation can occur, as shown in Figure 2(b). The load was applied using a 500 kN capacity actuator in displacement control, and tests were performed until the load decreased to less than 80% of the maximum strength.

As shown in Figure 1, nine strain gauges were installed in longitudinal reinforcement. In all specimens except for the MTF25-N specimen, a total of 12 strain gauges were attached to the transverse reinforcement, six on the side and six at the bottom of transverse reinforcement. Additionally, as shown in Figure 2(d), two LVDTs were installed on the front and back sides of the test specimen, respectively, at a location 800 mm away to the left and the right from the center of the test specimen.

4. Test Results and Discussion

4.1. Torsional Behavior of Test Specimens. Figure 3 shows the crack patterns and failure modes of the test specimens. All the specimens underwent torsional failure within the planned test sections. In addition, since the test specimens have a relatively small amount of torsional reinforcement, longitudinal and transverse torsional reinforcements yielded after the occurrence of cracks, as shown in Figures 4–6. The MT30-0.77 specimen with the smallest amount of torsional reinforcement exhibited a decrease in load immediately after the torsional cracking, as shown in Figure 4. The MT30-1.32 specimen with longitudinal reinforcement more than twice that of the MT30-0.77 specimen showed a critical torsional crack angle of approximately 45° at the final failure, and more cracks occurred compared to the MT30-0.77 specimen. However, while the MT30-1.32 specimen showed typical torsional failure, the member suffered premature failure as the load was rapidly applied due to the malfunction of the actuator at the point of torsional cracking, as shown in Figure 4.

As shown in Figure 5, the MT40-1.32 specimen showed a decrease in load as the critical torsional crack propagated rapidly after the torsional cracking strength. Ultimately, it failed to ensure the reserved strength and showed a similar behavior to that of the MT30-0.77 specimen. This is because the amount of torsional reinforcement placed in the specimen was not sufficient to ensure the reserved strength, and consequently, the concrete struts failed, as shown in Figure 3(c). In the case of the MT40-1.89 specimen with the largest amount of torsional reinforcement, multiple torsional cracks occurred in the test section, as shown in Figure 3(d). One critical crack was gradually propagated with the load increasing and caused the member failure. In addition, as shown in Figure 5, the MT40-1.89 specimen exhibited the highest reserved strength among all specimens and showed very ductile behavior up to the ultimate strength even after torsional cracking.

The MTF series specimens are members in which steel fibers are incorporated. The MTF25-0.77 specimen has the same reinforcement details as the MT30-0.77 specimen. As shown in Figure 3(e), the MTF25-0.77 specimen showed a tighter and denser distribution of cracks compared to the MT30-0.77. Moreover, it was observed that the crack opening was well controlled by the bridging effect of the fibers even after the occurrence of critical cracks. However, the damage was concentrated on the upper surface of the concrete at near the failure, as shown in the right side of Figure 3(e), and accordingly, significant strength improvement did not occur

TABLE 1: Details and properties of specimens.

Specimen names	f_c' (MPa)	Longitudinal reinforcement		Transverse reinforcement			Steel fiber reinforcement			
		Steel bars (ρ_l)	f_{yl} (MPa)	Steel bars (ρ_t)	f_{yt} (MPa)	S (mm)	V_f (%)	l_f (mm)	d_f (mm)	Fiber shape
MT30-0.77	29.3	6-D13 (0.43%)	489.8	D10 (0.34%)	467.5	180	Without fibers			
MT30-1.32	29.3	6-D19 (0.98%)	500.4	D10 (0.34%)	467.5	180	Without fibers			
MT40-1.32	40.3	6-D19 (0.98%)	500.4	D10 (0.34%)	467.5	180	Without fibers			
MT40-1.89	40.3	6-D19 (0.98%)	489.8	D13 (0.91%)	489.8	120	Without fibers			
MTF25-0.77	24.0	6-D13 (0.43%)	489.8	D10 (0.34%)	467.5	180	2.0	30	0.5	Hooked
MTF25-N	24.0	6-D13 (0.43%)	489.8	Without transverse steel			2.0	30	0.5	Hooked

(a)

(b)

(c)
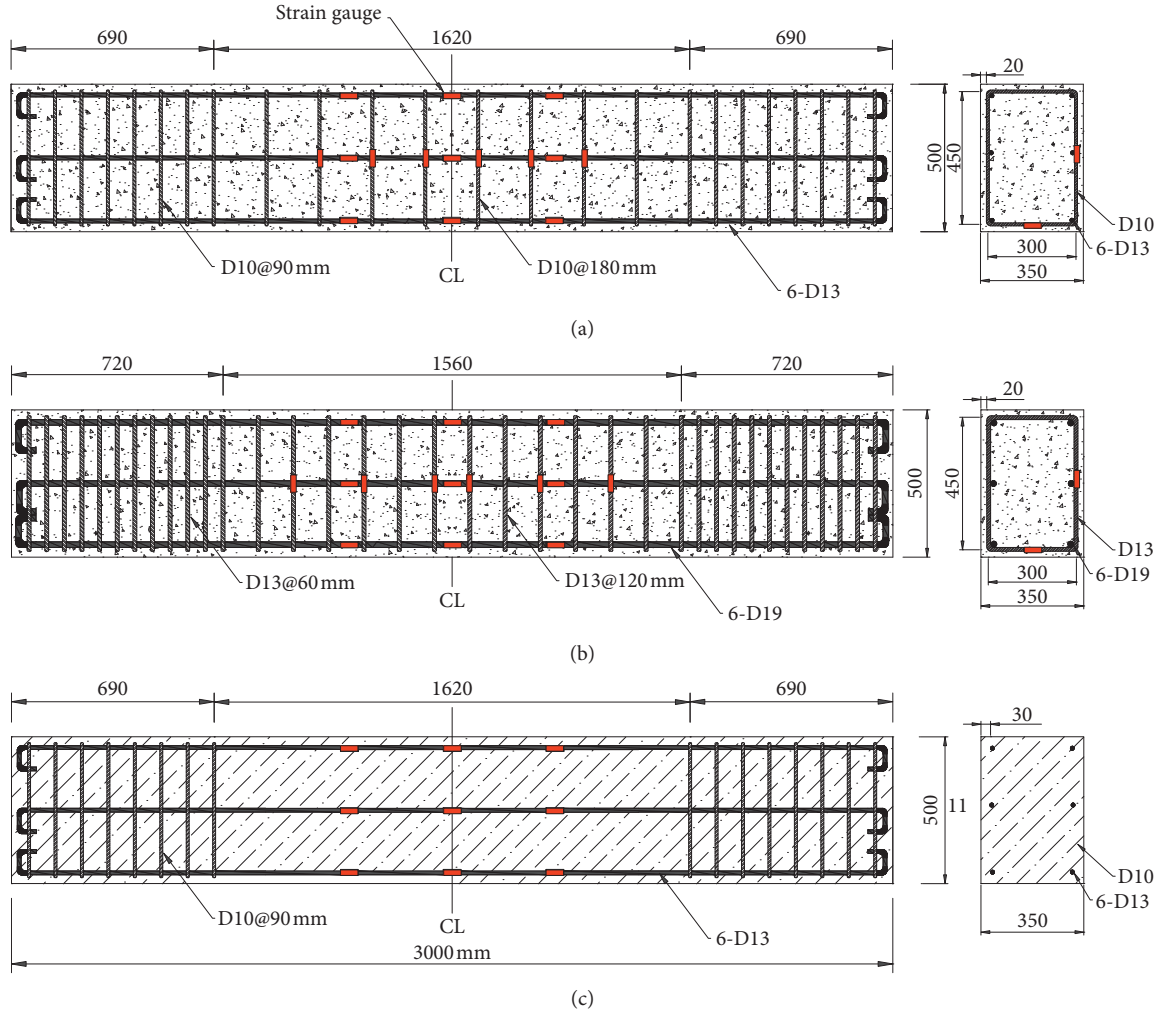
FIGURE 1: Details of specimens: (a) MT30-0.77; (b) MT40-1.89; (c) MTF25-N.

TABLE 2: Mix proportion.

Specimen series	W/C (%)	S/a (%)	Weight per m³					
			W	C	S	G	AE	SF
MT30 series	47	42	158.78	339.72	754.20	1042.24	0.15	—
MT40 series	40	42	158.78	395.10	712.11	1038.54	0.17	—
MTF25 series	47	42	158.78	339.72	754.20	1042.24	0.15	157.2

W/C: water-cement ratio; S/a: sand percent of total aggregate by weight; W: water; C: cement; S: sand; G: coarse aggregate; AE: air-entraining agent; SF: steel fiber.
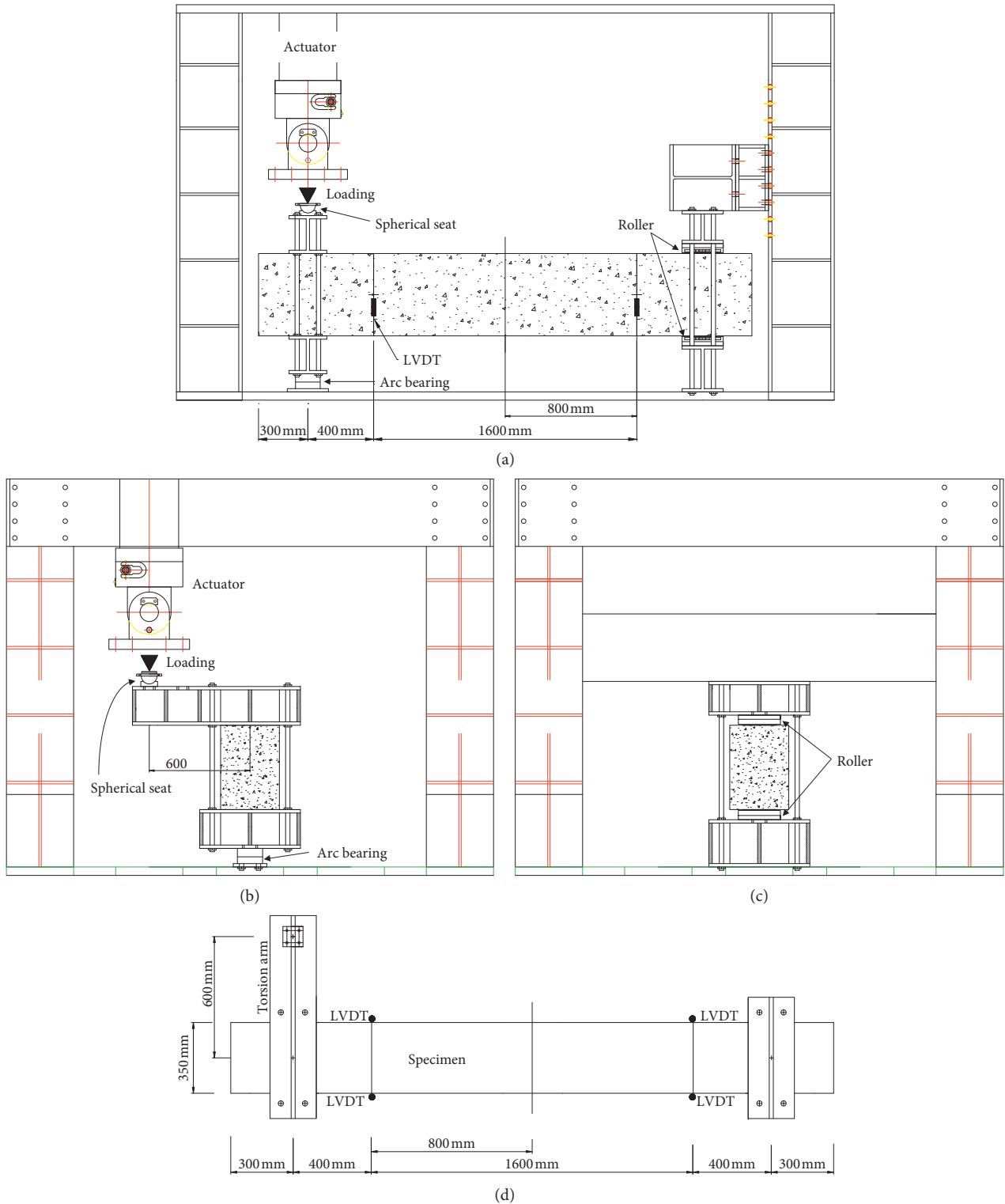
Figure 2: Test setup and location of LVDT: (a) front view; (b) left-end view (free to rotation); (c) right-end view (fixed against rotation); (d) top view of specimen and location of LVDT.

when compared to the MT30-0.77 specimen, as shown in Figure 6. This result appears to be due to the fiber balling phenomenon in the MTF25-0.77 specimen, which was confirmed by comparing fractions collected from the upper part of the MTF25-0.77 specimen shown in Figure 7(a) and those of

the MTF25-N specimen shown in Figure 7(b). It is expected that if the members were well manufactured so that the fibers can be evenly distributed, further reserved strength could be secured after torsional cracking even in the MTF25-0.77 specimen. Meanwhile, no transverse reinforcement was

(a)

(b)

(c)

(d)

(e)

(f)
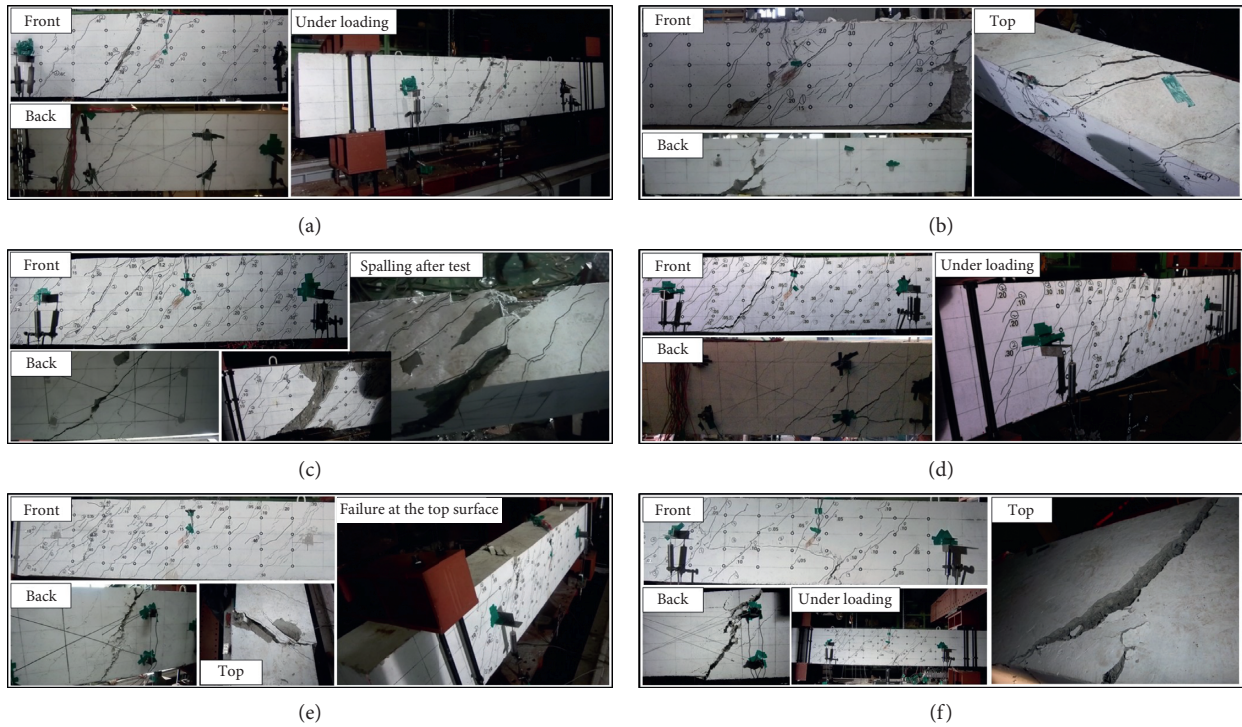
FIGURE 3: Crack pattern and failure of specimens: (a) MT30-0.77; (b) MT30-1.32; (c) MT40-1.32; (d) MT40-1.89; (e) MTF25-0.77; (f) MTF25-N.
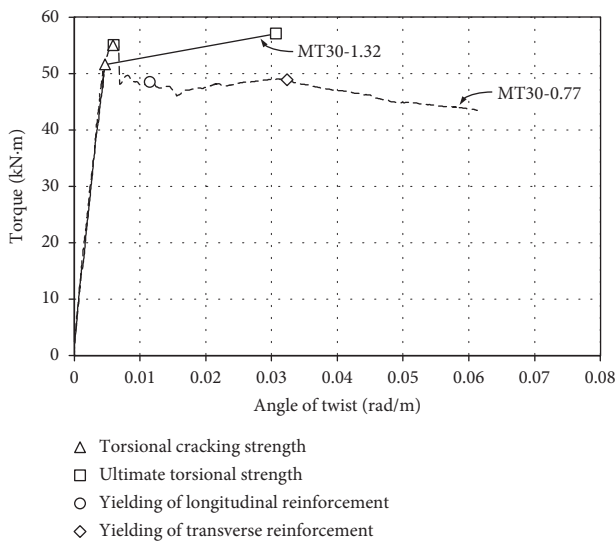
FIGURE 4: Torsional moment-twist of MT30 series.
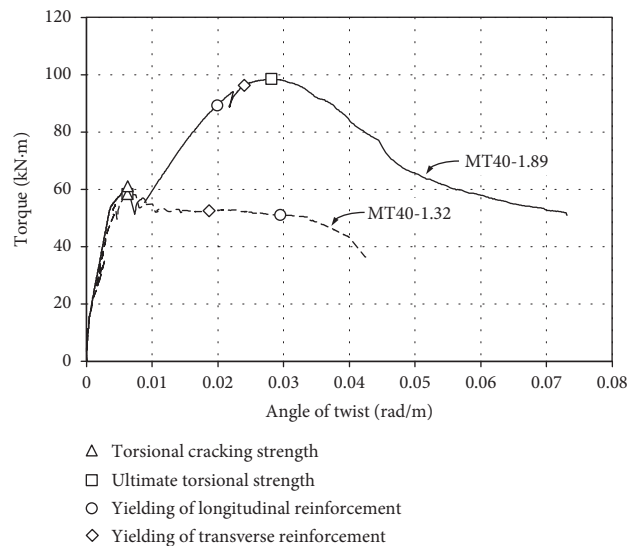
FIGURE 5: Torsional moment-twist of MT40 series.

placed; however, longitudinal reinforcement and 2% steel fibers were incorporated in the MTF25-N specimen. As shown in Figure 6, the MTF-25N specimen showed a rapid decrease in load after torsional cracking and reached failure as the width of the critical torsional crack was greatly expanded, as shown in Figure 3(f). Consequently, it failed to ensure the torsional reserved strength.

4.2. Evaluation of Reserved Strengths of Test Specimens. Table 3 summarizes the results of torsional tests performed in this study. The torsional cracking strengths of the MT40

series with a compressive strength of 40.3 MPa were greater than those of the MT30 series with a compressive strength of 29.3 MPa. The MT40-1.89 specimen with the largest amount of torsional reinforcement showed the highest torsional strength of 98.4 kN·m, whereas the MTF25-N specimen without transverse reinforcement showed the lowest torsional strength of 54.0 kN·m.

The MT30-0.77 specimen failed to exhibit the reserved strength after torsional cracking strength due to a low reinforcement ratio. In contrast, the MT30-1.32 specimen with
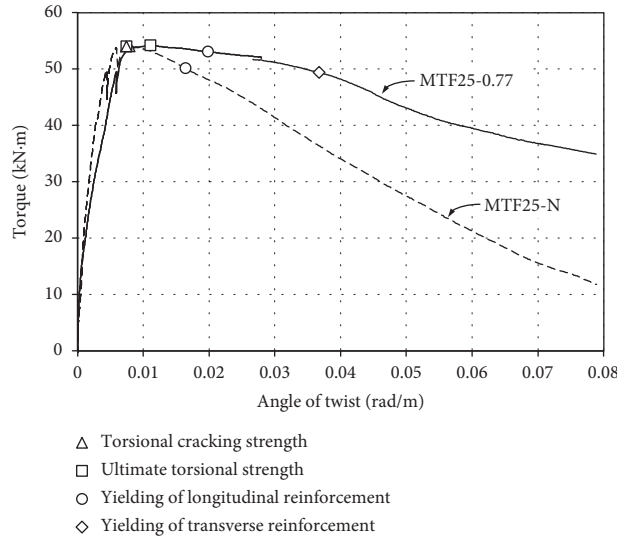
Figure 6: Torsional moment-twist of MTF25 series.

(a)

(b)

Figure 7: Fractions of SFRC members: (a) MTF25-0.77; (b) MTF25-N.

Table 3: Test results and validation of the proposed model.

| Specimen names | At cracking | | At ultimate | | At yielding of steel | | | | Reserved strength ratio | Ductility index |
| | | | | | Transverse | | Longitudinal | | | |
	θ_{cr} (rad/m)	T_{cr} (kN·m)	θ_u (rad/m)	T_u (kN·m)	θ_{yt} (rad/m)	T_{yt} (kN·m)	θ_{yl} (rad/m)	T_{yl} (kN·m)	T_u/T_{cr}	θ_u/θ_{cr}
MT30-0.77	0.0060	55.00	0.0060	55.00	0.0324	48.83	0.0116	48.49	1.00	1.00
MT30-1.32	0.0048	51.55	0.0307	57.04	0.0307	57.04	0.0307	57.04	1.11	6.46
MT40-1.32	0.0063	58.29	0.0063	58.29	0.0187	52.51	0.0295	51.14	1.00	1.00
MT40-1.89	0.0063	60.97	0.0282	98.40	0.0240	96.19	0.0200	89.23	1.61	4.48
MTF25-0.77	0.0080	54.00	0.0111	54.15	0.0367	49.39	0.0198	53.04	1.00	1.39
MTF25-N	0.0075	53.97	0.0075	53.97	-	-	0.0164	50.08	1.00	1.00

more longitudinal reinforcement showed an increase in strength after cracking; however, the increase was not significant (i.e., $\lambda = 1.11$). Even the MT40-1.32 specimen with the same cross-sectional details as the MT30-1.32 specimen failed to exhibit the reserved strength. This suggests that since the torsional cracking strength is high in the member with a relatively high concrete compressive

strength, a larger amount of torsional reinforcement is required to ensure the reserved strength. The MT40-1.89 specimen with 167% greater transverse reinforcement compared with the MT40-1.32 specimen exhibited sufficient reserved strength after torsional cracking, as shown in Figure 5. The reserved strength ratio ($\lambda = T_n/T_{cr}$) was estimated to be 1.61, which is greater than the target reserved

strength ratio of 1.35 proposed in the previous research [8]. On the contrary, the MTF series specimens (MTF25-0.77 and MTF25-N), which are SFRC members, showed no reserved strength. This is because the steel fiber volume fraction ratios (V_f) of 2.17% and 8.45% are required to satisfy the minimum fiber factor (F_{min}) presented in equation (4), as shown in Table 4, whereas V_f of these specimens was 2%.

Table 3 shows the ratio of the twist angle per length at the maximum torsional strength (θ_u) to that at the torsional cracking strength (θ_{cr}) as the ductility index. The MT30-1.32 specimen exhibited the highest ductility index of 6.46 despite a low reserved strength ratio. In addition, the ductility index of the MT40-1.89 specimen with the highest reserved strength was 4.48, indicating a significantly high ductility index compared to other specimens except for the MT30-1.32 specimen. Meanwhile, the MTF25-0.77 specimen failed to ensure the reserved strength but showed a ductility index of 1.39. In other words, it can be confirmed that the deformation capacity (i.e., ductility) of the torsional member is not significantly correlated with the reserved strength (T_n/T_{cr}). Since the torsional member should be at least designed to have the sufficient resistance capacity of the member against loads, the most important thing in the member design is to satisfy the design strength. The deformation capacity will be the next consideration. Therefore, as described above, the securing of the deformation capacities (i.e., ductility) of torsional members cannot guarantee that the strength of the member can be ensured. Thus, it is reasonable to specify the minimum torsional reinforcement ratio based on the reserved strength rather than the deformation capacity for the safe design of torsional members.

Figures 8(a) and 8(b) show the minimum torsional reinforcement ratio ($\rho_{tot,min}$) with respect to $\rho_t f_{yt}/\rho_l f_{yl}$ and f'_c, respectively. Since the minimum torsional reinforcement ratio specified in the ACI318 code [3] does not consider the ratio of $\rho_t f_{yt}/\rho_l f_{yl}$, it is shown only in Figure 8(b), and not in Figure 8(a). In addition, the reinforcement ratios in six test specimens are shown in the graphs of Figure 8. The specimens which failed to secure the reserved strengths (i.e., $\lambda \le 1.35$) from the test results were indicated by triangles ($\triangle$) and those ensuring the sufficient reserved strengths (i.e., $\lambda > 1.35$) by circles ($\bigcirc$). As shown in Figure 8 and Table 3, only the MT40-1.89 specimen ensured a reserved strength greater than 35%. It can be seen that the failure modes predicted by the proposed model are consistent with the test results, except for the MT30-1.32 specimen. However, it should be noted that the MT30-1.32 specimen failed prematurely as the torsional moment was applied rapidly to the member due to the malfunction of the actuator. On the contrary, Figure 8(b) indicates that all the specimens have the torsional reinforcement greater than the minimum amount specified in ACI318-14. Nevertheless, all the specimens did not have enough reserved strengths except for MT40-1.89, and as shown in Table 3, the MT30-0.77 and MT40-1.32 specimens showed abrupt failures right after torsional cracking. This suggests that the minimum

torsional reinforcement ratio specified in ACI318-14 does not ensure a proper margin of safety in design.

4.3. Required Minimum Amount of Steel Fibers for Ensuring Proper Reserved Strength. As described above, the remaining specimens, except for the MT40-1.89 specimen, failed to ensure the reserved strength. Therefore, additional reinforcement is required for the specimens to achieve a target reserved strength higher than 35% (i.e., $\lambda > 1.35$). In addition, when the member is reinforced with steel fibers, the required minimum amount of steel fibers (F_{min}) should be incorporated as represented in equation (4). Table 4 summarizes the minimum amount of steel fiber reinforcement (F_{min}) required for each specimen. In the case of the MT40-1.89 specimen, which showed sufficient reserved strength ratio in the test, and the MT30-1.32 specimen, which underwent premature failure due to the actuator malfunction, the required minimum fiber factor (F_{min}) was calculated to be zero. In addition, the minimum fiber factor (F_{min}) required for the MTF25-N specimen without transverse reinforcement was the largest (5.07), whereas the required fiber factor (F_{min}) for the MT40-1.32 specimen with a relatively higher torsional reinforcement ratio (ρ_{tot}^{rebar}) was estimated to be as small as 0.31. The minimum fiber factor (F_{min}) of the MTF25-0.77 specimen was smaller than that of the MT30-0.77 specimen with the same torsional reinforcement ratio (ρ_{tot}^{rebar}). This is because the concrete compressive strength (f'_c) of the MTF25-0.77 specimen was lower than that of the MT30-0.77 specimen and, therefore, resulted in a rather small estimated minimum torsional reinforcement ratio ($\rho_{tot,min}$) represented in equation (1). When the same fibers are used (i.e., $l_f = 30$ mm, $d_f = 0.5$ mm, and $\rho_f = 1.0$) as those incorporated in the specimens fabricated in this study, the steel fiber volume fraction (V_f) required for each specimen to ensure a reserved strength of 35% or more is estimated, as shown in Table 4. As mentioned in Section 4.2, the volume fraction ratio of steel fibers required for the MTF25-0.77 specimen was estimated to be 2.17%; however, 2.0% of steel fibers were incorporated in the test specimen, which failed to satisfy the amount of fiber reinforcement necessary to ensure a reserved strength of 35%. Even if this is taken into consideration, the test results show the reserved strength to be very low due to the fiber balling phenomenon as mentioned above. In the case of the MTF25-N specimen without transverse reinforcement, the required fiber volume fraction was estimated to be as high as 8.45%. However, since it is in fact impossible to incorporate such a large amount of steel fibers, it is difficult to replace torsional reinforcement with only the steel fibers in this case [12, 27]. Therefore, the design for torsion should be carried out using an appropriate amount of longitudinal and transverse reinforcement for such members.

5. Conclusions

In the present research, an experimental study on the total of six torsional members was carried out to verify the equation

TABLE 4: Application of the proposed minimum fiber factor to SFRC.

Specimen names	Total torsional reinforcement, ρ_{tot} (%)	$\rho_{tot, min} - \rho_{tot}^{rebar}$ (%)	Effective volume fraction, ξ	Required minimum fiber factor, F_{min}	Designed minimum fiber factor, F_{min}	Steel fiber used in design			
						V_f (%)	l_f (mm)	d_f (mm)	ρ_f
MT30-0.77	0.774	0.27	0.38	1.85	1.85	3.08	30	0.5	1.0
MT30-1.32	1.322	-0.15	0.38	-1.06	0.00	0.00	30	0.5	1.0
MT40-1.32	1.322	0.05	0.38	0.31	0.31	0.51	30	0.5	1.0
MT40-1.89	1.887	-0.71	0.38	-4.35	0.00	0.00	30	0.5	1.0
MTF25-0.77	0.774	0.17	0.38	1.30	1.30	2.17	30	0.5	1.0
MTF25-N	0.434	0.66	0.38	5.07	5.07	8.45	30	0.5	1.0
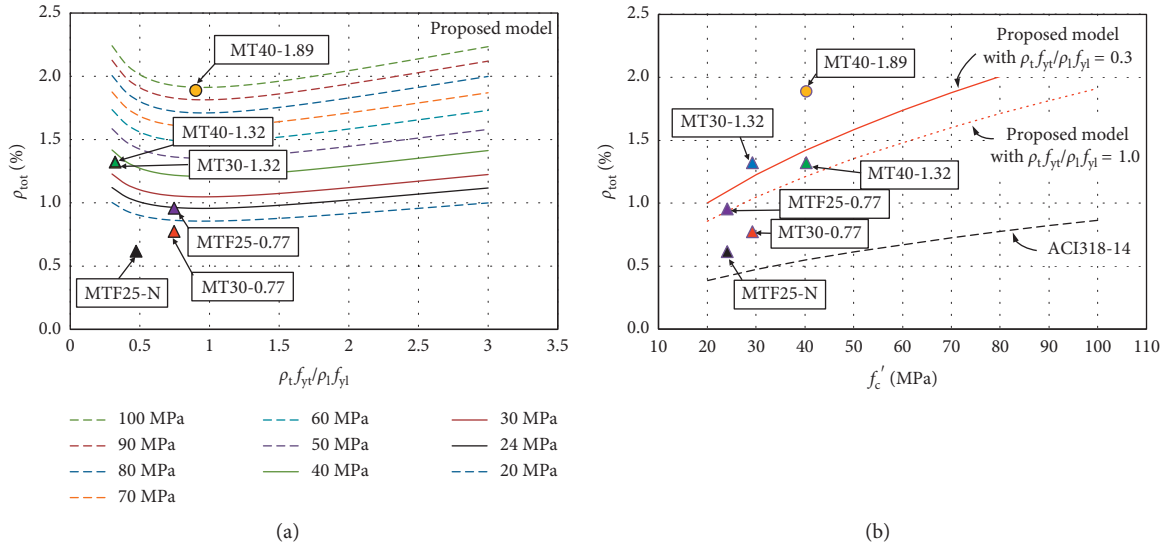
FIGURE 8: Estimation of reserved strength for torsional members: (a) total reinforcement ratio versus $\rho_t f_{yt}/\rho_l f_{yl}$; (b) total reinforcement ratio versus f_c'.

to calculate the minimum amount of torsional reinforcement for RC and SFRC members, which was proposed in the authors' previous research. The main test variables included the transverse and longitudinal torsional reinforcement ratios, the compressive strength of concrete, and the incorporation of steel fibers. The following conclusions were drawn from the test results and the verification process of the proposed model.

(1) As the total torsional reinforcement ratio (ρ_{tot}^{rebar}) increased, more smeared torsional cracks occurred. In addition, it was found that the additional incorporation of steel fibers in the specimen with the same reinforcement ratio made it possible to improve crack control by bridging effect of the steel fibers.

(2) If the concrete compressive strength (f_c') is high in a member with the same reinforcement details, the cracking torsional moment (T_{cr}) is relatively large. Therefore, a greater amount of torsional reinforcement is needed to ensure the reserved strength.

(3) The minimum torsional reinforcement ratio ($\rho_{tot, min}$) proposed for ensuring a reserved strength greater than 35% is calculated considering the transverse and longitudinal reinforcement ratios (ρ_t and ρ_l), steel fiber volume fraction (V_f), and concrete compressive strength (f_c'). It has also been proposed in the form of a minimum fiber factor (F_{min}) to facilitate application to SFRC members.

(4) It was possible to estimate the failure modes of the RC and SFRC torsional specimens accurately by examining whether the proposed minimum reinforcement requirement is satisfied. However, in the case of SFRC members, the reinforcing effects of steel fibers need to be evaluated more conservatively due to the low workability, fiber balling phenomenon, etc.

Data Availability

The experimental data used to support the findings of this study are included within the article.

Conflicts of Interest

The authors declare that they have no conflicts of interest.

Acknowledgments

References

[1] H. Ju, K. S. Kim, D. H. Lee, J.-H. Hwang, S.-H. Choi, and Y.-H. Oh, "Torsional responses of steel fiber-reinforced concrete members," *Composite Structures*, vol. 129, no. 1, pp. 143–156, 2015.

[2] L. F. A. Bernardo and S. M. R. Lopes, "Torsion in high-strength concrete hollow beams: strength and ductility analysis," *ACI Structural Journal*, vol. 106, no. 1, pp. 39–48, 2009.

[3] ACI Committee 318, *Building Code Requirements for Structural Concrete and Commentary (ACI 318-14)*, American Concrete Institute, Farmington Hills, MI, USA, 2014.

[4] CSA Committee A23.3-14, *Design of Concrete Structures, CAN/CSA-A23.3-14*, Canadian Standards Association, Ontario, Canada, 2014.

[5] Comite Euro-International du Beton, *CEB-FIP Model Code 2010*, Thomas Telford, Westminster, London, 2010.

[6] Comete European de Normalisation (CEN), *Eurocode 2: Design of Concrete Structures. Part 1-General Rules and Rules for Buildings, EN 1992-1:2004*, Comete European de Normalisation, Brussels, Belgium, 2004.

[7] H. Ju, D. H. Lee, J.-H. Hwang, K. S. Kim, and Y.-H. Oh, "Fixed-angle smeared-truss approach with direct tension force transfer model for torsional behavior of steel fiber-reinforced concrete members," *Journal of Advanced Concrete Technology*, vol. 11, no. 9, pp. 215–229, 2013.

[8] H. Ju, D. H. Lee, and K. S. Kim, "Minimum torsional reinforcement ratio for reinforced concrete members with steel fibers," *Composite Structures*, vol. 207, no. 1, pp. 460–470, 2019.

[9] N. Koutchoukali and A. Belarbi, "Torsion of high-strength reinforced concrete beams and minimum reinforcement requirement," *ACI Structural Journal*, vol. 98, no. 4, pp. 462–469, 2001.

[10] M. G. Ghoneim and J. G. MacGregor, "Evaluation of design procedures for torsion in reinforced and prestressed concrete," Report No. 184, Department of Civil Engineering, University of Alberta, Edmonton, Canada, 1993.

[11] J. G. MacGregor and M. G. Ghoneim, "Design for torsion," *ACI Structural Journal*, vol. 92, no. 2, pp. 211–218, 1995.

[12] J.-H. Hwang, D. Lee, H. Ju, K. Kim, S.-Y. Seo, and J.-W. Kang, "Shear behavior models of steel fiber reinforced concrete beams modifying softened truss model approaches," *Materials*, vol. 6, no. 10, pp. 4847–4867, 2013.

[13] P. Adebar, S. Mindess, D. St.-Pierre, and B. Olund, "Shear tests of fiber concrete beams without stirrups," *ACI Structural Journal*, vol. 94, no. 1, pp. 68–76, 1997.

[14] G. Batson, E. Jenkins, and R. Spatney, "Steel fibers as shear reinforcement in beams," *ACI Journal Proceedings*, vol. 69, no. 10, pp. 640–644, 1972.

[15] J. Susetyo, P. Gauvreau, and F. J. Vecchio, "Effectiveness of steel fiber as minimum shear reinforcement," *ACI Structural Journal*, vol. 108, no. 4, pp. 488–496, 2011.

[16] R. N. Swamy and H. M. Bahia, "Effectiveness of steel fibers as shear reinforcement," *Concrete International: Design and Construction*, vol. 7, no. 3, pp. 35–40, 1985.

[17] D. H. Lee, J.-H. Hwang, H. Ju, and K. S. Kim, "Application of direct tension force transfer model with modified fixed-angle softened-truss model to finite element analysis of steel fiber-reinforced concrete members subjected to shear," *Computers and Concrete*, vol. 13, no. 1, pp. 49–70, 2014.

[18] J.-H. Hwang, D. H. Lee, K. S. Kim, H. Ju, and S.-Y. Seo, "Evaluation of shear performance of steel fibre reinforced concrete beams using a modified smeared-truss model," *Magazine of Concrete Research*, vol. 65, no. 5, pp. 283–296, 2013.

[19] K. S. Kim, D. H. Lee, J.-H. Hwang, and D. A. Kuchma, "Shear behavior model for steel fiber-reinforced concrete members without transverse reinforcements," *Composites Part B: Engineering*, vol. 43, no. 5, pp. 2324–2334, 2012.

[20] D. H. Lee, J.-H. Hwang, H. Ju, K. S. Kim, and D. A. Kuchma, "Nonlinear finite element analysis of steel fiber-reinforced concrete members using direct tension force transfer model," *Finite Elements in Analysis and Design*, vol. 50, no. 1, pp. 266–286, 2012.

[21] R. Bredt, "Kritische bemerkungen zur drehungselastizitat. Z vereines Deutscher Ingenieure," *Band*, vol. 40, no. 28, pp. 785–790, 1896.

[22] R. Narayanan and A. S. Kareem-Palanjian, "A space truss model for fibre-concrete beams in torsion," *Structural Engineer*, vol. 63B, no. 1, pp. 14–19, 1985.

[23] J. Y. L. Voo and S. J. Foster, "Variable engagement model for fibre reinforced concrete in tension," UNICIV Report no. R-420, University of New South Wales, Sydney, Australia, 2003.

[24] F. J. Vecchio and M. P. Collins, "The response of reinforced concrete to in-plane shear and normal stresses," Publication no. 82-0, Department of Civil Engineering, University of Toronto, Toronto, Canada, 1982.

[25] P. Marti, T. Pfyl, V. Sigrist, and T. Ulaga, "Harmonized test procedures for steel fiber-reinforced concrete," *ACI Materials Journal*, vol. 96, no. 6, pp. 676–686, 1999.

[26] M. Harajli, M. Hout, and W. Jalkh, "Local bond stress-slip behavior of reinforcing bars embedded in plain and fiber concrete," *ACI Material Journal*, vol. 92, no. 4, pp. 343–354, 1995.

[27] C. E. Chalioris, "Analytical approach for the evaluation of minimum fibre factor required for steel fibrous concrete beams under combined shear and flexure," *Construction and Building Materials*, vol. 43, no. 1, pp. 317–336, 2013.

Research Article

Transverse Deformations and Structural Phenomenon as Indicators of Steel Fibred High-Strength Concrete Nonlinear Behavior

Iakov Iskhakov iD **and Yuri Ribakov** iD

Department of Civil Engineering, Ariel University, Ariel 40700, Israel

Correspondence should be addressed to Yuri Ribakov; ribakov@ariel.ac.il

As known, high-strength compressed concrete elements have brittle behavior, and elastic-plastic deformations do not appear practically up to their ultimate limit state (ULS). This problem is solved in modern practice by adding fibers that allow development of nonlinear deformations in such elements. As a rule, are applied steel fibers that proved high efficiency and contribute ductile behavior of compressed high-strength concrete (HSC) elements as well as the desired effect at long-term loading (for other types of fibers, the second problem is still not enough investigated). However, accurate prediction of the ULS for abovementioned compression elements is still very important and current. With this aim, it is proposed to use transverse deformations in HSC to analyze compression elements' behavior at stages close to ultimate. It is shown that, until the appearance of nonlinear transverse deformations (cracks formation), these deformations are about 5-6 times lower than the longitudinal ones. When cracks appear, the tensile stress-strain relationship in the transverse direction becomes nonlinear. This fact enables to predict that the longitudinal deformations approach the ultimate value. Laboratory tests were carried out on 21 cylindrical HSC specimens with various steel fibers content (0, 20, 30, 40, and 60 kg/m^3). As a result, dependences of transverse deformations on longitudinal ones were obtained. These dependences previously proposed by the authors' concept of the structural phenomenon allow proper estimation of the compressed HSC state up to failure. Good agreement between experimental and theoretical results forms a basis for further development of modern steel fibered HSC theory and first of all nonlinear behavior of HSC.

1. Introduction

The first experimental study on Poisson's ratio (relation between transverse and longitudinal deformations before the appearance of transverse cracks) was carried out more than 100 years ago and was associated with plain and reinforced concrete columns [1, 2]. During the last century, the issue of Poisson's deformations was widely investigated. To obtain Poisson's ratios related to cylinder strength and age, 58 specimens were tested [3]. Corresponding theory was developed. It was concluded that there is no experimental evidence relating Poisson's coefficient of concrete to its strength. At the same time, our experimental results demonstrate that this ratio grows after the appearance of transverse cracks [4]. However, in this case, it is not Poisson's coefficient, but a ratio between transverse and longitudinal deformations.

An experimental study on the influence of stirrup and steel fiber reinforcement on the strength and deformation characteristics of conventionally reinforced $150 \times 150 \times 750$ mm concrete columns was carried out [5]. Steel fibers ratios were between 0 and 3% of the total composite material volume. It was reported that the column specimens had an increased energy absorption, high lateral strain, and greater Poisson's coefficient. The strength of the compression members is unaffected by either steel fiber volume or stirrup spacing.

Steel fibered high-strength concrete (SFHSC) became in the recent decades a very popular material in structural engineering [6]. As a result of increased application of SFHSC, many experimental studies are conducted to investigate its properties and to develop new rules for proper design. One of the trends in SFHSC structures is to provide their ductile behavior that is desired for proper structural

response to dynamic loadings. Review of recent experimental results obtained in the field of SFHSC is presented, and possible ways for developing modern design techniques for SFHSC structures are given.

Experimental studies were carried out to select effective fiber contents as well as suitable fiber types, to study most efficient combination of fiber and regular steel bar reinforcement [4]. It was shown that steel fibers have little effect on beams' elastic deformations but increase the ultimate ones, due to additional energy dissipation potential of steel fibers. This effect was further studied in repaired bending elements (two-layer beams) [7, 8]. It was shown that combination of the normal strength concrete layer with SFHSC one leads to effective and low-cost solution that may be used in new structures and for retrofitting existing ones.

Effect of steel fibers on postcracking and fracture behavior of concrete was also recently studied [9]. Plain and fiberd concrete specimens were tested. The strength properties, crack opening displacement, postcracking, and fracture behavior were studied. In our opinion, investigating postcracking behavior of concrete is interesting also from the viewpoint of transverse deformations, which will be discussed in the present paper.

Model fracture parameters of steel fiberd self-compacting concrete were derived from numerical simulation of splitting tensile tests [10]. The research allowed a comparison between the stress-crack width relationship from the tests and from analysis. For this purpose, a comprehensive nonlinear three-dimensional finite element modeling strategy was developed. The postcracking tensile laws, obtained from the modeling, provided a relationship with those obtained from the tests. In our opinion, analysis of stress-crack relationship of such concrete elements from the viewpoint of transverse deformations is also important, as it will allow more deeper understanding of SFHSC compressed elements' behavior.

Analytical and experimental results were presented for flexural response of SFRC beams [11]. Steel fiber content of 0.0%, 0.5%, 1.0%, and 2.0% by volume was used. Compressive strength and elastic modulus showed negligible changes with the inclusion of steel fibers, while the strain capacity and postpeak behavior were improved. Addition of more than 1.0% of steel fibers (by volume) resulted in significant improvement of flexural strength, deflection capacity, and postpeak ductility. The fracture energy increased with the increase in the fiber content. The authors have previously shown that the total energy dissipation during a loading-unloading cycle increases up to the fiber weight ratio (FWR) = 30 kg/m^3, that is, about 1.2% by volume [4]. Increasing the FWR to 40 kg/m^3 (about 1.6% by volume) yields almost the same energy dissipation, but further increase in FWR causes strong decreasing in dissipated energy.

Poisson's effect of concrete with lightweight aggregate was investigated [12]. The reduction of peak stress and modulus of elasticity was observed with increase of the volume fraction of shale aggregate. From the ratio of the lateral strain to the axial one, a more significant Poisson's effect was viewed for the concrete with a higher content of the shale aggregate. A corresponding expression was proposed to calculate the lightweight concrete stress-strain relation. Longitudinal and transverse deformations were measured and plotted. Following the experimental stress-strain curve results, the maximum deformations in longitudinal and transverse directions are about 2.3‰ and 0.5‰, respectively. It should be mentioned that the ratio between these values is about 5 times, which is well known from the existing design codes. Therefore, this ratio should be studied for fibred and nonfibred high-strength concrete, which will be done in the present study.

2. High-Strength Concrete and Its Application Problems

In the last decades, high-strength concrete (HSC) became a widely used construction material. During this period, a definition of HSC was given [13]. The modern codes for design of reinforced concrete (RC) structures included HSC up to concrete class C 90 [14]. As a rule, HSC is used with fibers. For example, a review of steel fibered HSC applications has been performed [6]. Optimal content of steel fibers for such concrete was obtained [4, 15]. Figure 1 shows the plastic energy dissipation in HSC specimens, U, and the fibers' weight ratios, FWR. As it follows from Figure 1, increasing the steel fibers' content from 0 to 30–40 kg/m^3 yields an increase in the dissipated energy, and further increasing of FWR above 40 kg/m^3 yields a decrease in energy dissipation. Thus, the reviled optimal steel fiber ratio for HSC is 30–40 kg/m^3. This result was obtained, based on experimental investigation of 21 standard cylindrical specimens with FWR of 0, 20, 30, 40, and 60 kg/m^3 [4].

As known, HSC is a brittle material. For example, the stress-strain graph for concrete class C 90 according to [14] corresponds to a parabola with an exponent of 1.4 and has no descending branch (Figure 2 and Table 1). Comparison of the graphs for concrete classes C 90, C 70, and C 50 shows that plastic energy dissipation decreases for class C 70, compared to C 50, and remains almost constant for concrete class C 90. Therefore, C 70 is defined as the lowest HSC class [13]. As it is evident from Table 1, the total energy dissipation in HSC is almost twice lower than in normal-strength concrete (NSC).

Using steel fibers in HSC increase the plastic deformations almost twice, but just at the stage that is close to the concrete ultimate state [7]. Therefore, in spite of adding fibers, it is impossible to know the compressed concrete section state: elastic, elastic-plastic, or plastic. Hence, the aim of the present paper is to find alternative methods to solve the problem.

3. Essence of Structural Phenomenon

Many researchers have investigated the behavior of structures under loads that increase from the elastic state up to failure. In this case, following the results obtained by the authors [16], if a structure and the load are symmetric, usually structural parameters in the elastic state increase or decrease twice at failure. We have called such changes in parameters of a structure as "structural phenomenon". This
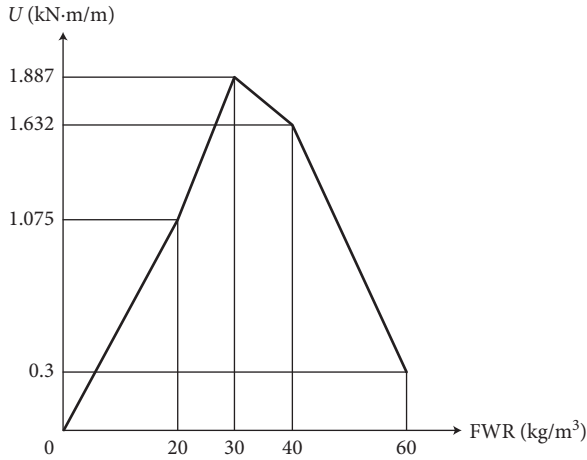
Figure 1: Energy dissipated during loading and unloading for cylindrical specimens with different FWRs [4].
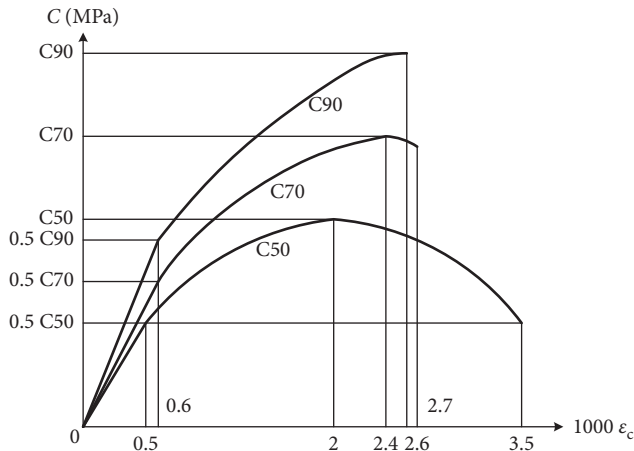

Figure 2: Stress-strain relationships for concrete classes C 50 (normal-strength concrete), C 70 (the lowest limit strength of high-strength concrete), and C 90 (high-strength concrete) [13].

Table 1: Energy dissipation comparison for concrete classes C 50, C 70, and C 90.

Energy dissipation from the graph $\sigma_c - \varepsilon_c$	Concrete class according to Eurocode 2		
	C 50	C 70	C 90
Graph exponent, n	2	1.45	1.4
Descending branch	Yes	No	No
Ratio between the area of the parabola to that of the described rectangle, $n/(n+1)$	0.667	0.592	0.584
Elastic energy dissipation, E_{el}	0.125 f_c (‰)	0.15 f_c (‰)	0.15 f_c (‰)
Plastic energy dissipation, E_{pl}	f_c (‰)	0.624 f_c (‰)	0.642 f_c (‰)
Total energy dissipation, E_{tot}	1.125 f_c (‰)	1.216 f_c (‰)	1.236 f_c (‰)
Ductility coefficient, E_{tot}/E_{el}	9.00	8.10	8.24

parameters, usually obtained experimentally or using some coefficients. Therefore, using this phenomenon can lead to developing proper design concepts and new RC theory, in which the number of empirical design coefficients will be minimal.

The above-described features of structural phenomenon enable to use it in the frame of the present study for obtaining a theoretical stress-strain curve of concrete. This approach is useful for many design aspects, including calculating the values of concrete elements ductility for high- and normal-strength concrete with and without fibers, which are usually obtained experimentally or using empirical dependences [19].

4. Evaluation of Available Experimental Data

Many experimental investigations were focused on studying SFHSC properties using cylindrical specimens with different steel fiber contents [4, 20, 21]. Table 2 summarizes available data from testing 21 cylindrical specimens, reported in the abovementioned studies. At the first stage [4], five different steel fiber contents were used, and at further stages [20, 21], optimal FWR = 30 kg/m^3 was used to obtain strength and deformation properties of the investigated SFHSC.

Investigating the deformation properties is focused on transverse tensile deformations in the tested specimens vs. the longitudinal ones. According to the available standards [14, 22, 23] and publications [15, 24], there are some differences in concrete transverse tensile deformations ε_{trans}, ultimate tensile deformations $\varepsilon_{ct\ ul}$, and Poisson's coefficient μ_c (Table 3). Therefore, the present study is based on available experimental data (Table 4).

Following this table, transverse tensile deformations are divided into two stages:

(i) Before the appearance of transverse cracks ($\varepsilon_{trans} \leq \varepsilon_{ct\ ul}$)

(ii) After the appearance of transverse cracks and up to specimen's failure ($\varepsilon_{trans} > \varepsilon_{ct\ ul}$)

These two stages are evident, for example, in response of RC columns to strong earthquake in Mexico, 2017 (Figure 3)

phenomenon was analyzed for the following groups of experiments:

(i) Investigation of structural concrete at the material level

(ii) Behavior of RC structures and elements under static loads

(iii) Response of RC structures and elements to dynamic loads

The phenomenon is based on two fundamental ideas:

(i) Quasi-isotropic state of a structure at the ultimate limit state (ULS) [17]

(ii) Mini-max principle [18]

Moreover, the phenomenon provides valuable indicators for experiments planning, estimation of the structural state (elastic, elastic-plastic, plastic, or failure), etc.

From the mathematical viewpoint, the phenomenon provides additional equation(s) that enable to calculate

TABLE 2: Available data from testing HSC cylindrical specimens.

Reference	Number of tested specimens	Compressive strength (MPa)	Fiber weight ratio (kg/m³)	Modulus of elasticity (MPa)
Holschemacher et al. [4]	15	86–91	0, 20, 30, 40, 60	—
Iskhakov et al., [18]	3	90.5*	30	41603*
Iskhakov et al., [21]	3	79.5*	30	39134*

*Average values.

TABLE 3: Poisson's ratio, μ_c, and ultimate tensile deformations, $\varepsilon_{ct\ ul}$.

Pos. No.	References	μ_c	$\varepsilon_{ct\ ul}$ (‰)
1	SI 466 [23]	0.15–0.25 (average. 0.2)	—
2	Bondarenko and Suvorkin [24]	0.2	0.1–0.2 (average 0.15)
3	BR [22]	0.2	0.15
4	Eurocode 2 [14]	0.2	—
5	Iskhakov [15]	0.15–0.2	0.07–0.12

TABLE 4: Experimental values of Poisson's coefficients for concrete class C 90 (pos. 1) and relation between transverse and longitudinal deformations (pos. 2).

Pos. no.	Limits of transverse deformations	Fiber weight ratio (FWR) (kg/m³)					Average	Average 2/Average 1
		0	20	30	40	60		
1	$\varepsilon_{trans} \leq \varepsilon_{ct\ ul}$	0.11	0.18	0.22	0.16	0.08	0.15	
2	$\varepsilon_{trans} > \varepsilon_{ct\ ul}$	0.20	0.32	0.44	0.40	0.14	0.30	2.0
3	Pos. 2/pos. 1	1.88	1.78	2.0	2.5	1.75	1.97	

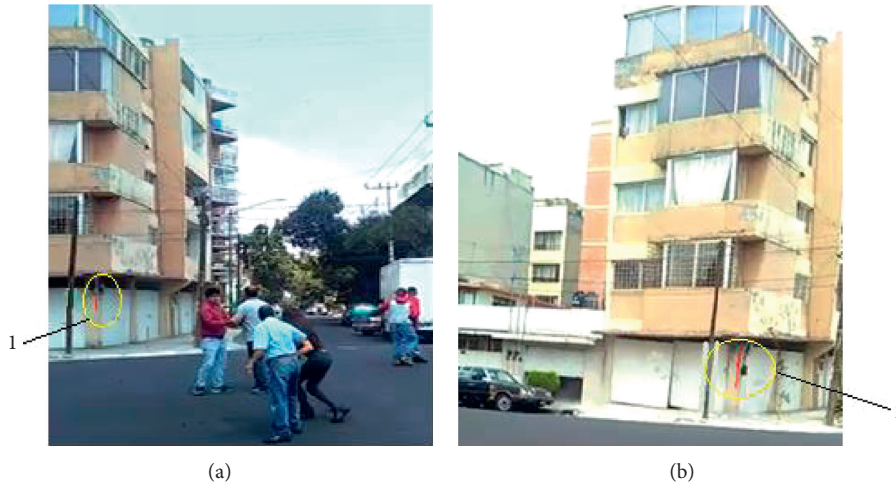(a)   (b)

FIGURE 3: Transverse cracks in a column during Mexico earthquake 2017 [25]: (a) 2 sec. (b) 15 sec. 1: crack initiation; 2: crack development.

[25]. As it follows from Figure 3, a crack due to transverse deformations (transverse cracks) appear at the 2nd second of the earthquake. Opening of the crack is a process, in which it develops in the longitudinal and transverse direction of the column (compare Figures 3(a) and 3(b)).

It should be mentioned that for SFHSC transverse deformations increase at both of the abovementioned stages up to FWR = 30 kg/m³ and decrease for a higher fiber content. The average transverse deformation at the first stage is 0.15, and at the second one, it is 0.30 (the value is increased twice), which corresponds to the structural phenomenon, proposed recently by the authors [16].

The abovementioned two stages have the following explanation: at ultimate longitudinal elastic deformations, $\varepsilon_c = 0.5$‰, and the transverse deformations $\varepsilon_{trans} \approx 0.1$‰, and it corresponds to concrete ultimate tensile deformations (Table 3). After that (at $\varepsilon_c > 0.5$‰), the transverse cracks opening process appears (Figure 4). At the same time, the second stage, according to the structural phenomenon, is divided into two subcases:

(i) cracks' development ($\varepsilon_{ct\ ul} < \varepsilon_{trans} \leq 2\ \varepsilon_{ct\ ul}$), corresponding to Figures 3(a) and 4(b)

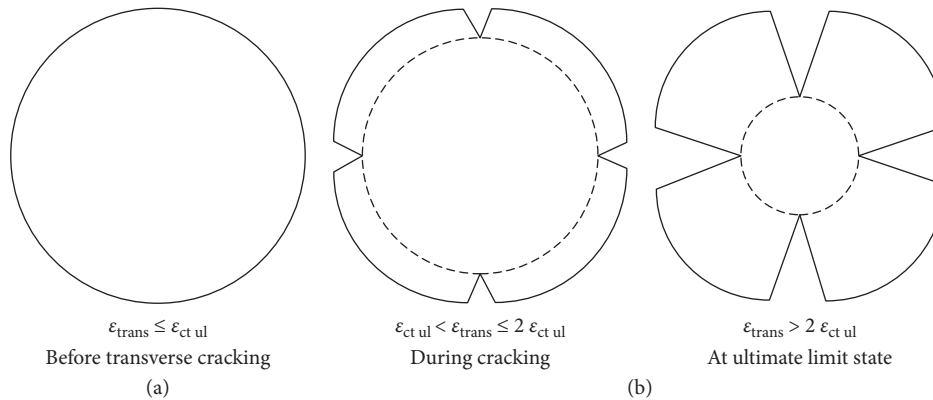(ii) failure ($\varepsilon_{trans} > 2\ \varepsilon_{ct\ ul}$), corresponding to Figures 3(b) and 4(c)

$\varepsilon_{\text{trans}} \leq \varepsilon_{\text{ct ul}}$

Before transverse cracking

(a)

$\varepsilon_{\text{ct ul}} < \varepsilon_{\text{trans}} \leq 2\,\varepsilon_{\text{ct ul}}$

During cracking

$\varepsilon_{\text{trans}} > 2\,\varepsilon_{\text{ct ul}}$

At ultimate limit state

(b)

FIGURE 4: Development of transverse deformations and cracks at stages 1 (a) and 2 (b) for cylindrical HSC specimens.

5. Detailed Analysis and Theoretical Interpretation of Experimental Results

5.1. Dependence of Load vs. Longitudinal and Load vs. Transverse Deformations. For cylindrical HSC specimens without fibers (Figure 5(a)), the dependences between load and longitudinal deformations as well as that between load and transverse ones are linear up to the ultimate state. In this case, the transverse deformations are actually also the Poisson ones, as nonlinear behavior is practically not evident. The specimens' behavior up to failure corresponds to Figure 4(a), i.e., transverse cracks do not appear. Poisson's coefficient is about 0.2. Similar results were obtained for the three specimens that were tested. It should be mentioned that both longitudinal and transverse deformations sharply increase at the ultimate state, which is explained by the specimens' failure process.

At fiber content (FWR) of $20\,\text{kg/m}^3$, the longitudinal deformations remain practically linear up to failure, at which plastic deformations develop. However, transverse deformations exhibit nonlinear behavior from about 70% of concrete strength, i.e., in this case, Poisson's coefficient can be calculated before nonlinear deformations initiate. Initiation of transverse cracks corresponds to stage 2 (Figure 4(b)), i.e., the specimens are in the stage of transverse cracks' development ($\varepsilon_{\text{ct ul}} \leq \varepsilon_{\text{trans}} \leq 2\,\varepsilon_{\text{ct ul}}$).

Increasing the FWR to 30 and $40\,\text{kg/m}^3$ leads to more evident nonelastic development of transverse deformations after reaching the limit tensile concrete deformations value $\varepsilon_{\text{ct ul}}$ (Figures 5(c) and 5(d)). Further increase in FWR to $60\,\text{kg/m}^3$ yields a decrease in development of transverse deformations (Figure 5(e)). Following Figure 5(e), appearance and development of transverse cracks is not reflected in longitudinal deformations, but it shows that a compressed element is at a state that is close to an ultimate one. This is the role of transverse deformations as an indirect indicator of compressed steel fibered concrete behavior.

5.2. Dependence of Transverse Deformations on Longitudinal Ones. As known, modern design codes operate with constant Poisson's ratios as relation between transverse

and longitudinal deformations $\mu_c = \varepsilon_{\text{trans}}/\varepsilon_{\text{long}}$ (Table 3). For example, following [14], Poisson's ratio may be taken equal to 0.2 for uncracked concrete and 0 for cracked one.

At the same time, as shows the experimental data [4], after the elastic limit is over, transverse deformations do not become equal to zero but develop nonlinearly within the limits $\varepsilon_{\text{ct ul}} \leq \varepsilon_{\text{trans}} \leq 2\,\varepsilon_{\text{ct ul}}$ (Figure 4(b) that corresponds to stage 2). This behavior satisfies the structural phenomenon concept. When $\varepsilon_{\text{trans}}$ exceeds the value of $2\,\varepsilon_{\text{ct ul}}$ (Figure 4(c)), the longitudinal deformations are not limited and the element approaches failure. Thus, analysis of the HSC behavior, considering transverse deformations, allows predicting of all concrete stages, including its nonlinear performance. By the way, these stages are evident from behavior of a concrete building column during an earthquake (Figure 3).

The abovementioned ideas correspond to experimental data presented in Figure 6 that shows dependences of transverse deformations on longitudinal ones for various FWR values from 0 to $60\,\text{kg/m}^3$. Analysis of the graphs in Figure 6 shows (especially in the cases when FWR = 30–$40\,\text{kg/m}^3$, corresponding to optimal fiber content, according to Figure 1) that there are three stages in concrete behavior:

(i) Linear

(ii) Nonlinear

(iii) Limit

It is evident from Figures 6(c) and 6(d) that, for $\varepsilon_{\text{trans}} \leq 0.2\permil$, transverse deformations develop proportionally to longitudinal ones, which corresponds to Poisson's deformations. When $\varepsilon_{\text{trans}} > 0.2\permil$, the graphs become nonlinear and the transverse deformations develop more intensively than longitudinal ones. For $\varepsilon_{\text{trans}} > 0.4\permil$ (that corresponds to the value of $2\,\varepsilon_{\text{ct ul}}$), transverse deformations sharply increase.

Further theoretical interpretation of such behavior of SFHSC (dependence between $\varepsilon_{\text{trans}}/\varepsilon_{\text{long}}$ vs. $\varepsilon_{\text{long}}$) is presented in Figure 7. The main feature in SFHSC behavior (that is evident from Figure 7) is that for longitudinal deformations $\varepsilon_{\text{long}} \leq 1\permil$ the ratio $\varepsilon_{\text{trans}}/\varepsilon_{\text{long}}$ is constant—it
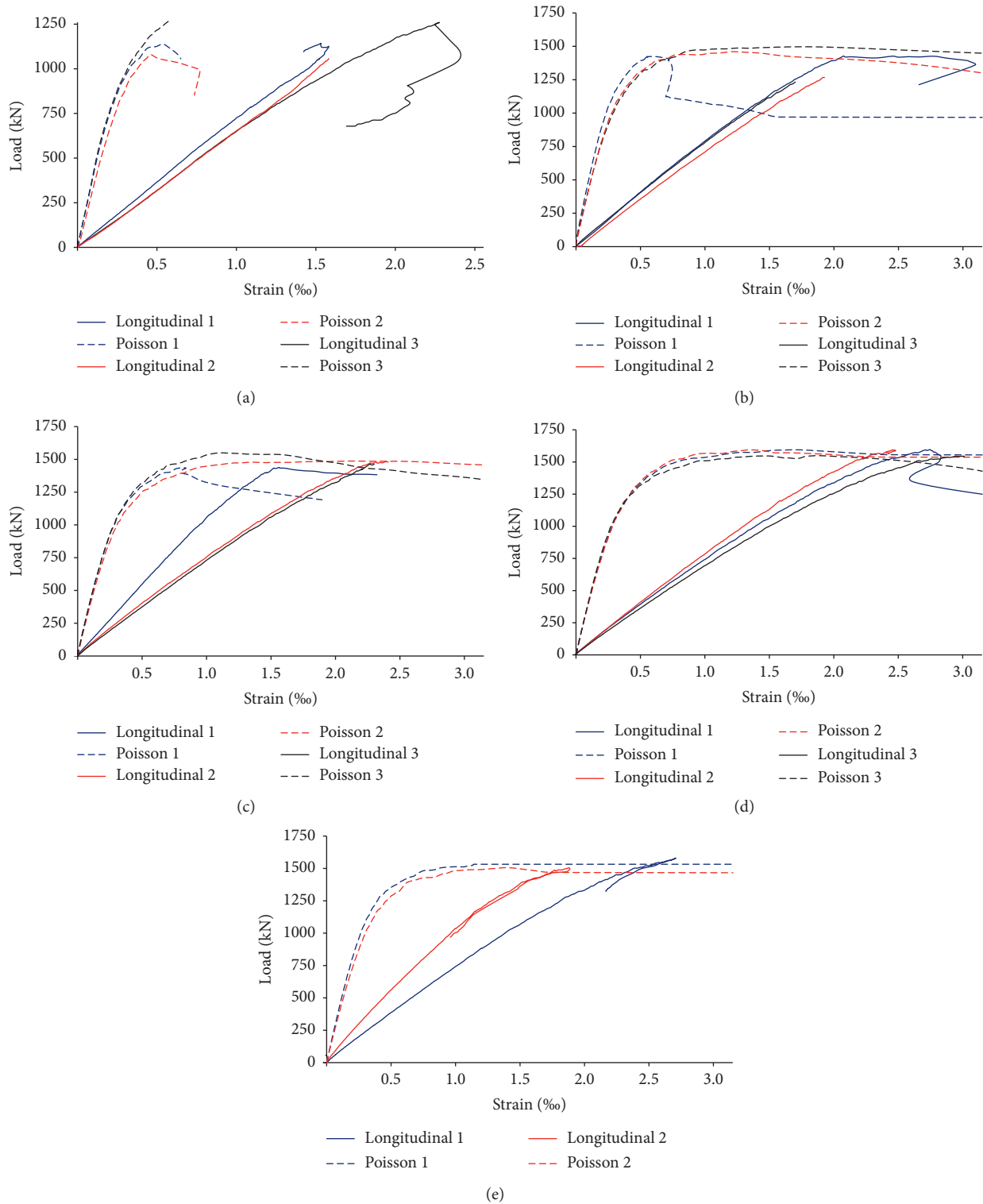
Figure 5: Load-strain diagrams for HSC with different FWRs. (a) FWR = 0; (b) FWR = 20 kg/m³; (c) FWR = 30 kg/m³; (d) FWR = 40 kg/m³; (e) FWR = 60 kg/m³.

indicates that the SFHSC behaves linearly. When $1‰ \leq \varepsilon_{long} \leq 2‰$, the SFHSC behaves nonlinearly, and for $\varepsilon_{long} > 2‰$, it approaches to failure.

The ratios between transverse and longitudinal deformations ($\varepsilon_{trans}/\varepsilon_{long}$) vs. the longitudinal ones (ε_{long}) are

presented in Table 5. As listed in Table 5, higher longitudinal deformations correspond to higher $\varepsilon_{trans}/\varepsilon_{long}$ ratios. Relation between the measured deformations' values and those proposed in the theoretical interpretation are shown in Figure 8. The obtained result enables to revile the main
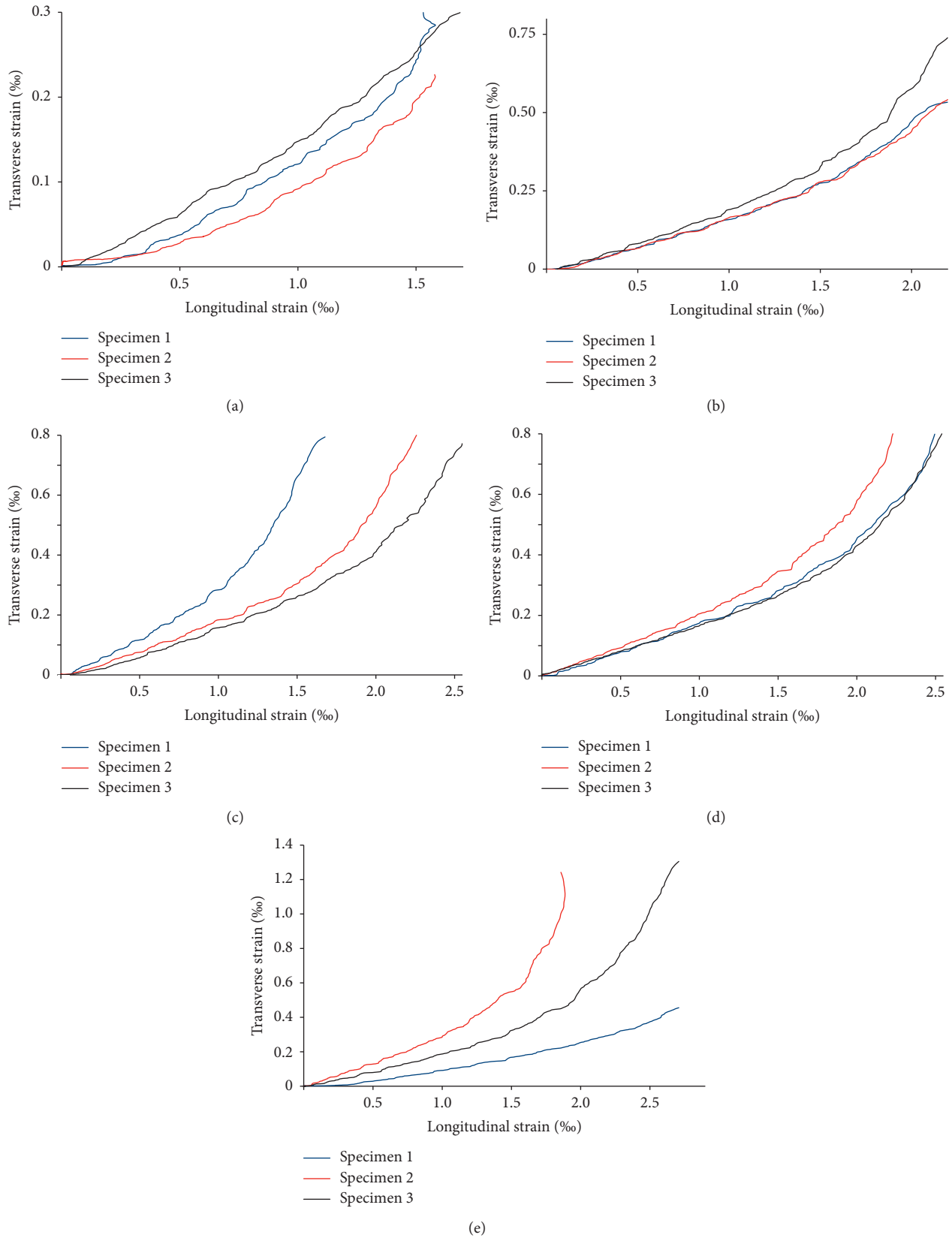
FIGURE 6: Dependence of transverse strain on longitudinal one for (a) FWR = 0; (b) FWR = 20 kg/m^3; (c) FWR = 30 kg/m^3; (d) FWR = 40 kg/m^3; (e) FWR = 60 kg/m^3.
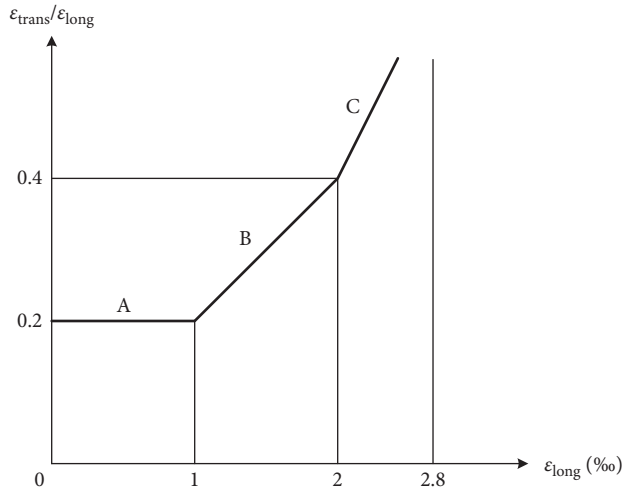
FIGURE 7: Proposed theoretical relationship between longitudinal deformations and transverse to longitudinal deformations' ratio: A, linear behavior of HSC; B, nonlinear behavior of HSC; C, stage before the HSC reaches the ULS.

TABLE 5: The ratio between transverse and longitudinal deformations ($\varepsilon_{trans}/\varepsilon_{long}$) vs. the longitudinal ones (ε_{long}).

FWR (kg/m³)	Specimen	$\varepsilon_{trans}/\varepsilon_{long}$		
		$\varepsilon_{long} \leq 1‰$	$1‰ \leq \varepsilon_{long} \leq 2‰$	$\varepsilon_{long} \geq 2‰$
0	1	0.12	0.22	—
	2	0.09	0.17	—
	3	0.14	0.25	0.5
	Average	0.12	0.21	0.5
20	1	0.18	0.30	—
	2	0.18	0.30	0.52
	3	0.20	0.28	0.65
	Average	0.19	0.29	0.58
30	1	—	—	—
	2	0.20	0.3	0.60
	3	0.15	0.25	0.80
	Average	0.18	0.28	0.70
40	1	0.18	0.22	0.80
	2	0.20	0.40	1.00
	3	0.18	0.22	0.80
	Average	0.19	0.28	0.87
60	1	—	—	—
	2	0.25	0.75	2.00
	3	0.20	0.25	—
	Average	0.23	0.50	2.00

stages in SFHSC behavior, and therefore, it is useful for more effective design of SFHSC elements.

It should be highlighted that the abovementioned analysis became possible due to application of the structural phenomenon concept, explained in Section 3.

6. Conclusions

Accurate prediction of nonlinear behavior of compressed steel fibered high-strength concrete (SFHSC) elements is investigated experimentally and theoretically. For the first time, development of nonlinear postcracking transverse
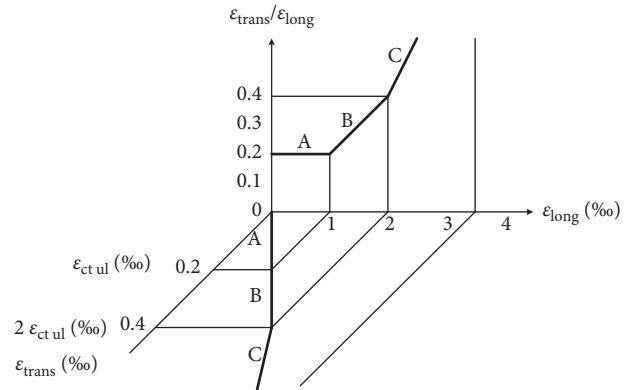

FIGURE 8: Theoretical dependences between transverse deformations vs. longitudinal deformations and transverse to longitudinal deformations' ratio vs. longitudinal deformations: A, linear behavior of HSC; B, nonlinear behavior of HSC; C, stage before the HSC reaches the ULS.

deformations was used to analyze nonlinear behavior of SFHSC compressed elements.

Using the structural phenomenon enables to revile three stages of transverse deformations' development in compressed SFHSC elements: linear ($\varepsilon_{trans} \leq \varepsilon_{ct\ ul}$), nonlinear ($\varepsilon_{ct\ ul} \leq \varepsilon_{trans} \leq 2\ \varepsilon_{ct\ ul}$), and ultimate ($\varepsilon_{trans} > 2\ \varepsilon_{ct\ ul}$).

Unlike in current normative documents, the physical meaning of Poisson's coefficient is expanded for cases, when transverse cracks appear in compressed concrete elements. It is shown that, at optimal fiber content, this coefficient increases up to twice, which completely corresponds to the structural phenomenon.

Dependences of transverse deformations on longitudinal ones were obtained experimentally and theoretically. These dependences previously proposed by the authors concept of the structural phenomenon allow proper estimation of compressed SFHSC states, including nonlinear behavior, up to failure.

Good agreement between experimental and theoretical results forms a basis for further development of modern steel fibered HSC theory (and first of all nonlinear behavior of SFHSC) that can be applied in modern design codes.

Data Availability

All required data are included in the manuscript.

Conflicts of Interest

The authors declare that there no conflicts of interest regarding the publication of this paper.

References

[1] A. N. Talbot, *Tests of Concrete and Reinforced Concrete Columns, Engineering Experiment Station*, University of Illinois, Bulletin No. 20, 1907.

[2] M. O. Withey, *Tests of ReinJorced Concrete Columns*, University of Wisconsin, Bulletin No. 466, 1911.

[3] A. E. Allos and L. H. Martin, "Factors affecting Poisson's ratio for concrete," *Building and Environment*, vol. 16, no. 1, pp. 1–9, 1981.

[4] K. Holschemacher, I. Iskhakov, Y. Ribakov, and T. Mueller, "Laboratory tests of two-layer beams consisting of normal and fibered high strength concrete: ductility and technological aspects," *Mechanics of Advanced Materials and Structures*, vol. 19, no. 7, pp. 513–522, 2012.

[5] P. S. Mangat and M. Motamedi Azari, "Influence of steel fibre and stirrup reinforcement on the properties of concrete in compression members," *International Journal of Cement Composites and Lightweight Concrete*, vol. 7, no. 3, pp. 183–192, 1985.

[6] A. A. Shah and Y. Ribakov, "Recent trends in steel fibered high-strength concrete," *Materials & Design*, vol. 32, no. 8-9, pp. 4122–4151, 2011.

[7] I. Iskhakov and Y. Ribakov, "A new concept for design of fibered high strength reinforced concrete elements using ultimate limit state method," *Materials & Design*, vol. 51, pp. 612–619, 2013.

[8] I. Iskhakov, Y. Ribakov, K. Holschemacher, and T. Mueller, "High performance repairing of reinforced concrete structures," *Materials & Design*, vol. 44, pp. 216–222, 2013.

[9] F. Bencardino, L. Rizzuti, G. Spadea, and R. N. Swamy, "Implications of test methodology on post-cracking and fracture behaviour of Steel Fibre Reinforced Concrete," *Composites Part B: Engineering*, vol. 46, pp. 31–38, 2013.

[10] A. Abrishambaf, J. A. O. Barros, and V. M. C. F. Cunha, "Tensile stress-crack width law for steel fibre reinforced self-compacting concrete obtained from indirect (splitting) tensile tests," *Cement and Concrete Composites*, vol. 57, pp. 153–165, 2015.

[11] D.-Y. Yoo, Y.-S. Yoon, and N. Banthia, "Predicting the post-cracking behavior of normal- and high-strength steel-fiber-reinforced concrete beams," *Construction and Building Materials*, vol. 93, pp. 477–485, 2015.

[12] B. Han and T.-Y. Xiang, "Axial compressive stress-strain relation and Poisson effect of structural lightweight aggregate concrete," *Construction and Building Materials*, vol. 146, pp. 338–343, 2017.

[13] I. Iskhakov and Y. Ribakov, "A design method for two-layer beams consisting of normal and fibered high strength concrete," *Materials & Design*, vol. 28, no. 5, pp. 1672–1677, 2007.

[14] *Eurocode 2: Design of Concrete Structures–Part 1-1: General Rules and Rules for Buildings*, 2004.

[15] I. Iskhakov, *Plastic Energy Dissipation, Ductility and Load-Carrying Capacity of RC Elements*, ALFA Publishers, 2012, in Hebrew

[16] I. Iskhakov and Y. Ribakov, "Structural phenomenon of cement-based composite elements in ultimate limit state," *Advances in Building Technologies and Construction Materials*, Article ID 4710752, 9 pages, 2016.

[17] I. Iskhakov, "Quasi-isotropic ideally elastic-plastic model for calculation of RC elements without empirical coefficients," in *Structural Engineering, Mechanics and Computation*, Vol. 1, A. Zingoni, Ed., Elsevier Press, Cape Town, South Africa, 2001.

[18] I. Iskhakov and Y. Ribakov, *Ultimate Equilibrium of RC Structures using Mini-Max Principle*, Nova Science Publishers, Inc., Hauppauge, NY, USA, 2014.

[19] I. Iskhakov, Y. Ribakov, and A. Shah, "Experimental and theoretical investigation of column - flat slab joint ductility," *Materials & Design*, vol. 30, no. 8, pp. 3158–3164, 2009.

[20] I. Iskhakov, Y. Ribakov, K. Holschemacher, and T. Mueller, "Experimental investigation of full scale two-layer reinforced concrete beams," *Mechanics of Advanced Materials and Structures*, vol. 21, no. 4, pp. 273–283, 2014.

[21] I. Iskhakov, Y. Ribakov, and K. Holschemacher, "Experimental investigation of continuous two-layer reinforced concrete beams," *Structural Concrete*, vol. 18, no. 1, pp. 205–215, 2017.

[22] *BR 52-101-2003, Non-pre-stressed concrete and reinforced concrete structures*, NIIZhB, Moscow, 2004, in Russian.

[23] *SI 466 Concrete code: General principles, part 1*, The Standards Institution of Israel, 2012.

[24] V. M. Bondarenko and D. G. Suvorkin, *Reinforced Concrete and Stone Structures*, Vysshaya Shkola, Moscow, 1987, in Russian.

[25] *Mexico earthquake September 2017*, 2018, https://twitter.com/nssoaxaca/status/910224886014136320?refsrc=twsrc%5Etfw%7Ctwcamp%5Etweetembed%7Ctwterm%5E910224886014136320&ref_url=https%3A%2F%2Fwww.businessinsider.com%2Fmexico-puebla-earthquake-photos-videos-twitter-facebook-2017-9.

Research Article

Experimental Study on Long-Term Ring Deflection of Glass Fiber-Reinforced Polymer Mortar Pipe

Sun-Hee Kim [ID],[1] **Soon-Jong Yoon,**[2] **and Wonchang Choi** [ID][3]

[1]*Assistant Professor, Department of Architectural Engineering, Gachon University, Seongnam, Gyeonggi-do 13120, Republic of Korea*
[2]*Professor, Department of Civil Engineering, Hongik University, Seoul 04066, Republic of Korea*
[3]*Associate Professor, Department of Architectural Engineering, Gachon University, Seongnam, Gyeonggi-do 13120, Republic of Korea*

Correspondence should be addressed to Wonchang Choi; wonchang.choi@gmail.com

Long-term pressurizing of buried glass fiber-reinforced polymer (GFRP) pipe will result in the reduction of stiffness in the pipes. It leads to excessive deflections in long-term design limits. In situ tests were performed for 664 days to measure deflections of buried GFRP pipe with a large diameter of 2,400 mm. Based on the field test results, finite element analysis was conducted to determine the pipe deflections with respect to the soil conditions and buried depth as variables. Regression analysis has been conducted to determine the long-term deflection of the GFRP pipe after 50 years of construction. The long-term deflection of the GFRP pipe was less than 5 percent suggested by the existing specifications including ASTM D5365 and AWWA M45. The comparison indicates the current specifications significantly conservative to predict long-term deflection of the buried GFRP pipe.

1. Introduction

Glass fiber-reinforced polymer (GFRP) pipe exhibits excellent resilience due to the stiffness and strength of the material compared to other types of pipes. GFRP pipes are compatible with other flexible pipes. Also, GFRP pipes are used in the construction industries due to the advantages of mechanical characteristics such as light weight, high specific strength and stiffness, and high corrosion resistance.

Furthermore, the mechanical properties of GFRP pipe, which depend on the arrangement and amount of reinforcing fibers, satisfy various conditions. GFRP pipes are classified as ductile pipes because, unlike rigid pipe, they interact with the ground and resist external loads. The structural behavior of underground pipes must be considered with regard to the possible effects of the foundation, the soil surrounding the pipe, and the characteristics of the backfill.

Most studies that have investigated the durability of the pipe material have examined the long-term properties of the pipe itself. For example, Farshad and Necola [1] conducted an experimental study of the short-term and long-term behavior of GFRP pipes in underwater environments. Their study's experimental results show that the stiffness of GFRP pipes does not decrease; regression analysis predicted the GFRP pipe strength to be about 7.5 kN after 50 years.

Farshad [2] predicted the long-term behavior of multilayer pipes according to internal water pressure. Farshad estimated the long-term strength of the composite pipe by combining secondary and linear regression analysis. The analysis, design, evaluation, residual analysis, and long-term estimation of the pipe were performed via "automated design and analysis of pipes" (ADAP) software. As a result, Farshad [2] derived a new long-term estimation method to predict the long-term life of pipes composed of various layers.

Faria et al. [3] investigated the creep and relaxation behavior of glass-reinforced thermosetting polymer plastic pipes using the same reliability as conventional methods by developing a method to replace the long-term characteristics of the pipe.

Faria and Guedes [4] compared measurement errors for four types of GFRP pipes using the standard method by regression analysis of the data to reduce the prediction time long-term behavior tests of the GFRP pipe. They found the measurement error to be 10 percent less than the measurement error derived from the standard method in short-term testing.

Sargand et al. [5] investigated the behavior of thermoplastic pipes for five years when installation under at least 6.1 m to 12.2 m was applied to thermoplastic pipes, high-density polyethylene (HDPE) pipe, and polyvinyl chloride (PVC) pipe. Their results confirmed that both seasonal temperature differences and soil moisture conditions affect the earth pressure. Based on Sargand et al.'s [5] theoretical analysis, both the changes in soil conditions changes and effects of earth pressure were found to be significant.

Kim et al. [6] predicted the turbulent deflection of glass fiber-reinforced thermosetting polymer plastic pipe embedded in nuclear cooling water. Ten thousand hours of experimental data are required to predict pipe bending strain.

Yoon and Oh [7] predicted the 50-year long-term failure of GRP pipes from failure pressure and time to failure which was tested up to 10,000 hours through the sustained internal pressure test.

Na et al. [8] tested the long-term ring-bending strain (Sb) of the GFRP pipe using the standard method to predict the life of the pipe after 50 years. A comparison of the standard method and an optimized statistical method via GFRP pipe tests showed that the error was less than 8 percent. This work confirmed that the bending strain of the pipe after 50 years can be predicted using the proposed statistical method without performing tests that take 10,000 hours.

Lee et al. [9] measured the short-term behavior of a 2,400 mm large diameter reinforced thermosetting resin pipe for 387 days in a buried pipe field test and predicted long-term behavior for 40 to 60 years.

Most studies have focused on the durability of flexible pipe. Also, long-term behavior of the flexible pipe was predicted by short-term experimental test results. In order to predict the exact long-term ring deflection of buried pipe underground, the structure should be buried for a long time. However, limitations of such work include high costs and a large budget, and finding an appropriate test site.

In this study, a large diameter reinforced polymer mortar pipe (RPMP) reinforced with resin and mortar was embedded between the resin and fiberglass sections, and the long-term ring deflection of the GFRP pipe was measured for 664 days.

The safety of a buried underground GFRP pipe can be determined through the finite element analysis and predicted pipe ring deflections using the Iowa formula proposed by the American Water Works Association (AWWA M45). To predict long-term ring deflection, the long-term behavior of the GFRP pipe was predicted statistically using initial measurement data (pipe ring deflection data) proposed in American Society for Testing and Materials (ASTM D5365) [10].

2. Design Procedure for Buried GFRP Pipe

2.1. Fabrication of GFRP Pipe.
The fabrication of the GFRP pipe involves a continuous filament winding process in which several mandrels are moved to wind up reinforcing fibers at multiple locations. The axial tensile strength of the pipe is increased by arranging the reinforcing fiber in the axial direction. The GFRP pipe used in this study was fabricated from RPMP that was reinforced with resin and mortar between sections that were composed of resin and glass fiber. Table 1 presents the mechanical properties of the GFRP pipe used in this study.

2.2. Structural Behavior of Buried Flexible Pipe.
The structural behavior of the pipe that is embedded underground differs according to the type of external pressure. When the external load is a static load, the vertical earth pressure that is acting on the buried pipe is determined by the load on the upper part of the pipe and the area to be loaded.

In this case, the pipe buried in the ground deforms to induce earth pressure in the horizontal direction, and the vertical earth pressure generated from the load becomes greater than the horizontal earth pressure generated by the pipe deflection.

Therefore, as shown in Figure 1, under normal loading conditions, the pipe is deformed by Δ_v in the vertical direction and deformed by Δ_h in the horizontal direction.

When a preload is applied to the upper part of the pipe without consideration of the effect of the surrounding soil on the pipe deflection, the amount of pipe deflection for each direction is calculated using the following equations [11]:

$$\Delta_v = 0.149 \frac{r^3}{EI} w, \tag{1}$$

$$\Delta_h = 0.137 \frac{r^3}{EI} w, \tag{2}$$

where Δ_v is the vertical deflection (mm), Δ_h is the horizontal deflection (mm), r is the mean radius of the pipe (mm), E is the modulus of elasticity for hoop direction (MPa), I is the moment of inertia of the pipe (mm^4/mm), and w is the line load applied on top of the soil (kN/m).

Although equations (1) and (2) will differ somewhat depending on the materials that constitute the pipe, a small deflection theory is adopted. The predictions are relatively accurate within about 3 percent of pipe strain, but the accuracy is diminished slightly due to material and geometric nonlinearities above 3 percent of the pipe strain [11].

In addition, pipe stiffness (PS) must be determined in order to predict the deflection of buried pipes. The PS can be determined using equations (3a) or (3b). The PS is determined from the original stiffness test and is the value obtained by dividing the force (F) per unit length that corresponds to the 5 percent pipe strain caused by vertical displacement. The PS can be computed by the ring flexural modulus (E). The moment of inertia (I) of the pipe can be obtained from equation (3b):

TABLE 1: Mechanical properties of the GFRP pipe.

| Material properties		GFRP pipe	Standard
	Diameter (mm)	2,400	—
	Thickness (mm)	44.5	—
Hoop	Tensile strength (MPa)	146	ASTM D2290-08 [12]
	Tensile elasticity modulus (GPa)	16.5	ASTM D2290-08 [12]
Axial	Tensile strength (MPa)	78.9	ASTM D638-10 [13]
	Tensile elasticity modulus (GPa)	9.45	ASTM D638-10 [13]
	Compressive strength (MPa)	149	ASTM D695 [14]
	Compressive modulus of elasticity (GPa)	8.97	ASTM D695 [14]
	Bending strength (MPa)	154	ASTM D790-10 [15]
	Bending modulus of elasticity (GPa)	11.5	ASTM D790-10 [15]
	Poisson's ratio	0.20	ISO 527-4 [16]
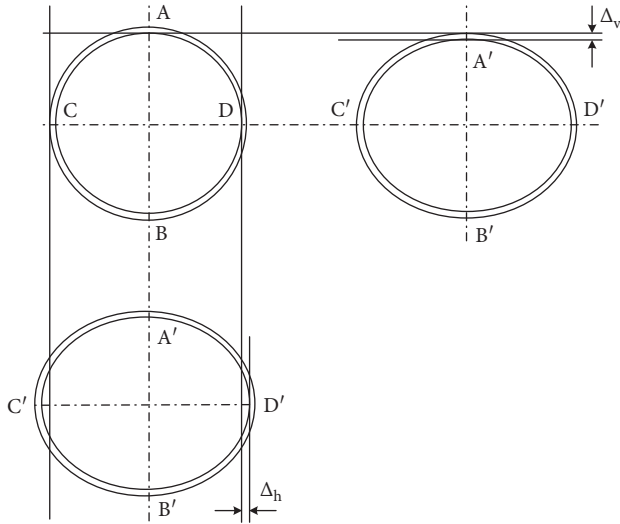
FIGURE 1: Ring deflection.

$$PS = \frac{F}{\Delta v}, \tag{3a}$$

$$PS = 6.7 \frac{EI}{r^3}, \tag{3b}$$

where E is the ring flexural modulus (GPa), I is the moment of inertia of unit length (mm^4/mm $= -(t)^3/12$), r is the mean pipe radius (mm $= (OD - t)/2$), F is the force, and Δ_v is the vertical deflection (%).

The Iowa formula proposed in ASTM D2412 [17] was applied in this study to predict the deflection of the flexible buried pipe. The Iowa formula is shown in equation (4) and includes load and boundary conditions, such as the stiffness of the flexible pipe, the soil reaction force coefficient of the rebound soil, and foundation conditions for flexible underground pipes. The behavior of the flexible pipe is clearly expressed in the buried underground:

$$\Delta_h = \frac{(D_L W_c + W_L) K_X}{0.149 PS + 0.061 E'}, \tag{4}$$

where D_L is the deflection lag factor to compensate for the time consolidation rate of the soil, dimensionless, W_c is the vertical soil load on the pipe (N/m^2), W_L is the live load on the pipe (N/m^2), K_X is the bending coefficient, dimensionless, PS is the pipe stiffness (kPa), E' is the composite soil constrained modulus (MPa), and Δ_h is the horizontal deflection (mm).

Equation (4) in the Iowa formula limits the deflection of the pipe to within 5 percent by applying a safety factor of 4 when pipe deflection occurs at about 20 percent. The reason for this limitation is to consider the safety of the pipe even for long-term ring deflection. The effects of pipe joint leakage also are considered [18].

3. Experimental Program

3.1. Full-Scale Field Experiments. In order to investigate the structural behavior of the GFRP pipe, the GFRP pipe composed of RPMP was buried and the soil was compacted at the underground location of the pipe. Field test was carried out at four sites of the buried GFRP pipe, as shown in Figure 2. Figure 3 shows the location of measurement for vertical and horizontal deflections of the GFRP pipe using a laser distance meter which was installed at each site.

3.2. Numerical Analysis. In order to analyze the structural behavior of the buried GFRP pipe and compare it with the field measurements, the finite-difference analysis (FDA) was carried out with respect to buried depth as variables. The MIDAS/GTS program [19] was used for two-dimensional numerical analysis. The Mohr–Coulomb failure criterion was adopted for the soil conditions which use an elasto-plastic modeling associated with a homogenous material. Linear elastic modeling was used for the beam elements for the GFRP pipe. Both end supports and bottom supports are assumed as a fixed boundary condition.

The characteristics of the pipe bedding material (PBM) are summarized in Table 2 which is obtained by field test results. Table 3 presents three cases of the compaction conditions for the GFRP pipe used for the numerical analysis in this study.

Analytical modeling takes place when 5 m, 10 m, and 16 m are filled in the upper part of the GFRP pipe, as shown in Figure 4(a). Figure 4(b) shows the grid mesh for the FDA.

Figure 5 presents displacement contour with FDA results for each case at a buried depth of 16 meter. The stress distribution surrounding the buried GFRP pipe is influenced by the characteristic of PBM. Table 4 provides a summary of the results of the FDA and experimental results. Based on the measurements, the vertical deflection and horizontal deflection were found to be the same as for the analytical results when the compaction condition of the ground around the GFRP pipe in Case 1 was well matched in the finite element
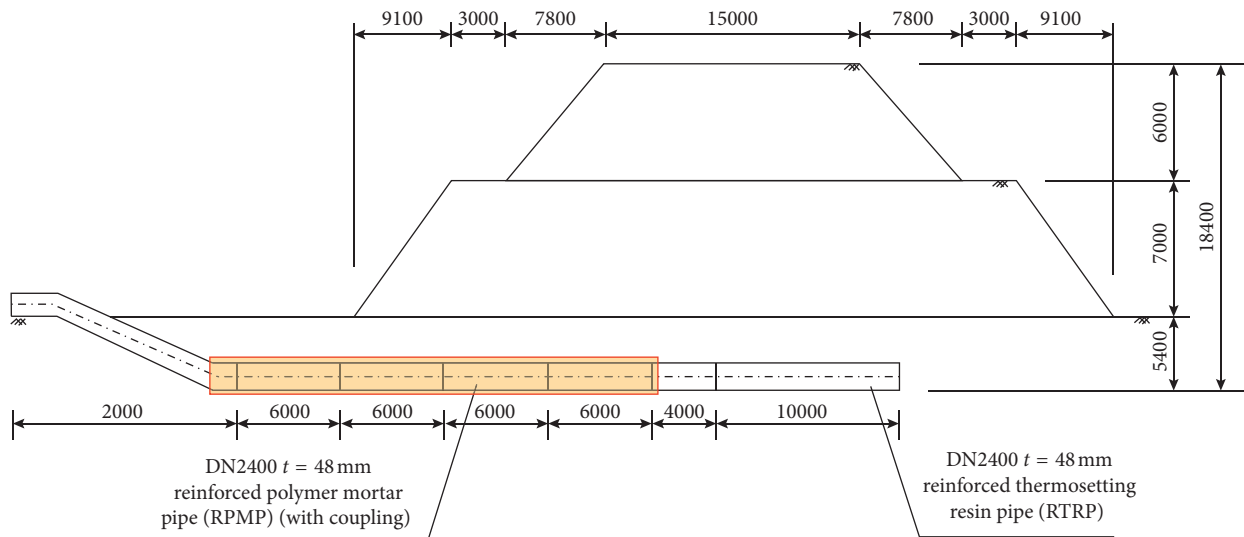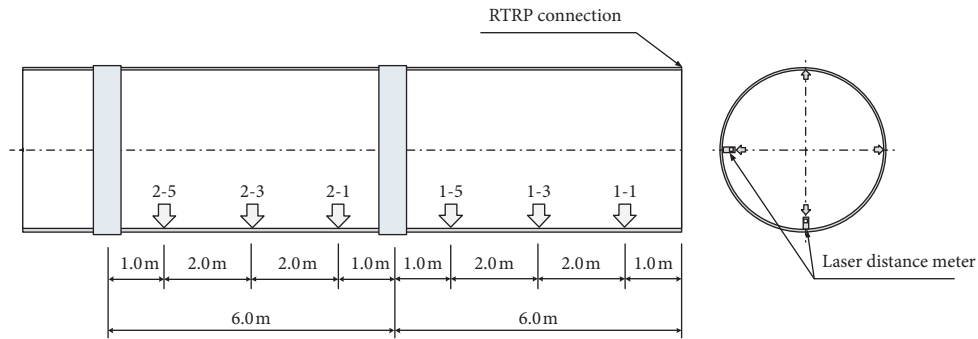
Figure 2: Side elevation of underground GFRP pipe.

(a)

(b)

Figure 3: Measurements of GFRP pipe deflections. (a) Locations of measurement. (b) Laser distance meter and taking measurements.

Table 2: Characteristics of the soil materials [9].

Description	Soil modulus, E (kN/m^2)	Poisson's ratio, ν	Unit weight, γ_t (kN/m^3)	Viscosity, C (kN/m^2)	Internal friction angle, φ (°)
General fill	40,000	0.30	20.19	0.0	35.0
PBM #1	30,000	0.30	17.85	0.0	30.0
PBM #2	3,000	0.30	17.85	0.0	30.0
Residual soil #1	50,000	0.30	18.00	0.0	34.0
Residual soil #2	80,000	0.30	19.00	0.0	40.0
Weathered rock	15,000	0.30	20.00	30.0	35.0
Soft rock	30,000	0.25	22.00	50.0	40.0

TABLE 3: Soil conditions around GFRP pipe for the finite-difference analysis [9].

Description	Buried depth (m)	Soil conditions around GFRP pipe	
		Domain	Soil characteristic
Case 1	5, 10, 16	Whole of soil around GFRP pipe	PBM #1
Case 2	5, 10, 16	Center of GFRP pipe (2D) in Figure 5(a)	PBM #2
Case 3	5, 10, 16	Center of GFRP pipe (3D) in Figure 5(a)	PBM #2

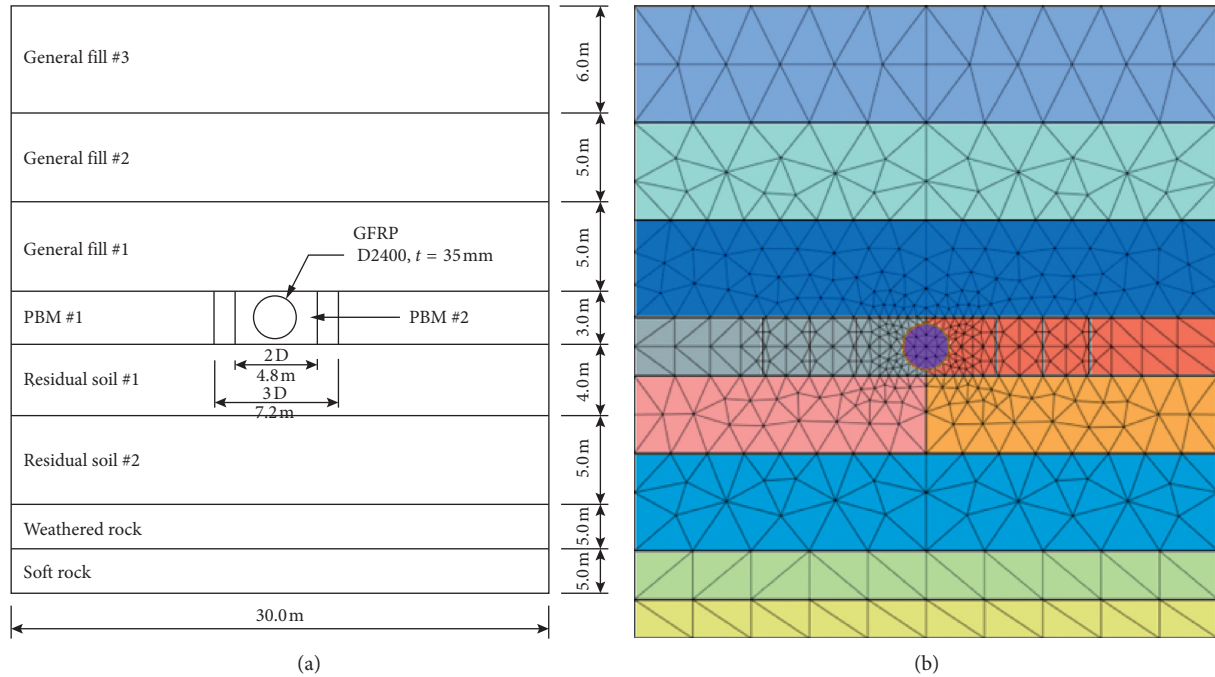(a)   (b)

FIGURE 4: Finite element analysis model. (a) Schematic view. (b) Finite element analysis mesh model (2D).

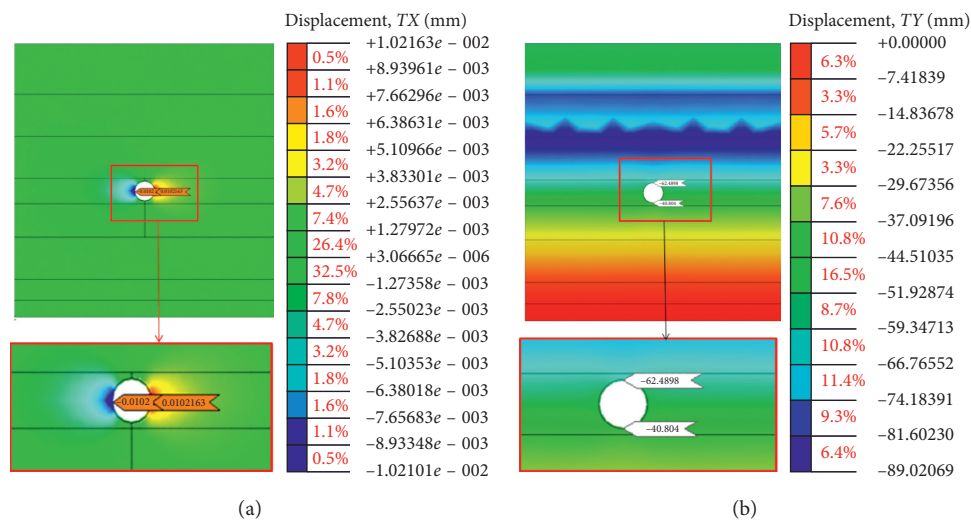(a)   (b)
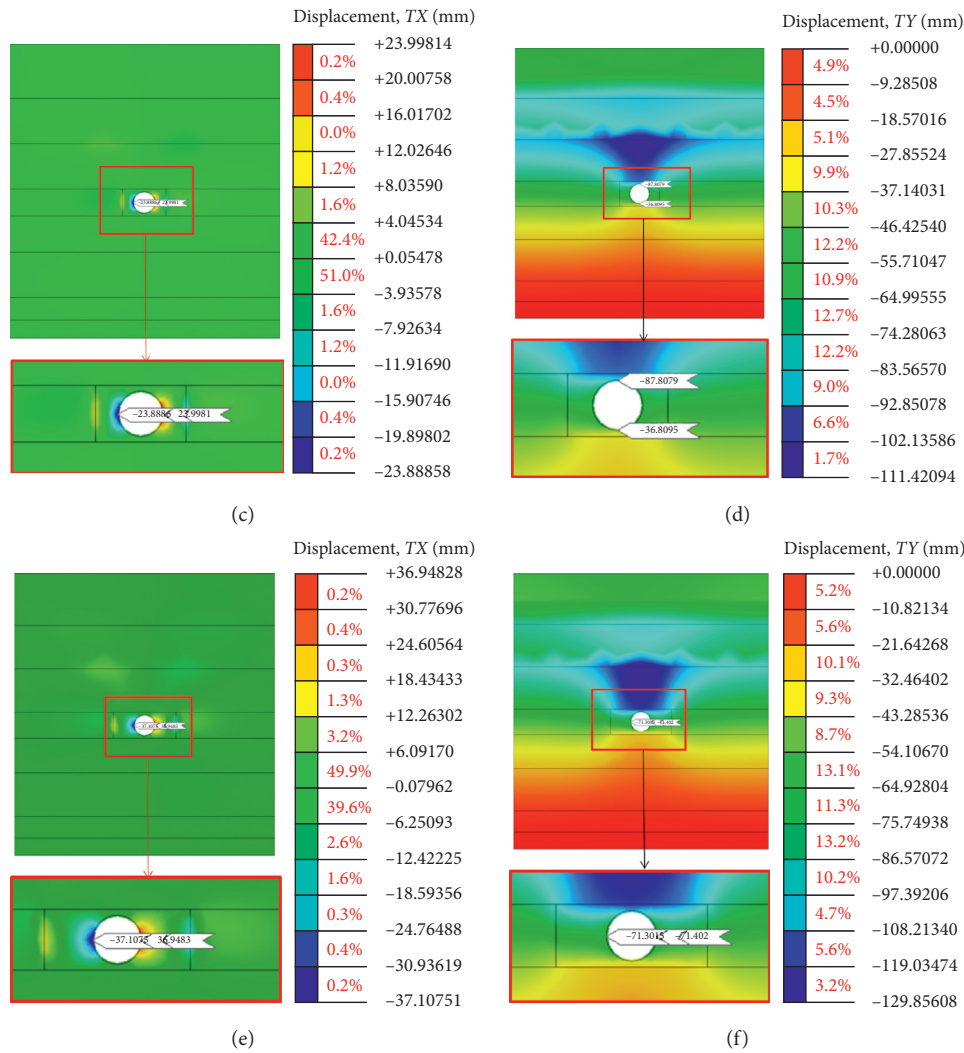
FIGURE 5: Continued.

FIGURE 5: Finite element analysis results. (a) Horizontal deflection for Case 1 (16 m). (b) Vertical deflection for Case 1 (16 m). (c) Horizontal deflection for Case 2 (16 m). (d) Vertical deflection for Case 2 (16 m). (e) Horizontal deflection for Case 3 (16 m). (f) Vertical deflection for Case 3 (16 m).

TABLE 4: Comparisons of numerical analysis results and experimental results.

Buried depth (m)	Two-dimensional analytical results (%)						Experimental results (%)		AWWA M45 (%)	
	Case 1		Case 2		Case 3					
	Δ_v	Δ_h	Δ_v	Δ_h	Δ_v	Δ_h	Δ_v	Δ_h	Δ_v	Δ_h
5	−0.28	0.27	−0.75	0.71	−1.17	1.18	−0.17	0.17	−0.52	0.52
10	−0.56	0.53	−1.38	1.30	−2.06	2.07	−0.38	0.38	−1.05	1.05
16	−0.90	0.85	−2.13	2.00	−3.08	3.09	−0.71	0.54	−1.67	1.67

Note: (+): increases in diameter; (−): decreases in diameter.

analysis. The accuracy of the FDA was validated by test results, and it proved to be capable of simulating ring deflection with respect to buried condition.

The horizontal ring deflections and vertical ring deflections in Case 1 calculated by the finite-difference analysis agreed with the experimental results. According to the comparison results, it can be seen that the compaction density of soil around the buried pipe affected on the deflection of the pipe embedded underground.

4. Test Result and Discussion

4.1. Field Test Results and Prediction of Pipe Deflection. Figure 6 shows the measured vertical and horizontal displacements at 1 m, 3 m, and 5 m from the entrance of the pipe. The measured pipe deflection was within 1.5 percent. Most of the total deflection occurred within the first 30 days after construction. As soil is placed over a buried GFRP pipe, the ring tends to deflect primarily into an ellipse with a
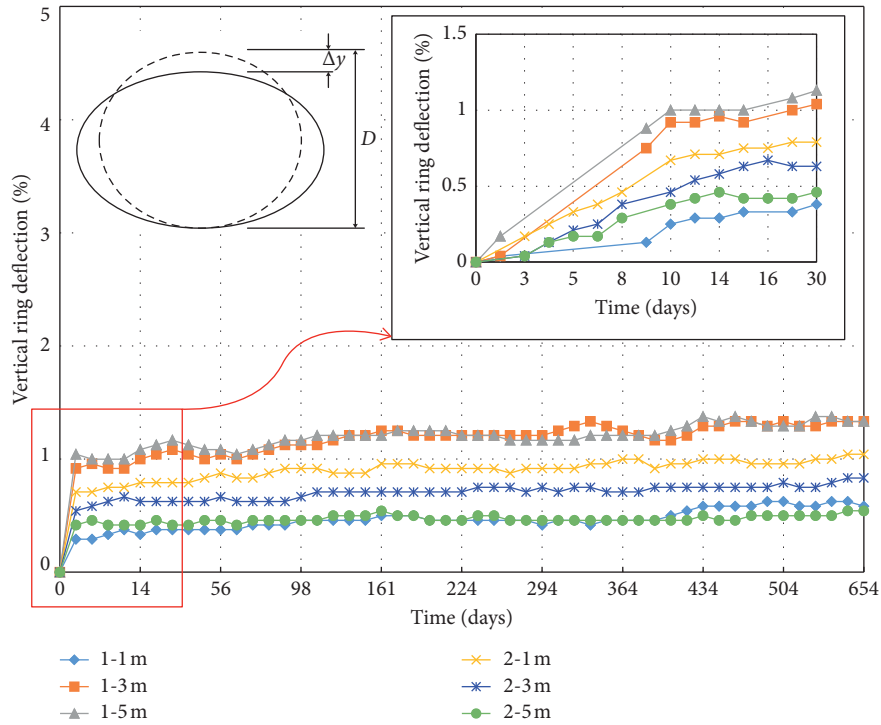
(a)
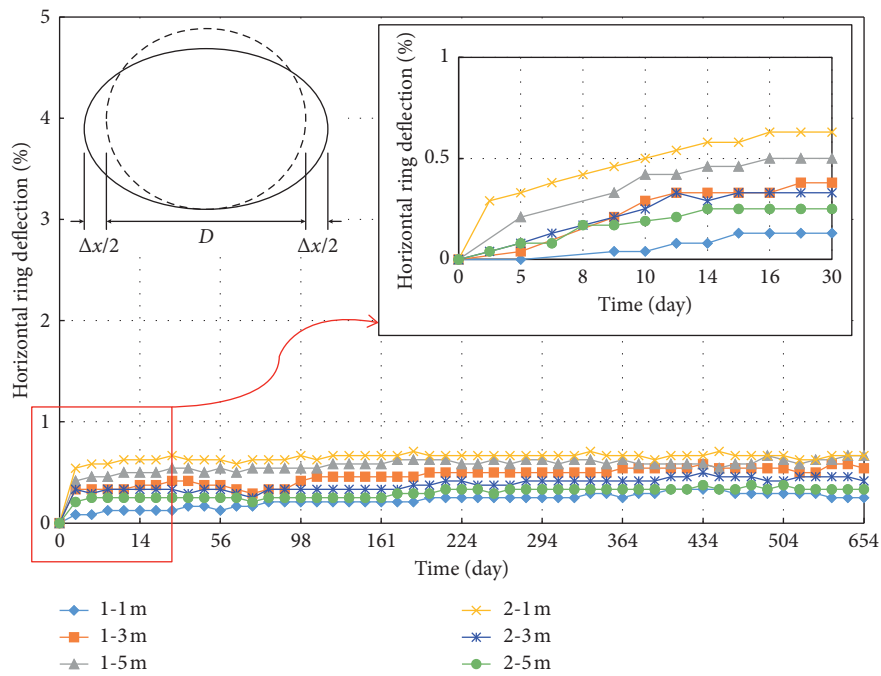
(b)

FIGURE 6: Measured deflections for the underground GFRP pipe.

decrease in vertical ring deflection and an almost equally increase in horizontal direction.

Figure 7 shows the comparisons between the vertical and horizontal pipe deflections and the pipe deflections in the AWWA M45 design method. The vertical pipe deflection for the case of the buried depth of 16 m is about 20 percent smaller than the pipe deflection predicted by AWWA M45. In that case,

the horizontal pipe deflection was estimated to be about 10 percent smaller than the deflection predicted by AWWA M45.

The vertical pipe deflection was also about 53 percent larger than the horizontal pipe deflection. However, the difference in the maximum pipe deflection that was actually measured is about 8 mm, which is almost negligible considering the measurement error of the design parameters,
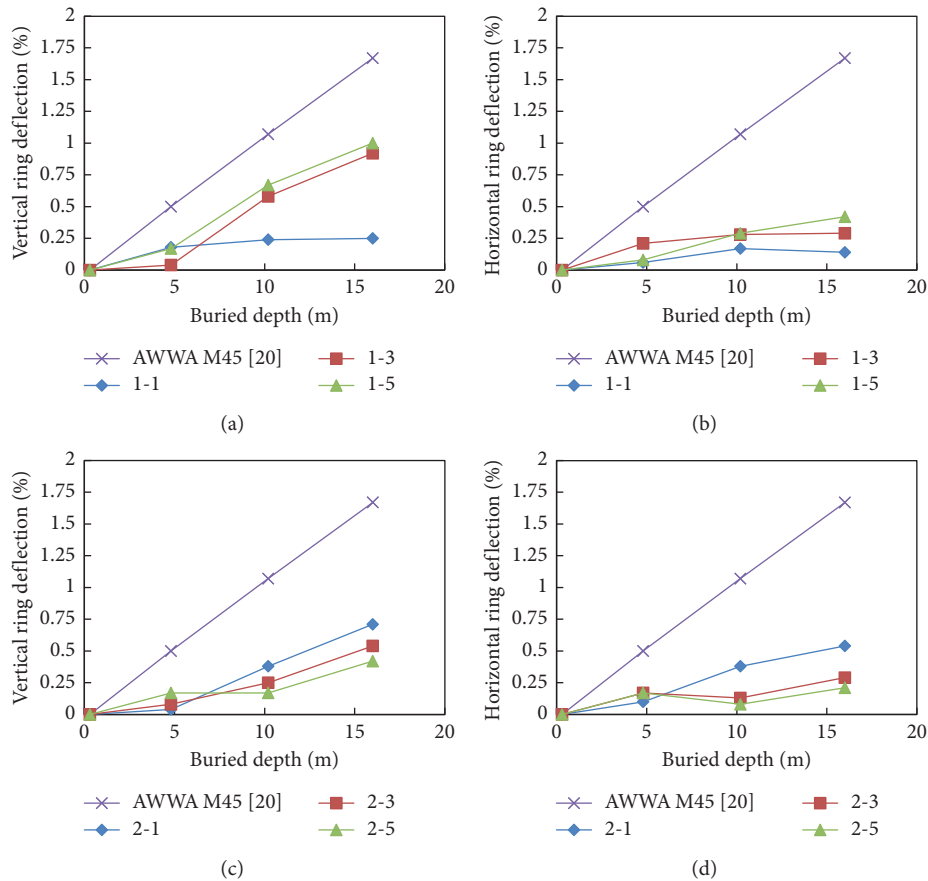
Figure 7: Comparison of ring deflection of the GFRP pipe with respect to buried depth.

such as the ground characteristics, given the 2,400 mm inner diameter of the pipe. In short, the AWWA M45 design method yields a conservative design, including the effects on long-term behavior.

The formula used in AWWA M45 for pipe deflection calculations was derived from the Iowa formula, which in turn was derived from an experimental study of small corrugated steel pipes. In the case of such small pipes, local excessive stress can be concentrated, and strict pipe deflection management is required. However, in the case of the pipe with a diameter of 2,400 mm, the curvature occurring in a pipe section is very small, and thus, the possibility of local excessive stress is negligible.

In addition, deflection occurs in the vertical direction due to the vertical load that is in turn due to the vertical deflection buried pipe, and this vertical deflection (Δ_v) is transferred to the horizontal deflection that is due to the characteristics of the circular section that is bound by the surrounding soil. Therefore, the vertical deflection is larger than the horizontal deflection ($\Delta_v > \Delta_h$) when the vertical load is not transmitted within all the horizontal deflections, but some of the energy accumulates in the pipe.

The Iowa formula is proposed to predict the horizontal deflection in this experimental study. However, in AWWA M45, the safety design (designed to produce less pipe deflection) is assumed to be the same ($\Delta_v \approx \Delta_h$) for both vertical and horizontal strains.

4.2. Effect of Pipe Stiffness in Ring Deflection. The parameters that determine the deflection of the underground GFRP pipe are the stiffness of the pipe, the stiffness of the ground, and the condition of the foundation. However, as time elapses, it is difficult to change the state of the foundation in the middle of these variables. Also, if the stiffness of the soil around the pipe is firmly consolidated, then any increase in the pipe deflection is mainly due to the mechanical properties.

In a previous study [9], the durability of the GFRP pipe did not change significantly under a low temperature range. However, the durability of the GFRP pipe may be decreased due to the various variables found in underground conditions that are used to predict pipe deflection in AWWA M45. Figure 8 shows the pipe deflection with respect to the various ring stiffness of the GFRP pipe. The pipe deflection was computed by equation (4).

The deflection of the GFRP pipe can be predicted by changing the PS from 288 kN/m² to zero, assuming that the GFRP pipe buried at 16 m has significantly reduced stiffness due to external environmental factors. When the PS is 288 kN/m², the pipe deflection is 2.515 mm, and when the PS is zero, the pipe deflection is 2.603 mm. Therefore, the effect of PS on pipe deflection is minor, having less than about 3.5 percent ring deflection. While the effect of PS and the soil foundation combined is about 96.5 percent, the fact indicates that the soil foundation is the dominant variable for pipe deflection.
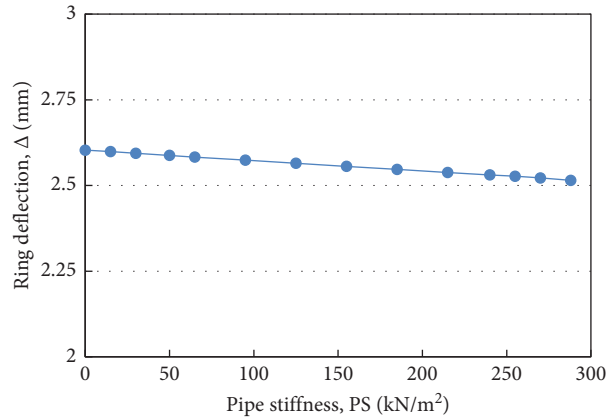
FIGURE 8: Ring deflection of GFRP pipe versus pipe stiffness.

TABLE 5: Predicted results of long-term ring deflection of pipe.

Period of time (year)	Long-term vertical deflection (%) location						Long-term horizontal deflection (%) location					
	1-1	1-3	1-5	2-1	2-3	2-5	1-1	1-3	1-5	2-1	2-3	2-5
10	0.7	1.49	1.44	1.11	0.86	0.55	0.47	0.69	0.72	0.73	0.53	0.42
20	0.77	1.57	1.5	1.17	0.9	0.56	0.55	0.76	0.75	0.75	0.57	0.45
30	0.81	1.62	1.54	1.2	0.92	0.58	0.6	0.8	0.77	0.76	0.6	0.47
40	0.84	1.66	1.56	1.22	0.94	0.58	0.65	0.83	0.79	0.77	0.62	0.49
50	0.86	1.68	1.58	1.25	0.95	0.59	0.68	0.85	0.8	0.77	0.65	0.5

4.3. Prediction of Long-Term Pipe Deflection. Although no specific method for predicting long-term pipe deflection has been developed yet, ASTM D5365 proposes a method to estimate long-term data for pipe deflection using statistical methods via the initial measurement data for pipe deflection. Equation (5) can be used to compute long-term deflection in accordance with ASTM D5365. The parameters a and b for pipe strain are defined as equations (6) and (7), respectively:

$$\text{ring deflection (\%)} = 10^{a - b \times \log_{10} t}, \tag{5}$$

where a and b are the parameters relating to ring deflection and t is the elapsed time (in hour):

$$a = Y - b \times X, \tag{6}$$

$$b = -(\gamma)^{0.5}, \tag{7}$$

where Y is the arithmetic mean of all the ring strain values, X is the arithmetic mean of all the time to failure in hours of observation, and γ is the slope of the load versus strain curve. The pipe deflection was predicted according to the time course proposed in ASTM D5365. This study predicted long-term pipe deflection up to 50 years after the GFRP pipe is buried. The computed results are summarized in Table 5.

Table 5 confirms that all of the pipe deflection that occurred after 50 years is within 5 percent. The allowable pipe deflection of 5 percent is considered to yield a very high safety factor of 4 from the structural point of view. Thus, judging from the fact that the standard of repair for pipe maintenance is limited to 7.5 percent in several of the

relevant design standards, the buried GFRP pipe has sufficient structural safety and long-term durability.

5. Conclusion

In this study, pipe ring deflections were measured in the field for the buried GFRP pipe. In addition, the FDA was carried out including various parameters, such as the soil compaction density of the bedding, backfill materials, and different depths. Both the analytical and experimental results were compared and discussed.

The pipe deflection measured by the field tests indicates that the vertical load increased with an increase in the soil depth at the initial stages of construction. The increase in the pipe deflection tended to decrease with the soil depth of 16 m.

The increase in pipe deflection after the completion of the embankment appears to have been caused by the fact that the backfill stabilized over time and that some load was added to the buried pipe due to the minor settlement of the soil around the pipe.

Field tests of the buried GFRP pipes were carried out for 664 days. The measured deflection of the GFRP pipes was less than 1.5 percent during these field tests. This measured deflection of 1.5 percent was less than the 5 percent pipe deflection suggested by AWWA M45. Also, the safety of the buried GFRP pipe was verified by field tests.

Data Availability

The data sets generated during and/or analyzed during the current study are available from the corresponding author on reasonable request.

Conflicts of Interest

Acknowledgments

References

[1] M. Farshad and A. Necola, "Effect of aqueous environment on the long-term behavior of glass fiber-reinforced plastic pipes," *Polymer Testing*, vol. 23, no. 2, pp. 163–167, 2004.

[2] M. Farshad, "Determination of the long-term hydrostatic strength of multilayer pipes," *Polymer Testing*, vol. 24, no. 8, pp. 1041–1048, 2005.

[3] H. Faria, A. Vieira, J. Reis, A. T. Marques, R. M. Guedes, and A. J. M. Ferreira, "Long-term behaviour of GRP pipes," *Science and Engineering of Composite Materials*, vol. 12, no. 1-2, pp. 55–62, 2005.

[4] H. Faria and R. M. Guedes, "Long-term behaviour of GFRP pipes: reducing the prediction test duration," *Polymer Testing*, vol. 29, no. 3, pp. 337–345, 2010.

[5] S. Sargand, T. Masada, B. Tarawneh, and D. Gruver, "Deeply buried thermoplastic pipe field performance over five years," *Journal of Geotechnical and Geoenvironmental Engineering*, vol. 134, no. 8, pp. 1181–1191, 2008.

[6] S.-H. Kim, J.-S. Park, and S.-J. Yoon, "Long-term ring deflection prediction of GFRP pipe in cooling water intake for the nuclear power plant," *Journal of the Korean Society for Advanced Composite Structures*, vol. 3, no. 3, pp. 1–8, 2012.

[7] S. H. Yoon and J. O. Oh, "Prediction of long term performance for GRP pipes under sustained internal pressure," *Composite Structures*, vol. 134, pp. 185–189, 2015.

[8] L. Na, Z. Sirong, C. Jianzhong, and F. Xi, "Long-term behavior of GFRP pipes: optimizing the distribution of failure points during testing," *Polymer Testing*, vol. 48, pp. 7–11, 2015.

[9] Y.-G. Lee, S.-H. Kim, J.-S. Park, J. W. Kang, and S.-J. Yoon, "Full-scale field test for buried glass-fiber reinforced plastic pipe with large diameter," *Composite Structures*, vol. 120, pp. 167–173, 2015.

[10] ASTM D5365, *Standard Test Method for Long-Term Ring-Bending Strain of "Fiberglass" (Glass-Fiber-Reinforced Thermosetting-Resin) Pipe*, ASTM, West Conshohocken, PA, USA, 2012.

[11] P. S. Bulson, *Buried Structures-Static and Dynamic Strength*, Chapman and Hall, London, UK, 1985.

[12] ASTM D2290, *Standard Test Method for Apparent Hoop Tensile Strength of Plastic or Reinforced Plastic Pipe by Split Disk Method*, ASTM, West Conshohocken, PA, USA, 2008.

[13] ASTM D638, *Standard Test Method for Tensile Properties of Plastics*, ASTM, West Conshohocken, PA, USA, 2010.

[14] ASTM D695, "Standard test method for compressive properties of rigid plastics," *Journal of Transportation Engineering*, 2010.

[15] ASTM D790, *Standard Test Method for Flexural Properties of Unreinforced and Reinforced Plastics and Electrical Materials*, ASTM, West Conshohocken, PA, USA, 2010.

[16] ISO 527-4, *Plastics-Determination of Tensile Properties-Part 4: Test Conditions for Isotropic and Orthotropic Fibre-Reinforced Plastic Composites*, ISO, Geneva, Switzerland, 1997.

[17] ASTM D2412, *Standard Test Method for Determination of External Loading Characteristics of Plastic Pipe by Parallel-Test Loading*, ASTM, West Conshohocken, PA, USA, 2012.

[18] J. K. Jeyapalan and B. A. Boldon, "Performance and selection of rigid and flexible pipes," *Journal of Transportation Engineering*, vol. 112, no. 5, pp. 507–524, 1986.

[19] MIDAS/GTS, *Analysis Reference*, MIDAS Information Technology Co., Ltd., Victoria, Australia, 2016.

[20] AWWA M45, *Fiberglass Pipe Design*, American Water Works Association, Denver, CO, USA, 2nd edition, 2005.